



UNIVERSITY OF
BIRMINGHAM

MICROFLUIDICS INVESTIGATION OF FOAM STABILITY

By

Leslie Anne LABARRE

A thesis submitted to the University of Birmingham for the degree of

DOCTOR OF PHILOSOPHY

School of Chemical Engineering

College of Physical and Engineering Sciences

University of Birmingham

June 2019

UNIVERSITY OF
BIRMINGHAM

University of Birmingham Research Archive

e-theses repository

This unpublished thesis/dissertation is copyright of the author and/or third parties. The intellectual property rights of the author or third parties in respect of this work are as defined by The Copyright Designs and Patents Act 1988 or as modified by any successor legislation.

Any use made of information contained in this thesis/dissertation must be in accordance with that legislation and must be properly acknowledged. Further distribution or reproduction in any format is prohibited without the permission of the copyright holder.

ABSTRACT

Aqueous foams are dispersions of gas bubbles in a liquid continuous phase and they are important for various applications from biological systems to Enhanced Oil Recovery. Foam stability relies on the use of surfactants/nanoparticles and on the rheological properties of the foaming liquid. One of nowadays challenges is to solve key foam industrial issues while considering their environmental impact. This duality is addressed by employing microfluidics to study static and dynamic foam stability.

In this thesis the foam stability is first studied in static conditions by investigating the use of highly stable bubbles termed bulk nanobubbles as potential surface-active agent on non-ionic and anionic surfactant-stabilised foams. This work has shown that the presence of nanobubbles in solution impacted significantly the foam stability and foamability. These findings suggest that nanobubbles attracted surfactant molecules at their interface and that nanobubbles adsorbed at the foam gas-liquid interface.

At low surfactant concentration, nanobubbles attraction removed surfactants molecules from the gas-liquid interface. This effect increased destabilisation of non-ionic surfactant foam. Oppositely, for anionic surfactant foams, the presence of nanobubbles enhanced foam stability. Indeed, nanobubbles enhanced the disjoining pressure within the thin liquid film due to an increase in the electrostatic repulsive forces between the two contiguous interfaces forming the film.

Subsequently, the rheological properties of the foaming liquid are considered. In particular, the influence on the “dynamic” foam stability or the property of the foam to resist and/or recover after the deformation was evaluated in a microchannel. This work

proposed a microfluidics approach to determine qualitatively the foam hysteretic behaviour after an induced deformation. This study has found that the viscosity and the bulk elasticity reduced the foam recovery. The result of this investigation showed that two mechanisms led to foam structural hysteresis after deformation: a retardation effect linked to the increase in viscosity and a tension thickening effect arising from the bulk elasticity.

À tous ceux que j'aime.

ACKNOWLEDGEMENTS

I would like to thank my supervisor Dr. Daniele Vigolo for his support, his guidance, and above all his trust, in my abilities and ideas throughout this experience.

I would like to thank also my co-supervisor Dr. Zhenyu Jason Zhang for his support and his guidance from my very first steps on the AFM until the last few months of my PhD.

I would like to express my appreciation to the Department of Chemical Engineering, University of Birmingham, UK, for founding this PhD.

Lastly, I would like to thank my family and my friends for their support and love throughout this experience and for making me who I am.

TABLE OF CONTENTS

Abstract	i
Dedication	ii
Acknowledgements	iii
Contents	iv
List of Figures	v
List of Tables	vi
List of Equations	vii
Abbreviations	viii
Nomenclature	ix
Chapter 1 Introduction.....	1
1.1 Introduction	2
1.2 Aims & objectives	4
1.3 Scope of research / Thesis outline	4
1.4 Research dissemination	6
Chapter 2 General background	8
2.1 Foams: description, properties and stability	9
2.1.1 Foam structure and properties	9

2.1.2 Foam destabilising phenomena	12
2.1.3 Foam surface active agents	13
2.1.2.1 Amphiphilic molecules	13
2.1.2.2 Particles as stabilising agents	18
2.1.2.3 Particles as destabilising agents	21
2.1.2.4 Bulk nanobubbles: a potential new kind of surface-active agent	22
2.2 Foam rheology: a key parameter for foam stability	29
2.2.1 Foam rheology: main properties	29
2.2.1.1 Macroscopic foam rheology: both a solid and a liquid	30
2.2.1.2 Thixotropy	32
2.2.1.3 Viscoelasticity	40
2.2.1.4 Surface rheology	41
2.2.2 Foam rheology studied via rheometry	45
2.2.2.1 Rotational test to study foam rheology	45
2.2.2.2 Oscillatory test to investigate foam rheology	46
2.2.2.3 Creep, three-step and hysteresis loop tests	48
2.2.2.4 Diffusive wave-spectroscopy combined rheometry	50
2.3 Microfluidics rheometry applied to foam: a new way to study foam rheological properties	52

2.3.1 Foam generation and study via microfluidics	53
2.3.2 Microfluidics rheometry for single phase fluids	55
2.4 Conclusions	59
2.5 List of references	61
Chapter 3 Materials & Methods	72
3.1 Materials	73
3.2 Methods	74
3.2.1 Solutions preparation.....	74
3.2.2 Microfluidics fabrication	75
3.2.2.1 Silicon wafer fabrication via rapid prototyping	75
3.2.2.2 PDMS device fabrication	76
3.2.3 Foam and nanobubbles generation methods via microfluidics	77
3.2.3.1 In-situ foam generation method and study in a microchannel	77
3.2.3.2 Microfluidics nanobubble generation method	79
3.2.4 In-situ investigation of 2D foam hysteretic behaviour	81
3.2.4.1 Three-step test description	82
3.2.4.2 Hysteresis evaluation	83
3.2.4.3 Flow curve extraction.....	84
3.2.5 3D foam generation for study bulk nanobubble effect on foam properties ..	86

3.2.6 Characterisation Methods	87
3.2.6.1 Dynamic surface tension characterisation	87
3.2.6.2 Rheological characterisation via rheometry	88
3.2.6.3 Surface characterisation: Atomic Force Microscopy (AFM)	89
3.2.6.4 Dynamic Light Scattering for Size measurement	90
3.2.6.5 Zeta Potential (ζ) measurement	95
3.3 List of references	99
Chapter 4 Investigating bulk nanobubble generation via microfluidics	102
4.1 Introduction	103
4.2 Results and discussions	105
4.2.1 Evidence of bulk nanobubbles generation	105
4.2.1.1 Bulk characterisation experiments	106
4.2.2 Effect of experimental conditions on bulk nanobubble generation	109
4.2.2.1 Effect of nozzle diameter on the bulk nanobubble properties	109
4.2.2.2 Effect of gas inlet pressure for a fixed liquid flow rate.....	111
4.2.2.3 Effect of generation cycle on the nanobubble size distribution	112
4.2.3. Effect of various additives on bulk nanobubble generation	114
4.2.3.1 Effect of surfactant on nanobubbles formation & stability	114
4.2.3.2 Effect of nanoparticles on nanobubbles formation & stability	119

4.3 Conclusions	130
4.4 List of references	132
Chapter 5 Effect of bulk nanobubbles on surfactant stabilised foam properties ..	134
5.1. Introduction	135
5.2. Results & discussions	139
5.2.1. Effect of bulk nanobubbles on the stability of foams solely stabilised by Triton X-100	140
5.2.1.1 0.5 cmc Triton X100	147
5.2.1.2 1 cmc Triton X-100	150
5.2.1.3 2.5 cmc TX100	152
5.2.1.4 5 cmc TX100	154
5.2.2 Effect of bulk nanobubbles on the stability of foams solely stabilised by SDS	156
5.2.2.1 0.5 cmc SDS	161
5.2.2.2 1 cmc SDS	163
5.2.2.3 2.5 cmc SDS	164
5.2.2.4 5 cmc SDS	166
5.3 Conclusion	167
5.4. List of references	169

Chapter 6 Microfluidics approach to investigate foam hysteretic behaviour	172
6.1 Introduction	173
6.2 Results and discussion	175
6.2.1 Foaming solutions properties and foam regime map	175
6.2.2 Reference solution: 5 cmc SDS	180
6.2.3 Effect of viscosity on hysteresis	184
6.2.3.1 5 cmc SDS + 20 wt. % glycerol	184
6.2.3.2 5 cmc SDS + 40 wt. % glycerol	187
6.2.4 Effect of surface elasticity	193
6.2.5 Effect of shear-thinning property	198
6.3 Conclusions	203
6.4 List of references	205
Chapter 7 Study of the effect of bulk versus surface elasticity on foam hysteresis in a microchannel	208
7.1 Introduction	209
7.2 Results and discussions	212
7.2.1 Reference solution: 5 cmc TTAB	215
7.2.2 Effect of surface elasticity on foam hysteresis	220
7.2.2.1 5 cmc TTAB + 0.05 g L ⁻¹ DOH	220

7.2.2.2 5 cmc TTAB + 0.2 g L ⁻¹ DOH	224
7.2.3 Effect of bulk elasticity on foam hysteresis	228
7.2.3.1 TTAB + 0.05 g L ⁻¹ DOH + PEO Mw = 3 x 10 ⁵ g mol ⁻¹ at 100 ppm	230
7.2.3.2 TTAB + 0.05 g L ⁻¹ DOH + PEO Mw = 3 x 10 ⁵ g mol ⁻¹ at 300 ppm	235
7.2.3.3 TTAB + 0.05 g L ⁻¹ DOH + PEO Mw = 1x10 ⁶ g mol ⁻¹ at 100 ppm	240
7.2.3.4 TTAB + 0.05 g L ⁻¹ DOH + PEO Mw = 1 x 10 ⁶ g mol ⁻¹ at 300 ppm	243
7.3 Conclusions	247
7.4 List of references	250
Chapter 8: Conclusions and Future Work	253
8.1 Conclusions	254
8.2 Future work	257
Appendices	264
A.1 Surface characterisation of nanobubbles via Atomic Force Microscopy	264
A.1.1 Direct force measurement: Atomic Force Microscopy (AFM)	269
A.1.2 Results and discussion	275
A.1.2.1 Pure water versus bulk nanobubbles water generated via microfluidics .	275
A.1.2.2 Bubbles in acidic solution versus bubbles generated via electrochemical reaction	284
A.2 Effect of gas inlet pressure for a fixed liquid flow rate and nozzle diameter ..	289
A.3 Effect of generation cycle on the nanobubble size distribution per nozzle	291

A.4 Effect of viscosity on nanobubbles formation & stability	294
A.5 List of references	297

LIST OF FIGURES

Figure 2. 1 Schematic representation of foam structure with one single plateau border, junction of three thin liquid films.	10
Figure 2. 2 Schematic representation of the three possible stages of surfactant monomer structure in water (free monomers, absorbed at the interface and micelles).	14
Figure 2. 3 Schematic representation of the surfactant behaviour evolution and its effect on the surface tension for an increasing surfactant concentration.	16
Figure 2. 4 Schematic representation of the position of a particle at an air-water interface for a contact angle (measured through aqueous phase) and the corresponding configuration of particles at a curved air-water interface.	20
Figure 2. 5 Consecutives stages for the thin films rupturing mechanisms caused by the presence of hydrophobic nanoparticles within the thin liquid film.	22
Figure 2. 6 Schematic representations of the three protocols employed to evaluate foam time-dependency by rheometry: (a) creep test, (b) three-step test and (c) the hysteresis loop test.	48
Figure 2. 7 Schematic representation of various microfluidic geometries employed for foam generation: (a) T-junction, (b) co-flow, and (c) flow-focusing.	54
Figure 3. 1 Schematic illustrating the micropatterning steps to fabricate the silicon master.	76
Figure 3. 2 Schematic of the 25 μm depth flow-focusing device (left) and a zoomed in view of the flow focusing junction (right) for foam generation.	78
Figure 3. 3 Schematic of the two-depth ($d_1 = 25 \mu\text{m}$ & $d_2 = 55 \mu\text{m}$) flow-focusing device (left) and a zoomed in view of the two-depth flow focusing junction (right) for bulk nanobubbles generation.	80
Figure 3. 4 Schematic representation of the cross-sectional view of flow-focusing two-depths device employed for bulk nanobubbles generation.	80
Figure 3. 5 Schematic representation of the zeta potential	96
Figure 4. 1 Bulk nanobubbles size distribution time evolution by intensity (a) & number (b) in pure water (30 min, blue - 1 week, orange - 1 month, green) via the 15 μm nozzle microfluidic device. The results represent the average of two experiments.	106
Figure 4. 2 Effect of nozzle diameter on bubble size distribution by intensity for one cycle of generation with the 10, 15 and 20 μm nozzle distribution represented as blue, red and purple lines respectively. The results represent the average of two to three measurements per nozzle.	109
Figure 4. 3 Effect of nozzle diameter on the Z-average (a) and the Polydispersity Index (PDI, (b)) evolution diameter evolution after 1 generation cycle with the 10 (blue), 15 (red) and 20 μm (purple) nozzle distribution. The results represent the average of two to three measurements per nozzle.	110
Figure 4. 4 Bulk nanobubbles intensity size distributions evolution in pure water 30 minutes (a) and 1 week after generation (b) through three generation cycles (C1, blue - C2, red - C3, green) via the 20 μm nozzle microfluidic device. The results represent the average of three experiments.	112
Figure 4. 5 Evolution of the Z-average diameter (a) and the Polydispersity Index (PDI, (b)) describing the bulk nanobubbles distribution in solution per cycle of generation for the 20 μm nozzle. The results represent the average of three experiments.	113
Figure 4. 6 Bulk nanobubbles size distributions by intensity 30 minutes (a) and one week after generation via the 20 μm nozzle device from a 0.5 cmc SDS solution through 3 generation cycles (C1, blue - C2, red - C3, green lines). The results represent the average of two	115

experiments.	
Figure 4. 7 Evolution of the Z-average diameter (a) and Polydispersity Index (PDI, (b)) describing the bulk nanobubbles distribution in 0.5 cmc SDS solution per cycle of generation for the 20 μ m nozzle. The results represent the average of two experiments.	115
Figure 4. 8 Bulk nanobubbles size distributions by intensity 30 minutes (a) and 1 week after generation (b) via 20 μ m nozzle device from a 0.6 cmc Triton X-100 solution through 3 generation cycles (C1, blue - C2, red - C3, green). The results represent the average of three experiments.	117
Figure 4. 9 Evolution of the Z-average diameter (a) and the Polydispersity Index (PDI, (b)) describing the bulk nanobubbles distribution in Triton X-100 solution per cycle of generation for the 20 μ m nozzle. The results represent the average of three experiments.	118
Figure 4. 10 200 nm hydrophilic polystyrene particle size distribution by intensity over time (1h, orange – 1 week, blue – 2 weeks, green lines). The results represent the average of two experiments.	120
Figure 4. 11 Bulk nanobubbles-nanoparticles size distributions by intensity 30 minutes (a) and one week (b) after generation from a nanoparticle aqueous solution through 3 generation cycles (C1, blue - C2, red - C3, green lines). The results represent the average of two experiments.	120
Figure 4. 12 Evolution of the Z-average diameter describing the bulk nanobubbles - nanoparticles distribution per cycle of generation for the 20 μ m nozzle. The results represent the average of two to three measurements per sample (cycle or reference).	121
Figure 4. 13 Evolution of the Polydispersity Index (PDI) describing the bulk nanobubbles - nanoparticles distribution per cycle of generation for the 20 μ m nozzle. The results represent the average of two to three measurements per sample (cycle or reference).	122
Figure 4. 14 200 nm hydrophilic polystyrene - Triton X-100 dispersion particle size distribution by intensity.	124
Figure 4. 15 Bulk nanobubbles-nanoparticles size distributions by intensity (a) 30 minutes and (b) one week after generation from a 1.2 cmc Triton X-100 + nanoparticle aqueous solution through 3 generation cycles (C1, blue – C2, red - C3, green lines). The results represent the average of three experiments.	125
Figure 4. 16 Evolution of the Z-average diameter (a) and Polydispersity Index (PDI, (b)) describing the bulk nanobubbles - nanoparticles – Triton X-100 distribution per cycle of generation for the 20 μ m nozzle. The results represent the average of two to three measurements per sample (cycle or reference).	126
Figure 4. 17 Reference silica nanoparticle size distribution by intensity. The results represent the average of two experiments.	127
Figure 4. 18 Bulk nanobubbles-nanoparticles size distributions by intensity 30 minutes (a) and one week (b) after generation from silica nanoparticle aqueous solution through 3 generation cycles (C1, blue - C2, red - C3, green lines). The results represent the average of three experiments.	128
Figure 4. 19 Evolution of the Z-average diameter (a) and Polydispersity Index (PDI, (b)) describing the bulk nanobubbles - nanoparticles distribution per cycle of generation for the 20 μ m nozzle. The results represent the average of two to three measurements per sample (cycle or reference).	128
Figure 5. 1 Dynamic Surface Tension results for the set of Triton X-100 solutions from 0.5 (◆,◇), 1 (■,□), 2.5 (▲,△ and 5 cmc (●,○) described by filled symbols for reference and by unfilled symbols for nanobubble-surfactant solutions. Each curve represents the average of three experiments per formulation.	140
Figure 5. 2 Z-average diameter & Polydispersity evolution for the nanobubble-surfactant dispersion before and after foaming for various surfactant concentrations. Each value is	142

obtained from an average of three experiments per sample.	
Figure 5. 3 Zeta potential evolution of the nanobubble-surfactant dispersion in water for various Triton X-100 concentrations (0.5, 1, 2.5 and 5 cmc) before (blue) and after (green) foaming. Each value is obtained from an average of three experiments per sample.	143
Figure 5. 4 Foam structure evolution after 5s deposition on a glass slide under a cover slip for various concentration of Triton X-100 (0.5 (a), 1 (b), 2.5 (c), 5 (d)) solutions & Triton X-100 – nanobubbles solutions at 0.5 (a'), 1 (b'), 2.5 (c') and 5 cmc (d').	144
Figure 5. 5 Foam height (a) and normalised foam height (b) evolution after 1-minute foaming for 0.5 (white), 1 (blue), 2.5 (purple) and 5 (green) cmc Triton X-100 solution (plain colours) versus bulk nanobubbles + Triton X-100 solution for 0.5 (dotted light grey), 1 (dotted blue), 2.5 (dotted dark grey) and 5 cmc (dotted green). Each value is obtained from an average of three experiments per sample.	146
Figure 5. 6 Initial foam liquid fraction for Triton X-100 solutions (filled symbols) versus bulk nanobubbles + Triton X-100 solutions (unfilled symbols) for various surfactant concentrations. Each value is obtained from an average of three experiments per sample.	147
Figure 5. 7 Schematic representation of the gas-liquid interface for the nanobubble-Triton X-100 mixture.	149
Figure 5. 8 Dynamic surface tension results for the set of SDS solutions from 0.5 (◆,◇), 1 (■,□), 2.5 (▲,△ and 5 cmc (●,○) described by filled symbols for reference and by unfilled symbols for nanobubble-surfactant solutions. Each curve represents the average of three experiments per formulation.	156
Figure 5. 9 Z-average diameter & Polydispersity (PDI) evolution for the SDS nanobubble-surfactant dispersion before and after foaming for various surfactant concentrations (0.5, 1, 2.5 and 5 cmc). Each value is obtained from an average of three experiments per sample.	157
Figure 5. 10 Zeta potential evolution of the nanobubble-surfactant dispersion in water for various SDS concentrations (0.5, 1, 2.5 and 5 cmc) before (blue) and after (green) foaming. Each value is obtained from an average of three experiments per sample.	158
Figure 5. 11 Foam structure evolution after 5s deposition on a glass slide under a cover slip for various concentration of SDS (0.5 (a), 1 (b), 2.5 (c), 5 (d)) solutions & SDS – nanobubbles solutions at 0.5 (a'), 1 (b'), 2.5 (c') and 5 cmc (d').	159
Figure 5. 12 Foam height (a) and normalised foam height (b) evolution after 1-minute foaming for 0.5 (white), 1 (blue), 2.5 (purple) and 5 (green) cmc SDS solution (blank colours) versus bulk nanobubbles + SDS solutions for 0.5 (dotted light grey), 1 (dotted blue), 2.5 (dotted dark grey) and 5 cmc (dotted green). Each value is obtained from an average of three experiments per sample.	160
Figure 5. 13 Initial foam liquid fraction evolution for SDS solutions (filled symbols) versus bulk nanobubbles + SDS solutions (unfilled symbols) at various surfactant concentrations. Each value is obtained from an average of three experiments per sample.	161
Figure 6. 1 Schematic of the three-step test consisting in an ascending and descending pressure ramp obtained by varying the gas pressure for a constant liquid pressure	174
Figure 6. 2 Rheological properties of solutions investigated: (A) 5 cmc SDS, (B) 5 cmc SDS + 20% (wt.) glycerol, (C) 5 cmc SDS + 40% (wt.) glycerol, (D) 5 cmc SDS + 0.15 g L ⁻¹ DOH and (E) 5 cmc SDS + 0.01 g L ⁻¹ XG + 5% (wt.) glycerol.	176
Figure 6. 3 Foam regime maps for the following solutions: (A) 5 cmc SDS, (B) 5 cmc SDS + 20% (wt.) glycerol, (C) 5 cmc SDS + 40% (wt.) glycerol, (D) 5 cmc SDS + 0.15 g L ⁻¹ DOH and (E) 5 cmc SDS + 0.01 g L ⁻¹ XG + 5% (wt.) glycerol. The red arrows from left to right represent the low (P1) and high (P2) pressure ranges investigated for each formulation.	177
Figure 6. 4 Hysteresis evolution for 5 cmc SDS at low (P1, black) and high pressure (P2, grey) sets for both pressure ramps (0.5 & 2 mbar s ⁻¹). In the inset, a typical hysteresis curve for P1 at 0.5 mbar s ⁻¹ .	181

Figure 6. 5 Experimental flow curves plotting the shear stress due to the drag force versus the shear rate for 5 cmc SDS solution at P2 and 0.5 mbar s ⁻¹ obtained from the ascending (blue) and descending (red) pressure ramps.	182
Figure 6. 6 Time lapses of the T1 bubble rearrangements for a fixed pressure set (P _{gas} = 400 mbar, P _{liq} = 600 mbar) for 5 cmc SDS from (a-f).	183
Figure 6. 7 Hysteresis evolution for 5 cmc SDS + 20% (wt.) glycerol at low (P1, black) and high (P2, grey) pressure sets for both pressure ramps (0.5 & 2 mbar s ⁻¹). In the upper graph, a typical curve presenting the hysteresis versus the pressure ratio for P2 at 2 mbar s ⁻¹ .	185
Figure 6. 8 Experimental flow curves plotting the shear stress due to the drag force versus the shear rate for 5 cmc SDS solution (filled symbols) at P2 (800 mbar liquid pressure) and 0.5 mbar s ⁻¹ versus 5 cmc SDS + 20% wt. GLY (unfilled symbols) at P1 (800 mbar liquid pressure) and 0.5 mbar s ⁻¹ obtained from the ascending (blue) and descending (red) pressure ramps.	185
Figure 6. 9 Time lapses describing the local bubble rearrangement for 5 cmc SDS + 20% wt. glycerol for 700 mbar gas pressure and 800 mbar liquid pressure.	186
Figure 6. 10 Hysteresis evolution for 5 cmc SDS + 40% (wt.) glycerol at low pressure set (P1, black) for both pressure ramps (0.5 & 2 mbar s ⁻¹). In the inset, a typical curve for P1 at 2 mbar s ⁻¹ .	188
Figure 6. 11 Hysteresis evolution for 5 cmc SDS + 40% (wt.) glycerol at high pressure set (P2, grey) for both pressure ramps (0.5 & 2 mbar s ⁻¹). In the inset, a typical curve for P2 at 2 mbar s ⁻¹ .	190
Figure 6. 12 Experimental flow curves plotting the shear stress due to the drag force versus the shear rate of the reference (filled symbols) versus the 40 % glycerol in water solution at P2 and 0.5 mbar s ⁻¹ (unfilled symbols) obtained for the ascending (blue) - descending (red) pressure ramps.	192
Figure 6. 13 Hysteresis evolution for 5 cmc SDS + 0.15 g L ⁻¹ DOH with the pressure ramp at low (P1, black) and high (P2, grey) pressure sets.	194
Figure 6. 14 Time lapses of the T1 bubble rearrangements for a fixed pressure set (P _{gas} = 400 mbar, P _{liq} = 600 mbar) for 5 cmc SDS + 0.15 g L ⁻¹ DOH from (a-f).	195
Figure 6. 15 Experimental flow curves plotting the shear stress due to the drag force versus the shear rate of the reference (filled symbols) versus the 5 cmc SDS + 0.15 g L ⁻¹ DOH in water solution at P2 and 0.5 mbar s ⁻¹ (unfilled symbols) obtained for the ascending and descending pressure ramps.	197
Figure 6. 16 Hysteresis evolution for 5 cmc SDS + 0.01 g L ⁻¹ XG + 5 % (wt.) glycerol at low (P1, black) and high (P2, grey) pressure sets for both pressure ramps (0.5 & 2 mbar s ⁻¹).	200
Figure 6. 17 Experimental flow curves plotting the shear stress due to the drag force versus the shear rate of the 5 cmc SDS (filled symbols) versus the 5 cmc SDS + XG solution at P2 & 0.5 mbar s ⁻¹ (unfilled symbols) obtained for the ascending (blue) -descending (red) pressure ramps.	202
Figure 7. 1 Dynamic surface tension measurements for various solutions made of 5 cmc TTAB.	212
Figure 7. 2 Rheological properties of the solutions: flow curves plotting the viscosity versus the shear rate.	214
Figure 7. 3 Foam regime maps plotting the gas inlet pressure (P _{gas}) versus the liquid inlet pressure (P _{liq}) for three solutions: (A) 5 cmc TTAB, (B) 5 cmc TTAB + 0.05 g L ⁻¹ DOH and (C) 5 cmc TTAB + 0.2 g L ⁻¹ DOH.	216
Figure 7. 4 Graph (a) introduces hysteresis evolution in an ascending (continuous black line – black dots) and descending (dotted black line – empty black dots) pressure ramps fixed at 0.5 mbar s ⁻¹ for a low pressure set (P1) from 300 to 650 mbar air pressure for a constant liquid pressure of 600 mbar. Histogram (b) summarises the hysteresis evolution for 5 cmc TTAB for	216

two pressure sets, low pressure set (P1, black) & high pressure set (P2, grey) for two pressure ramps (0.5 and 2 mbar s⁻¹). The red line represents the average value of hysteresis to describe negligible hysteresis.

Figure 7. 5 Experimental flow curves plotting the shear stress due to the drag force versus the shear rate for 5 cmc TTAB solution at P1 and 0.5 mbar s⁻¹ obtained from the ascending (blue dots) and descending (red dots) pressure ramps. 218

Figure 7. 6 Time lapses describing the T1 rearrangement at 450 mbar gas pressure and 600 mbar liquid pressure from (a) to (g) and at 500 mbar gas pressure and 600 mbar liquid pressure from (a') to (f') for 5 cmc TTAB. 219

Figure 7. 7 Graph (a) presents 5 cmc TTAB + 0.05 g L⁻¹ DOH hysteresis evolution in an ascending (continuous black line – black dots) and descending (dotted black line – empty black dots) pressure ramps fixed at P1 and 0.5 mbar s⁻¹. Histogram (b) summarises the hysteresis evolution for 5 cmc TTAB + 0.05 g L⁻¹ for two pressure sets, low pressure set (P1, black) & high pressure set (P2, grey) for two pressure ramps (0.5 and 2 mbar s⁻¹). 221

Figure 7. 8 Experimental flow curves plotting the shear stress due to the drag force versus the shear rate for 5 cmc TTAB solution (full circle) vs 5 cmc TTAB + 0.05 g L⁻¹ (empty circle) at P1 and 0.5 mbar s⁻¹ obtained from the ascending (blue) and descending (red) curves. 222

Figure 7. 9 Time lapses describing the T1 rearrangement at 450 mbar gas pressure and 600 mbar liquid from (a) to (g) and at 500 mbar gas pressure and 600 mbar liquid pressure from (a') to (f') for 5 cmc TTAB + 0.05 g L⁻¹ DOH. 223

Figure 7. 10 Graph (a) describes 5 cmc TTAB + 0.2 g L⁻¹ hysteresis evolution in an ascending (continuous black line – black dots) and descending (dotted black line – empty black dots) pressure ramp fixed at 2 mbar s⁻¹ at P1. Histogram (b) summarises the hysteresis evolution for 5 cmc TTAB + 0.2 g L⁻¹ DOH for two pressure sets, low pressure set (P1, black) & high pressure set (P2, grey) for two pressure ramps (0.5 and 2 mbar s⁻¹). 225

Figure 7. 11 Experimental flow curves plotting the shear stress due to the drag force versus the shear rate for 5 cmc TTAB solution (full circle) vs 5 cmc TTAB + 0.2 g L⁻¹ (empty circle) at P1 and 2 mbar s⁻¹ obtained from the ascending (blue) and descending (red) curves. 226

Figure 7. 12 Time lapses describing the T1 rearrangement at 450 from (a) to (e) and 500 mbar from (a') to (g') gas pressures for 600 mbar liquid pressure for 5 cmc TTAB + 0.2 g L⁻¹ DOH. 227

Figure 7. 13 Foam regime maps plotting the gas inlet pressure (P_{gas}) versus the liquid inlet pressure (P_{liq}) for the four solutions investigated: (D) 5 cmc TTAB solution + 0.05 g L⁻¹ DOH + 100 ppm Mw = 3x10⁵ g mol⁻¹ PEO, (E) 5 cmc TTAB solution + 0.05 g L⁻¹ DOH + 300 ppm Mw = 3 x 10⁵ g mol⁻¹ PEO, (F) 5 cmc TTAB solution + 0.05 g L⁻¹ DOH + 100 ppm Mw = 1 x 10⁶ g mol⁻¹ PEO and (G) 5 cmc TTAB solution + 0.05 g L⁻¹ DOH + 300 ppm Mw = 1 x 10⁶ g mol⁻¹ PEO. 230

Figure 7. 14 Graph (a) presents the 5 cmc TTAB + 0.05 g L⁻¹ + 100 ppm Mw = 3 x 10⁵ g mol⁻¹ PEO hysteresis evolution in an ascending (continuous black line – black dots) and descending (dotted black line – empty black dots) pressure ramps fixed at 2 mbar s⁻¹ and P2. Histogram (b) summarises of the hysteresis evolution for 5 cmc TTAB + 0.05 g L⁻¹ DOH + 100 ppm Mw = 3 x 10⁵ g mol⁻¹ PEO for two pressure sets, low pressure set (P1, black) & high pressure set (P2, grey) for two pressure ramps (0.5 and 2 mbar s⁻¹). 231

Figure 7. 15 Experimental flow curves plotting the shear stress due to the drag force versus the shear rate for 5 cmc TTAB + 0.05 g L⁻¹ solution (empty circle) vs 5 cmc TTAB + 0.05 g L⁻¹ + 100 ppm Mw = 3 x 10⁵ PEO (full circle) at P2 and 2 mbar s⁻¹ obtained from the ascending (blue dots) and descending (red dots) curves. 232

Figure 7. 16 Time lapses describing the T1 rearrangement at 450 from (a) to (g) and 500 mbar from (a') to (g') gas pressure and 600 mbar liquid pressure for 5 cmc TTAB + 0.05 g L⁻¹ DOH + 3 x 10⁵ g mol⁻¹ PEO. 234

Figure 7. 17 Graph (a) introduces 5 cmc TTAB + 0.05 g L⁻¹ + 300 ppm Mw = 3 x 10⁵ g mol⁻¹ PEO hysteresis evolution in an ascending (continuous black line – black dots) and descending (dotted black line – empty black dots) pressure ramps fixed at 2 mbar s⁻¹ for the highest pressure set (P2). Histogram (b) summarises of the hysteresis evolution for 5 cmc TTAB + 0.05 g L⁻¹ DOH + 300 ppm Mw = 3 x 10⁵ g mol⁻¹ PEO for two pressure sets, low pressure set (P1, black) & high pressure set (P2, grey) for two pressure ramps (0.5 and 2 mbar s⁻¹). 235

Figure 7. 18 Experimental flow curves plotting the shear stress due to the drag force versus the shear rate for 5 cmc TTAB + 0.05 g L⁻¹ 100 ppm Mw = 3 x 10⁵ g mol⁻¹ PEO solution (full circle) vs 5 cmc TTAB + 0.05 g L⁻¹ + 300 ppm Mw = 3 x 10⁵ PEO g mol⁻¹ (empty circle) at P2 and 2 mbar s⁻¹ obtained from the ascending (blue) and descending (red) curves. 236

Figure 7. 19 Graph (a) illustrates 5 cmc TTAB + 0.05 g L⁻¹ + 100 ppm Mw = 1 x 10⁶ g mol⁻¹ PEO hysteresis evolution in an ascending (continuous black line – black dots) and descending (dotted black line – empty black dots) pressure ramps fixed at 2 mbar s⁻¹ for the highest pressure set (P2). Histogram (b) summarises the hysteresis evolution for 5 cmc TTAB + 0.05 g L⁻¹ DOH + 100 ppm Mw = 1 x 10⁶ g mol⁻¹ PEO for two pressure sets, low pressure set (P1, black) & high pressure set (P2, grey) for two pressure ramps (0.5 and 2 mbar s⁻¹). 241

Figure 7. 20 Experimental flow curves plotting the shear stress due to the drag force versus the shear rate for 5 cmc TTAB + 0.05 g L⁻¹ 100 ppm Mw = 3 x 10⁵ PEO solution (empty circle) vs 5 cmc TTAB + 0.05 g L⁻¹ + 100 ppm Mw = 1 x 10⁶ PEO (full circle) at P2 and 2 mbar s⁻¹. 242

Figure 7. 21 Graph (a) depicts 5 cmc TTAB + 0.05 g L⁻¹ + 300 ppm Mw = 1 x 10⁶ g mol⁻¹ PEO hysteresis evolution in an ascending (continuous black line – black dots) and descending (dotted black line – empty black dots) pressure ramps fixed at 2 mbar s⁻¹ for the highest pressure set (P2). Histogram (b) summarises of the hysteresis evolution for 5 cmc TTAB + 0.05 g L⁻¹ DOH + 300 ppm Mw = 1 x 10⁶ g mol⁻¹ PEO for two pressure sets, low pressure set (P1, black) & high pressure set (P2, grey) for two pressure ramps (0.5 and 2 mbar s⁻¹). 244

Figure 7. 22 Experimental flow curves plotting the shear stress due to the drag force versus the shear rate for 5 cmc TTAB + 0.05 g L⁻¹ 300 ppm Mw = 3 x 10⁵ g mol⁻¹ PEO solution (empty circle) vs 5 cmc TTAB + 0.05 g L⁻¹ + 300 ppm Mw = 1 x 10⁶ g mol⁻¹ PEO (full circle) at P2 and 2 mbar s⁻¹. 245

LIST OF TABLES

Table 3. 1 Summary of the surfactants employed and their properties	73
Table 3. 2 Summary of additives used in foaming solutions.	73
Table 3. 3 Summary of nanoparticles properties investigated.	74
Table 6. 1 Summary of foaming solutions investigated: (A) 5 cmc SDS, (B) 5 cmc SDS + 20% (wt.) glycerol, (C) 5 cmc SDS + 40% (wt.) glycerol (D) 5 cmc SDS + 0.15 g L ⁻¹ DOH and (D) 5 cmc SDS + 0.01 g L ⁻¹ XG+ 5% (wt) glycerol. An average of three measurements were performed for each formulation.	175

LIST OF EQUATIONS

(2-1)	9
(2-2)	11
(2-3)	11
(2-4)	12
(2-5)	18
(2-6)	19
(2-7)	30
(2-8)	38
(2-9)	38
(2-10)	40
(2-11)	41
(2-12)	42
(2-13)	42
(2-14)	43
(2-15)	44
(2-16)	44
(2-17)	46
(2-18)	46
(2-19)	46
(2-20)	47
(2-21)	47
(3-1)	84
(3-2)	85
(3-3)	85
(3-4)	87
(3-5)	90
(3-6)	91
(3-7)	91
(3-8)	92
(3-9)	92
(3-10)	92
(3-11)	93
(3-12)	96
(3-13)	97

ABBREVIATION

Abbreviation	Description
AFM	Atomic Force Microscopy
cmc	Critical micellar concentration [mol L^{-1}]
DLS	Dynamic Light Scattering
DOH	Dodecanol
DTS	Diffuse-transmission Spectroscopy
DWS	Diffusing-wave Spectroscopy
DLVO	Derjaguin–Landau–Verwey–Overbeek
FRM	Foam regime map
GLY	Glycerol
HLB	Hydrophilic Lipophilic Balance
HOPG	Highly Orientated Pyrolytic Graphite
LDV	Laser Doppler Velocimetry
LVR	Linear Viscoelastic Range
MEMS	Micro-electro-mechanical systems
NTA	Nanoparticle Tracking Analysis
PAH	Poly(allylamine hydrochloride)
PB	Plateau border
PDMS	Polydimethyl Siloxane
PEO	Poly(ethylene) oxide
PDI	Polydispersity Index
PF-QNM	Peak-Force Quantitative Nanomechanics
PIV	Particle Image Velocimetry
Ppm	Part per million [$1 \text{ ppm} = 1 \text{ mg kg}^{-1}$]
PSPD	Position sensitive photo-detector

PSS	Poly(sodium 4-styrenesulfonate)
RMM	Resonant Mass Measurement
SDS	Sodium Dodecyl Sulfate
SEM	Scanning Electron Microscopy
SiOH	Surface silanol groups
SPM	Scanning probe microscopy
TAS	Total Analysis Systems
TPC	Three-phase contact line
TTAB	Tetradecyltrimethylammonium Bromide
TX100	Triton X-100
XG	Xantham Gum

NOMENCLATURE

Latin letter	Description
a	Particle radius [m]
A	Area, mean bubble area [m ²]
A_{cuv}	Cross-section of measuring cylinder [m ²]
c	Flow coefficient or consistency factor [Pa s]
C	Normalised circularity [-]
C_S	Surfactant concentration [mol L ⁻¹]
Ca	Capillary number [-]
d	Tip-sample separation distance, depth of channel [m]
d_1, d_2	Depth for the two-depths flow-focusing microfluidic device [m]
d_p	Particle separation distance [-]
D	Diffusion coefficient [m ² s ⁻¹]
E	Interfacial energy [J]
$E^*, E' \text{ or } E_S,$ E'', E_∞	Complex, elastic, loss and limiting surface dilatational moduli [Pa]
E_p	Energy required to remove a particle [J]
f	Frequency [s ⁻¹]
F	Force resulting from the tip-sample interaction for a constant load applied [N]
F_{drag}	Drag force [N]
F_S	Shear force [N]
$g^{(1)}(\tau)$	Normalised correlation function
G_0	Static elastic modulus [Pa]
G_S	Surface shear modulus [Pa]
G^*, G', G''	Complex, storage and loss moduli for purely elastic material [Pa]
$G_I(\tau)$	Correlation function for the intensity
h	Channel height [m]
h_f	Thin liquid film thickness at the channel wall [m]
h_{foam}	Foam height in the measuring cylinder [m]
h_g	Set distance or gap between two plates [m]
$\langle I(t) \rangle$	Average intensity of scattered light
k_b	Bubble spring constant [N m ⁻¹]
k_B	Boltzmann constant (1.38×10^{-23} m ² kg s ⁻² K ⁻¹)
k_c	Cantilever spring constant [N m ⁻¹]
k_{eff}	Slope measured in the contact line of force versus distance curve [N m ⁻¹]
k_s	Sample spring constant [N m ⁻¹]
K	Bubble network permeability [m ²]
L	Channel length [m]
L_B	Apparent bubble perimeter [m]
MW	Molecular weight [g mol ⁻¹]
n	"Herschel-Bulkley index" or flow index [-]
n_i	Solution refractive index [-]
N_1	First normal stress [Pa]
P_{gas}	Gas inlet pressure [mbar]
P_{liq}	Liquid inlet pressure [mbar]
$P(r, t 0,0)$	Probability density function [-]

r	Pressure ratio [-]
r_p	Radius of particle [m]
R	Mean bubble radius [m]
R_1, R_2	Principal radii of curvature [m]
s	Deflection path [m]
S	Channel cross-section [m ²]
$S_I(\omega)$	Frequency spectrum of the intensity of scattered light
T	Temperature [K]
U	Mean bubble superficial velocity [m s ⁻¹]
U_E	Electrophoretic mobility [m ² s ⁻¹ V ⁻¹]
V	Average liquid velocity [m.s ⁻¹]
V_b	Average bubble velocity [m s ⁻¹]
V_L, V_G	Volume of liquid and gas [m ³]
V_{foam}	Foam volume [m ³]
w	Channel width [m]
w_n	Nozzle width [m]
Z_c	Cantilever deflection [m]
Z_p	Cantilever position via piezoelectric translator normal to the surface [m]
Greek letter	Description
α	Exponent for surface elasticity [-]
α_p	Permeability coefficient of the medium [-]
δ	Tip indentation [m]
$\dot{\gamma}$	Shear rate [s ⁻¹]
$\gamma, \gamma(t)$	Shear strain [%]
$\Gamma(\theta)$	Width of Lorentzian shaped line
ΔA	Variation of surface area [m ²]
$\Delta\gamma_S$	Variation of dynamic surface tension [[N m ⁻¹]
$\Delta G_{T,P,n}$	Variation of free Gibbs energy [J]
ΔP	Laplace pressure [Pa]
Δx	Distance between two bubbles [m]
ε	Dielectric constant [-]
ϵ	Gibbs elasticity [Pa]
ζ	Zeta potential [mV]
η	Shear viscosity [Pa s]
η^*	Complex shear viscosity for purely viscous material [Pa s]
θ	Contact angle or scattering angle [°]
κ	Surface dilatational viscosity [Pa s]
κ^{-1}	Debye length [m]
λ	Incident light wavelength [m]
μ_s	Surface shear viscosity [Pa s]
v	Plate velocity from two-plate model [m s ⁻¹]
v_{T1}	Speed of T1 rearrangement [m s ⁻¹]
v_{foam}	Average foam velocity [m s ⁻¹]
Π_0	Osmotic pressure [Pa]
Π_D	Disjoining pressure [Pa]
ρ_L	Volumetric mass density of foaming liquid [kg m ⁻³]
σ	Surface tension [N m ⁻¹]
σ_{12}	Shear stress in the direction normal to the plan of deformation [Pa]
τ	Shear stress [Pa]
τ_B	Bubble life time [s]
τ_{drag}	Shear stress due to drag force [Pa]
τ_M	Tangential stress from Gibbs- Marangoni effect [Pa]
τ_{T1}	Relaxation time associated to T1 local bubble rearrangements [s]

τ_Y	Yield stress from Herschel-Bulkley model [Pa]
φ_l	Liquid volume fraction.
$\varphi_{l,rcp}$	Liquid volume fraction at the jamming transition.
φ_S	Deflection angle [rad]
ω	Angular frequency [rad s ⁻¹]

CHAPTER 1

INTRODUCTION

1.1 Introduction

Foams can be desirable or undesirable but they are present in everyone's and everyday life from the morning shaving foam and shampoo for a fresh start in the day to the milk foamed added to the coffee to make an invigorating latte at coffee break, to the chocolate mousse for dessert at lunch, to the refreshing ice-cream in summer time or to the foam obtained from the pouring of cold and freshly brewed beer. This detailed list, yet, not complete, is only a short sample of all the innumerable foam industrial applications.

This has led foam field of research to spread across numerous directions and dimensions for decades. Indeed, foams are versatile fluids that imply several levels of scaling from the macroscale illustrated by the assembly of millimetre-size bubbles down to the nanometre scale represented by the distribution of amphiphilic molecules at the gas-liquid interface.

This universality takes its origin in foam adaptability and resistance to its surrounding. Adaptability and resistance underline the foam property of longevity, that is, foam stability. Foam stability relies on several parameters from the surfactant nature, concentration, to the rheological property of the liquid phase. Foam ability to resist to its surrounding can be studied in static conditions by evaluating the foam decay time. Another way to study foam longevity is to analyse the foam property evolution while the foam is subjected to a continuous deformation. These two aspects are necessary to better understand the mechanisms at stake in foam stability. Thereby, this work gathers these two definitions of foam stability to investigate the parameters influencing this property at microscale.

Beneath the importance of foam stability in industry, one of nowadays industrial challenges is to reduce the impact of the industry on the environment. Several paths can be followed to achieve this goal. This project proposes to employ a cost-effective and environmental-friendly technique to generate and study foam properties. Indeed, microfluidics, defined as the study of fluid flow in micron-sized channel (Tabeling and Chen, 2005), is used here to tackle two problematics of foam stability. The first one aims to determine the effect of a new kind of surface-active agent, termed bulk nanobubbles, on foam properties that are generated by and employed to form foams via microfluidics. Bulk nanobubbles are highly stable bubbles naturally present in aqueous solutions and showing an average diameter below 1 micron (Alheshibri *et al.*, 2016). Bulk nanobubbles could offer a very interesting and harmless alternative to amphiphilic molecules and nanoparticles to stabilise foams.

The second objective of this project is to suggest a microfluidic approach to the common rheometric method to evaluate foam stability in dynamic conditions by studying the foam recovery properties after a deformation and to determine the parameters influencing this property. Indeed, foam time-dependent rheological properties are currently studied via rheometry (Bekkour and Scrivener, 1998a; Marze *et al.*, 2008). However, foam aging, in addition to the quantity of product required and the cost of the equipment, demonstrate the limitations of macroscale rheometry to study foams. Since a decade, an innovative use of microfluidics have been developed to analyse the rheological properties of single-phase fluids (Pipe and McKinley, 2009). Microfluidics rheometry matches the standards of its macroscopic counterpart with the benefits of requiring much less amount of sample and lower

cost. Thus, extending this use of microfluidics to foams can bring a new perspective for the evaluation of “dynamic” foam stability.

1.2 Aims & objectives

The present work aims to answer the following research questions:

- How microfluidics can be employed to evaluate and to improve foam stability in static conditions?
- How microfluidics can be used to evaluate foam dynamic stability?

The thesis sets out to investigate via microfluidics several aspects affecting foam stability. The main objectives are:

- (i) To assess the potential of bulk nanobubbles generated via microfluidics by optimising its generation and studying its interaction with various additives.
- (ii) To evaluate the performance of bulk nanobubbles as a potential stabilising or destabilising agent for foams via microfluidics.
- (iii) To establish an alternative method to the rheometric approach to evaluate foam recovery properties via microfluidics.
- (iv) To identify the parameters influencing foam hysteresis in a microchannel.

1.3 Scope of research / Thesis outline

The various concepts and topics involved throughout this thesis and employed to tackle the problematics addressed are reviewed and summarised in Chapter 2. It comprises a general background on the foam fundamental knowledge, such as its structure, properties and the mechanisms involved in foam stability. The link between foam and microfluidics is also explained throughout the evolution of the use of

microfluidics to investigate various aspects of foams and further to study the rheological properties of fluids.

In Chapter 3 are summarised the materials and methods employed throughout the thesis.

Chapter 4 introduces the generation of bulk nanobubbles via microfluidics and the study of the effect of various parameters (experimental conditions, addition of hydrophilic nanoparticles, addition of non-ionic and anionic surfactants) on bulk nanobubble properties. The repeat of the generation process enhanced the number of nanobubbles in solution. Furthermore, the presence of surfactants did not prevent the formation of bulk nanobubbles in solution.

In Chapter 5, the effect of bulk nanobubbles on foam stabilised by two kinds of surfactants (non-ionic and anionic) at various surfactant concentrations for a fixed amount of nanobubbles in solution was analysed. For the non-ionic and anionic surfactants, bulk nanobubbles affected significantly foam stability and foamability.

In Chapter 6, a novel approach to evaluate qualitatively the foam recovery properties after a deformation was developed. Furthermore, the effects of the viscosity, the surface tension, the surface elasticity and the shear-thinning property on foam hysteretic behaviour were studied. The viscosity caused an increase in foam hysteresis leading to a retardation effect. The viscosity of the foaming liquid solution was identified as being the main parameter influencing the foam recovery properties after a gradual deformation in a microchannel.

In Chapter 7, based on the previous study, the impact of the surface and bulk elasticities on foam hysteresis after a gradual deformation for various levels of

shearing at the microchannel wall is evaluated. At high surface elasticity, the foam hysteresis was emphasized due to a rise in surface tension whereas at low surface elasticity, the hysteresis was negligible. A much greater hysteresis was observed with bulk elasticity by introducing a tension-thickening effect.

Chapter 8 presents the general conclusions of this work and suggestions for future research in this field.

1.4 Research dissemination

The research presented in this thesis was disseminated as follows:

(i) Journal articles

This work has so far produced two publications:

- *A Microfluidics approach to investigate foam hysteretic behaviour*, L. Labarre, D. Vigolo, accepted for publication the 8/11/19 in *Microfluidics and Nanofluidics Journal*.
- *Microfluidics investigation of the effect of bulk nanobubbles on foam properties*, L. Labarre, D. Vigolo, in preparation for submission to *Langmuir Journal*.

(ii) Conference participation

This work was presented at two conferences:

- A poster presentation was given at the University Research Conference (University of Birmingham) about the characterisation of nanobubbles via Atomic Force Microscopy.

- An oral presentation entitled “Investigation of foam hysteretic behaviour via microfluidics” at the European Foam Conference *EUFOAM* at Lieges held in July 2018.

CHAPTER 2

GENERAL BACKGROUND

2.1 Foams: description, properties and stability

2.1.1 Foam structure and properties

Aqueous foam can be defined as a suspension of gas bubbles in a liquid medium.

Foams are thermodynamically unstable colloidal systems which can be classified in two categories (dry and wet foams) depending on how much liquid it contains. Two parameters are used to classify foams: the bubble size and the liquid fraction. These two factors play a crucial role in controlling foam physical properties. The foam liquid fraction φ_L is defined as the amount of liquid present within the foam and is expressed as follow:

$$\varphi_L = \frac{V_L}{V_{foam}} = \frac{V_L}{V_G + V_L} \quad (2-1)$$

with V_L and V_G , the volume of liquid and gas respectively. Foams can be classified in terms of their liquid fraction as follow:

- $\varphi_L \geq 36\%$: bubbly liquid with spherical and independent bubbles. The thickness of the liquid film between two neighbouring bubbles is generally between 10 nm to a few microns.
- $36\% \geq \varphi_L \geq 5\%$: wet foams composed of bubbles that become more and more compressed with the decrease in liquid fraction until they change from spherical to polyhedral shape. $\varphi_L \approx 36\%$ corresponds to random close packing of sphere structure. Wet foams are defined as foams presenting the highest amount of liquid with spherical bubbles. The transition between bubbly liquid to wet foam will vary depending on the foam polydispersity.

- $5\% \geq \varphi_L \geq 0\%$: dry foams described with polyhedral bubbles which contain the smaller amount of liquid. The bubble edges in dry foams are called Plateau borders (PBs); their junctions constitute vertices. From Plateau's rules, 3D foams in the dry limit and in equilibrium present three films joining at each PB at mutual angles of 120° , and four Plateau borders must form tetrahedral symmetric vertices (Weaire and Phelan, 1996). Edges and vertices of valence higher than those described previously are mechanically unstable and dissociate into stable ones.

Schematically, foams can be represented as illustrated in Figure 2. 1:

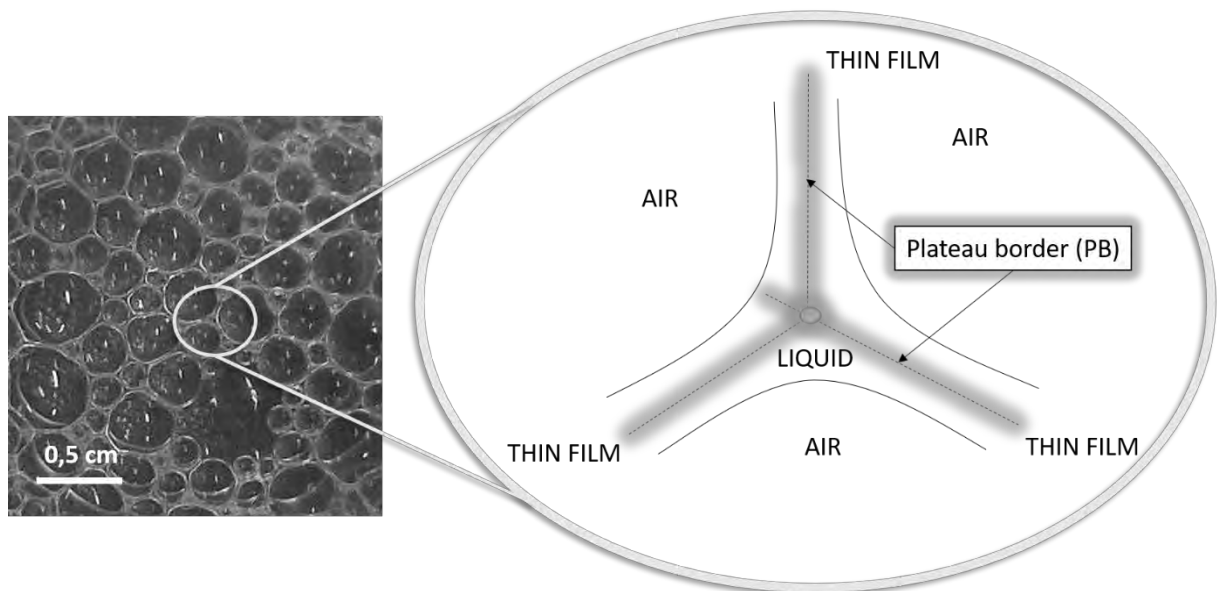


Figure 2. 1 Schematic representation of foam structure with one single plateau border, junction of three thin liquid films.

The liquid fraction isn't constant throughout the foam due to gravity: the liquid fraction increases from the top to the bottom of the foam height.

When a bubble is created within a continuous liquid phase, two forces are taking place: on one hand, the attractive Van der Waals forces ensure the liquid cohesion. On the other hand, a new interface is created. This creation is favourable because

the surface and the energy of the newly formed interface are minimised. Thus, the interface newly formed can resist against the Van der Waals forces acting to restore the continuity of the liquid phase. Therefore, bubble formation and stability rely on the balance between these two forces. Thereby, bubble existence and persistence are determined by evaluating how favourable is the formation of an interface. The surface tension σ is defined as the variation of Gibbs free energy $\Delta G_{T,P,n}$ for designated surface ΔA :

$$\Delta G_{T,P,n} = \sigma \Delta A \quad (2-2)$$

Surface tension is one of the key parameters influencing foam stability. Indeed, a pressure difference arises from the interfacial tension existing across a curved interface. Capillary or Laplace pressure is defined as the difference in pressure between the gas and the liquid phase due to surface tension. This difference can be expressed by the Young-Laplace equation that describes the pressure variation ΔP present across the curved surface between the PB and the gas bubble (Schramm, 2005):

$$\Delta P = \left(\frac{1}{R_1} + \frac{1}{R_2} \right) \sigma \quad (2-3)$$

with ΔP , the Laplace pressure and R_1 and R_2 the principal radii of curvature. For spherical bubbles such as in a wet foam, Plateau's law states that the Laplace pressure ΔP varies linearly with the surface tension σ and the mean interfacial curvature R as follow (Wilson, 1989):

$$\Delta P = \frac{2\sigma}{R} \quad (2-4)$$

Partially because of this pressure difference, foams are intrinsically unstable, and their structures evolve over time due to drainage, gas diffusion across the films separating neighbouring bubbles (coarsening) and film rupture (coalescence).

2.1.2 Foam destabilising phenomena

Drainage occurs when the gravity is acting upon the liquid flow within the PBs. Due to gravity, the liquid flows through films, PBs and vertices, thus, thinning the films driven by capillary suction. Capillary suction is generated by the pressure difference existing between the PB and the gas phase.

The coarsening or also called Ostwald ripening is driven by Laplace pressure difference between neighbouring bubbles which drives gas diffusion through the liquid films (Cantat *et al.*, 2013). This Laplace pressure difference causes the growth of larger bubbles from smaller ones. Coarsening leads also to swapping between neighbouring bubbles: the change in bubble edges causes a build-up of local strain. Once the edge length reaches zero, an unstable configuration is obtained, and two neighbouring bubbles are switched (Weaire and Hutzler, 2001). This process can occur naturally while foam structure evolves with time or it can also be induced by applying a macroscopic strain.

Finally, the thin liquid films become very film, break and lead to coalescence (Cantat *et al.*, 2013). Coalescence is driven by dynamic mechanisms and fluctuations arising in the film thickness causing film rupture. Between two bubbles, the film thins over time due to the gravity, but above all, because of the capillary suction in the plateau borders. The existence of significant repulsive forces within the film can help limiting coalescence by balancing the capillary suction.

Pure water cannot foam due to its high interfacial free energy. For foaming to occur, the presence of a solute able to adsorb itself at the gas-liquid interface is required. The solute employed is a surface-active agent which can alter the surface energy by adsorbing itself reversibly (amphiphilic molecule) or irreversibly (particle) at the interface.

2.1.3 Foam surface active agents

Up to now, two surface-active agents have been mainly used to stabilise gas-liquid interface: amphiphilic molecules and particles. However, the continuous need to improve foam formulations due to innovation faces another topical issue that is, the limitation of the environmental impact. Thus, a new kind of surface-active agent is introduced in the last section: bulk nanobubbles.

2.1.2.1 Amphiphilic molecules

Amphiphilicity can be described as the property of an entity to present a hydrophobic or non-polar group (strong affinity for non-polar solvent) and a hydrophilic or polar group (strong attraction to water or polar solvents). A surfactant is an amphiphilic molecule or surface-active agent that can adsorb and desorb reversibly at interfaces. By this action, it lowers the interfacial energy and the surface tension (Cantat *et al.*,

2013). Thus, it is easier to create and maintain a newly formed interface. There are four main classes of surfactant depending on the nature of the hydrophilic part: non-ionic (inorganic salt as hydrophilic head), anionic (negatively charged hydrophilic head), cationic (positively charged hydrophilic head), and zwitterionic (positively and negatively charged) surfactants.

The surfactant adsorption at the gas-liquid interface relies on the diffusion of the surfactant molecules from the bulk to the surface and on the continuous exchange between the adsorbed surfactant molecules between the bulk and the interface (Cantat *et al.*, 2013). Therefore, surfactants are present at once in the bulk, close to the surface and at the interface as illustrated in Figure 2. 2.

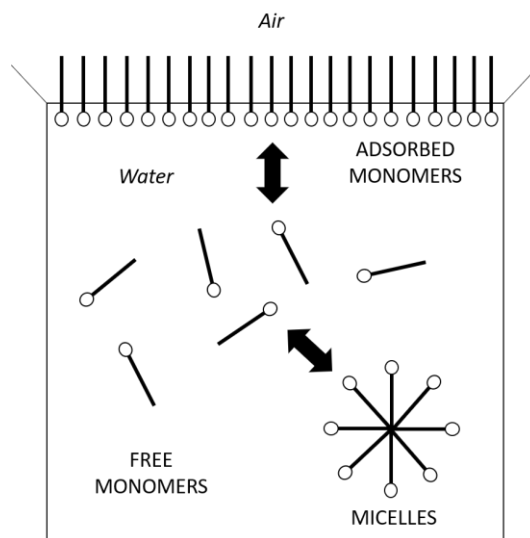


Figure 2. 2 Schematic representation of the three possible stages of surfactant monomer structure in water (free monomers, adsorbed at the interface and micelles).

The surfactant adsorbs itself at the interface to reduce the surface tension by placing its hydrophilic head in the water and its hydrophobic tail (hydrocarbon chain) directed towards the air. A continuous process of migration between the bulk and the surface is occurring due to the interaction forces existing between the surfactant molecules

and with the surrounding liquid. A subsidiary dynamic equilibrium is created to balance the lack of monomers present at the surface via a fast replacement process by diffusion from the bulk molecules. The surfactant adsorption efficiency will depend on the surfactant nature and structure. Indeed, ionic surfactants are better foamers than non-ionics because their ionic head groups increase the stability of the foam through electrostatic repulsion between the two sides of the foam lamella (Schramm, 2005). A third surfactant structure exists in solution in which surfactant monomers organise themselves to form aggregates or “micelles” in solution. This organisation process is also called micellization. Micellization is an energetically-favourable process driven by the intermolecular attraction between the non-polar tails and by the hydrogen bond (water-water molecule interaction). This process relies on the balance between the favourable forces (Van der Waals and hydrophobic forces) and the unfavourable ones (electrostatic repulsion). This structure requires a minimum number of surfactants in the bulk solution to be formed. Thus, the critical micellar concentration (cmc) is defined as the minimum concentration of surfactants required to form the first micelle in water at a specific temperature. These aggregates can arrange themselves in a broad range of structures including spherical, cylindrical, ellipsoidal, disk-shaped and rod-like arrangements (Cantat *et al.*, 2013). The most common micelle structure in water is represented in Figure 2. 2 with the non-polar tails gathered in the centre of a spherical monomer aggregate and the polar heads pointing towards the water. Micellization is an important process to stabilise durably an interface. Indeed, the micelles once formed act as surfactant reservoirs and ensure the constant number of surfactants adsorbing at the interface. Thus, from the cmc, the surface tension plateaus as illustrated in Figure 2. 3 and reaches its lowest

value because the interface is now fully covered by surfactants. By adding surfactants to the solution beyond the cmc, more free monomers are available to form more micelles in solution. Despite the reversible mechanism of surfactant adsorption-desorption, the surfactant monolayer is not altered because the micelles act as surfactant reservoirs and thus promote to the interfacial stability.

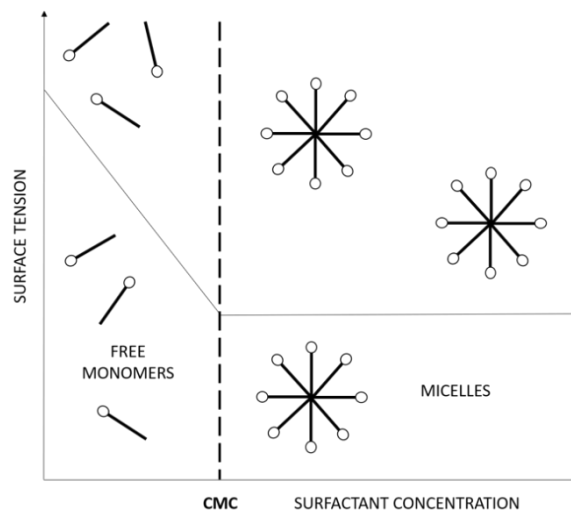


Figure 2. 3 Schematic representation of the surfactant behaviour evolution and its effect on the surface tension for an increasing surfactant concentration.

Thus, the interfacial stability and the foaming ability or “foamability” reach their maximum at or above the cmc. Two key factors to foam stability need to be considered: the diffusion rate of monomers from the bulk to the interface and from the bulk to the micelles. These two factors depend on the surfactant concentration C_S and on the surfactant nature.

At $C_S < cmc$, the main driving force to stabilise the interface is the diffusion rate of the free surfactant molecule from the bulk to the interface. The diffusion opposes the flow of liquid from the surface to the bulk directed towards the PBs causing the film to thin. Thus, the foam thins quickly and ruptures or remains in a metastable state called

“Newton black film” in which the film reaches an equilibrium thickness (Exerowa *et al.*, 1981).

At $C_S \geq cmc$, the diffusion process is dominated by the dynamic equilibrium of micelles formation, stability and its break-up into single molecules again. Consequently, the stable film persists at equilibrium.

Foam stability relies also on the foam structure: dry foams are more stable than wet foams because they present thinner films inducing a tighter packing of monomers along the interface that creates stronger repulsive forces, keeping the two interfaces forming the liquid film from getting closer.

These repulsive forces underline another contribution to foam stability: the disjoining pressure. The disjoining pressure π_d can be defined as the net pressure difference between the pressure in the thin film and the pressure in the bulk liquid from which the thin film extends (Schramm, 2005). The thinner the foam film is, the stronger the force becomes. This pressure comprises several simultaneous contributions acting on the foam film stability (Bergeron, 1999):

- The Van der Waals attractive forces between molecules in the foam film that bring the molecules together and thus, promote film thinning.
- The double layer repulsive forces resulting from the gathering of polar heads from the ionic surfactants present on each side of the film that get closer and repulse each other with the decrease in the foam film thickness.
- A steric contribution arising from the tight packing of surfactant molecules at the interface.

The higher the disjoining pressure due to a high electrical double layer repulsion, the more stable the foam becomes thanks to the decrease in the rate of film thinning and rupture. Nevertheless, this mechanism is not enough to sustain foam stability. An additional phenomenon is needed to balance the destabilisation process: if liquid flows along a surface containing surfactants, this surface can withstand a tangential stress thanks to the establishment of a surface tension gradient. Indeed, the liquid flow sweeps some surfactant molecules causing an excess in surfactant molecules, and a further decrease in surface tension downstream. The existence of the surface tension gradient causes streaming of the adjacent liquid. Thus, the stress τ_M caused by the velocity gradient due to the liquid and the one resulting from the surface tension gradient counterbalance each other. This effect is termed the Gibbs-Marangoni effect (Wilson, 1989) and can be expressed as follow:

$$\tau_M = \eta \left(\frac{dv_x}{dy} \right)_{y=0} = - \frac{d\sigma}{dx} \quad (2-5)$$

All in all, all these different mechanisms are contributing to foam stabilisation or destabilisation and need to be considered to understand how a specific component acts upon foam stability. This action can be reversible as for amphiphilic molecules or irreversible for particles as depicted in the following section.

2.1.2.2 Particles as stabilising agents

Particles have been considered as potential stabilising agents because they can adsorb irreversibly at an interface. A particle adsorbs irreversibly because it demonstrates a larger detachment energy to the interface unlike a single surfactant molecule (Hunter *et al.*, 2008). Foams stabilised by nanoparticles can be termed “Pickering foams” (Lam *et al.* 2014).

To evaluate this energy (E_p), a particle of radius r_p is considered initially dispersed in liquid and adsorbed at the interface. The energy required to attach or remove a particle from an interface is dependent upon the contact angle θ and the surface tension γ . The energy can be estimated for a particle with a diameter below 1 micron (gravity negligible) via this equation (Hunter *et al.*, 2008):

$$E_p = \pi r_p^2 \sigma (1 \pm \cos \theta)^2 \quad (2-6)$$

The resulting energy is very high compared to thermal energy (kT). Thus, particles once adsorbed at the interface can be thought as being irreversibly adsorbed contrarily to amphiphilic molecules.

One of the key parameters is the contact angle θ formed by the particle with the interface as illustrated in Figure 2. 4.

The most common particles employed to stabilise gas-liquid interface are silica nanoparticles. Since almost three decades, their effect has been investigated extensively by several researchers (Binks and Horozov, 2005; Horozov, 2008; Hunter *et al.*, 2008). Factors such as the effect of the wettability of the particle, the concentration and size of particles were studied on foam stability.

For hydrophilic particles such as metal oxide, θ measured in the aqueous phase is below 90° . The majority of the particle surface is placed in the water phase compared to the air (Binks, 2002). On the contrary, for hydrophobic particles such as hydrophobized silica, θ is greater than 90° and the particle resides more in the air than in the water phase. Thus, aqueous foams tend to be stabilised by partially hydrophobized particles such as silica which form monolayers curving so that the

larger area of the particle resides on the external side, in the water phase (Binks, 2002).

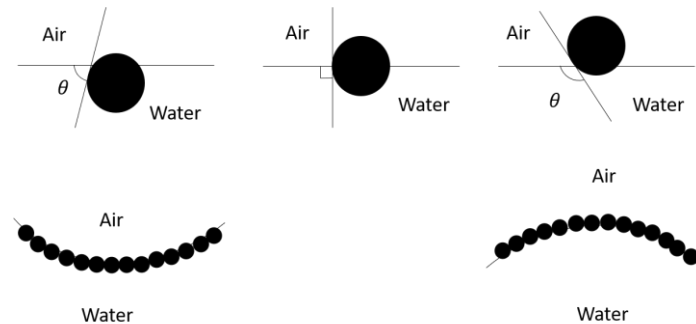


Figure 2. 4 Schematic representation of the position of a particle at an air-water interface for a contact angle (measured through aqueous phase) and the corresponding configuration of particles at a curved air-water interface.

Since almost three decades, the potential of solid nanoparticles alone for stabilising foams has been fully demonstrated (Den engelsen *et al.*, 1994; Binks and Horozov, 2005). Solid particles have also been employed in combination with surfactants to stabilise aqueous foams for many years, and their effect on the formation and foam stability relies strongly on the surfactant type, particle size and concentration. For hydrophilic particles, foam stability is enhanced because the particles in the liquid contained within the films and the plateau borders, slow down drainage. On the contrary, hydrophobic particles, can cause destabilisation because they enter the gas-liquid interface and lead to bridging-dewetting mechanism (Horozov, 2008).

This property of nanoparticles has been particularly of interest in froth flotation process which is commonly used as a particle separation method for minerals based on the attachment of particles to bubbles when the particles are dispersed in the liquid (Hunter *et al.*, 2008). Foams can also be stabilised by mixtures of surfactant-nanoparticles such as in Enhanced Oil Recovery (EOR) application whose foams are subjected to very harsh conditions of pressure and temperature (Arriaga *et al.*, 2012).

All these findings suggested that the main parameters influencing the properties of foam stabilised solely by particles were particle shape, size, concentration and hydrophobicity. However, particles can have a countereffect on foam stability as explained in the next section.

2.1.2.3 Particles as destabilising agents

Foams are sometimes undesirable in industrial processes. Consequently, researchers looked for ways to prevent their formation (antifoaming) or to break effectively the foam once formed (defoaming).

The history of antifoams can be split into two periods: a first period of “oil” antifoaming agents and a second period starting in 1970s until now dedicated to the combination of oil and hydrophobic nanoparticles (Karakashev and Grozdanova, 2012). These antifoaming agents are added to the aqueous phase, prior to foam formation and act to prevent or inhibit foam formation from within the aqueous phase. Several antifoaming agents have been used in industry such as oil droplets which reduce the surface elasticity by replacing the adsorbed surfactants on the interface with an insoluble film of oil (Pugh, 1996). This then leads to film rupture. Oil “lenses” can also break the foam by bridging: the drop first enters one surface and forms a lens followed by thinning, causing it to enter the other surface forming an oil bridge.

A similar mechanism was considered for partially hydrophobic nanoparticles leading to rupture of the thin film. For large hydrophobic spherical particles which can touch both surfaces of the film, dewetting occurs easily. The Laplace pressure in the film adjacent to the particle causes the liquid to flow away from the particle leading to enhanced drainage and the formation of a hole (Pugh, 1996). This peculiar effect is

strongly dependent on the particle size and degree of hydrophobicity. A decade later, Miller, (2008) stressed out that hydrophobic solid particles present in small quantity (not enough to cover bubble surfaces) could cause a bridging mechanism and thus foam destabilisation. Karakashev and Grozdanova (2012) further explained the film breaking ability by its dependence on the critical receding contact angle between the foam film and the particle. As described in Figure 2. 5, for spherical particles, if the receding contact angle is greater than 90° , then the particle can thin and break the film due to the emergence of a convex flow caused by the local capillary force near the particle.

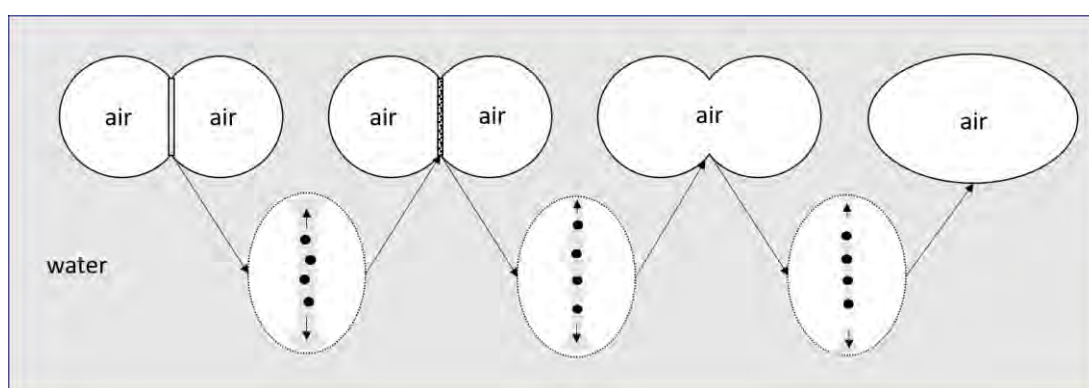


Figure 2. 5 Consecutive stages for the thin films rupturing mechanisms caused by the presence of hydrophobic nanoparticles within the thin liquid film.

The bridging-wetting mechanism of solid nanoparticles is composed of two stages: the junction of the two films via the particles approaching and entering the film, followed by the liquid dewetting from the nanoparticle and the resulting perforation of the three-phase contact (TPC) line on the particle surface (Denkov, Marinova and Tcholakova, 2014).

2.1.2.4 Bulk nanobubbles: a potential new kind of surface-active agent

Very recent studies demonstrate that this field of research is still very active due to the need of continuous improvement of the actual foam formulations to better solve

industrial problems (AlYousef *et al.*, 2017; McClure *et al.*, 2017; Wang *et al.*, 2017). All the studies reviewed so far, however, suffer from the fact that most nanoparticles or surfactants are bad for the environment. A natural progression of this work is to find new alternatives to stabilise foams in the line with one of nowadays topical issue which is the reduction of the impact of our industries on the environment. This change can be brought by the development of more environmental-friendly surface-active agents in the shape of biodegradable surfactants or nanoparticles. Another choice involves introducing a completely new kind of surface-active specie termed bulk nanobubbles.

There are two kinds of nanobubbles: surface nanobubbles defined as gas-filled spherical caps of 10 to 100 nm height and a contact line radius between 50 to 500 nm present on hydrophobic surfaces and bulk nanobubbles described as gas-filled spherical bubbles with a diameter below 1 micron located in the bulk of an aqueous solution (Alheshibri *et al.*, 2016).

Both kinds present an extraordinary stability: the evidence of stable nanobubbles with a diameter below 1 micron generated by shear in brine was reported for the first time by Johnson and Cooke (1981). Their gaseous nature was demonstrated because their size was increasing under vacuum and decreasing under pressure. Thus far, the surface nanobubble field of research has been the strongest compared to bulk nanobubbles.

a. Surface nanobubbles

Indeed, surface nanobubbles were firstly imaged 20 years ago by Lou *et al.* (2000) via Atomic Force Microscopy (AFM) on Highly Orientated Pyrolytic Graphite (HOPG).

Since then, several groups over the years studied the existence and the properties of surface nanobubbles on various surfaces and in several solutions via AFM. Other techniques have been employed to study nanobubbles such as total internal reflection microscopy (TIRM) (Jin *et al.*, 2008), via cryo-scanning electron microscopy (cryo-SEM) (Hernandez *et al.*, 2017) and also via optical microscopy (magnified 1000 times) by contrasting with methylene blue dye as reported by Azevedo *et al.*, (2016).

Surface nanobubbles can be generated by several techniques from direct immersion of a hydrophobic surface in an aqueous solution (Ishida *et al.*, 2000), via solvent-water exchange (Zhang *et al.*, 2005), to electrolysis of water (Zhang *et al.*, 2006).

Several theories for surface nanobubbles stability have been proposed: from the contaminants stabilising layer theory (Ducker, 2009), the contact-line pinning theory, the dynamic equilibrium model in which a gas influx and outflux replenished the spherical cap at the contact line due to gas attraction to hydrophobic surface (Brenner and Lohse, 2008), to very recently, the hydrophobic attraction stabilisation theory in which an attractive hydrophobic potential at the solid substrate was found to compensate the effect of gas saturation in solution (Tan *et al.*, 2018).

However, thus far, none of them gives all the answers to this topical problem. Indeed, such small bubble should exhibit a large internal Laplace pressure for a water surface tension considered to be 72.8 mN m^{-1} at 20°C . Consequently, they should present a very short lifetime from classical diffusion theory so that $\tau_B \approx \frac{R^2}{D} \approx 10 \mu\text{s}$ with D , the diffusion coefficient (Seddon *et al.*, 2012).

Furthermore, a pinning-supersaturation requirement to surface nanobubble stability was established throughout the years of research in the field (Lohse and Zhang,

2015). Yet, An *et al.* (2016) demonstrated that nanobubbles could exist in open systems and in undersaturated environment.

Most of the literature about nanobubbles focused on the properties and existence of surface nanobubbles. Fewer theories explained the existence and stability of bulk nanobubbles. Moreover, researchers haven't shed light on the link between these two bubble species.

b. Bulk nanobubbles

Bulk nanobubbles can be generated via a wide number of techniques from hydrodynamic cavitation (Oliveira *et al.*, 2018), ultrasonication (Cho *et al.*, 2005), solvent-water exchange (Zhang and Ducker, 2007; Zhang *et al.*, 2017), electrolysis of aqueous solutions (Yang *et al.*, 2009) to strong mechanical agitation (Ohgaki *et al.*, 2010). However, all these methods are energetically-costly and often imply the generation of contaminants. Nonetheless, Peyman *et al.* (2012, 2016) developed a microfluidics method to generate high throughput contrast agents for ultrasound imaging. Yet, no attempt was made to evaluate the parameters influencing bulk nanobubble generation via microfluidics.

Furthermore, bulk nanobubbles take already part in a wide range of applications from biomedical applications (Peyman *et al.*, 2012), froth flotation (Fan *et al.*, 2010) and cleaning of surfaces (Liu *et al.*, 2008; Chen *et al.*, 2009; Liu and Craig, 2009; Alheshibri and Craig, 2019).

Thereby, there is a real need to generate bulk nanobubbles in a environmental-friendly, well-controlled and safe manner at high throughput.

Thus far, their presence and properties have been studied in various solutions via Dynamic Light Scattering (DLS) (Jin *et al.*, 2007), via scanning-electron microscopy (SEM) (Ohgaki *et al.*, 2010), via Nanoparticle Tracking Analysis (NTA, Nanosight) (Nirmalkar *et al.*, 2018), and very recently via a resonant mass measurement (RMM) technique (Hernandez *et al.*, 2019).

Unlike surface nanobubbles, bulk nanobubbles are mobile and exhibit Brownian motion in solution (Seddon *et al.*, 2012). Furthermore, they present a negative zeta potential which was measured in various solutions (Cho *et al.*, 2005). The reason for this negative zeta potential was reported by Jin *et al.* (2007), in the line with previous results obtained by Marinova *et al.* (1996) showing that an interface is negatively charged because of the presence of hydroxyl ions from the dissociation-association of water molecules remaining at the interface. This negative surface charge generates both hydrodynamic and electrostatic repulsive forces arising respectively from the Brownian velocity and from the electrostatic double-layer repulsion, and thus limiting coalescence (Seddon *et al.*, 2012). Besides, other work demonstrated that the addition of salt in bulk nanobubbles could lead to their coalescence and aggregation due to charge screening (Jin *et al.*, 2007).

A very recent case reported by Nirmalkar *et al.* (2019) confirmed that bulk nanobubbles in pure water are stabilized by their surface charge arising from the adsorption of hydroxyl ions produced by self-ionization of water. Indeed, it was showed that nanobubbles cannot exist in concentrated aqueous organic solvent solutions simply because organic solvents do not self-ionize. Besides, the nanobubble zeta potential decreased with the solvent content led by the preferential adsorption of organic solvent molecules at the nanobubble interface. However,

nanobubble persisted in solution thanks to the significant hydrogen bonding near its interface.

Surface tension is likely to be a key parameter in bulk nanobubbles stability. Indeed, Zhang *et al.* (2017) showed that bulk nanobubble generation can be enhanced by the use of ethanol-water solution which change not only the gas solubility in solution but also the air-water interfacial tension. The effect of surface tension on bulk nanobubbles via the addition of a triblock copolymer surfactant Pluronic L10 has been investigated via optical tensiometry and Langmuir-Blodgett trough (Hernandez *et al.*, 2018). In this paper, the tensiometry results were not conclusive but the Langmuir-Blodgett trough highlighted an interesting effect of Pluronic on the nanobubble equilibrium surface tension for different levels of compression where the surface tension decreased by almost 30%. However, these results showed too much variability in terms of monolayer structure and compositions to be conclusive.

Yasui *et al.* (2018) reported and discussed several bulk nanobubbles stability theories. Nirmalkar *et al.* (2018) reported that consecutive steps of freezing-thawing of nanobubbles solution were drastically reducing the number of nanobubbles in solution without destroying completely all nanobubbles from the solution. Furthermore, it was found that in acidic medium, nanobubbles became unstable whereas in basic medium, they showed an enhanced stability. It was also briefly mentioned that the addition of Sodium Dodecyl Sulfate (SDS, anionic surfactant) to the solution was enhancing the negative zeta potential of the nanobubble dispersion; therefore, enhancing the stability of the nanobubbles.

Fewer attention has been given to the study of the effect of bulk nanobubbles on colloidal systems. The literature based on surface nanobubbles suggest that these bulk nanobubbles could play an important role in various colloidal phenomena without even being noticed.

Indeed, one of the mechanism proposed to explain the long-range hydrophobic attraction relies on the coalescence and bridging of surface nanobubbles present on hydrophobic surfaces (Attard, 2003).

Stöckelhuber *et al.* (2004) explained the process of rupture of foam thin liquid film on a surface by the action of nanobubbles on the surface. It was demonstrated that in the process of wetting film drainage on a hydrophobic surface, a nanometre-size liquid foam film could be created between the surface nanobubble and the wetting film surface. An additional capillary pressure arising from the Derjaguin – Landau – Verwey – Overbeek (DLVO) (repulsive in wetting film and attractive in the foam film) forces enhanced the foam film destabilisation leading to film breakage. Later, Karakashev and Nguyen (2009) established that the migration of dissolved gas was impacted significantly the film rupture. All these findings suggest that nanobubble could act as surface-active agents notably in the case of foams stabilised by nanoparticles. Indeed, Zhang and Seddon (2016) demonstrated that nanobubbles could nucleate or attach to gold nanoparticles above a critical diameter of 60 nm. Furthermore, Knüpfer *et al.* (2017) found that the presence of bulk nanobubbles in a solution containing hydrophobic nanoparticles within a stirred vessel was enhancing the amount of hydrophobic agglomerates obtained. Very recently, Tao *et al.* (2019) pushed forward the nanobubble-nanoparticle interaction investigation by observing the effect of nanobubbles on the trajectory of solid particles of different levels of

hydrophobicity. It was found that the particle hydrophobicity enhanced the particle-bubble interaction process by modifying the balance between the hydrodynamic and surface forces controlling the trajectory of a particle moving around a bubble surface. Additionally, the case study related by Zhang *et al.* (2019) confirmed the importance of the action of bulk nanobubbles in colloidal systems. Indeed, nanobubbles showed the property to induce a charge inversion of positively charged latex nanoparticles leading to an increase in particle hydrodynamic diameter and further aggregation. Overall, these cases support the view that nanobubbles could affect significantly Pickering foam stability.

The nature of the surface-active agent either amphiphilic molecule or nanoparticle, is of great importance in foam stability. The stabilising effect of the surfactant depends on the solubility of the amphiphilic molecule within the continuous phase, but also on the flow of liquid within the plateau borders. This flow relies on the continuous rheological properties such as its viscosity and its viscoelasticity.

Foam stability often refers to the foam left to evolve with time in static conditions. However, in everyday life, foams are submitted to numerous deformations. Thus, the studies of the flow properties of foams and of foam stability in static and in dynamic conditions are required to evaluate how the foam responds to the deformation. This prerequisite leads us to the study of foam rheology.

2.2 Foam rheology: a key parameter for foam stability

2.2.1 Foam rheology: main properties

Rheology is defined as the science of deformation and flow of complex fluids whose behaviour varies between liquid-like and solid-like fluid. Foam rheology can be

examined at different scales from the macroscale which describes the foam as a soft solid, the micron-scale for the study of the flow of bubble to the sub-micron/nanometre range for the evaluation of the flow of liquid within the PBs.

2.2.1.1 Macroscopic foam rheology: both a solid and a liquid

Aqueous foams can behave as liquid-like or solid-like fluids depending on the applied deformation and on the experimental timescale. This duality is characterised by the existence of a yield stress at which the foam behaviour changes from solid-like (elastic) to liquid-like (viscous). This behaviour can also be qualified as “jammed” for solid-like and “unjammed” for liquid like. The transition between these two states is called the “jamming transition” (Nordstrom *et al.*, 2010). Indeed, below this critical stress, the foam elasticity prevails because the small applied stress enhances the gas-liquid interfacial area and thus, the energy per unit volume (Höhler and Cohen-Addad, 2005). Beyond this threshold value, irreversible local bubble rearrangements are occurring, and the foam behaves like a viscous non-Newtonian fluid.

To describe this complex behaviour, the Herschel-Bulkley model is commonly employed in rheometry to characterise foam rheological behaviour (Weaire, 2008):

$$\tau = \tau_Y + c \dot{\gamma}^n \quad (2-7)$$

with τ_Y , the yield stress (Pa) according to this model, c , the flow coefficient or consistency factor (Pa s) and n , the exponent also called “Herschel-Bulkley index” or flow index which counts $n > 1$ for shear-thickening fluid, $n < 1$ for shear-thinning fluid and $n = 1$ for “Bingham behaviour” (Mezger, 2014). Indeed, Bingham model can also be used to illustrate foam behaviour in which foam is considered only as a yield stress fluid.

Furthermore, Hershel-Bulkley model presumes that the flow is always homogeneous at any shear rates providing that the shear stress is also homogeneous throughout the geometry.

For foams, n is below 1 because above yield stress, foams behave like viscous non-Newtonian fluids, more precisely like shear-thinning fluids. Indeed, foam viscosity η (Pa s) decreases for an increasing shear rate $\dot{\gamma}$ (s^{-1}). At low shear rates, a shear localization is occurring in small regions inducing high local shear rate and bubble rearrangements whereas the remaining fluid behaves like a solid-like fluid. At high shear rate, foams behave like liquid-like fluids above a threshold stress value: the yield stress. Nevertheless, the yield stress is not a constant value or a material characteristic: since it depends on the sample shear history (preparation, test conditions) (Møller *et al.*, 2006).

This stresses out a key aspect in foam rheology: its dependence over time. Foam yield stress is linked to the microscopic mechanisms occurring within the foam. These microscopic events originate from the resistance of the individual bubbles to deformation and reorganization. Foam resistance to the deformation is expressed at bubble scale by the local rearrangements. Indeed, the yield stress for foams is considered as the onset of the bubble rearrangements. The yielding process is intrinsically related to the occurrence of the local bubble rearrangement. Parallely, the destruction and restructuration over time of such microstructure by flow is believed to be the origin of thixotropy (Møller *et al.*, 2006). Thixotropy is an important property for complex fluids. There is to be very few if any examples of yield stress fluids which are not also thixotropic. This characteristic property is explained in the following section.

2.2.1.2 Thixotropy

Thixotropy refers to a shear-thinning flow which is time dependent. As studied by Weltmann (1943) for the first time, thixotropy can be expressed at a constant applied shear rate when the fluid viscosity decreases and returns to its original value after a certain time once the deformation has ceased.

In a flow curve representing the viscosity evolution versus the shear rate applied, the phenomenon leads to the creation of a hysteresis or a difference in viscosity evolution. Thus, thixotropic behaviour can also be termed as hysteretic. As well described by Møller *et al.* (2006), the main explanation for thixotropy is that the change in viscosity is due to the change in microstructure of the constitutive components in the fluid that interconnect and resist large rearrangements. When deformed, the fluid structure is destroyed, and the resulting viscosity decreases. Then, when left at rest, the microstructure slowly rebuilds itself and the viscosity recovers its original value. Sometimes, a viscosity increase linked to microstructure build-up of a sample left at rest is called “aging”. Reversely, the viscosity reduction and microstructure destruction in time under deformation (thixotropy) is termed “shear rejuvenation” (Møller *et al.*, 2006). Indeed, the destruction and restructuration of the structure is seen as to rejuvenate the initial structure.

Foam aging is driven by three destabilising events (drainage, coalescence and coarsening) (Cantat *et al.*, 2013). If the right amount of surfactants is used, coalescence can be neglected. 3D foams age mainly due to drainage. The aging process is driven by coarsening that leads to bubble rearrangements and local relaxation of interfacial energy. The rate of these events decreases as the foam ages (Cohen-Addad *et al.* 2013).

The hysteretic behaviour is dependent not only upon the magnitude of the applied shear but also on the time interval over which the shear is applied (Schramm, 2005). In a continuous medium, thixotropy arises because after the deformation, it takes some time for the interparticle or intermolecular structure to recover. In the same way, after the deformation has stopped, some time is needed for the original configuration to be restored. If enough time is given to the system to recover fully, then it will eventually regain its original structure. Coussot *et al.* (2002) depicted another time-dependent phenomenon for granular fluids termed “viscosity bifurcation” in which the viscosity for a constant stress evolved either towards an infinite value or towards the lowest value depending on the shear rate history of the sample. An interesting phenomenological model described by Coussot *et al.* (2002) considered the viscosity evolution to illustrate the instantaneous state of material structure. The granular structure evolution was determined by the balance between the restructuration driven by the fluid structure versus the destruction process dominated by the instantaneous shear rate. Thus, at low deformation, the restructuration process dominating, the viscosity increased until the jamming transition and the fluid ceased to flow. On the contrary, at high deformation, the destruction stage led to an acceleration of the fluid flow.

Da Cruz *et al.* (2002) demonstrated that foams become more and more fluid after a rapid shear deformation and restructure under a small applied stress. Regarding the phenomenological interpretation of this time-dependent behaviour, another attempt was made to describe foam time-dependent behaviour via a rheological model describing dry granular materials as further explained by Da Cruz *et al.* (2002). Indeed, it was pointed out that the viscosity variations in granular systems were

linked to the change of spatial particle configuration (coordination number, friction repartition). It was stressed out that for foams, the relationship between microstructure and hysteretic behaviour was more complex because it implied other phenomena such as local and collective rearrangements at rest whereas at high deformation, the bubbles were deformed.

The model employed to describe the balance between structuration and destruction summed up the two forces acting on a single grain, namely a trapping force F_0 and a second force F_∞ representing the steady motion controlled by both the collisional dissipation and the gravity. Despite a good fitting for their experimental data obtained with Gillette foam, this model did not consider any microscopic origins or characteristic times at stake in foam dynamics. It was underlined that there was more at stake than the simple exhibition or annihilation of flow in response to a deformation.

Later, a simple model for yield stress fluids taking into account thixotropy was proposed by Møller *et al.* (2006) in which a structural parameter λ , represented the local degree of interconnection of the microstructure or a measure of the number of connections per unit volume. The number of connections per unit volume could be related to the elastic modulus of a physical gel.

For foams, it can be thought as a measure of the jamming level of the foam structure. Consequently, the fluid viscosity should increase with an increasing λ . More complex models describing thixotropic fluids were detailed in the literature (Mewis and Wagner, 2009; de Souza Mendes and Thompson, 2012; Larson, 2015).

Thixotropy causes other phenomena to occur such as the one termed “avalanche” seen in granular materials in which a decrease in viscosity leads to an acceleration of the fluid flow rate, which then promotes the fluid reduction in viscosity (Barés *et al.*, 2017). The term “avalanche” has been also used in foams to illustrate the shear deformation, topology change of network or rearrangements of bubbles intermittently occurring in large strain regimes (Gunes *et al.*, 2010).

T1 local bubble rearrangements can be defined as irreversible bubble neighbour switching events (Dennin, 2004). T1 local bubble rearrangements or also called individual plastic events (irreversible and localized structural changes) are occurring in dry foams driven by local mechanical and thermodynamic equilibria led by Plateau’s laws. In foams, rheology and geometry are linked. Indeed, since as the foam structure is altered, rearrangements occur until a configuration is obtained which satisfies Plateau’s laws described previously.

Durand and Stone (2006) associated the relaxation time τ_{T1} with the process of bubble rearrangement was related to two parameters, $\frac{\mu_s + \kappa}{\sigma}$ and $\frac{\mu_s + \kappa}{\epsilon}$ with μ_s and κ , the shear and dilatational viscosities, σ , the surface tension and ϵ , the Gibbs elasticity.

Thus, for a fixed surface tension, the typical relaxation time after a T1 event is related to the viscoelastic properties of the gas-liquid interface, notably, the surface μ_s and dilatational viscosities κ and the Gibbs elasticity ϵ . A characteristic rearrangement time of about 30 ms was estimated for a solution of SDS for their specific experimental conditions.

From the existing relationship described by Durand and Stone (2006) limited to the case of dry foams at low strain rate regime, the T1 bubble rearrangement relaxation time τ_{T1} was described as the product of the shear rate times the ratio of surface dilatational viscosity κ over the surface tension γ such as $\tau_{T1} \approx \frac{\kappa}{\sigma} \times \dot{\gamma}$. All in all, bubble rearrangements are driven by the surface tension pulling on the film and are limited by viscous friction due to the bulk viscosity μ and by the dilatational surface viscosity κ (Cohen-Addad *et al.*, 2013).

These rearrangements played an important role in the research focusing on the transition between “microfluidic crystals”. These crystals are simply foam patterns (bamboo foam, single to multiple rows of bubbles) generated via microfluidics that self-assemble in ordered lattices. These configurations exist because the foam needs to minimise its interfacial energy. They were firstly reported by Garstecki and Whitesides, (2006). More work focused on the transition between the “hex-one” or bamboo pattern corresponding to a single layer containing a single row of bubbles, to the “hex-two” or alternate or two-row of bubbles pattern describing a single layer containing two rows of bubbles.

Raven *et al.* (2006) observed a non-linear response in the evolution of the foam velocity plotted versus the applied gas pressure in a microchannel. More precisely, a discontinuity in pressure drop was visible upon the transition between the two-row to the bamboo foam pattern caused by the bubble rearrangement.

This discrepancy originated from the intermittent existence of the two foam states driven by pulsating gas flow rate for a given liquid flow rate. Raven and Marmottant (2006) linked the topology change based within an oscillating foam flow to the foam

volume evolution and velocity in a micro-channel. Indeed, it was showed that for a fixed set of parameters (liquid and gas inputs), the foam frequency of formation was constant (only depending upon the liquid flow rate) and the velocity homogeneous over the channel. The foam behaved like a plug flow despite the oscillating foam pattern between two structures. The oscillation cycle started with a two-row pattern which while the flow rate grew, increased the volume of newly formed bubbles. This increase caused a transition from two-row to bamboo pattern and local bubble rearrangements to occur. Afterwards, the bubble volume at the channel entrance reduced and the reverse transition was observed until the last slice of two-row pattern had reached the channel exit.

Additionally, Marmottant et al. (2008) described the elastic (low strain rate, linked to reversible bubble deformation) to plastic (high strain rate, related to irreversible bubble motion relative to each other) transition in a 2D foam by linking the foam macroscopic behaviour to the dynamics of its individual components, the bubbles. It was demonstrated that plastic rearrangements were obtained from a combination of both elastic strain and total strain rate.

Topological bubble rearrangements are also termed plastic events. Yet, a topological rearrangement implies a change from a stable elastic configuration to another. It is followed by a relaxation over time determined by the ratio of dissipation to elastic force. The rate of rearrangement is determined by the shear rate.

Furthermore, Raven and Marmottant (2009) defined the speed of rearrangement or T1 wave velocity v_{T1} such as:

$$v_{T1} = \frac{\Delta x}{\tau_{T1}} \quad (2-8)$$

with $\Delta x = V_b/hw$ the distance between two bubbles in the bamboo structure. The existence of three transition regimes correlated to the difference between the foam velocity, v_{foam} , and v_{T1} , the speed of rearrangement was demonstrated:

- for $v_{foam} < -v_{T1}$, the flow reached a periodically oscillating flow.
- when $v_{foam} = -v_{T1}$, then a stationary instability of the two-row/bamboo was set;
- when $v_{foam} > -v_{T1}$, the instability could be described as advected (driven by its surrounding).

Furthermore, an estimation of the interfacial energy E was obtained for one bubble per foam pattern via the relation:

$$E = \sigma h L_B \quad (2-9)$$

with h the channel height, and L_B , the apparent bubble perimeter assuming dry foam in local equilibrium (Raven and Marmottant, 2009).

Thus, the two-row structure presented the lowest energy and a stable state whereas the bamboo pattern was depicted as metastable state. In addition, it was also reported that the bamboo pattern presented a higher resistance to the flow than the two-row pattern.

In static conditions, coarsening causes a local strain build-up which releases via intermittent T1 bubble rearrangements. Thus, the elastic energy of the bubble

packing reduces and on average, the macroscopically applied strain relaxes (Labiausse *et al.* (2007).

To sum-up, at shear rate below the inverse of the relaxation time, the foam has time to relax towards a new local equilibrium and the total energy dissipated is defined by the difference between the energy barrier and the new local energy minimum. The foam remains in this new configuration, so the deformation is plastic (irreversible). Indeed, each relaxation following a T1 involves an irreversible dissipation that represents the plastic dissipation/T1 relaxation rate (Marmottant *et al.*, 2008). Due to the irreversibility of the relaxation process, the system can go back to the original local minimum (before the T1 rearrangement occurred) but the path to reach this local minimum is different from the initial one and present a hysteresis or difference.

At higher shear rate compared to the inverse of the T1 relaxation time, a shear-banding develops through a self-amplification process. Indeed, T1 events locally weaken the foam structure by increasing its “frozen” stress disorder which imposes an additional mechanical constraint to the foam (Kabla and Debrégeas, 2003). Thus, both at low and high shear rates compared to the inverse of the relaxation time, a hysteretic behaviour linked to the bubble rearrangement dynamics is likely to occur.

This section has reviewed several models that could be used to described foam hysteretic behaviour. These findings so far highlighted the fact that the hysteretic behaviour was linked to the changes occurring in the foam microstructure. However, no specific rheological model dedicated to foams was found in the literature. Additionally, few researchers have been able to draw on any systematic research into the parameters influencing foam thixotropy.

In foams, as for the yield stress, several parameters could affect thixotropy from the surfactant nature and concentration, to the continuous phase properties (viscosity, elasticity). Foam hysteretic behaviour is intrinsically linked to the foam viscoelastic properties that are further explained in the following section.

2.2.1.3 Viscoelasticity

Viscoelastic fluids present elastic properties in addition to their viscous counterparts. When under shear, such fluids exhibit a normal stress in addition to a shear stress (Schramm, 2005). Foams can exhibit viscoelasticity. Indeed, subjected to small deformation, aqueous foams demonstrate solid-like viscoelastic behaviour. In this case, the elasticity stems from the interfacial energy density that is proportional to the ratio of the surface tension over the mean bubble radius, that increases as the bubbles are being deformed.

The static elastic modulus G_0 can be expressed as follow for polydisperse foams of mean bubbles radius R (Cohen-Addad *et al.*, 2013):

$$G_0 = \frac{\sigma}{R}(1 - \varphi_l)(\varphi_{l,rcp} - \varphi_l) \quad (2-10)$$

with φ_l the liquid volume fraction, and $\varphi_{l,rcp}$ the liquid volume fraction at the jamming transition. Thus, G_0 mainly depends on σ/R and disappears at the jamming transition when the foam behaviour evolves from solid-like to liquid-like. For an increasing deformation, non-linear viscoelastic response sets in and finally, beyond a yield strain, a cross-over to non-Newtonian liquid-like behaviour is observed.

When an elastic material such as foam is subjected to intermediate shear strains that are insufficient to induce significant yielding, the induced tangential shear stress is

coupled to an additional shear stress in the normal direction to the tangential shear deformation, phenomenon termed as the Poynting effect. This phenomenon sets that the first normal stress difference N_1 and the shear strain γ are related such as (Labiausse *et al.*, 2007):

$$N_1 = \sigma_{12}\gamma \quad (2-11)$$

with σ_{12} , the shear stress in the direction normal to the plan of deformation. As explained above, foams are yield stress fluids that conserve a rheological memory of the flow in the shape of anisotropic trapped stresses. These stresses can add an offset to the first normal stress difference or to the applied strain (Labiausse *et al.*, 2007).

These anisotropic trapped stresses are therefore directly related to the foam hysteretic behaviour introduced earlier. The parameters influencing the normal stress difference such as the bulk elasticity should impact significantly the foam hysteretic behaviour.

Moving on now to consider the flow of liquid at bubble scale, important feature in foam rheology, which can be described via surface rheology.

2.2.1.4 Surface rheology

Surface rheology deals with the functional relationships that link the dynamic behaviour of a surface to the stress to which it is submitted to. Both elastic and viscous resistances oppose the expansion and deformation of surface films.

An important property is the interfacial viscosity that can be thought as the two-dimensional counterpart of bulk viscosity (Cantat *et al.*, 2013). As bubbles in a foam

approach each other, the film thinning and their resistance to rupture are of great importance to the ultimate stability of the overall foam. Thus, a high interfacial viscosity can enhance greatly foam stability by decreasing the film drainage velocity and the rate of bubble coalescence (Schramm, 2005).

For liquid-like interfaces with Newtonian behaviour, two quantities can be defined to relate the stress to the surface deformation: the surface dilatational viscosity κ (magnitude of the viscous forces during a rate expansion of a surface element) and the surface shear viscosity μ_s (rate of yielding of a fluid layer to an applied shear stress) (Schramm, 2005).

For elastic interfaces, a generalized Hooke's law with surface dilatational elastic modulus E_s , and surface shear modulus G_s describe the relation between stress and surface deformation. The surface dilatational elastic modulus can be defined as:

$$E_s = A \left(\frac{d\sigma}{dA} \right) \quad (2-12)$$

with A the surface area. This relation illustrates the resistance of the interface to surface tension variations for homogeneous dilatation (Cohen-Addad *et al.*, 2013).

As in bulk rheology, the interface response to a dilatation performed at a frequency f can be depicted via a complex surface dilatational modulus E^* such as:

$$E^* = E'(f) + i E''(f) \quad (2-13)$$

with E' and E'' , the elastic and loss dilatational moduli respectively. The interfacial property will vary depending on the frequency of dilatation:

- At low frequency, surfactants have time to travel between the surface and the bulk and the interface doesn't resist deformation ($E', E'' \rightarrow 0$).
- At intermediate frequency, the interface remains viscoelastic (Cohen-Addad *et al.*, 2013).
- At high frequency, the interface will behave as an insoluble monolayer: $E' \rightarrow E_\infty$, the limiting elasticity and $E'' = 2\pi f \mu_S$ is diminished to μ_S , a small intrinsic viscous contribution corresponding to the dilatational shear viscosity.

A third parameter can be defined to combine these quantities: in the case of a thin liquid film being stretched in a single direction for a small area change, the dynamic surface tension difference $\Delta\sigma_S$ between the starting and the ending positions can be approximated by the surface dilatational elastic modulus, E_S such as (Cantat *et al.*, 2013):

$$\Delta\sigma_S = E_S \Delta \ln A + (\kappa + \mu_S) \left(\frac{d \ln A}{dt} \right) \quad (2-14)$$

with A , the surface area, κ , the surface dilatational viscosity, and μ_S , the surface shear viscosity. Furthermore, the interfacial properties rely strongly on the surfactant composition. Indeed, surfactants showing a low solubility such as dodecanol (DOH) are employed to increase both the shear and dilatational moduli and viscosities, and to enhance surface rigidity (Karakashev and Nguyen, 2007).

Thereby, when foam is flowing, and the interface is being sheared and dilated, because $\mu_S \gg \eta$ and $E_S \gg G_0$, the dominant force acting against the deformation are the dilatational surface properties. On the contrary, when foam is subjected to

drainage, interfaces being essentially sheared, the main resisting force is the shear viscosity η (Cohen-Addad *et al.*, 2013).

Additionally, interfacial properties impact the bubble rearrangement dynamics. In coarsening wet foams, rigid interfaces promote longer bubble rearrangement duration compared to mobile interfaces whose driving force, the osmotic pressure Π_o , pushes the bubbles against each other (capillary suction).

Indeed, as a bubble travels a distance d upon rearrangement, a volume of liquid is moved through the interstices of the bubble network such as K , the network permeability that can be expressed as (Lorenceanu *et al.*, 2009):

$$K = \alpha_p R^2 \quad (2-15)$$

with α_p the permeability coefficient of the medium and R , the average pore or bubble radius of the network. This displacement, slowed down by a viscous friction acting against the capillary force defines the relaxation time τ_{T1} such as:

$$\tau_{T1} \approx \eta \varphi_l / (\Pi_o \alpha_p) \quad (2-16)$$

with η , the liquid viscosity, φ_l the liquid fraction, Π_o the osmotic pressure and α_p the permeability coefficient of the medium. The relaxation time diverges at the jamming transition ($\Pi_o \rightarrow 0$) (Le Merrer *et al.*, 2012; Cohen-Addad *et al.*, 2013).

This section has analysed the different aspects of foam rheology. To study all these properties, rheometry have been extensively employed, and its several uses have been summarised in the next part.

2.2.2 Foam rheology studied via rheometry

Rheometry is, by definition, the technology used to determine rheological data (Mezger, 2014). Firstly, rheometers are instruments that can be employed to characterise viscous behaviour via rotational tests and to evaluate viscoelastic behaviour via creep, relaxation and oscillatory tests. This section presents a brief overview of the common techniques employed to study foam rheological properties via rheometry.

2.2.2.1 Rotational test to study foam rheology

As for many fluids, it is possible to obtain a flow curve such as $\tau = \eta \dot{\gamma}$ from a foam sample by applying a steady shear stress τ (Pa) or shear rate $\dot{\gamma}$ (s^{-1}) and by obtaining the resulting fluid viscosity η (Pa s) via controlled shear stress or controlled shear rate rotational rheometer. In a controlled shear stress, the torque (mN m) is pre-set and the rotational speed (min^{-1}) is measured whereas in controlled shear rate, it is reversely applied. In a rotational test, a shear stress or shear rate ramp is applied, and the resulting shear rate or shear stress is measured. Several geometries can be employed in rheometry from the parallel plate, the cone-plate, to concentric cylinders to study fluid rheological behaviour (Mezger, 2014).

However, foams are fragile materials. Therefore, foam samples are often damaged during the test. In addition, foam sample is subjected to aging: its structure evolves over time. Consequently, foam structure has changed even while the sample is being placed on the rheometer. Because oscillatory unlike rotational tests are considered as non-invasive, they have been used to assess foam rheological properties.

2.2.2.2 Oscillatory test to investigate foam rheology

Oscillatory test have been developed to present a less-intrusive alternative to study foam properties (Saint-Jalmes, 2009). A two-plate model was considered in which the sample is placed with a stationary bottom plate (deflection $s = 0$) and a set distance or gap h_g between the two plates. In the oscillatory test, the upper plate of sheared area A is moved back and forth by a motor that applies a torque translated into a shear force ($\pm F_S$). The motion of the upper plate causes the sample to be sheared showing a deflection path ($\pm s$) and a deflection angle ($\pm \varphi_S$). If the sample shows adhesion to both plates without any slip at the wall and the sample is deformed homogeneously throughout the entire gap, then shear stress and shear strain are expressed such as (Mezger, 2014):

$$\pm \tau = \frac{\pm F_S}{A}. \quad (2-17)$$

$$\pm \gamma = \frac{\pm s}{h_g} = \pm \tan \varphi_S \quad (2-18)$$

For a purely elastic material, the shear stress can be expressed as (Hooke's law):

$$\tau (t) = G^* \times \gamma (t) \quad (2-19)$$

with G^* , the complex modulus and $\gamma (t)$ the time dependent shear strain such as $\gamma (t) = \gamma \cos \omega$ with γ , the shear strain and ω , the angular frequency. Oppositely, for a purely viscous material, it can be written as:

$$\tau(t) = \eta^* \times \dot{\gamma}(t) \quad (2-20)$$

with η^* , the complex viscosity. To model the viscoelastic properties of a sample, the complex moduli G^* can be described such as:

$$G^* = G' + i G'' \quad (2-21)$$

with G' defined as the storage modulus and G'' , as the loss modulus (White, 1970).

This test is commonly used to measure the viscoelastic properties (G^*, G', G'') of a sample by applying a very low strain which is within a domain called the Linear Viscoelastic Range (LVR). This range is determined previously via an amplitude or strain sweep test for a fixed frequency. The upper limit of this range of strain or stress for a specific frequency is considered as the yield strain for foams; namely, the strain at which the foam behaviour evolves from a solid-like to a liquid-like behaviour. The upper limit of the regime is determined by the strain limit at which the elastic and loss modulus cross-over for a specific frequency. This frequency is selected depending on the kind of deformation the foam is subjected to. Typically for foams, the linear viscoelastic range is set at very low stress or strain with the upper limit of the range set between 0.1 to 1 Pa (Cohen-Addad *et al*, 1998). Below this strain limit, the deformation applied is considered as being non-invasive.

This test can be combined with other methods such as the creep test to study the time-dependent viscoelastic properties of foams.

2.2.2.3 Creep, three-step and hysteresis loop tests

In this section, the tests employed to evaluate the foam time-dependency via rotational and/or oscillatory rheometry namely, creep, three-step and the hysteresis loop tests are depicted in Figure 2. 6.

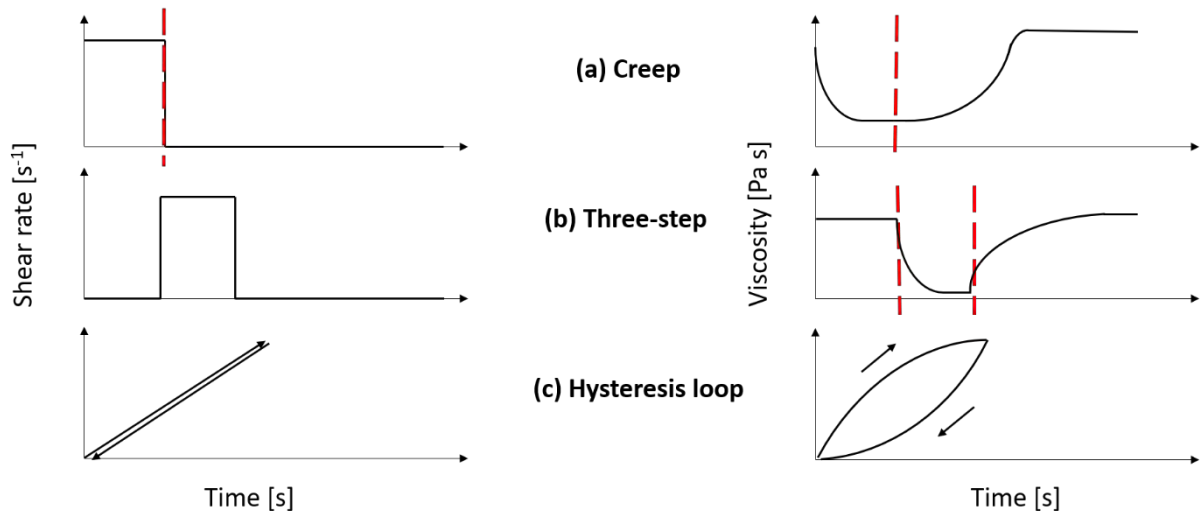


Figure 2. 6 Schematic representations of the three protocols employed to evaluate foam time-dependency by rheometry: (a) creep test, (b) three-step test and (c) the hysteresis loop test.

The creep test consists in applying a sharp deformation to a sample and in studying how the sample recovers its original properties such as its viscosity over time after this sharp deformation. This test can be performed either via a rotational test in which the viscosity recovery is measured over time or via oscillatory rheology in which the complex moduli G^* (elastic or storage G' and loss modulus G'') evolution is studied after the deformation (Mezger, 2014). Besides, Höhler *et al.* (1999) described in details the study of the memory effect of aqueous foams performed by oscillatory rheometry.

Another method is called the three-step test. This method is composed of three consecutive stages of rest/low deformation – high deformation – rest/low deformation. The first rest stage is used as reference to compare the sample

properties after the high deformation stage during the second episode of rest. This alternative can also be performed via rotational or oscillatory rheometry.

A subsidiary protocol which is more commonly used in industry is called “hysteresis loop”. The main difference with the two previous tests resides in the kind of deformation applied to the sample. Instead of a sharp deformation, a gradual ramp of deformation is applied in an ascending and descending cycle of deformation. The ascending and descending ramp of deformation can also be called “loading” and “unloading” curves (Bekkour and Scrivener, 1998). Thus, the evolution of the viscosity throughout the loop can be studied. If the evolution is similar in the up and down flow curve, then the sample doesn’t present any time-dependency or hysteretic behaviour. If there is a difference, then the sample structure is time-dependent and the behaviour is hysteretic. Bekkour and Scrivener (1998) highlighted the thixotropic and anti-thixotropic (rheopectic) behaviours of foams made of SDS and PEO at low molecular weight for various PEO concentrations from 0.01 to 0.3% (wt.) via hysteresis loop test. In this example, the thixotropic or hysteretic behaviour was explained by the degradation of the foam inner structure via flocculation and bubble coalescence. In addition, it was pointed out that the rheopectic behaviour was emphasized by the decrease in ascent time. Thus, a faster deformation caused the foam hysteretic behaviour to increase.

Da Cruz *et al.* (2002) evidenced foam hysteretic behaviour of foam in an up-and-down stress ramp where a sufficiently strong shear caused the viscosity to decrease in time. These two techniques have also been employed by Miquelim and Da Silva Lannes, (2009) to study the effect of a specific component from the foam formulation on foam hysteretic behaviour.

Saint-Jalmes (2009) improved the oscillatory three-step test by adding some preparation steps in the protocol such as a pre-shearing step. Despite these improvements, this test was still time-consuming and did not prevent the foam aging during the measurement and thus did not consider the change of foam structure over time. Therefore, researchers chose to design a rheometric approach to probe the microstructural changes occurring while a foam is being deformed. Thereby, researchers decided to combine diffusive wave spectroscopy with rheometry for a deeper understanding of the mechanisms at stake in foam rheology.

2.2.2.4 Diffusive wave-spectroscopy combined rheometry

A multiple light scattering probe was firstly developed by Durian *et al.* (1991) to probe in-situ 3D foam structure and dynamics either induced by the applied shear or by the foam coarsening during aging.

This technique consists in illuminating a sample with a laser and in collecting information from the transmitted or backscattered light which forms a speckled interference pattern whose temporal fluctuations illustrate the internal structural change dynamics (Höhler *et al.*, 2014). This technique is either based on diffuse light transmission (diffuse-transmission spectroscopy, DTS) or on speckle patterns (diffusing-wave spectroscopy, DWS). As an example, Earnshaw and Jaafar (1994) developed a technique which combined the use of a rheometer with multi-speckle DWS to visualise the mechanisms occurring when a foam is subjected to a deformation.

In parallel, rheometers with glass geometries confining the sample were also employed by Höhler *et al.* (1999) for in situ simultaneous optical and rheological

testing. The yielding mechanism occurring in a model fluid (Gillette shaving foam) was studied via oscillatory rheometry (parallel plate Couette geometry) by applying a strain equivalent to yield strain and by measuring the resulting complex moduli. An experimental time scale small enough was employed so that the drainage and coalescence became negligible compared to coarsening. Thus, the aging process in this peculiar case was directly related to coarsening, and the mean bubble radius grew with time following a parabolic law as reported previously by Durian et al. (1991). The equivalent of an oscillatory three-step test was adapted.

Later, Marze et al. (2008) coupled DWS with a rheometer via a glass cone-plate geometry to determine the effect of surfactant, liquid volume fraction and rheometer surface roughness on the flow of 3D aqueous foams. However, in this case, the DWS measurement required time to adjust its measurement (temporal fluctuation of intensity) which allowed foam to age whilst completing a full flow curve. Therefore, only single point measurement (one shear rate) was performed per foam sample. Thus, this technique was still time-consuming and required a significant amount of sample.

Le Merrer *et al.* (2012; 2013) probed and measured via DWS the dynamic of bubble rearrangements between neighbouring bubbles. One year later, Höhler *et al.* (2014), a complete overview of the advances in multiple light scattering to study foam and emulsion dynamics was given.

Despite all the new promising methods which have been or are still being developed, these instruments remain expensive, energetically costly, time-consuming and they

require a substantial amount of sample. Therefore, the choice of miniaturization was made to reduce the material and energy consumption.

In the past two decades, some researchers implemented miniaturized sliding plate rheometers that required only a few microliters to analyse the complex fluid shear viscosity probed via a piezoelectric method (Dhinojwala and Granick, 1996, 1997; Clasen and McKinley, 2004). However, in such devices, the alignment of the two parallel plates, which required high precision measurements, remained a difficult and time-consuming step. This fact led researchers to find alternative methods such as “microfluidics rheometry” (Pipe and McKinley, 2009) to measure the rheological properties of various fluids in a much cheaper, environmental-friendly and fast manner.

The section 2.3 introduces the advances in this field throughout the years and summarizes the growing interest that has acquired microfluidics from its usage in the foam research to its development towards rheometry, until the scope of this work which is to apply microfluidics rheometry to investigate foam stability in dynamic conditions.

2.3 Microfluidics rheometry applied to foam: a new way to study foam rheological properties

Within the last two decades, considerable progress has been made in the field of miniaturization for all kinds of systems from mechanical, fluidic, electromechanical or thermal, down to sub-micron scale. These novelties gave birth first to a new field called MEMS (micro-electro-mechanical systems) and later in the 1990s, miniaturized Total Analysis Systems (TAS) in the field of analytical chemistry, were developed

allowing portable systems and a reduction of sample and reagent consumption (Manz *et al.* 1990). Further work led to the creation of a new discipline known as microfluidics with some of the earliest devices made in glass or silicon as described in (Manz and Simon, 1987; Verpoorte *et al.*, 1992) and further developed in PDMS (Tabeling and Chen, 2005).

Microfluidics is by definition the science and technology of systems that process or manipulate very small amount of fluid in geometries with characteristic length-scale ranging from tens to hundreds of micrometres (Whitesides, 2006). Microfluidics is a well-established field of research covering a wide range of industrial applications from chemical, biological and biomedical applications.

Foams present characteristic structures on length scales ranging from macroscopic to molecular scale. Due to the interplay between all these length scales, foam properties are complexed and require a fine tuning of its properties to facilitate their study. Consequently, microfluidics has been widely used in the last two decades to study selectively different level of foam research from the flow of foam, to the study of single bubble generation, down to creation and study of a single thin film.

2.3.1 Foam generation and study via microfluidics

Microfluidics has shown to be a versatile tool to study numbers of aspects of foams. Originally, microfluidics has been employed as a mean to generate foams in a very well-controlled way. Throughout the literature, several devices have been used from the (a) T-junction (Ahmad *et al.*, 2012), to the (b) co-flow (Van der Net *et al.*, 2007) and the (c) flow-focusing device (Lorenceanu *et al.*, 2006) represented below in Figure 2. 7.

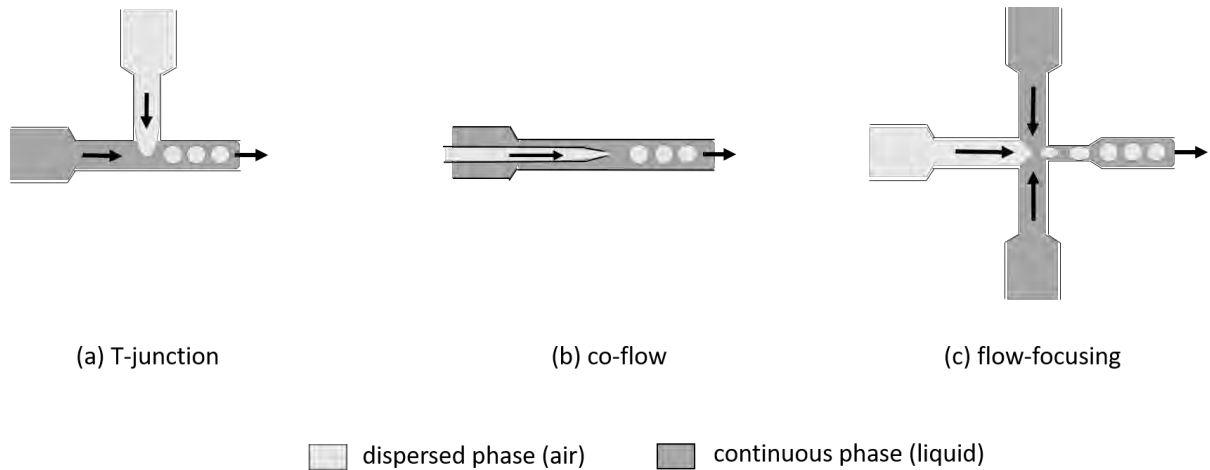


Figure 2. 7 Schematic representation of various microfluidic geometries employed for foam generation: (a) T-junction, (b) co-flow, and (c) flow-focusing.

Researchers such as Vuong and Anna (2012) established geometrical models to predict the foam structure for a specific geometry. Other researchers studied all the different foam structures available for a fixed geometry by varying the liquid and gas inlet flow-rates or pressures (Coleman and Garimella, 1999; Liu and Sur, 2009; Zhao and Middelberg, 2011). The equivalent of a foam phase diagram was drawn per specific geometry which is called “foam regime map”. Different foam patterns were reported in the literature: from a single row of bubble called “hex-one” to two-row of bubble called “hex-two” and so on, up to four rows of bubbles as reported in (Garstecki and Whitesides, 2006). The foam patterns available are function of the geometry and of the gas and liquid inlet pressures.

Later, scientists studied how the properties of the continuous phase such as the surfactant type and concentration (Liu and Sur, 2009; Micheau *et al.*, 2016), the viscosity (Lu *et al.*, 2014), the elasticity (Olivieri *et al.*, 2011) were affecting the single bubble generation.

Microfluidics has also supported the foam field of research for a wide range of applications from food industry (Laporte *et al.*, 2016), the fabrication of biocompatible scaffold (Chung *et al.*, 2009; Costantini *et al.*, 2015; Andrieux *et al.*, 2017) to the improvement of foam recovery efficiency in Enhanced Oil Recovery (EOR) (Quennouz *et al.*, 2014).

This section has highlighted the advantages to use microfluidics to study fragile products such as foams. In the following part, the fine microfluidic tuning of the fluid flow becomes a key advantage to apply microfluidics to study of the flow and the rheological properties of single-phase fluid.

2.3.2 Microfluidics rheometry for single phase fluids

Microfluidics rheometry has been firstly developed to facilitate the measurement of the viscosity of fluids by using a straight-forward, low sample volume and cheap technique by creating an on-chip viscosimeter. One of the first on-chip viscosimeter was implemented by Srivastava *et al.* (2005) based on a capillary pressure-driven viscosimeter.

Kang *et al.* (2005) evaluated the total pressure drop along a microchannel for an imposed flow rate via a pressure sensor. Thus, the rheological properties of various polymer solutions were measured for a wide range of shear rates. To do so, an external pressure transducer was used to measure the sum of the true microchannel pressure drop and those due to the inlet and outlet by means of complex calibrations and corrections.

Groisman (2003) mixed by interdiffusion two miscible fluids flowing side by side in the outlet channel of T-junction device. Convection occurring faster than diffusion in the

experimental conditions, the interface of the two fluids can be determined and controlled by the ratio of the flow rates and viscosities of the two fluids. By measuring the interface position via fluorescence microscopy, the viscosity of one of the two fluids could be determined knowing the flow rates and the viscosity of the other fluid.

Later, Guillot *et al.* (2006) based the evaluation of single-phase fluid viscosity on laminar parallel flow in a T-junction microchannel for Newtonian and non-Newtonian fluids. The sample was flowing contiguously to an immiscible reference fluid of known viscosity for a specific range of flow rates. Thus, by means of optical microscopy, knowing the inlet flow rates, the channel geometry, the mean shear rate applied and the position of the interface between the fluids, the fluid viscosity and the pressure drop in the microchannel could be determined. Flow curves were obtained for viscosities from 2 to 70 mPa s for shear rates ranging from 0.2 to 2000 s⁻¹ with only 300 µL sample. Further optimising their previous technique towards an automated micro-rheometer Guillot *et al.* (2008) reduced the standard deviation by using a lower viscosity reference fluid and the analysis process continuity was improved by adding a mixing step.

A good and straight-forward alternative to measure the rheological properties of a single-phase fluid is to use Particle Image Velocimetry (PIV) which is based on the measure in a spatially resolved way of tracer motion embedded in a fluid. Degré *et al.* (2006) used this technique to quantify the bulk non-linear rheology of shear-thinning fluid. The only drawback of this technique is that the tracers must be monodisperse and the suspension stable enough so that the tracers do not aggregate in the fluid studied during the duration of the experiment. This technique is suitable for liquids two-phase systems in which one of the continuous phases can

contain the tracers. However, the tracers must not affect the properties of the liquid-liquid interface. More importantly, the refractive index of the tracer particles must match the one of the medium in which the tracers are dispersed. This technique is suitable in the case of the flow of a single bubble in a fluid containing tracers. Nevertheless, this method is not suitable to study the flow of liquid in the PBs while a foam is being deformed.

Chevalier and Ayela (2008) presented a capillary on chip rheometer. Wall shear stress and shear rate measurements were performed on silicon oil and ethanol-based solution. Local pressure drop measurements were realised via interdigitated comb electrodes sputtered on one channel wall. The measurement required the use of electrorheological nanofluids whose apparent viscosity was controlled by the applied electric field strength. Moreover, the fabrication of this device was quite complex and time-consuming compared to a normal microfluidic chip.

In the case of compressible fluids, the pressure drop cannot be measured accurately in the microchannel; therefore, this system cannot be used to study foam rheological properties.

Microfluidics rheometry has also found a niche field of research in the study of low viscosity elastic liquids. Indeed, Campo-Deaño *et al.* (2011) employed a microfluidic device equipped with a hyperbolic contraction to stretch a fluid flowing through the contraction. The fluid stretching resulted in the formation of a filament. The fluid relaxation time could be estimated from the study of the stretching dynamic and the filament evolution. Afterwards, Galindo-Rosales *et al.* (2013) reviewed and compared some microfluidics set-ups employed to explore the rheological properties of dilute

polymer solutions to conventional extensional rheometers. It was demonstrated that microfluidics rheometry could achieve results in the line with the one obtained by conventional rheometry. These results suggested that microfluidics could be a preferable alternative for dilute polymer solutions due to the range of measurable relaxation times compared to the limited range of conventional extensional rheometry.

Further research was also made to develop devices capable of measuring simultaneously the viscosity as function of the shear rate for a number of samples (Solomon and Vanapalli, 2014). Thus, a multiplexed viscometer could be used for rapidly analysing a wide selection of complex fluids.

Most of microfluidics rheometry has focused on steady-state rheology. However, microfluidics has also been employed to study other rheological properties such as fluid viscoelasticity and the fluid time-dependent rheological properties. Time-dependent behaviour has been firstly reported by Ganan-Calvo *et al.* (2006) for liquids jets generated via a flow-focusing device. Alongside, Cheow *et al.* (2007), Toepke *et al.* (2007), Cybulski and Garstecki (2010) employed microfluidics to mimic the hysteretic behaviour of bi-stable electronic components by exploiting the non-Newtonian behaviour of fluids or by using multiphase droplet-based systems. Furthermore, Zagnoni *et al.* (2010) studied the hysteretic behaviour of two-phase fluid made of two immiscible liquids in a T-junction microfluidic device. In this paper, researchers stressed out the effect of the shear history upon the flow behaviour of the two fluids mixture. Indeed, different flow patterns were obtained not only according to the ratio of the two immiscible liquids but also depending on the history of the applied phase flow rates.

A microfluidic-based method was specifically designed by Koser *et al.* (2013) to study the recovery of single-phase fluid after being subjected to a sharp deformation. The analogous of a creep recovery test was adapted on a microfluidic chip. To do so, a steady pressure-driven flow was firstly applied, and then suddenly the pressure was released. The fluid was then allowed to relax and to recover after the deformation. A general viscoelastic model (Bird *et al.*, 1987) was used to obtain the relaxation times of a broad range of polymeric solutions by extraction of local strains from the time-dependent velocity profiles.

This paper summarized well the advantages of using microfluidics to study time-variant rheological properties: not only the method was simple and cost-effective but also, the sample was continuously renewed. This minimized the sample degradation during experiment compared to standard rheometry. This technique, yet, very interesting, would not be suitable for compressible products. This last paragraph demonstrates the need to expand the use of microfluidic rheometry for the handling and analysis of fragile two-phase fluids such as foams.

2.4 Conclusions

The literature above identifies from the current state-of-the-art the need to find more environmental-friendly alternatives to stabilise foam and to study foam stability. Further work needs to be undertaken to improve and to evaluate foam stability via microfluidics which is the aim of this thesis.

In summary, it has been shown that bulk nanobubbles could present an interesting additional component to foam formulation to potentially enhance or reduce foam stability. The environmental friendliness could be improved by reducing the number

of surfactants or nanoparticles required to adsorb at the gas-liquid interface to stabilise foam.

Alongside, it has been demonstrated that there is a real need to expand the use of microfluidics rheometry to two-phase gas-liquid system to study time-dependent properties such as the foam recovery property after a gradual deformation. Thereby, microfluidics presents a “greener” approach to evaluate foam hysteretic behaviour by reducing the amount of sample and energy required to perform the study.

Chapter 3 describes the procedures and methods used in this investigation. The chapters that follow move on to the complete microfluidic investigation of two aspects of foam stability. The question of foam stability in static conditions will be addressed by studying the action of a new kind of surface-active agent and its effect on foam stability via microfluidics. The matter of foam stability in dynamic conditions will be tackled by the study of foam recovery property after a gradual deformation via microfluidics and by evaluating the parameters influencing this property.

2.5 List of references

- Ahmad, B., Stride, E. and Edirisinghe, M. (2012) 'Calcium Alginate Foams Prepared by a Microfluidic T-Junction System: Stability and Food Applications', *Food and Bioprocess Technology*, 5, pp. 2848–2857. doi: 10.1007/s11947-011-0650-3.
- Alheshibri, M. *et al.* (2016) 'A History of Nanobubbles', *Langmuir*, 32, pp. 11086–11100. doi: 10.1021/acs.langmuir.6b02489.
- Alheshibri, M. and Craig, V. S. J. (2019) 'Generation of nanoparticles upon mixing ethanol and water; Nanobubbles or Not?', *Journal of Colloid and Interface Science*, 542, pp. 136–143. doi: <https://doi.org/10.1016/j.jcis.2019.01.134>.
- AlYousef, Z., Almobarky, M. and Schechter, D. (2017) 'Enhancing the Stability of Foam by the Use of Nanoparticles', *Energy & Fuels*. American Chemical Society, 31(10), pp. 10620–10627. doi: 10.1021/acs.energyfuels.7b01697.
- An, H. *et al.* (2016) 'Stability of Nanobubbles Formed at the Interface between Cold Water and Hot Highly Oriented Pyrolytic Graphite', *Langmuir*. American Chemical Society, 32(43), pp. 11212–11220. doi: 10.1021/acs.langmuir.6b01531.
- Andrieux, S., Drenckhan, W. and Stubenrauch, C. (2017) 'Highly ordered biobased scaffolds: From liquid to solid foams', *Polymer*. doi: <http://doi.org/10.1016/j.polymer.2017.04.031>.
- Arriaga, L. R. *et al.* (2012) 'On the long-term stability of foams stabilised by mixtures of nano-particles and oppositely charged short chain surfactants', *Soft Matter*, 8, pp. 11085–11097. doi: 10.1039/c2sm26461g.
- Attard, P. (2003) 'Nanobubbles and the hydrophobic attraction', *Advances in Colloid and Interface Science*, 104, pp. 75–91. doi: [http://doi.org/10.1016/S0001-8686\(03\)00037-X](http://doi.org/10.1016/S0001-8686(03)00037-X).
- Azevedo, A. *et al.* (2016) 'Aqueous dispersions of nanobubbles: Generation, properties and features', *Minerals Engineering*, 94, pp. 29–37. doi: <https://doi.org/10.1016/j.mineng.2016.05.001>.
- Barés, J. *et al.* (2017) 'Local and global avalanches in a two-dimensional sheared granular medium', *Phys. Rev. E*. American Physical Society, 96(5), p. 52902. doi: 10.1103/PhysRevE.96.052902.
- Bekkour, K. and Scrivener, O. (1998a) 'Time-Dependent and Flow Properties of Foams', *Mechanics of Time-Dependent Materials*, 2, pp. 171–193. doi: 10.1023/a:1009841625668 LB - Bekkour1998.
- Bekkour, K. and Scrivener, O. (1998b) 'Time-Dependent and Flow Properties of Foams', *Mechanics of Time-Dependent Materials*, 2, pp. 171–193. doi: 10.1023/a:1009841625668 LB - Bekkour1998.
- Bergeron, V. (1999) 'Forces and structure in thin liquid soap films', *Journal of Physics: Condensed Matter*. IOP Publishing, 11(19), pp. R215–R238. doi: 10.1088/0953-8984/11/19/201.

- Binks, B. P. (2002) 'Particles as surfactants—similarities and differences', *Current Opinion in Colloid & Interface Science*, 7(1), pp. 21–41. doi: [https://doi.org/10.1016/S1359-0294\(02\)00008-0](https://doi.org/10.1016/S1359-0294(02)00008-0).
- Binks, B. P. and Horozov, T. S. (2005) 'Aqueous Foams Stabilized Solely by Silica Nanoparticles', *Angewandte Chemie International Edition*. Wiley-Blackwell, 44(24), pp. 3722–3725. doi: 10.1002/anie.200462470.
- Bird, R. B., Armstrong, R. C. and Hassager, O. (1987) *Dynamics of polymeric liquids Vol 1, 2nd Ed: Fluid mechanics*. United States: John Wiley and Sons Inc. Available at: http://inis.iaea.org/search/search.aspx?orig_q=RN:18088690.
- Brenner, M. P. and Lohse, D. (2008) 'Dynamic Equilibrium Mechanism for Surface Nanobubble Stabilization', *Phys. Rev. Lett.* American Physical Society, 101(21), p. 214505. doi: 10.1103/PhysRevLett.101.214505.
- Campo-Deaño, L. *et al.* (2011) 'Flow of low viscosity Boger fluids through a microfluidic hyperbolic contraction', *Journal of Non-Newtonian Fluid Mechanics*, 166, pp. 1286–1296. doi: <http://dx.doi.org/10.1016/j.jnnfm.2011.08.006>.
- Cantat, I. *et al.* (2013) *Foams: Structure and Dynamics*. OUP Oxford. Available at: <https://books.google.fr/books?id=yShoAgAAQBAJ>.
- Chen, H. *et al.* (2009) 'Defouling and cleaning using nanobubbles on stainless steel', *Biofouling*, 25, pp. 353–357. doi: 10.1080/08927010902807645.
- Cheow, L. F., Yobas, L. and Kwong, D.-L. (2007) 'Digital microfluidics: Droplet based logic gates', *Applied Physics Letters*. American Institute of Physics, 90(5), p. 54107. doi: 10.1063/1.2435607.
- Chevalier, J. and Ayela, F. (2008) 'Microfluidic on chip viscometers', *Review of Scientific Instruments*, 79, p. 76102. doi: 10.1063/1.2940219.
- Cho, S.-H. *et al.* (2005) 'Ultrasonic formation of nanobubbles and their zeta-potentials in aqueous electrolyte and surfactant solutions', *Colloids and Surfaces A: Physicochemical and Engineering Aspects*, 269, pp. 28–34. doi: <http://dx.doi.org/10.1016/j.colsurfa.2005.06.063>.
- Chung, K. *et al.* (2009) 'Fabricating scaffolds by microfluidics', *Biomicrofluidics*, 3, p. 22403. doi: <http://dx.doi.org/10.1063/1.3122665>.
- Clasen, C. and McKinley, G. H. (2004) 'Gap-dependent microrheometry of complex liquids', *Journal of Non-Newtonian Fluid Mechanics*, 124(1–3 SPEC. ISS.), pp. 1–10. doi: 10.1016/j.jnnfm.2004.07.015.
- Cohen-Addad, S., Hoballah, H. and Höhler, R. (1998) 'Viscoelastic response of a coarsening foam', *Phys. Rev. E*. American Physical Society, 57(6), pp. 6897–6901. doi: 10.1103/PhysRevE.57.6897.
- Cohen-Addad, S., Höhler, R. and Pitois, O. (2013) 'Flow in Foams and Flowing Foams', *Annual Review of Fluid Mechanics*, 45, p. 241. Available at: <http://dx.doi.org/10.1146/annurev-fluid-011212-140634>.
- Coleman, J. W. and Garimella, S. (1999) 'Characterization of two-phase flow patterns

in small diameter round and rectangular tubes', *International Journal of Heat and Mass Transfer*, 42, pp. 2869–2881. doi: [http://dx.doi.org/10.1016/S0017-9310\(98\)00362-7](http://dx.doi.org/10.1016/S0017-9310(98)00362-7).

Costantini, M. *et al.* (2015) 'Microfluidic Foaming: A Powerful Tool for Tailoring the Morphological and Permeability Properties of Sponge-like Biopolymeric Scaffolds', *ACS Applied Materials and Interfaces*, 7, pp. 23660–23671. doi: 10.1021/acsami.5b08221.

Coussot, P. *et al.* (2002) 'Viscosity bifurcation in thixotropic, yielding fluids', *Journal of Rheology*. The Society of Rheology, 46(3), pp. 573–589. doi: 10.1122/1.1459447.

Da Cruz, F. *et al.* (2002) 'Viscosity bifurcation in granular materials, foams, and emulsions', *Physical Review E*, 66, p. 51305. Available at: <https://link.aps.org/doi/10.1103/PhysRevE.66.051305>.

Cybulski, O. and Garstecki, P. (2010) 'Dynamic memory in a microfluidic system of droplets traveling through a simple network of microchannels', *Lab on a chip*. Cambridge [England] :, pp. 484–493. doi: 10.1039/b912988j.

Degré, G. *et al.* (2006) 'Rheology of complex fluids by particle image velocimetry in microchannels', *Applied Physics Letters*. American Institute of Physics, 89(2), p. 24104. doi: 10.1063/1.2221501.

Denkov, N. D., Marinova, K. G. and Tcholakova, S. S. (2014) 'Mechanistic understanding of the modes of action of foam control agents', *Advances in Colloid and Interface Science*, 206, pp. 57–67. doi: <https://doi.org/10.1016/j.cis.2013.08.004>.

Dennin, M. (2004) 'Statistics of bubble rearrangements in a slowly sheared two-dimensional foam', *Phys. Rev. E*. American Physical Society, 70(4), p. 41406. doi: 10.1103/PhysRevE.70.041406.

Dhinojwala, A. and Granick, S. (1996) 'New approaches to measure interfacial rheology of confined fluids', *Faraday transactions online*. [London] :, pp. 619–623. doi: 10.1039/ft9969200619.

Dhinojwala, A. and Granick, S. (1997) 'Micron-gap rheo-optics with parallel plates', *Journal of Chemical Physics*, 107(20), pp. 8664–8667. doi: 10.1063/1.475018.

Ducker, W. A. (2009) 'Contact Angle and Stability of Interfacial Nanobubbles', *Langmuir*, 25, pp. 8907–8910. doi: 10.1021/la902011v.

Durand, M. and Stone, H. A. (2006) 'Relaxation Time of the Topological T1 Process in a Two-Dimensional Foam', *Physical Review Letters*, 97, p. 226101. Available at: <https://link.aps.org/doi/10.1103/PhysRevLett.97.226101>.

Durian, D. J., Weitz, D. A. and Pine, D. J. (1991) 'Multiple Light-Scattering Probes of Foam Structure and Dynamics', *Science*. New York, N.Y. :, pp. 686–688. doi: 10.1126/science.252.5006.686.

Durian, D. J., Weitz, D. A. and Pine, D. J. (1991) 'Scaling behavior in shaving cream', *Phys. Rev. A*. American Physical Society, 44(12), pp. R7902–R7905. doi: 10.1103/PhysRevA.44.R7902.

Earnshaw, J. C. and Jaafar, A. H. (1994) 'Diffusing-wave spectroscopy of a flowing foam', *Physical Review E*, 49, pp. 5408–5411. Available at: <https://link.aps.org/doi/10.1103/PhysRevE.49.5408>.

Den engelsen, C. W., Gooijer, H. and Wassink, J. G. (1994) 'Foamability of Silica Suspensions in a Rotor-Stator Mixer', *Textile Research Journal*. SAGE Publications Ltd STM, 64(11), pp. 626–632. doi: 10.1177/004051759406401102.

Exerowa, D., Nikolov, A. and Zacharieva, M. (1981) 'Common black and Newton film formation', *Journal of Colloid and Interface Science*, 81(2), pp. 419–429. doi: [https://doi.org/10.1016/0021-9797\(81\)90424-0](https://doi.org/10.1016/0021-9797(81)90424-0).

Fan, M. *et al.* (2010) 'Nanobubble generation and its application in froth flotation (part I): nanobubble generation and its effects on properties of microbubble and millimeter scale bubble solutions', *Mining Science and Technology (China)*, 20, pp. 1–19. doi: [https://doi.org/10.1016/S1674-5264\(09\)60154-X](https://doi.org/10.1016/S1674-5264(09)60154-X).

Galindo-Rosales, F. J., Alves, M. A. and Oliveira, M. S. N. (2013) 'Microdevices for extensional rheometry of low viscosity elastic liquids: a review', *Microfluidics and Nanofluidics*, 14, pp. 1–19. doi: 10.1007/s10404-012-1028-1 LB - Galindo-Rosales2013.

Ganan-Calvo, A., Pascual, P. and Riesco-Chueca, P. (2006) 'Jetting–dripping transition of a liquid jet in a lower viscosity co-flowing immiscible liquid: the minimum flow rate in flow focusing', *Journal of Fluid Mechanics*. 2006/04/06. Cambridge University Press, 553, pp. 75–84. doi: DOI: 10.1017/S0022112006009013.

Garstecki, P. and Whitesides, G. M. (2006) 'Flowing Crystals: Nonequilibrium Structure of Foam', *Physical Review Letters*, 97, p. 24503. Available at: <https://link.aps.org/doi/10.1103/PhysRevLett.97.024503>.

Groisman, A. (2003) 'Microfluidic Memory and Control Devices', *Science*. New York, N.Y. :, pp. 955–958. doi: 10.1126/science.1083694.

Guillot, P. *et al.* (2006) 'Viscosimeter on a Microfluidic Chip', *Langmuir*, 22, pp. 6438–6445. doi: 10.1021/la060131z.

Guillot, P. *et al.* (2008) 'Towards a continuous microfluidic rheometer', *Microfluidics and Nanofluidics*, 5, pp. 619–630. doi: 10.1007/s10404-008-0273-9 LB - Guillot2008.

Gunes, D. Z. *et al.* (2010) 'Avalanches of coalescence events and local extensional flows – Stabilisation or destabilisation due to surfactant', *Journal of Colloid and Interface Science*, 343(1), pp. 79–86. doi: <https://doi.org/10.1016/j.jcis.2009.11.035>.

Hernandez, C. *et al.* (2017) 'Cryo-EM Visualization of Lipid and Polymer-Stabilized Perfluorocarbon Gas Nanobubbles - A Step Towards Nanobubble Mediated Drug Delivery', *Scientific Reports*, 7, p. 13517. doi: 10.1038/s41598-017-13741-1.

Hernandez, C. *et al.* (2018) 'Role of Surface Tension in Gas Nanobubble Stability under Ultrasound', *ACS Applied Materials and Interfaces*, 10, pp. 9949–9956. doi: 10.1021/acsami.7b19755.

Hernandez, C. *et al.* (2019) 'Sink or float? Characterization of shell-stabilized bulk nanobubbles using a resonant mass measurement technique', *Nanoscale*, 11(3), pp.

851–855. doi: 10.1039/c8nr08763f.

Höhler, R. and Cohen-Addad, S. (2005) 'Rheology of liquid foam', *Journal of Physics: Condensed Matter*, 17, p. R1041. Available at: <http://stacks.iop.org/0953-8984/17/i=41/a=R01>.

Höhler, R., Cohen-Addad, S. and Asnacios, A. (1999) 'Rheological memory effect in aqueous foam', *EPL (Europhysics Letters)*, 48(1), p. 93. Available at: <http://stacks.iop.org/0295-5075/48/i=1/a=093>.

Höhler, R., Cohen-Addad, S. and Durian, D. J. (2014) 'Multiple light scattering as a probe of foams and emulsions', *Current Opinion in Colloid & Interface Science*, 15(3), pp. 242–252. Available at: <http://dx.doi.org/10.1016/j.cocis.2014.04.005>.

Horozov, T. S. (2008) 'Foams and foam films stabilised by solid particles', *Current Opinion in Colloid & Interface Science*, 13(3), pp. 134–140. doi: <https://doi.org/10.1016/j.cocis.2007.11.009>.

Hunter, T. N. *et al.* (2008) 'The role of particles in stabilising foams and emulsions', *Advances in Colloid and Interface Science*, 137(2), pp. 57–81. doi: <https://doi.org/10.1016/j.cis.2007.07.007>.

Ishida, N. *et al.* (2000) 'Nano Bubbles on a Hydrophobic Surface in Water Observed by Tapping-Mode Atomic Force Microscopy', *Langmuir*, 16, pp. 6377–6380. doi: 10.1021/la000219r.

Jin, F. *et al.* (2007) 'Effects of pH and ionic strength on the stability of nanobubbles in aqueous solutions of α -cyclodextrin', *Journal of Physical Chemistry B*, 111(40), pp. 11745–11749. doi: 10.1021/jp074260f.

Jin, F. *et al.* (2008) 'Direct measurement of the nanobubble-induced weak depletion attraction between a spherical particle and a flat surface in an aqueous solution', *Soft Matter*, 4(5), pp. 968–971. doi: 10.1039/b802326c.

Jin, F., Ye, X. and Wu, C. (2007) 'Observation of kinetic and structural scalings during slow coalescence of nanobubbles in an aqueous solution', *Journal of Physical Chemistry B*, 111(46), pp. 13143–13146. doi: 10.1021/jp077190l.

Johnson, B. D. and Cooke, R. C. (1981) 'Generation of Stabilized Microbubbles in Seawater', *Science*, 213, pp. 209–211. doi: 10.1126/science.213.4504.209.

Kabla, A. and Debrégeas, G. (2003) 'Local stress relaxation and shear banding in a dry foam under shear', *Physical Review Letters*, 90(25), pp. 2583031–2583034. Available at: <https://www.scopus.com/inward/record.uri?eid=2-s2.0-0043269803&partnerID=40&md5=48e8806b361a5f806afda87ad904d11a>.

Kang, K., Lee, L. J. and Koelling, K. W. (2005) 'High shear microfluidics and its application in rheological measurement', *Experiments in Fluids*, 38(2), pp. 222–232. doi: 10.1007/s00348-004-0901-4.

Karakashev, S. I. and Grozdanova, M. V. (2012) 'Foams and antifoams', *Advances in Colloid and Interface Science*, 176–177, pp. 1–17. doi: <https://doi.org/10.1016/j.cis.2012.04.001>.

Karakashev, S. I. and Nguyen, A. V (2007) 'Effect of sodium dodecyl sulphate and dodecanol mixtures on foam film drainage: Examining influence of surface rheology and intermolecular forces', *Colloids and Surfaces A: Physicochemical and Engineering Aspects*, 293, pp. 229–240. doi: <http://doi.org/10.1016/j.colsurfa.2006.07.047>.

Karakashev, S. I. and Nguyen, A. V (2009) 'Do Liquid Films Rupture due to the So-Called Hydrophobic Force or Migration of Dissolved Gases?', *Langmuir*. American Chemical Society, 25(6), pp. 3363–3368. doi: 10.1021/la8034648.

Knüpfer, P., Ditscherlein, L. and Peuker, U. A. (2017) 'Nanobubble enhanced agglomeration of hydrophobic powders', *Colloids and Surfaces A: Physicochemical and Engineering Aspects*, 530, pp. 117–123. doi: 10.1016/j.colsurfa.2017.07.056.

Koser, A. E. *et al.* (2013) 'Measuring material relaxation and creep recovery in a microfluidic device', *Lab on a Chip*, 13, pp. 1850–1853. doi: 10.1039/c3lc41379a.

Labiausse, V., Hohler, R. and Cohen-Addad, S. (2007) 'Shear induced normal stress differences in aqueous foams', *Journal of Rheology*, 51, p. 479. Available at: <http://dx.doi.org/10.1122/1.2715392>.

Lam, S., Velikov, K. P. and Velev, O. D. (2014) 'Pickering stabilization of foams and emulsions with particles of biological origin', *Current Opinion in Colloid & Interface Science*, 19(5), pp. 490–500. doi: <https://doi.org/10.1016/j.cocis.2014.07.003>.

Laporte, M. *et al.* (2016) 'Characteristics of foams produced with viscous shear thinning fluids using microchannels at high throughput', *Journal of Food Engineering*, 173, pp. 25–33. doi: <http://dx.doi.org/10.1016/j.jfoodeng.2015.10.032>.

Larson, R. G. (2015) 'Constitutive equations for thixotropic fluids', *Journal of Rheology*, 59, pp. 595–611. doi: 10.1122/1.4913584.

Liu, D. and Sur, A. (2009) 'Two-phase flow with surfactants in a microchannel', in *Proceedings of the ASME Summer Heat Transfer Conference 2009, HT2009*, pp. 399–407. doi: 10.1115/HT2009-88446.

Liu, G. and Craig, V. S. J. (2009) 'Improved cleaning of hydrophilic protein-coated surfaces using the combination of nanobubbles and SDS', *ACS Applied Materials and Interfaces*, 1, pp. 481–487. doi: 10.1021/am800150p.

Liu, G., Wu, Z. and Craig, V. S. J. (2008) 'Cleaning of protein-coated surfaces using nanobubbles: An investigation using a Quartz Crystal Microbalance', *Journal of Physical Chemistry C*, 112, pp. 16748–16753. doi: 10.1021/jp805143c.

Lohse, D. and Zhang, X. (2015) 'Pinning and gas oversaturation imply stable single surface nanobubbles', *Phys. Rev. E*. American Physical Society, 91(3), p. 31003. doi: 10.1103/PhysRevE.91.031003.

Lorenceanu, E. *et al.* (2006) 'A high rate flow-focusing foam generator', *Physics of Fluids*, 18, p. 97103. Available at: <http://dx.doi.org/10.1063/1.2353799>.

Lou, S.-T. *et al.* (2000) 'Nanobubbles on solid surface imaged by atomic force microscopy', *Journal of Vacuum Science & Technology B*, 18, pp. 2573–2575. doi: <http://dx.doi.org/10.1116/1.1289925>.

- Lu, Y. *et al.* (2014) 'Scaling of the bubble formation in a flow-focusing device: Role of the liquid viscosity', *Chemical Engineering Science*, 105, pp. 213–219. doi: <http://dx.doi.org/10.1016/j.ces.2013.11.017>.
- Manz, A., Graber, N. and Widmer, H. M. (1990) 'Miniaturized total chemical analysis systems: A novel concept for chemical sensing', *Sensors and Actuators B: Chemical*, 1(1), pp. 244–248. doi: [https://doi.org/10.1016/0925-4005\(90\)80209-I](https://doi.org/10.1016/0925-4005(90)80209-I).
- Manz, A. and Simon, W. (1987) 'Potentiometric detector for fast high-performance open-tubular column liquid chromatography', *Analytical Chemistry*. American Chemical Society, 59(1), pp. 74–79. doi: 10.1021/ac00128a016.
- Marinova, K. G. *et al.* (1996) 'Charging of Oil–Water Interfaces Due to Spontaneous Adsorption of Hydroxyl Ions', *Langmuir*. American Chemical Society, 12(8), pp. 2045–2051. doi: 10.1021/la950928i.
- Marmottant, P., Raufaste, C. and Graner, F. (2008) 'Discrete rearranging disordered patterns, part II: 2D plasticity, elasticity and flow of a foam', *The European Physical Journal E*, 25, pp. 371–384. doi: 10.1140/epje/i2007-10300-7 LB - Marmottant2008.
- Marze, S., Langevin, D., Saint-Jalmes, A. (2008) 'Aqueous foam slip and shear regimes determined by rheometry and multiple light scattering', *Journal of Rheology*, 52, p. 1091. Available at: <http://dx.doi.org/10.1122/1.2952510>.
- Marze, S., Langevin, D. and Saint-Jalmes, A. (2008) 'Aqueous foam slip and shear regimes determined by rheometry and multiple light scattering', *Journal of Rheology*, 52, p. 1091. Available at: <http://dx.doi.org/10.1122/1.2952510>.
- McClure, D. D. *et al.* (2017) 'An experimental investigation into the behaviour of antifoaming agents', *Chemical Engineering Science*, 160, pp. 269–274. doi: <https://doi.org/10.1016/j.ces.2016.11.033>.
- Le Merrer, M., Cohen-Addad, S. and Hoehler, R. C. N.-01239411 (2013) 'Duration of bubble rearrangements in a coarsening foam probed by time-resolved diffusing-wave spectroscopy: Impact of interfacial rigidity', *Physical Review E: Statistical, Nonlinear, and Soft Matter Physics*. Institut des Nanosciences de Paris (INSP) Laboratoire de Physique des Matériaux Divisés et des Interfaces (LPMDI), 88, p. 22303. doi: 10.1103/PhysRevE.88.022303.
- Le Merrer, M., Cohen-Addad, S. and Höhler, R. (2012) 'Bubble Rearrangement Duration in Foams near the Jamming Point', *Physical Review Letters*, 108. Available at: <http://dx.doi.org/10.1103/PhysRevLett.108.188301>.
- Mewis, J. and Wagner, N. J. (2009) 'Thixotropy', *Advances in Colloid and Interface Science*, 147–148, pp. 214–227. doi: <https://doi.org/10.1016/j.cis.2008.09.005>.
- Mezger, T. G. (2014) *The Rheology Handbook, 4th Edition For users of rotational and oscillatory rheometers*. 4th Editio. Edited by European Coating Tech Files. Hanover, Germany: Vincents Network.
- Micheau, C. *et al.* (2016) 'Microfluidic comparative study of foam flow between a classical and a pH sensitive surfactant', *Colloids and Surfaces A: Physicochemical and Engineering Aspects*, 501, pp. 122–131. doi: 10.1016/j.colsurfa.2016.04.061.

- Miller, C. A. (2008) 'Antifoaming in aqueous foams', *Current Opinion in Colloid & Interface Science*, 13(3), pp. 177–182. doi: <https://doi.org/10.1016/j.cocis.2007.11.007>.
- Miquelim, J. N. and Da Silva Lannes, S. C. (2009) 'Egg albumin and guar gum influence on foam thixotropy', *Journal of Texture Studies*, 40, pp. 623–636. doi: [10.1111/j.1745-4603.2009.00201.x](https://doi.org/10.1111/j.1745-4603.2009.00201.x).
- Møller, P. C. F., Mewis, J. and Bonn, D. (2006) 'Yield stress and thixotropy: on the difficulty of measuring yield stresses in practice', *Soft Matter*. The Royal Society of Chemistry, 2(4), pp. 274–283. doi: [10.1039/B517840A](https://doi.org/10.1039/B517840A).
- van der Net, A. *et al.* (2007) 'Crystalline arrangements of microbubbles in monodisperse foams', *Colloids and Surfaces A: Physicochemical and Engineering Aspects*, 309(1), pp. 117–124. doi: <https://doi.org/10.1016/j.colsurfa.2006.11.056>.
- Nirmalkar, N., Pacek, A. W. and Barigou, M. (2018) 'On the Existence and Stability of Bulk Nanobubbles', *Langmuir*, 34, pp. 10964–10973. doi: [10.1021/acs.langmuir.8b01163](https://doi.org/10.1021/acs.langmuir.8b01163).
- Nirmalkar, N., Pacek, A. W. and Barigou, M. (2019) 'Bulk Nanobubbles from Acoustically Cavitated Aqueous Organic Solvent Mixtures', *Langmuir*. doi: [10.1021/acs.langmuir.8b03113](https://doi.org/10.1021/acs.langmuir.8b03113).
- Nordstrom, K. N. *et al.* (2010) 'Microfluidic Rheology of Soft Colloids above and below Jamming', *Physical Review Letters*, 105, p. 175701. Available at: <https://link.aps.org/doi/10.1103/PhysRevLett.105.175701>.
- Ohgaki, K. *et al.* (2010) 'Physicochemical approach to nanobubble solutions', *Chemical Engineering Science*, 65(3), pp. 1296–1300. doi: [10.1016/j.ces.2009.10.003](https://doi.org/10.1016/j.ces.2009.10.003).
- Oliveira, H., Azevedo, A. and Rubio, J. (2018) 'Nanobubbles generation in a high-rate hydrodynamic cavitation tube', *Minerals Engineering*, 116, pp. 32–34. doi: <https://doi.org/10.1016/j.mineng.2017.10.020>.
- Olivieri, G. *et al.* (2011) 'Effects of viscosity and relaxation time on the hydrodynamics of gas–liquid systems', *Chemical Engineering Science*, 66, pp. 3392–3399. doi: <http://dx.doi.org/10.1016/j.ces.2011.01.027>.
- Peyman, S. A. *et al.* (2012) 'Expanding 3D geometry for enhanced on-chip microbubble production and single step formation of liposome modified microbubbles', *Lab on a Chip*, 12, pp. 4544–4552. doi: [10.1039/C2LC40634A](https://doi.org/10.1039/C2LC40634A).
- Peyman, S. A. *et al.* (2016) 'On-chip preparation of nanoscale contrast agents towards high-resolution ultrasound imaging', *Lab on a Chip*, 16, pp. 679–687. doi: [10.1039/C5LC01394A](https://doi.org/10.1039/C5LC01394A).
- Pipe, C. J. and McKinley, G. H. (2009) 'Microfluidic rheometry', *Mechanics Research Communications*, 36, pp. 110–120. doi: <https://doi.org/10.1016/j.mechrescom.2008.08.009>.
- Pugh, R. J. (1996) 'Foaming, foam films, antifoaming and defoaming', *Advances in Colloid and Interface Science*, 64, pp. 67–142. doi: <https://doi.org/10.1016/0001->

8686(95)00280-4.

Quennouz, N. *et al.* (2014) 'Microfluidic study of foams flow for enhanced oil recovery (EOR)', *Oil and Gas Science and Technology*, 69, pp. 457–466. doi: 10.2516/ogst/2014017.

Raven, J.-P. and Marmottant, P. (2006) 'Periodic Microfluidic Bubbling Oscillator: Insight into the Stability of Two-Phase Microflows', *Physical Review Letters*, 97, p. 154501. Available at: <https://link.aps.org/doi/10.1103/PhysRevLett.97.154501>.

Raven, J.-P. and Marmottant, P. (2009) 'Microfluidic Crystals: Dynamic Interplay between Rearrangement Waves and Flow', *Physical Review Letters*, 102, p. 84501. Available at: <https://link.aps.org/doi/10.1103/PhysRevLett.102.084501>.

Raven, J.-P., Marmottant, P. and Graner, F. (2006) 'Dry microfoams: Formation and flow in a confined channel', *European Physical Journal B*, 51(1), pp. 137–143. doi: 10.1140/epjb/e2006-00197-6.

Saint-Jalmes, S. M. R. M. G. A. (2009) 'Oscillatory rheology of aqueous foams: surfactant, liquid fraction, experimental protocol and aging effects', *Soft Matter*, 5, p. 1937. Available at: <http://dx.doi.org/10.1039/b817543h>.

Schramm, L. L. (2005) *Emulsions, Foams and Suspensions: Fundamentals and Applications*. Weinheim: Wiley-VCH Verlag GmbH & Co. KGaA.

Seddon, J. R. T. *et al.* (2012) 'A Deliberation on Nanobubbles at Surfaces and in Bulk', *ChemPhysChem*, 13, pp. 2179–2187. doi: 10.1002/cphc.201100900.

Solomon, D. E. and Vanapalli, S. A. (2014) 'Multiplexed microfluidic viscometer for high-throughput complex fluid rheology', *Microfluidics and Nanofluidics*, 16, pp. 677–690. doi: 10.1007/s10404-013-1261-2 LB - Solomon2014.

de Souza Mendes, P. R. and Thompson, R. L. (2012) 'A critical overview of elasto-viscoplastic thixotropic modeling', *Journal of Non-Newtonian Fluid Mechanics*, 187–188, pp. 8–15. doi: <https://doi.org/10.1016/j.jnnfm.2012.08.006>.

Srivastava, N., Davenport, R. D. and Burns, M. A. (2005) 'Nanoliter viscometer for analyzing blood plasma and other liquid samples', *Analytical Chemistry*, 77(2), pp. 383–392. doi: 10.1021/ac0494681.

Stöckelhuber, K. W. *et al.* (2004) 'Rupture of Wetting Films Caused by Nanobubbles', *Langmuir*. American Chemical Society, 20(1), pp. 164–168. doi: 10.1021/la0354887.

Tabelling, P. and Chen, S. (2005) *Introduction to Microfluidics*. OUP Oxford. Available at: <https://books.google.fr/books?id=S9ATDAAAQBAJ>.

Tan, B. H., An, H. and Ohl, C.-D. (2018) 'Surface Nanobubbles Are Stabilized by Hydrophobic Attraction', *Physical Review Letters*, 120(16). doi: 10.1103/PhysRevLett.120.164502.

Tao, D., Sobhy, A. and Li, L. (2019) 'Nanobubble effects on hydrodynamic interactions between particles and bubbles', *Powder Technology*. doi: <https://doi.org/10.1016/j.powtec.2019.02.024>.

- Toepke, M. W., Abhyankar, V. V and Beebe, D. J. (2007) 'Microfluidic logic gates and timers', *Lab on a chip*. Cambridge [England] :, pp. 1449–1453. doi: 10.1039/b708764k.
- Verpoorte, E. *et al.* (1992) 'A silicon flow cell for optical detection in miniaturized total chemical analysis systems', *Sensors and Actuators B: Chemical*, 6(1), pp. 66–70. doi: [https://doi.org/10.1016/0925-4005\(92\)80032-S](https://doi.org/10.1016/0925-4005(92)80032-S).
- Vuong, S. M. and Anna, S. L. (2012) 'Tuning bubbly structures in microchannels', *Biomicrofluidics*, 6. doi: 10.1063/1.3693605.
- Wang, G., Wang, K. L. and Lu, C. J. (2017) 'Advances of Researches on Improving the Stability of Foams by Nanoparticles', *IOP conference series. Materials science and engineering / Institute of Physics*. [Bristol] :, p. 12020. doi: 10.1088/1757-899X/242/1/012020.
- Weaire, D. (2008) 'The rheology of foam', *Current Opinion in Colloid & Interface Science*, 13(3), pp. 171–176. doi: <https://doi.org/10.1016/j.cocis.2007.11.004>.
- Weaire, D. L. and Hutzler, S. (2001) *The Physics of Foams*. Clarendon Press. Available at: <https://books.google.fr/books?id=mEHIZ9ZodFsC>.
- Weaire, D. and Phelan, R. (1996) 'The physics of foam', *Journal of Physics: Condensed Matter*, 8, p. 9519. Available at: <http://stacks.iop.org/0953-8984/8/i=47/a=055>.
- Weltmann, R. N. (1943) 'Breakdown of thixotropic structure as function of time', *Journal of Applied Physics*, 14(7), pp. 343–350. doi: 10.1063/1.1714996.
- White, G. W. (1970) 'Rheology in food research', *International Journal of Food Science & Technology*. John Wiley & Sons, Ltd (10.1111), 5(1), pp. 1–32. doi: 10.1111/j.1365-2621.1970.tb01539.x.
- Whitesides, G. M. (2006) 'The origins and the future of microfluidics', *Nature*, 442, pp. 368–373. Available at: <http://dx.doi.org/10.1038/nature05058>.
- Wilson, A. J. (1989) *Foams: Physics, Chemistry and Structure*. Springer. Edited by Springer London. Berlin Heidelberg New York: Springer-Verlag. doi: 10.1007/978-1-4471-3807-5.
- Yang, S. *et al.* (2009) 'Electrolytically Generated Nanobubbles on Highly Orientated Pyrolytic Graphite Surfaces', *Langmuir*, 25, pp. 1466–1474. doi: 10.1021/la8027513.
- Yasui, K., Tuziuti, T. and Kanematsu, W. (2018) 'Mysteries of bulk nanobubbles (ultrafine bubbles); stability and radical formation', *Ultrasonics Sonochemistry*, 48, pp. 259–266. doi: 10.1016/j.ultsonch.2018.05.038.
- Zagnoni, M., Anderson, J. and Cooper, J. M. (2010) 'Hysteresis in Multiphase Microfluidics at a T-Junction', *Langmuir*, 26, pp. 9416–9422. doi: 10.1021/la1004243.
- Zhang, L. *et al.* (2006) 'Electrochemically Controlled Formation and Growth of Hydrogen Nanobubbles', *Langmuir*, 22, pp. 8109–8113. doi: 10.1021/la060859f.
- Zhang, L. *et al.* (2017) 'Formation and Stability of Bulk Nanobubbles Generated by

Ethanol-water Exchange', *ChemPhysChem*. doi: 10.1002/cphc.201700010.

Zhang, M. and Seddon, J. R. T. (2016) 'Nanobubble–Nanoparticle Interactions in Bulk Solutions', *Langmuir*, 32, pp. 11280–11286. doi: 10.1021/acs.langmuir.6b02419.

Zhang, M., Seddon, J. R. T. and Lemay, S. G. (2019) 'Nanoparticle–nanobubble interactions: Charge inversion and re-entrant condensation of amidine latex nanoparticles driven by bulk nanobubbles', *Journal of Colloid and Interface Science*, 538, pp. 605–610. doi: 10.1016/j.jcis.2018.11.110.

Zhang, X. H. *et al.* (2005) 'Nanobubbles at the interface of hopg and ethanol solution', *International Journal of Nanoscience*, 04, pp. 399–407. doi: 10.1142/s0219581x05003152.

Zhang, X. H. and Ducker, W. (2007) 'Formation of Interfacial Nanodroplets through Changes in Solvent Quality', *Langmuir*, 23, pp. 12478–12480. doi: 10.1021/la702453g.

Zhao, C.-X. and Middelberg, A. P. J. (2011) 'Two-phase microfluidic flows', *Chemical Engineering Science*, 66, pp. 1394–1411. doi: <https://doi.org/10.1016/j.ces.2010.08.038>.

CHAPTER 3

MATERIALS & METHODS

3.1 Materials

All the materials employed in this project are reported in the following paragraphs. All the surfactants employed in this work are purchased from Sigma Aldrich and their properties are summarised in Table 3. 1.

Table 3. 1 Summary of the surfactants employed and their properties

Surfactants	Type	Mw (g mol ⁻¹)	HLB	cmc (mM) at 25°C
Sodium Dodecyl Sulfate (SDS)	Anionic	288	40	8.2
Tetradecyltrimethylammonium Bromide (TTAB)	Cationic	336	24	5
Polyethylene glycol tert-octylphenyl ether (Triton X-100)	Non-ionic	625	13.5	0.9

All the additives reported in Table 3. 2 are dedicated to the study of foam study by microfluidics:

Table 3. 2 Summary of additives used in foaming solutions.

Additives (foam)	Nature	Mw (g mol ⁻¹)	Quantity
Dodecanol (DOH)	Co-surfactant	186	0.05 g L ⁻¹
Glycerol (GLY)	Polymer	92	5 - 40 wt. %
Polyethylene oxide (PEO)	Polymer	3 x 10 ⁵ & 1 x 10 ⁶	100 & 300 ppm
Xantham Gum (XG)	Polysaccharide	-	0.01 wt. %

SDS is commonly employed in foam industry as an anionic surfactant. SDS is also employed at various concentrations from 0.5 to 5 cmc.

TTAB is a cationic surfactant used in several industrial applications. In chapter 7, five times cmc is also employed in combination with DOH (0.05 and 0.2 g L⁻¹) and PEO at two different molecular weight (3 x 10⁵ and 1 x 10⁶ g mol⁻¹) and concentrations (100 and 300 ppm). Triton X-100 is a non-ionic surfactant useful for many industrial

applications. Triton being non-ionic, it presents a strong affinity to non-polar components (Hunter *et al.*, 2009).

Other additives such as nanoparticles were employed to investigate the interaction between nanobubbles and nanoparticles. Thereby, two kinds and sizes of nanoparticles were selected to investigate the interactions with the bulk nanobubbles generated via microfluidics. The properties of the two kinds of nanoparticles investigated are summarised in Table 3. 3.

Table 3. 3 Summary of nanoparticles properties investigated.

Nanoparticles	Diameter (nm)	Properties	Concentration (wt. %)
Polystyrene nanoparticles (10 % solids)	200	Hydrophilic	0.01
LUDOX AS-30 colloidal silica (30 wt. % in water)	30	Mw = 60.08 g mol ⁻¹ Hydrophilic: Amino groups (NH ₃) on the surface. pH (pure) = 9.1 – 9.7	0.01

3.2 Methods

3.2.1 Solutions preparation

All the foaming solutions are made by mixing with a magnetic stirrer a certain quantity of surfactant in Millipore water (18.2 mS m⁻¹ conductivity, pH 6.5). Once mixed properly, the resulting solution is filtered with a 0.2 µm Acrodisc syringe filter adapted onto a clean plastic syringe (5 -10 mL). The nanoparticles solutions are prepared from their buffer solution via several dilution steps in pure water until the final

concentration has been reached. They are stored in a fridge at 5°C and whirl-mixed for 1 min prior to experimentation to prevent from any aggregation. The particle size distribution in pure water is checked via Dynamic Light Scattering (DLS) before any experiment to verify the suspension stability.

3.2.2 Microfluidics fabrication

3.2.2.1 Silicon wafer fabrication via rapid prototyping

Microfluidic systems are commonly fabricated in glass or oxidized silicon (Wilding *et al.*, 1994). The microchannels previously designed in a CAD program are employed to generate a silicon master using rapid prototyping (combination of printing and contact photolithography) (Duffy *et al.*, 1998). The generation of the silicon master is made via microcontact printing (Grzybowski *et al.*, 1998). This process can be described via the following steps as illustrated in Figure 3. 1: a CAD file is printed on a flexible transparent material (poly(methyl) methacrylate or chrome) by using high-resolution printing. This transparent material is used as a photomask in contact photolithography. A specific amount of permanent epoxy negative photoresist (SU8 2075, MicroChem) is deposited onto a silicon wafer placed on a spin coater. The rotation speed is set to obtain a specific deposited layer of photoresist on the wafer. The silicon wafer is submitted to a soft or pre-bake (3 min at 65°C). Then the photomask is aligned with the silicon wafer and exposed to UV-light. After exposure, the wafer is baked (1 min at 65°C) again to further cross-link the structure and finally developed.

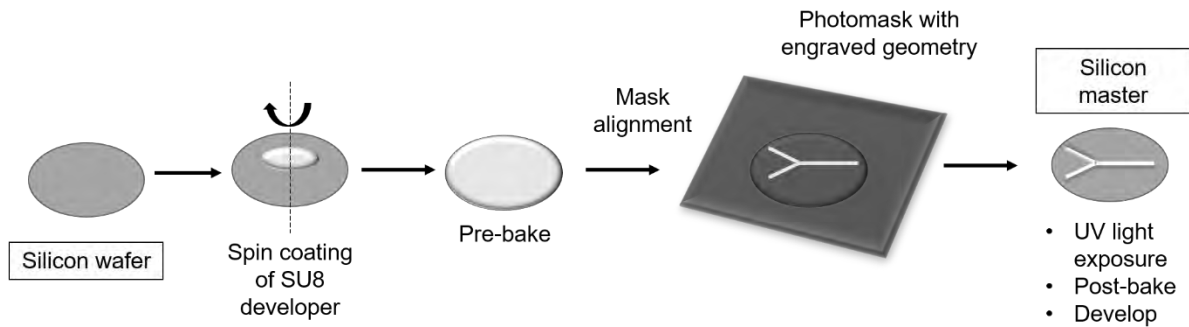


Figure 3. 1 Schematic illustrating the micropatterning steps to fabricate the silicon master.

After development, the pattern of photoresist on the silicon wafer is employed as the master to cast replicas of PDMS as further explained in the next section. For the two-depth flow-focusing device, two layers of SU8 2075 (MicroChem) and two alignments-exposure-development stages are needed to produce the two different depths required for the device.

3.2.2.2 PDMS device fabrication

The device is fabricated in Polydimethylsiloxane (PDMS, SYLGARD™ 184 Silicone Elastomer Kit, Dow Chemical) via soft lithography (Kim *et al.*, 2008). The curing agent is added to the silicon elastomer in a plastic container in the ratio 10:1 (w/w). The mixture is thoroughly agitated with a plastic spatula for 1 minute to mix homogeneously the two components. The mixture is poured onto the silicon wafer so that the flow of the solution follows the flow in the channel (from the inlet to the outlet on the engraved device). After the degassing and curing step at 70°C for an hour, the PDMS device is cut and removed carefully from the silicon wafer using a sharp knife. The inlet and outlet channels are prepared by piercing the PDMS in the desired area using a pinching tool. The PDMS device is then irreversibly bonded to a microscope glass slide by corona discharge (Peak Based Implant System, SiSoMM) (Mark *et al.*, 2008). In order to assure a homogeneous foam formation in the channel, the device

is surface treated to become hydrophilic via a layer-by-layer technique by flowing alternately segments of poly(allylamine hydrochloride) (PAH, Sigma Aldrich) and poly(sodium 4-styrenesulfonate) (PSS, Sigma Aldrich) solutions (both 0.1% w/v in 0.5 M aqueous NaCl solution) with aqueous NaCl washing solution (0.1 M) segments in between (Bauer *et al.*, 2010). Indeed, the flow pattern depends strongly on the wetting properties of the fluid-wall interface. To get ordered patterns, it is required to get a complete wetting of the continuous phase on the wall of the channel.

Shao *et al.*, (2009) showed that the lack of affinity to the channel wall would favour the formation of bubbles. Besides, Cubaud *et al.*, (2006) demonstrated that in hydrophobic channel, the liquid does not lubricate the wall; the hysteresis and friction effects make the flow axisymmetric with respect to the axial direction.

This protocol is valid for the fabrication of the two-depth device further described for the generation of bulk nanobubbles via microfluidics.

3.2.3 Foam and nanobubbles generation methods via microfluidics

3.2.3.1 In-situ foam generation method and study in a microchannel

The microfluidic device used consists of a rectangular cross-section microchannel of $d = 25 \mu\text{m}$ depth with a $w_1 = 50 \mu\text{m}$ wide gas inlet which meets at a flow-focusing junction with two $w_2 = 100 \mu\text{m}$ wide liquid inlets as shown in Figure 3. 2. The foam is formed and studied in $w_3 = 280 \mu\text{m}$ wide channel.

Two reservoirs of air and liquid are connected via a pressure controller (OB1 MK3, Elveflow) to the two inlets via 0.020" x 0.060" OD Tygon microbore tubing (Cole-Parmer Instrument Co. Ltd., UK) to accurately control the gas and liquid inlet

pressures. The pressure named P_{gas} for the gas and P_{liq} for the foaming solution are upstream applied pressures above atmospheric pressure.

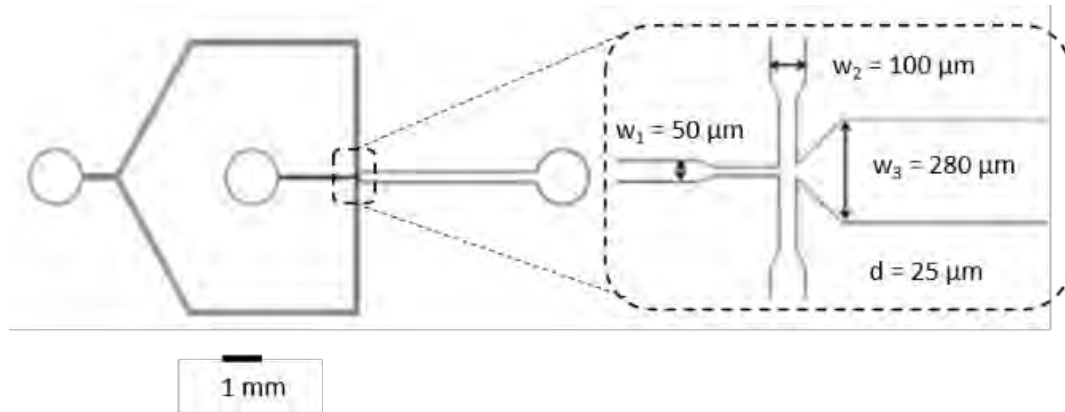


Figure 3. 2 Schematic of the 25 μm depth flow-focusing device (left) and a zoomed in view of the flow focusing junction (right) for foam generation.

3.2.3.2 Microfluidics nanobubble generation method

The microfluidic device employed consists of a rectangular cross-section microchannel of 25 μm (d_1) depth in a first part of the device that further develops with a 55 μm (d_2) depth expansion channel as illustrated in Figure 3. 3 and Figure 3. 4. A 50 μm wide gas inlet meets at a flow-focusing junction with two 100 μm wide liquid inlets as shown in Figure 3. 4.

The nanobubbles are generated and collected at the exit of the channel. One reservoir of air is connected via a pressure controller (OB1 MK3, Elveflow) to the gas inlet via 0.020" x 0.060" OD Tygon microbore tubing (Cole-Parmer Instrument Co. Ltd., UK) to accurately control the gas inlet pressure. A 10 mL plastic syringe filled with the sample is connected to the liquid inlet via the same tubing, and its flow rate is finely controlled via a syringe pump (Harvard Syringe Pump 11 Pico Plus Elite, Harvard Apparatus).

Three nozzle widths (w_n , 10, 15, 20 μm) are chosen to study the effect of the nozzle size on the bulk nanobubble generation (see in Figure 3. 3, the schematic representation of the 10 μm nozzle device). One of the main peculiarities of this design is the change in depth between the nozzle and the expansion channel. Peyman *et al.* (2012, 2016) explained that to produce the atomization-like spray, the depth is doubled (from $d_1 = 25 \mu\text{m}$ to $d_2 = 55 \mu\text{m}$) so that the pressure drop is highly increased.

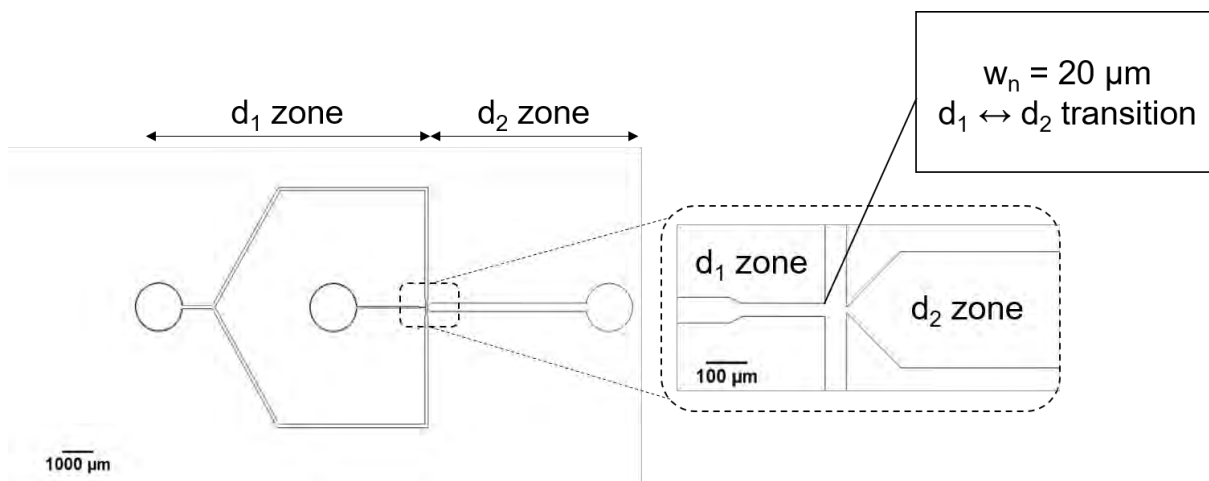


Figure 3. 3 Schematic of the two-depth ($d_1 = 25 \mu\text{m}$ & $d_2 = 55 \mu\text{m}$) flow-focusing device (left) and a zoomed in view of the two-depth flow focusing junction (right) for bulk nanobubbles generation.

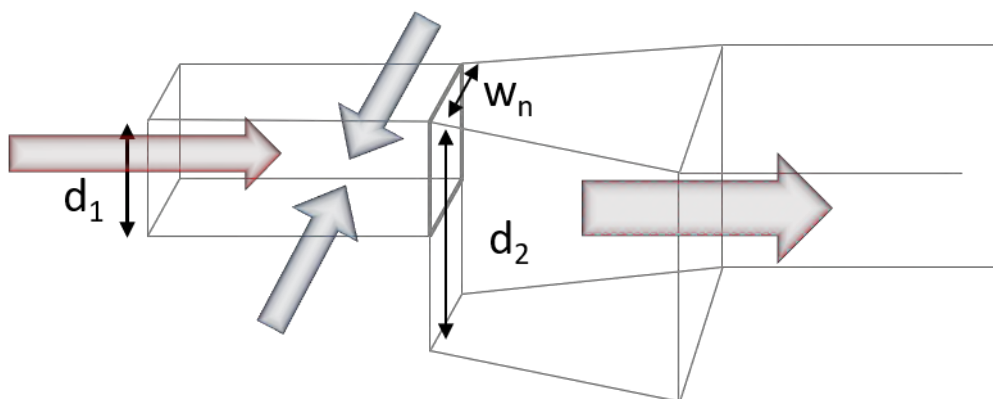


Figure 3. 4 Schematic representation of the cross-sectional view of flow-focusing two-depths device with air stream (red arrow) that meets two liquid streams (blue arrows) at the nozzle entrance to generate bulk nanobubbles (red and blue arrow).

Nanobubbles are generated by injecting simultaneously pure distilled water previously filtered and air into a 10 to 20 μm width (w_n) nozzle two-depth ($d_1 = 25 \mu\text{m}$, $d_2 = 55 \mu\text{m}$) flow-focusing device. The liquid flow rate is set at $90 \mu\text{L min}^{-1}$ and the gas inlet pressure is varied from 1000 to 1800 mbar. The microfluidic device used for the generation of nanobubbles is cleaned thoroughly by flowing for 10 min at $90 \mu\text{L min}^{-1}$ pure water prior to any collection. The nanobubble sample is collected into a DST0012 disposable plastic cuvette and/or into a clean and dry glass beaker.

The bubble size distributions in pure water and in various solutions are analysed at 25 °C via Dynamic Light Scattering (DLS) prior to and after microfluidic generation. The nanobubble sample are analysed only 30 min after collection by DLS to separate nanobubbles from the potential microbubbles generated which disappeared instantly unlike bulk nanobubbles. The details of the DLS protocol are summarised in section 3.2.6.4 The solution's zeta potentials are measured also via the Zetasizer Nano ZSP (Malvern Ltd).

3.2.4 In-situ investigation of 2D foam hysteretic behaviour

In chapter 4, the SDS concentration is kept at five time the cmc to ensure a constant concentration throughout the whole duration of the experiment.

The combination of SDS with glycerol is selected to study the effect of increasing the viscosity on the foam recovery properties after a gradual deformation at two concentrations (20% and 40% wt.). Then, a third formulation made of SDS and DOH is chosen to observe the effect of surface elasticity on foam hysteresis. Thirdly, the effect of the addition of Xantham Gum (XG) and a small quantity of glycerol (5 % wt.) added to facilitate the dissolution to the reference solution is studied on the foam hysteretic behaviour. In this case, the focus is given to the impact of the shear-thinning property of the continuous phase deriving from the thickener nature of XG on the foam recovery properties after deformation.

TTAB is selected to investigate the effect of two kinds of elasticity (surface and bulk elasticity) on foam thixotropy based on the method introduced in chapter 7. Indeed, TTAB unlike SDS, do not form complexes with PEO. Indeed, Safouane *et al.* (2006)

showed that the combination of SDS and PEO can lead to complexation which will change the properties of the resulting solution.

A foam regime map (FRM), which gives detailed view of all the different foam patterns available for a specific geometry, is firstly generated for each solution by changing the gas and inlet pressures between 200 and 1400 mbar. Thus, areas of steady patterns of bamboo and two-row foam are identified and selected for the study.

The “bamboo” pattern or “hex-one” is described as a single layer of bubbles containing only one bubble in the full width of the channel (Garstecki and Whitesides, 2006). The “two-row” pattern or “hex-two” can be depicted as a single layer containing two rows of bubbles in the width of the channel (Garstecki and Whitesides, 2006).

3.2.4.1 Three-step test description

In the bamboo pattern, the deformation at the wall during the continuous foam generation and flow in the channel is considered as higher than the two-row due to the largest surface area in contact with the wall. Indeed, the average bubble surface area against the channel wall is estimated by image analysis and it is found that the bamboo pattern one varies from 30000 to 40000 μm^2 whereas the two-row pattern presents an average surface ranging from 4000 to 6000 μm^2 .

The deformation at the wall can then be tuned by varying the gas and liquid inlet pressures which also control the foam pattern and velocity. It was shown that for a steady liquid flow rate, increasing the gas pressure will increase the gas flow rate up

to a plateau due to a self-regulation mechanism for which the foam structure changes from bamboo to two-row continuously (Raven and Marmottant, 2006, 2009).

In the study, the pressure sets are chosen so that the beginning and the end of the deformation cycle present a steady foam pattern. Here, it is considered that the foam velocity during the deformation is mainly controlled by the liquid pressure. Thus, two ways can be employed to vary the degree of deformation at the wall: by changing the pressure sets (gas and liquid) which will also modify the gas and liquid flow rates, or by altering the pressure ramp (i.e., the variation of pressure over time). Indeed, the amount of energy needed to deform the foam varies significantly with the pressure ramp. By modifying the pressure ramp from 0.5 to 2 mbar s⁻¹, the foam lamella has less time to rearrange/recover for the same level of deformation applied and so to reach its equilibrium state by dissipating the energy to its surrounding.

3.2.4.2 Hysteresis evaluation

The evolution of the apparent mean bubble diameter derived from the mean bubble area measured over time is obtained via image analysis of snap shots collected by a high-speed camera (Photron SA5) at up to 20000 frames per second (fps) via an inverted optical microscope (Nikon Ti-U) for specific pressure ratio ($r = \frac{P_{gas}}{P_{liq}}$) in the ascending and descending pressure ramps.

From each snap shot, the mean bubble diameter is obtained using the ImageJ software (Schneider *et al.*, 2012) and normalised by the channel width (280 µm). By plotting the apparent normalised mean bubble diameter versus the pressure ratio, the hysteresis is then evaluated by measuring the area between the ascending and descending curves. A solution of five times the critical micellar concentration (cmc) of

Sodium Dodecyl Sulfate (SDS, Sigma Aldrich) is used as reference because it presents negligible hysteresis.

3.2.4.3 Flow curve extraction

Further work is attempted to extract the analogous of a flow curve plotting the shear stress at the wall τ_{drag} versus the shear rate $\dot{\gamma}(t)$.

The mean bubble velocity U is measured via the PIVlab application on MATLAB (William Thielicke, 2014) by processing consecutive images taken with a high-speed camera for bubbly, two-row and bamboo flows. This application is originally used to measure the particles velocities and flow field. The velocities measured manually and via PIV-lab were compared and similar bubble velocities were obtained.

The shear rate $\dot{\gamma}(t)$ (s^{-1}) is estimated simply by dividing the bubble velocity by the estimated film thickness h_f (m) at the wall via image analysis such as:

$$\dot{\gamma}(t) = \frac{U(t)}{h_f} \quad (3-1)$$

From ImageJ software (Schneider *et al.*, 2012), the mean bubble area A and the film thickness h_f are determined. By geometric means, the film thickness h_f can be estimated by subtracting to the width of the channel the highest bubble length normal to the wall. By considering the area of circle, an average apparent bubble diameter can be obtained. This measurement is suitable for the two-row structures and the smallest bamboo structures. However, for the largest bamboo structures whose apparent diameter is greater than the width of the channel, the film thickness is directly measured via image analysis. Therefore, for the largest bamboo structures, a constant film thickness is obtained.

The shear stress at the wall due to the drag force τ_{drag} (Pa) is approximated by the expression employed by Rabaud *et al.* (2011) stating that the drag force is a sum of the viscous drag (liquid on bubble) and the friction force between the bubbles and the wall:

$$\tau_{drag} = \frac{F_{drag}}{S} = \frac{12\pi\mu R^2}{h} (2V - U) - \eta h [Ca]^{-\alpha} U \quad (3-2)$$

with τ_{drag} (Pa) shear stress due to drag force, F_{drag} (N) the drag force, S , the channel cross-section (m^2), V , the average liquid velocity ($m s^{-1}$), R , the bubble mean radius (m) and h , the channel height (m). The exponent α varies with the surface elasticity: for low surface elasticity (SDS), $\alpha = 1/2$ and for high surface elasticity (SDS + DOH), $\alpha = 1/3$. The liquid velocity is obtained by measuring experimentally the liquid flow rate at the channel exit per set of gas and liquid inlet pressures.

From the velocity estimation, the capillary number Ca is estimated as follow with U , the mean bubble superficial velocity ($m s^{-1}$), η the bulk viscosity (Pa s) and γ , the surface tension ($N m^{-1}$):

$$Ca = \frac{\eta U}{\gamma} \quad (3-3)$$

From the velocities and pressure ratios obtained during the FRM experiment, a relationship between the capillary number and the gas pressure is obtained for a fixed liquid inlet pressure. This correlation permits to calculate the capillary number throughout the ascending-descending pressure ramp and thus, the shear stress at the wall.

3.2.5 3D foam generation to study bulk nanobubble effect on foam properties

As a preliminary step, the reference foaming solution is used to generate bulk nanobubbles via one generation cycle through the two-depth 20 μm nozzle device described in Figure 3. 3 and in Figure 3. 4.

The reference solution is analysed by DLS (size and zeta potential) and via tensiometry before and after passing through the device. Two kinds of surfactant are investigated at various concentration ranging from 0.5, 1, 2.5 and 5 cmc: Triton X-100 and SDS. Then, a 2D foam is generated by co-injection of foaming solution and air in the device described by the schematic representation in Figure 3. 2. The gas and liquid inlet pressures are set for each formulation at 1000 mbar and 1900 mbar respectively. Then the 2D foam is transferred from the outlet via a 15 cm length tubing, 0.020" x 0.060" OD Tygon microbore tubing (Cole-Parmer Instrument Co. Ltd., UK), and collected into a glass cuvette previously clean (water & ethanol) and dried with air. The foaming time is fixed at 1 minute after the first bubble contacts the glass vessel.

The height evolution of the foam is measured manually by marking the top and the bottom of the foam column over time (up to 24h depending on the foam stability). The foam height is normalised by dividing the value at t by the initial value obtained. The foamability is determined by the initial foam height obtained after 1-minute (TX100) or 2-minute (SDS) foaming. The foam liquid fraction is evaluated by weighting the amount of liquid (m_L) within the foam.

The foam liquid fraction φ_L is computed from the following expression:

$$\varphi_L = \frac{V_L}{V_{foam}} = \frac{m_L}{h_{foam} A_{cuv} \rho_L} \quad (3-4)$$

With h_{foam} , the foam height, A_{cuv} , the cross-section of the measuring cylinder and ρ_L , the volumetric mass density of the foaming liquid.

Thus, foam heights and liquid fraction can be compared between the various surfactant concentrations investigated. These two measurements are essential to evaluate the effect of bulk nanobubbles on the surfactant dynamics within the plateau borders and on the resulting foam properties (foamability and foam stability).

Once the foam has disappeared, the resulting solution is removed from the measuring glass vessel and placed in a plastic cuvette for DLS and zeta potential measurements.

3.2.6 Characterisation methods

In this section are described all the physical and chemical characterisation techniques employed for the results chapters.

3.2.6.1 Dynamic surface tension characterisation

The maximum Bubble Pressure method is employed to evaluate the evolution of the dynamic surface tension for all the solutions investigated.

Principle

This method allows for the measurement of the maximum pressure that can be applied to a bubble at the tip of a capillary placed vertically in a liquid before the bubble detaches (Schramm, 2005). The instrument used here is the Maximum Bubble Pressure Tensiometer BPA-1 (SINTERFACE).

Protocol

The dynamic surface tension of water is checked between each measurement after a thorough rinsing of 15 min of the capillary placed in pure water while performing the “capillary air drying mode” in a clean beaker. To ensure that the instrument works effectively, the surface tension for pure water is checked. The measurement is validated if the value obtained is equal to $72 \pm 5 \text{ mN m}^{-1}$. After this cleaning/verification step, the measurement consists in placing the 0.13 mm diameter capillary in the solution studied contained within a clean and dry 25 mL beaker. The standard measurement method termed “M1” is characterised by a maximum bubble life time of 100 s and a maximum duration of experiment of 120 min.

All the foaming solutions and the solutions dedicated to nanobubbles study are analysed in the same manner. Thus, the effect of a specific component on the dynamic surface tension can be evaluated.

3.2.6.2 Rheological characterisation via rheometry

Rheology can be defined as the science of deformation and flow of fluids. It is used to describe the flow behaviour of fluids whose rheological characteristic oscillates between two extremes: the ideal viscous liquid and the ideal elastic solid behaviours. Most fluid behaviour lies between these two and are called viscoelastic. The technique employed to evaluate rheological data is termed rheometry.

Principle

Three fundamental rheological parameters can be defined from the two-plates-model. In this model, the upper plate of area A is moved by the force F_s while the bottom plate is fixed ($v = 0$). The liquid placed between the two plates separated by a distance h is sheared. It is assumed that the sample placed between the two plates

adheres (no slip conditions) and the flow is laminar. The velocity v is determined when the fluid is set in motion.

From this model, the following variables can be expressed (Mezger, 2014):

- The shear stress such as $\tau = F_s/A$ (Pa).
- The shear rate such as $\dot{\gamma} = v/h$ (s^{-1}).
- The shear viscosity such as $\eta = \tau/\dot{\gamma}$ (Pa s) for an ideal viscous fluid.

Thus, a flow curve can be obtained such as $\tau = \eta \dot{\gamma}$ from a fluid by simply applying a steady shear stress τ (Pa) or shear rate $\dot{\gamma}$ (s^{-1}) and by obtaining the resulting fluid viscosity η (Pa s) via controlled shear stress or controlled shear rate rotational rheometer (Mezger, 2014). In a rotational test, an increasing shear stress or shear rate ramp is applied for a selected range and the resulting shear rate or shear stress is measured.

Protocol

Here, the viscosity of the various foaming solutions only is investigated via rheometry. The viscosity of the different solutions is checked on a Rheometer DHR-1 (TA) at 25°C using cone-plate geometry (60 mm diameter, 2 degree of truncation) in a flow sweep test from 5 to 100 s^{-1} . The results representing the viscosity versus the shear rate for the different foaming solutions are presented in the dedicated results chapters (Chapter 6 & 7).

3.2.6.3 Surface characterisation: Atomic Force Microscopy (AFM)

All the details about the AFM protocol and working principle are presented in Appendix A-1.

3.2.6.4 Dynamic Light Scattering for Size measurement

Principle

The technique called Dynamic Light Scattering (DLS) is employed to evaluate the size of particles by directing a laser through a solution containing spherical particles in Brownian motion. Brownian motion describes the particles erratic dance caused by the bumps of the surrounding molecules and atoms contained within the medium in which they are dispersed in, resulting from thermal forces. When the laser hits the moving particle, a shift is generated, changing the wavelength of the incoming light. The intensity fluctuations in scattered light are related and analysed to obtain the size of the particles (Malvern, 2004).

The theory behind this technique is based on two assumptions. The first one is that the particles in solution are in Brownian motion. Following this first condition, the probability density function describing the conditional probability that a particle originally located at $r = 0$ and $t = 0$ will be found within a volume d^3r around r some time t later can be obtained from the following formula (Clark *et al.*, 1970):

$$P(r, t|0,0) = (4\pi Dt)^{-\frac{3}{2}} e^{\left(\frac{-r^2}{4Dt}\right)} \quad (3-5)$$

with D , the diffusion coefficient. The second condition is that the particles can be considered as spheres and present a diameter large compared to the molecular dimension.

Considering the erratic dancing of particles in solution, smaller particles move faster than larger particles. Therefore, the temporal evolution of equation (3-5) is driven by

the diffusion coefficient D . This physical relationship is well illustrated by the Stokes-Einstein equation through which the diffusion coefficient can be expressed such as:

$$D = \frac{k_B T}{6\pi\eta a} \quad (3-6)$$

with a , the radius of the particle, k_B , the Boltzmann constant, T , the temperature (Kelvin) and η , the solvent viscosity.

The spectral shape of the scattered light permits to confirm experimentally the evolution of equation (3-7) and to obtain the diffusion coefficient. Indeed, in a solution containing monodisperse particles, each illuminated particles will scatter light because its refractive index is different from that of its surrounding medium (Clark *et al.*, 1970). Thus, the light scattered of angles closed to a reference value θ is collected via a photomultiplier that translates the intensity variation into a voltage variation. Nevertheless, the intensity fluctuates around an average value due to the time evolution of the phase field scattered by each particle relative to the other particles while the particles are moving. Thereby, it is possible to obtain a measure of the random motion of scattering particles in a solution by studying the spectrum of the scattered light. Then, the frequency spectrum $S_I(\omega)$ of the intensity of the scattered light can be represented by a Lorentzian shaped line of width Γ is dependent upon the diffusion coefficient D and the scattering angle θ such as (Clark *et al.*, 1970):

$$S_I(\omega) \propto \frac{\Gamma(\theta)}{[\omega^2 + \Gamma^2(\theta)]} \quad (3-7)$$

with $\omega = 2\pi f$ and with $\Gamma(\theta)$ whose dependence can be described by as follow:

$$\Gamma(\theta) = 2D \left(\frac{4\pi}{\lambda/n_i} \sin^2 \frac{\theta}{2} \right)^2 \quad (3-8)$$

with λ , the incident light wavelength, n_i , the solution refraction index. To characterise the scattered light, two quantities are needed; namely, the average intensity $\langle I(t) \rangle$ and $G_I(\tau) = \langle I(t) I(t + \tau) \rangle$ the correlation function for the intensity. The spectrum of the scattered light can be described via the Wiener-Khintchine theorem (Clark *et al.*, 1970):

$$S_I(\omega) = \int_{-\infty}^{+\infty} e^{i\omega\tau} G_I(\tau) d\tau \quad (3-9)$$

From this equation, the normalised field correlation function for a monodisperse suspension of particles can be derived as follow (Bunkin *et al.*, 2014):

$$g^{(1)}(\tau) = \sum_i A_i e^{(-\frac{|\tau|}{t_{ci}})} \quad (3-10)$$

Thus, the normalised correlation function $g^{(1)}(\tau)$ can be represented by a sum of decaying exponentials characterised by the correlation time $t_{ci} = 1/(D_i q^2)$ with q , the scattering wave factor and A_i , a size constant.

The size distribution by intensity in solution and the particle's motion in solution can therefore be analysed by measuring the particle diffusion coefficient and by using the correlation function (Malvern Panalytical Ltd, 2018). In fact, the rate of decay of the correlation function is linked to the size of particle as it is much faster for smaller particles than for larger ones. From a solution of nanoparticles dispersed in a

solution, the initial size distribution by intensity from the spectrum of scattered light can be assessed. Then, two additional distributions by volume and by number can be obtained.

By plotting the relative percentage in class versus the diameter, a number distribution will show similar peak areas in a polydisperse solution if all particles show the same number of particles (Malvern, 2004).

In the case of a volume distribution, the peak area takes into consideration not only the number difference between the two particles populations but also the difference in volume between the two populations of particles.

Finally, the intensity distribution will tend to enhance the influence of the biggest particles because the scattering intensity is correlated to the sixth power of its diameter (Malvern, 2004).

In the case of polydisperse distribution, an expansion in series in powers of τ can be applied to the correlation function such as:

$$\ln g^1(\tau) = -\Gamma\tau + C_2\tau^2 + C_3\tau^3 + \dots \quad (3-11)$$

with Γ , the first coefficient allowing to calculate the mean effective particle radius, C_2 and C_3 characterising the width of the particle distribution and its asymmetry (Bunkin *et al.*, 2014). From these coefficients, the Z-average size and the Polydispersity Index (PDI) can be obtained.

Bulk nanobubbles are subjected to Brownian motion and are big compared to molecular dimension therefore Dynamic Light Scattering can be employed to study

the evolution of a bulk nanobubbles population in aqueous solution (Takenouchi, 2010).

Protocol

The Zetasizer NanoZSP (Malvern instruments Ltd) is employed to measure the size distribution of bulk nanobubbles in various solutions. This instrument can be used to measure size ranging from 0.3 nm up to 10 μm (Malvern, 2004). The laser power is attenuated. The attenuation index can vary from 0 to 11 describing 0 (total laser block) to 100 % (full laser power) nominal transmission or percentage of laser light entering the sample cuvette. This instrument is fitted with a red laser (power of 10 mW and wavelength of 632.8 nm). 1 mL of solution is placed in a disposable cuvette (referenced as DTS0012, cuvettes square macro 4 mL container) via a plastic syringe and sealed via a clean plastic cap. This cuvette is placed within the analysis chamber of the instrument. The measurement distance is set at 4.65 mm. The size measurement is operated at a measurement angle of 173° (back scatter angle). Furthermore, the measurements are performed with the following settings: three measurements per sample are realised with 11 runs per measurement and 10s between each run.

To compare qualitatively the distribution between the various solutions employed, it is considered in each case that the dispersed phase is composed of polystyrene nanoparticles and the dispersant is simply water. Consequently, its refractive index and viscosity are set at 1.33 and at 0.9974 cP at 25°C .

The refractive index corresponding to polystyrene nanoparticles is set at 1.59 and its absorption (quantity of light adsorbed by the material when suspended in the dispersant) is fixed at 0.01. The refractive index of air is supposed to be equal to 1 for

this range of wavelength. The equilibrium time (time before which the first measurement is taken) is set at 120 s to ensure that the cell is at the right temperature (25°C).

Prior to experimentation, purified water and all buffer solutions are initially analysed prior to any nanobubble generation to ensure that no nanoscale entities are detected.

Results are obtained in terms of bubble size distribution per intensity, volume and number. In this work, the Z-average size based on the intensity distribution and the PDI are employed to compare the effect of the various experimental conditions on the bulk nanobubbles distribution.

3.2.6.5 Zeta Potential (ζ) measurement

Principle

The zeta potential ζ is a key parameter to determine colloidal stability. Indeed, the zeta potential is a physical property exhibited by any particle in suspension, macromolecule or surface in a liquid. The zeta potential arises from the DVLO theory (Derjaguin, Verwey, Landau and Overbeek) describing the mechanisms driving the stability of particles in solution, notably, its total potential energy function. This potential energy function is made of three main contributions, namely, the solvent contribution, the Van der Waals attractive forces and the electrical double layer repulsive forces. The solvent contribution being small compared to the total potential energy; the balance between the attractive and repulsive contributions and more precisely, the sum of these two forces existing between two particles as they approach each other is determining for colloidal stability. The repulsive contribution can be expressed as follow:

$$V_R = 2\pi\epsilon a \zeta^2 e^{(-\kappa d_p)} \quad (3-12)$$

with ϵ , the dielectric constant, a , the particle radius, ζ , the zeta potential, κ^{-1} , the Debye length and d_p , the particle separation distance. This repulsive force prevents the particle aggregation. Its magnitude is determined partly by the value of zeta potential that represents the potential originated by the presence of ions at the surface of hydrodynamic shear (slipping plane), at the boundary of the electrical double layer composed of the stern layer and the diffuse layer (Hunter *et al.*, 2013) as illustrated in Figure 3. 5.

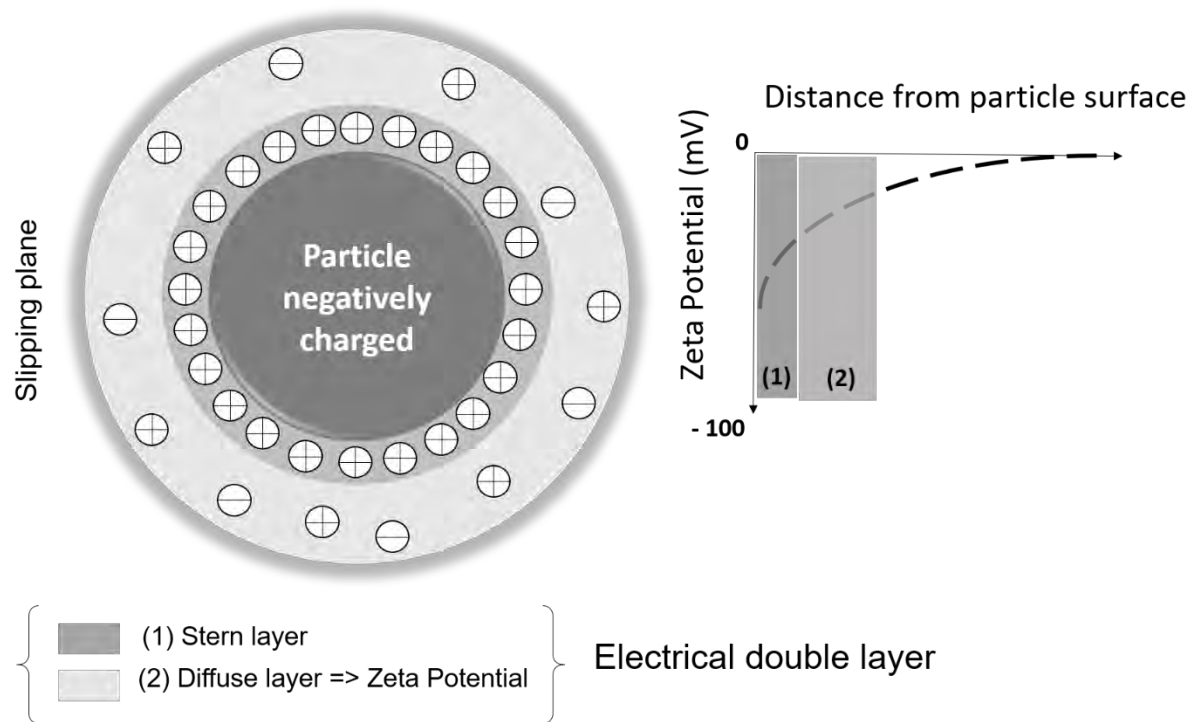


Figure 3. 5 Schematic representation of the zeta potential

A suspension is considered as stable if the particles dispersed in solution exhibit a large value (negative or positive) of the zeta potential. Thus, the particles will tend to repel each other, thus preventing particle aggregation. On the contrary, a low value

of zeta potential will imply less repulsion and will lead to particle aggregation (Malvern, 2004). Parameters such as pH, conductivity and concentration of dispersed entities in solution are key parameters affecting the zeta potential. Consequently, due to the presence of electrical charges on their surface, the particles can interact with an electric field. Then, the phenomenon of electrophoresis can be used to evaluate the density of charges on a surface and the resulting zeta potential. This phenomenon occurs when an electric field is applied across a solution containing charged entities, then these charged entities dispersed in solution are directed towards the pole of opposite charge with a constant velocity. This motion is opposed by the viscous forces acting on the particles until equilibrium is reached. The velocity of a particle is proportional to the applied electric field, and the resulting electrophoretic mobility is illustrated by the Henry equation (Malvern, 2004):

$$U_E = \frac{2\varepsilon\zeta f(\kappa a)}{3\eta} \quad (3-13)$$

with U_E , the electrophoretic mobility, ζ the zeta potential, ε , the dielectric constant, η , the solvent viscosity and $f(\kappa a)$, Henry's function (Malvern, 2004) and κ^{-1} , the Debye length (Malvern Panalytical Ltd, 2018). The parameter ' a ' refers to the radius of the particle and therefore κa measures the ratio of the particle radius to electrical double layer thickness (Malvern, 2004).

In this work, the Smoluchowski model is used which approximates $f(\kappa a)$ by 1.5 (Sze *et al.*, 2003). Despite the size of our bubbles (100 to 200 nm), the solvent used is water, so this approximation is chosen.

A technique called “Laser Doppler Velocimetry” (LDV) is employed to extract the electrophoretic mobility. It is based on the Doppler effect that describes the change in frequency of a wave in relation to the relative motion between to the wave and an observer (Briers, 2001). So, the frequency change being related to the change in source (light) and observer (object reflecting or scattering the light) velocities, the Doppler effect can be employed to evaluate velocities. Nevertheless, the direct measure of the frequency change is tedious due to the high frequency of light wave. Thereby, the reflected (or scattered) Doppler shifted light is mixed with the original light to detect a beat frequency equal to the frequency shift and correlated to the velocity of the object (Briers, 2001). Another method to evaluate the particles velocities in a liquid is to use laser speckle. When the illuminated object is a moving fluid, the speckle pattern fluctuates, leading to a time-varying laser speckle (Briers, 2001). The intensity fluctuation rate being correlated to the particle velocity, the velocity of the scattering particles and further, the electrophoretic mobility can be measured.

Protocol

The zeta potential of the nanobubbles is measured using a Zetasizer NanoZSP (Malvern instruments Ltd). Less than 1 mL of solution is placed in a “DST1060” capillary cell via a disposable 1 mL plastic syringe (Malvern, 2004). This cuvette is placed within the analysis chamber of the zetasizer. The following SOP (Standard Operating Procedure) is applied: three zeta potential measurements per sample are realised. Each completed measurement is composed of 11 runs. The cell and the cell caps are cleaned with water and ethanol three times prior any experimentation and dried with air.

3.3 List of references

- Bauer, W. A. C. *et al.* (2010) 'Hydrophilic PDMS microchannels for high-throughput formation of oil-in-water microdroplets and water-in-oil-in-water double emulsions', *Lab on a Chip - Miniaturisation for Chemistry and Biology*, 10, pp. 1814–1819. doi: 10.1039/c004046k.
- Briers, J. D. (2001) 'Laser Doppler, speckle and related techniques for blood perfusion mapping and imaging', *Physiological Measurement*. IOP Publishing, 22(4), pp. R35–R66. doi: 10.1088/0967-3334/22/4/201.
- Bunkin, N. F. *et al.* (2014) 'Study of the nanobubble phase of aqueous NaCl solutions by dynamic light scattering', *Quantum electronics*. Woodbury, NY :, pp. 1022–1028. doi: 10.1070/QE2014v044n11ABEH015462.
- Clark, N. A., Lunacek, J. H. and Benedek, G. B. (1970) 'A Study of Brownian Motion Using Light Scattering', *American Journal of Physics*. American Association of Physics Teachers, 38(5), pp. 575–585. doi: 10.1119/1.1976408.
- Cubaud, T., Ulmanella, U. and Ho, C.-M. (2006) 'Two-phase flow in microchannels with surface modifications', *Fluid Dynamics Research*, 38, pp. 772–786. doi: <http://dx.doi.org/10.1016/j.fluiddyn.2005.12.004>.
- Duffy, D. C. *et al.* (1998) 'Rapid Prototyping of Microfluidic Systems in Poly(dimethylsiloxane)', *Analytical chemistry*. Washington, DC :, pp. 4974–4984. doi: 10.1021/ac980656z.
- Garstecki, P. and Whitesides, G. M. (2006) 'Flowing Crystals: Nonequilibrium Structure of Foam', *Physical Review Letters*, 97, p. 24503. Available at: <https://link.aps.org/doi/10.1103/PhysRevLett.97.024503>.
- Grzybowski, B. A. *et al.* (1998) 'Generation of micrometer-sized patterns for microanalytical applications using a laser direct-write method and microcontact printing', *Analytical Chemistry*, 70(22), pp. 4645–4652. doi: 10.1021/ac9807621.
- Hunter, R. J., Ottewill, R. H. and Rowell, R. L. (2013) *Zeta Potential in Colloid Science: Principles and Applications*. Elsevier Science (Colloid science). Available at: <https://books.google.fr/books?id=9I3-BAAAQBAJ>.
- Hunter, T. N. *et al.* (2009) 'Non-ionic surfactant interactions with hydrophobic nanoparticles: Impact on foam stability', *Colloids and Surfaces A: Physicochemical and Engineering Aspects*, 347, pp. 81–89. doi: <https://doi.org/10.1016/j.colsurfa.2008.12.027>.
- Kim, P. *et al.* (2008) 'Soft Lithography for Microfluidics: a Review', *Biochip Journal*, 2, pp. 1–11. Available at: [internal-pdf://0720923336/soft lithography description.pdf](internal-pdf://0720923336/soft%20lithography%20description.pdf).
- Malvern, I. L. (2004) *Zetasizer Nano Series User Manual*. [online]. Available at: http://www.biophysics.bioc.cam.ac.uk/files/Zetasizer_Nano_user_manual_Man0317-1.1.pdf.
- Malvern Panalytical Ltd (2018) *Zeta Potential - an introduction in 30 minutes*, [online]. Available at: <https://www.malvernpanalytical.com/en/learn/knowledge->

center/technical-notes/TN101104ZetaPotentialIntroduction (Accessed: 22 June 2018).

Mark, A. E., Michael, A. J. and Bruce, K. G. (2008) 'Determining the optimal PDMS–PDMS bonding technique for microfluidic devices', *Journal of Micromechanics and Microengineering*, 18, p. 67001. Available at: <http://stacks.iop.org/0960-1317/18/i=6/a=067001>.

Mezger, T. G. (2014) *The Rheology Handbook, 4th Edition For users of rotational and oscillatory rheometers*. 4th Editio. Edited by European Coating Tech Files. Hanover, Germany: Vincents Network.

Peyman, S. A. *et al.* (2012) 'Expanding 3D geometry for enhanced on-chip microbubble production and single step formation of liposome modified microbubbles', *Lab on a Chip*, 12, pp. 4544–4552. doi: 10.1039/C2LC40634A.

Peyman, S. A. *et al.* (2016) 'On-chip preparation of nanoscale contrast agents towards high-resolution ultrasound imaging', *Lab on a Chip*, 16, pp. 679–687. doi: 10.1039/C5LC01394A.

Rabaud, D. *et al.* (2011) 'Manipulation of confined bubbles in a thin microchannel: Drag and acoustic Bjerknes forces', *Physics of Fluids*, 23, p. 42003. doi: 10.1063/1.3579263.

Raven, J.-P. and Marmottant, P. (2006) 'Periodic Microfluidic Bubbling Oscillator: Insight into the Stability of Two-Phase Microflows', *Physical Review Letters*, 97, p. 154501. Available at: <https://link.aps.org/doi/10.1103/PhysRevLett.97.154501>.

Raven, J.-P. and Marmottant, P. (2009) 'Microfluidic Crystals: Dynamic Interplay between Rearrangement Waves and Flow', *Physical Review Letters*, 102, p. 84501. Available at: <https://link.aps.org/doi/10.1103/PhysRevLett.102.084501>.

Safouane, M. *et al.* (2006) 'Viscosity effects in foam drainage: Newtonian and non-newtonian foaming fluids', *European Physical Journal E*, 19, pp. 195–202. doi: 10.1140/epje/e2006-00025-4.

Schneider, C. A., Rasband, W. S. and Eliceiri, K. W. (2012) 'NIH Image to ImageJ: 25 years of Image Analysis', *Nature methods*, 9, pp. 671–675. Available at: <http://www.ncbi.nlm.nih.gov/pmc/articles/PMC5554542/>.

Schramm, L. L. (2005) *Emulsions, Foams and Suspensions: Fundamentals and Applications*. Weinheim: Wiley-VCH Verlag GmbH & Co. KGaA.

Shao, N., Gavriilidis, A. and Angeli, P. (2009) 'Flow regimes for adiabatic gas-liquid flow in microchannels', *Chemical Engineering Science*, 64, pp. 2749–2761. doi: 10.1016/j.ces.2009.01.067.

Sze, A. *et al.* (2003) 'Zeta-potential measurement using the Smoluchowski equation and the slope of the current–time relationship in electroosmotic flow', *Journal of Colloid and Interface Science*, 261(2), pp. 402–410. doi: [https://doi.org/10.1016/S0021-9797\(03\)00142-5](https://doi.org/10.1016/S0021-9797(03)00142-5).

Takenouchi, T. (2010) 'Behavior of hydrogen nanobubbles in alkaline electrolyzed water and its rinse effect for sulfate ion remained on nickel-plated surface', *Journal of*

Applied Electrochemistry, 40, pp. 849–854. doi: 10.1007/s10800-009-0068-z LB - Takenouchi2010.

Wilding, P. *et al.* (1994) 'Manipulation and flow of biological fluids in straight channels micromachined in silicon.', *Clinical Chemistry*, 40(1), p. 43 LP-47. Available at: <http://clinchem.aaccjnls.org/content/40/1/43.abstract>.

William Thielicke, E. J. S. (2014) 'PIVlab – Towards User-friendly, Affordable and Accurate Digital Particle Image Velocimetry in MATLAB', *Journal of Open Research Software*, 2(1). doi: <http://doi.org/10.5334/jors.bl>.

CHAPTER 4

INVESTIGATING BULK NANOBUBBLE

GENERATION VIA MICROFLUIDICS

4.1 Introduction

This chapter introduces the first part of the microfluidics investigation concerning the effect of a new kind of potential surface-active agent namely, bulk nanobubbles, on the foaming properties. Peyman *et al.* (2012, 2016) reported that an atomisation-like spray caused the generation of bulk nanobubbles via microfluidics due to the strong pressure drop created by the change of depth in the microchannel (from 25 to 50 μm). However, there has been no detailed examination of the mechanisms at stake in nanobubble generation process. In addition, no research has been found that surveyed the parameters influencing bulk nanobubbles generation via microfluidics. This study provides an overview of the parameters influencing bulk nanobubbles generation via microfluidics.

In this chapter, two mechanisms are considered for the formation of nanobubbles in solution: hydrodynamic cavitation and the Rayleigh-Taylor hydrodynamic instability.

Hydrodynamic cavitation occurs in a liquid when the pressure within the liquid becomes locally lower than the liquid vapour pressure. Then, the liquid evaporates to form gaseous cavities, namely, bubbles. Etchepare *et al.* (2017) and Oliveira *et al.* (2018) developed techniques to generate nanobubbles at high concentration based on this principle. Furthermore, Nirmalkar *et al.* (2018) showed that hydrodynamic cavitation was employed to generate nanobubbles in a single-depth microfluidic channel submitted to very high liquid flow rate and gas pressure.

Secondly, the Rayleigh-Taylor dynamic instability is thought to be the second mechanism leading to the generation of bulk nanobubbles via microfluidics. This instability is more often observed when a gas is being sprayed by a liquid. For the

nanobubble case, a gas stream in a microchannel is being squeezed by a strong two-side liquid stream through a nozzle and submitted to a strong pressure drop forming bubbles. Interestingly, the work reported by Gaillard (2016) suggested that submicron bubbles were generated during the foaming process via a double-syringe technique because of Rayleigh-Taylor instability. Indeed, a series of constrictions within the system could generate locally a pressure drop that could lead to sub-micron bubble generation.

The Rayleigh-Taylor instability is driven by surface tension and tends to force the jet to minimize its surface energy. The smaller the jet diameter, the greater the surface to volume ratio, and the more energetically favourable it is to transform this jet into bubbles (Gaillard, 2016). Thus, the narrower the nozzle at the junction is, and the smaller the bubbles are generated. This work suggests that the presence of additives able to reduce the interfacial tension could strongly affect bulk nanobubble generation.

The present research explores, for the first time, the effects of various parameters on bulk nanobubbles generation via microfluidics. Indeed, the impact of the device geometry, the generation cycle, and the control parameters on the nanobubbles properties (size distribution and zeta potential) was examined. The study offers some important insights into the existing interactions between nanobubbles and several additives in solution (nanoparticles, surfactants). Thus, it is hoped that this research will contribute to a deeper understanding of the influence of nanobubble-surfactant foaming liquid on the foam gas-liquid interface and the resulting foam stability.

The results and discussion section will be divided in three parts: the first one will establish the gaseous nature of the nanoscale entities generated via microfluidics via bulk and surface characterisations. The second part will summarise the impact of external parameters such as the nozzle diameter, the gas inlet pressure and the cycle of generation on the bulk nanobubbles properties in solution. The third part will report the influence of several additives in water (nanoparticles, surfactants) on the nanobubble population in solution.

4.2 Results and discussions

The strong interest to use nanobubbles as a potential surface agent resides in two things: its extraordinary stability and its gaseous nature. However, these two features combined are counterintuitive. Indeed, such small bubble should exhibit a large internal Laplace pressure and thereby, should disappear almost instantly from classical diffusion theory (Seddon *et al.*, 2012). Therefore, the first step in any nanobubble research is to prove the gaseous nature of the nanobubbles. Thus far, Atomic Force Microscopy (AFM) has been widely employed to characterise surface nanobubbles (Lou *et al.*, 2002). Dynamic Light Scattering (DLS) have been employed to characterise dispersions of bulk nanobubbles in various solutions (Bunkin *et al.*, 2014). In this work, these two techniques were employed to study the properties and to prove the gaseous nature of nanobubbles.

4.2.1. Evidence of bulk nanobubbles generation

The first step in the study of the generation of bulk nanobubbles via microfluidics was to prove that what had been generated was indeed made of gas, and not a solid nanoparticle. Three experiments were realised for this purpose. The gaseous nature

was firstly evidenced in the bulk via DLS characterisation and then on a surface via AFM. The surface characterisation results are in section A.1.2.1 of Appendix A-1.

4.2.1.1 Bulk characterisation experiments

Firstly, the nature of the entities generated via the two-depth microfluidic device was verified. Indeed, the pressure drop generated due to the change in depth could lead to the detachment of some PDMS from the wall and produce PDMS residues. To do so, pure water was flowed through the single-depth microfluidic device employed for foam generation. No entities in water were observed before and after flowing through the single depth device for the same set of gas inlet pressure and liquid flow rate.

Secondly, the single study of the bubble size evolution over time for the 15 μm nozzle supported the hypothesis that the entities generated were made of gas as illustrated in Figure 4. 1.

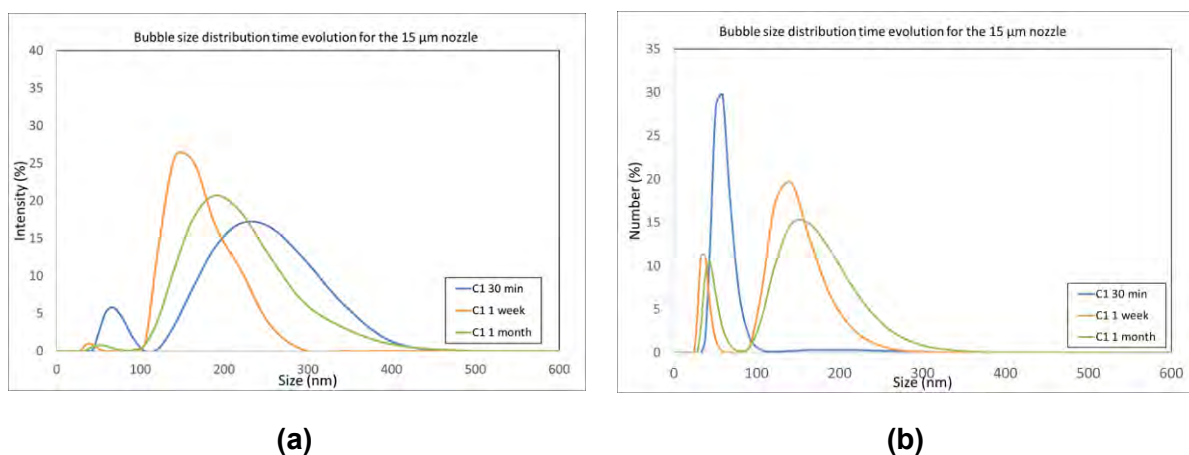


Figure 4. 1 Bulk nanobubbles size distribution time evolution by intensity (a) & number (b) in pure water (30 min, blue - 1 week, orange - 1 month, green) via the 15 μm nozzle microfluidic device. The results represent the average of two experiments.

Each plot represented the result of one generation cycle via the 15 μm and its evolution after 30 minutes, 1 week and 1 month after generation. It was observed that smaller bubbles were merging into bigger bubbles. Indeed, the intensity and

number bimodal distribution evolved over time: 30 minutes after collection, the number of smaller nanobubbles was greater than the 200 nm bubbles. Then, after one week, two clear peaks in the number distribution were observed. This result suggested that the number of smaller bubbles had decreased compared to the number of 200 nm bubbles in solution. It is possible also that the coalescence occurred in solution leading to the increase in the number of 200 nm bubbles in solution. After one month, the two bubble populations had decreased slightly but persisted still. Thereby, these evolutions showed that unlike residual impurities or nanoparticles that could have sedimented or agglomerate over time, nanobubbles were stable in solution.

Thirdly, Nirmalkar *et al.* (2018) simply demonstrated the gaseous nature of bulk nanobubbles by freezing pure water containing nanobubbles over night at -18°C and thawing the resulting frozen solution. The result was that the population of nano-entities in solution had drastically decreased. This result demonstrated that bulk nanobubbles were made of gas and not solid nanoparticles because nanoparticles would have aggregated strongly after such experiment.

A similar experiment with a bulk nanobubble solution obtained via one generation cycle with the $15\ \mu\text{m}$ nozzle device was performed. A 5 mL bulk nanobubbles sample contained within a glass vial was frozen by dipping it for 30s in liquid nitrogen and by thawing at room temperature for a whole day. After this experiment, no nanobubbles could be detected via DLS.

To further confirm the gaseous nature of the entities dispersed in solution, Atomic Force Microscopy (AFM) was chosen as a mean to study what was left on a dry and

clean hydrophobic surface after deposition and settling of a droplet of nanobubble water for 30 minutes prior to imaging. Thus, impurities acquired during the experiment could sediment on the surface and be detected and probed via AFM. Furthermore, the influence of the presence of bulk nanobubbles in solution on the number of surface nanobubbles on the surface could be analysed. All the surface characterisation results are reported in section A.1.2 in Appendix A.1.

All in all, by considering the two sets of experiment reported in Appendix A.1, it was demonstrated that what had been generated by direct deposition of acidic solution and by electrochemical generation presented the same properties. These findings strongly suggest that the entity that was analysed in the previous cases studied was indeed a bubble and not a droplet which could be also softer than the surface.

The scope of this combined work of bulk and surface characterisations was to prove that the nanoentities generated via microfluidics were bubbles and not solid contaminants. It was showed that over 1 month the bubble size distribution was evolving due to potential coalescence in solution. Then, AFM was employed to prove that no sedimented particles were found on the surface after deposition of bulk nanobubbles solution. Furthermore, the AFM study demonstrated that the only entities found on the surface showed the same physical properties that the one present in pure and acidic water, before and after electrochemical generation. The freezing-thawing experiment completed the demonstration that bulk nanobubbles generated via microfluidics showed a gaseous nature.

In the next section, the different parameters influencing bulk nanobubble generation and properties are studied via DLS.

4.2.2. Effect of experimental conditions on bulk nanobubble generation

In this section, the impact of several external parameters on bulk nanobubble generation via microfluidics was investigated.

4.2.2.1 Effect of nozzle diameter on the bulk nanobubble properties

The effect of the size of three different nozzle diameters (10, 15 and 20 μm) on nanobubble size distribution for one cycle of generation via microfluidics, 30 minutes after collection, for a gas inlet pressure of 1000 mbar and a liquid flow rate of 90 $\mu\text{L min}^{-1}$ is represented in Figure 4. 2.

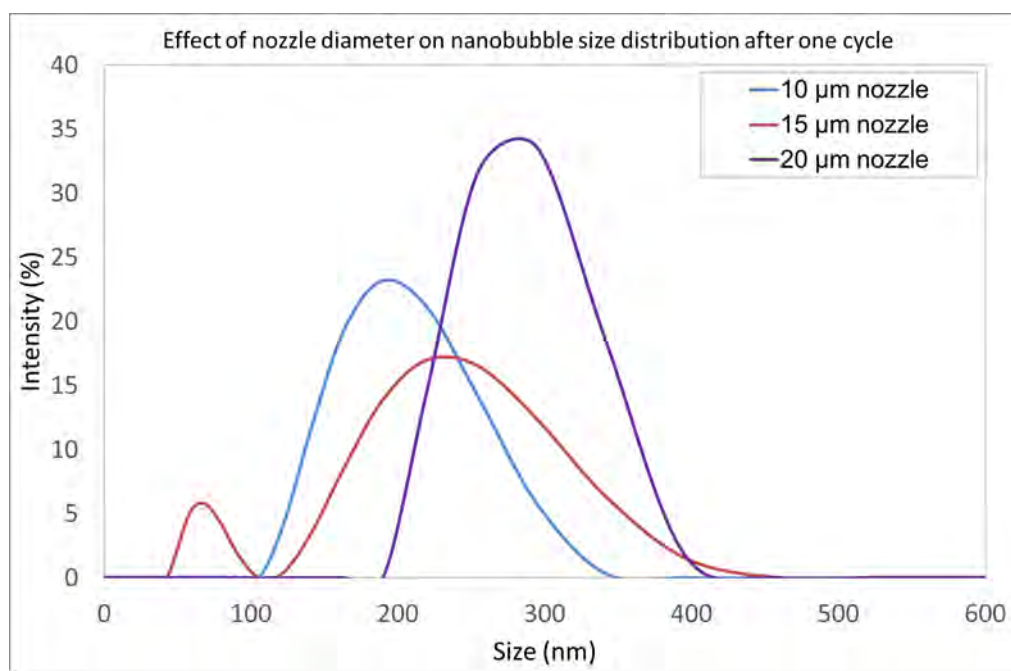


Figure 4. 2 Effect of nozzle diameter on bubble size distribution by intensity for one cycle of generation with the 10, 15 and 20 μm nozzle distribution represented as blue, red and purple lines respectively. The results represent the average of two to three measurements per nozzle.

From the intensity distribution, it appeared that each nozzle provided a range of bubble size varying from 50 nm up to 400 nm. The 10 μm nozzle distribution showed a monodisperse distribution centred at 200 nm. The 15 μm nozzle distribution presented a bimodal distribution with a smaller peak below 100 nm and a second

peak centred at 250 nm. Lastly, the 20 μm nozzle distribution depicted a single peak centred at 300 nm. Each nozzle and resulting bubble distribution presented the same stability up to one month as illustrated in Figure 4. 3 summarising the results obtained for two to three repeats of the same experiment.

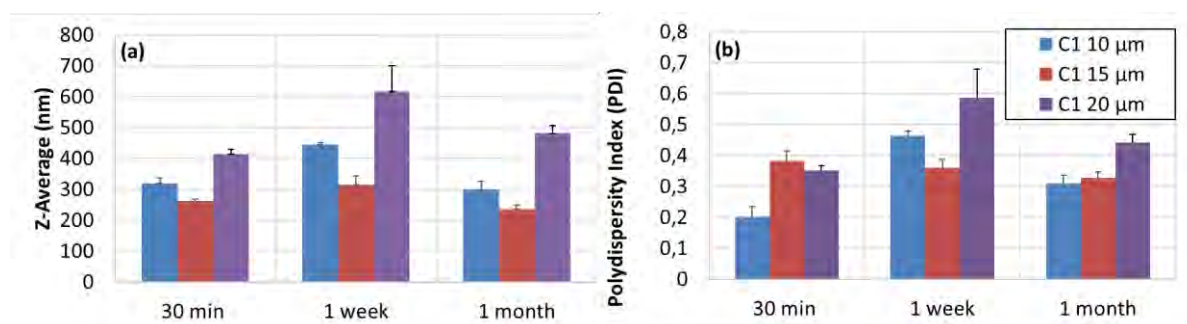


Figure 4. 3 Effect of nozzle diameter on the Z-average (a) and the Polydispersity Index (PDI, (b)) evolution diameter evolution after 1 generation cycle with the 10 (blue), 15 (red) and 20 μm (purple) nozzle distribution. The results represent the average of two to three measurements per nozzle.

The evolution represented in Figure 4. 3 (a) indicated that the increase in nozzle diameter enhanced the Z-average diameter. Thus, the Z-average diameter obtained for the 20 μm nozzle was almost twice the value for 10 μm nozzle after 1 month. In Figure 4. 3 (b), the PDI evolution demonstrated that a greater nozzle diameter increased the polydispersity of the nanobubble distribution. Indeed, the 15 μm nozzle distribution was bimodal compared to the 10 μm distribution. From the 15 μm nozzle number distribution, the peak below 100 nm was much more significant compared to the 200 nm peak. This demonstrated that 50 nm nanobubbles were dominant in solution compared to the 200 nm nanobubbles. It appeared that the smaller the diameter and the more uniform the spraying was, leading to the formation of more monodisperse distributions of nanobubbles in solution. Thereby, by increasing the diameter, both the average diameter and the polydispersity increased due to a reduction of the spraying efficiency, causing the formation of smaller and bigger

nanobubbles in solution. These results showed that the differences between the three nozzles were significant because the resulting nanobubbles distributions were directly correlated to the spraying efficiency of the nozzle. It was found that the broader the nozzle and the greater were the average bubble diameter and the polydispersity index. This statement is in the line with what should happen in the case of a mechanism based partly on the Rayleigh-Taylor instability. Indeed, the mean bubble diameter produced by the jet coming through the nozzle should depend strongly on the nozzle diameter. For the next study regarding the effect of the gas inlet pressure for a fixed liquid flow rate, the 20 μm nozzle was employed.

4.2.2.2 Effect of gas inlet pressure for a fixed liquid flow rate

In this section, the effect of the gas inlet pressure for a fixed liquid flow rate was examined because it has been demonstrated in the literature that gas saturation impacted strongly the nanobubbles properties (Tuziuti *et al.*, 2018). Thus, by varying the gas pressure, both amount of gas brought to the system and gas flow rate were changed. Because the gas was continuously flowing, it was considered that the gas saturation was maintained in solution during the nanobubble generation. From the results presented in Appendix A.2, the gas inlet pressure did not influence significantly the nanobubbles zeta potential, and thus their stability. Indeed, the gas oversaturation was constantly reached as the gas was continuously injected in solution. Therefore, no more gas could be dissolved in solution, and the gas diffusion was limited.

4.2.2.3 Effect of generation cycle on the nanobubble size distribution

Etchepare *et al.* (2017) determined that the repeat of a cycle of flow and consecutive recycling of aqueous solution through a venturi was enhancing the concentration of nanobubbles in solution generated by hydrodynamic cavitation.

Here, this effect was verified at microscale by repeating the cycle of flow and recycling by simply re-injecting the same pure water solution through the microfluidics device up to three times. Three cycles of generation-recycling were performed and their effect on the bulk nanobubble population was studied for each nozzle (10, 15 and 20 μm nozzles). In this paragraph, the results for the 20 μm nozzle are reported. For the results for the 10 and the 15 μm , see Appendix A.3.

i. 20 μm nozzle

In Figure 4. 4, the effect of the generation cycle on the bubble size distribution realised via the 20 μm nozzle microfluidic device for a fixed gas pressure of 1000 mbar and a liquid flow rate of 90 $\mu\text{L min}^{-1}$ is illustrated over time. The generation cycles are denoted “C1”, “C2” and “C3” for first, second and third cycles respectively.

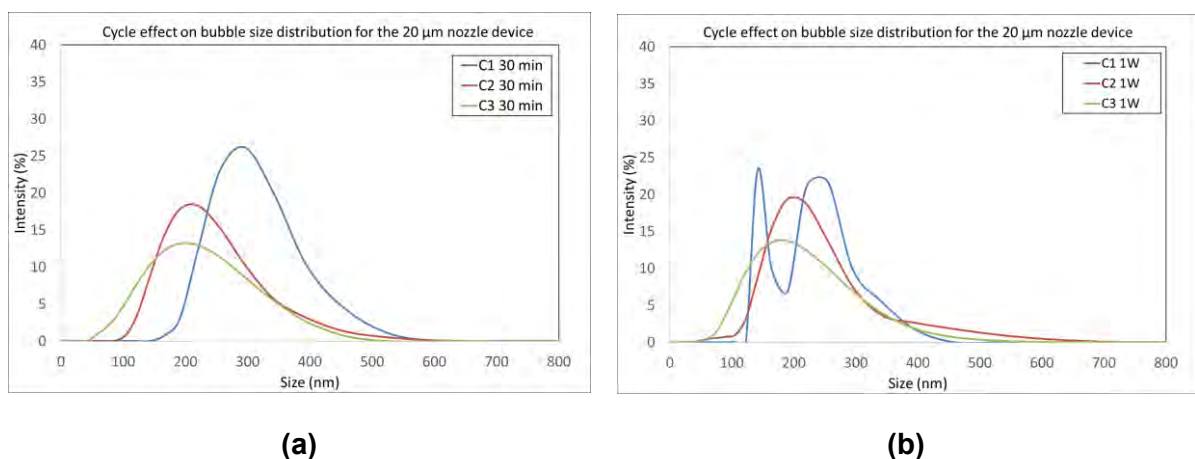


Figure 4. 4 Bulk nanobubbles intensity size distributions evolution in pure water 30 minutes (a) and 1 week after generation (b) through three generation cycles (C1, blue - C2, red - C3, green)

via the 20 μm nozzle microfluidic device. The results represent the average of three experiments.

From Figure 4. 4 graph (a) obtained from the collection of bulk nanobubbles 30 minutes after their generation, it was showed that the cycle had an important impact on the bubble size distribution. Indeed, by C1, a single peak centred at 300 nm was observed. Then, by C2 and C3, the distribution shifted towards the smaller bubble sizes centred at 200 nm. Indeed, repeating the generation cycle enhanced the number of smaller bubbles compared to the 200 nm bubble population that seem to disappear to the profit of the 100 nm bubble population in solution.

The graph (b) represented the bulk nanobubble distribution by intensity 1 week after generation. The initial single peak obtained by C1 presented a bimodal distribution after 1 week. Indeed, the Z-average diameter value obtained for C1 was divided by two at C3 as reported in Figure 4. 5.

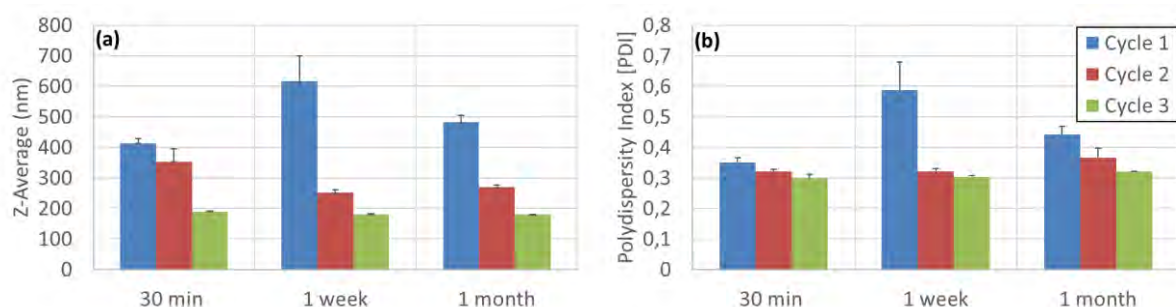


Figure 4. 5 Evolution of the Z-average diameter (a) and the Polydispersity Index (PDI, (b)) describing the bulk nanobubbles distribution in solution per cycle of generation for the 20 μm nozzle. The results represent the average of three experiments.

It was observed again that the cycle repeat enhanced the generation of smaller nanobubbles. Indeed, from C1 to C3, the distribution was shifted towards the smallest size. Thereby, from C1 to C3, the Z-average diameter was halved. The resulting PDI was also narrowed down with the cycle generation. All these

nanobubble samples were stable up to one month. Indeed, the average zeta potential obtained for all the cycles (2 to 3 repeats per sample) was measured at -40 ± 3 mV.

Over the three parameters studied, the nozzle diameter and the cycle generation showed the two strongest impact on bubble size distribution obtained for a fixed pressure and liquid flow rate. On one hand, the broader the nozzle diameter and the larger the initial bubble diameter was obtained. On the other hand, the more cycle repeat, the smaller the bulk nanobubbles were obtained in solution for each nozzle investigated.

Now that a better understanding and control on bulk nanobubbles generation via microfluidics were acquired, those determining factors were fixed to evaluate how different additives such as surfactant and nanoparticles could influence the bubble size distribution.

4.2.3. Effect of various additives on bulk nanobubble generation

Here were investigated the bulk nanobubbles-additives (surfactants, nanoparticles, polymers) interactions that can occur in various colloidal systems (foams, emulsions). The 20 μm nozzle device was used for the following experiments.

4.2.3.1 Effect of surfactant on nanobubbles formation & stability

i. Effect of anionic surfactant: Sodium Dodecyl Sulfate (SDS)

In this part, the effect of SDS (Sodium Dodecyl Sulfate), an anionic surfactant at the concentration of 0.5 times the critical micellar concentration (cmc) was evaluated on the bubble size distribution generated via microfluidics through three generation cycles as described in Figure 4. 6.

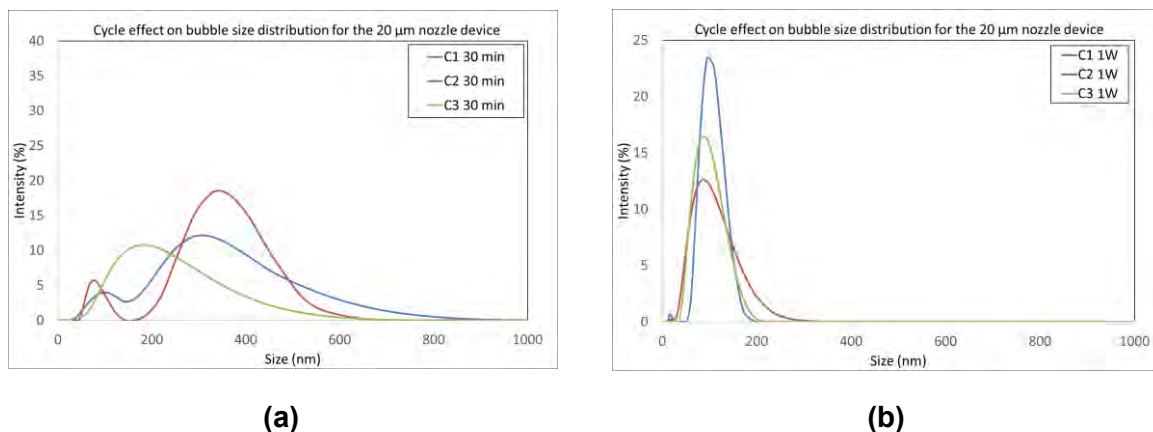


Figure 4. 6 Bulk nanobubbles size distributions by intensity 30 minutes (a) and one week after generation via the 20 μm nozzle device from a 0.5 cmc SDS solution through 3 generation cycles (C1, blue - C2, red - C3, green lines). The results represent the average of two experiments.

The graphs (a) and (b) in Figure 4. 6 illustrate respectively the bubble size distribution 30 minutes and 1 week after generation via microfluidics. C1 and C2 presented two bimodal distributions with one peak slightly below 100 nm annexed to a broader peak centred at about 350 nm. C3 showed a monodispersed distribution centred at 200 nm. These observations are further supported by the evolution of the Z-average diameter and PDI in Figure 4. 7. From C1 to C3, the Z-average diameter decreased with the cycle repeat as illustrated by the slow shift of the nanobubble distribution towards the smallest size.

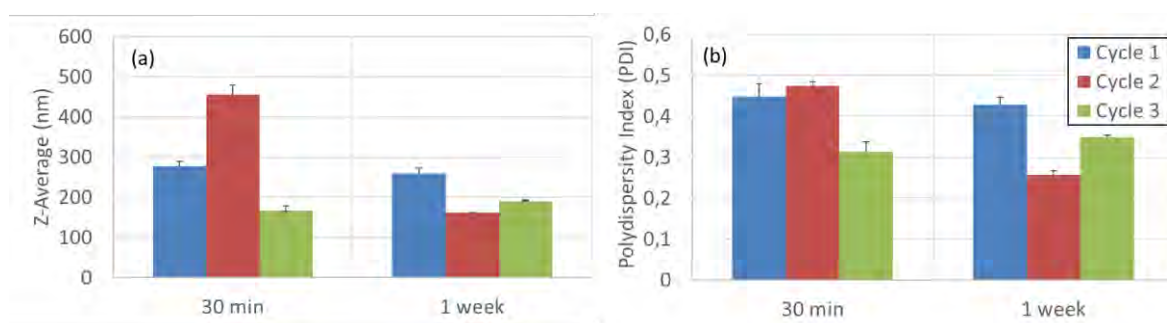


Figure 4. 7 Evolution of the Z-average diameter (a) and Polydispersity Index (PDI, (b)) describing the bulk nanobubbles distribution in 0.5 cmc SDS solution per cycle of generation for the 20 μm nozzle. The results represent the average of two experiments.

After one week, the three cycles showed a monodisperse distribution centred at 100 nm. However, the more the cycle, the broader became the peak. Indeed, the C1 ranged from 50 to 200 nm and the C2 from 50 up to 350 nm.

However, a small peak below 50 nm at 0.6 % intensity was visible at C1 but decreased down to 0.2 % intensity at C2 and disappeared completely at C3. Consequently, unlike previously, it seemed that repeating the cycle tended to increase the bubble diameter by a potential coalescence of the smallest range of bubbles. From Figure 4. 7 (b), it is showed that the PDI decreased with the repeat of the cycle of generation.

Furthermore, the zeta potential was measured and averaged for two experiments over the three generation cycles at about $- 86 \pm 4$ mV. This results is in the line with what had been described by Nirmalkar *et al.* (2018). It was explained that SDS increased the bulk nanobubbles negative charged and thus enhanced their stability in solution. Despite the increase in the zeta potential which should have enhanced the bubble stability, the disappearance of smaller bubbles was observed to form intermediate size bubbles as expressed in the transition from C2 to C3. The destabilising mechanism behind the merging of two bubbles despite the increase of surface charge and the action of SDS in the network of nanobubbles in solution remains unclear at this stage of the work.

ii. Effect of non-ionic surfactant: Triton X-100

In this section, Triton X-100 was chosen to study if the addition of a non-ionic surfactant enhances the stability of nanobubbles in solution. A concentration of 0.6 cmc was chosen to ensure the coverage of the nanobubble of about 200 nm without

enhancing the foaming of the solution based on the concentration required to saturate the surface of a 200 nm diameter particle as described in (Braibanti, Vigolo and Piazza, 2008). For this calculation, nanobubbles concentration of 10^9 bubbles per mL was selected based on the concentration reported in the literature for nanobubble generation via microfluidics in similar experimental conditions (Peyman *et al.*, 2012, 2016).

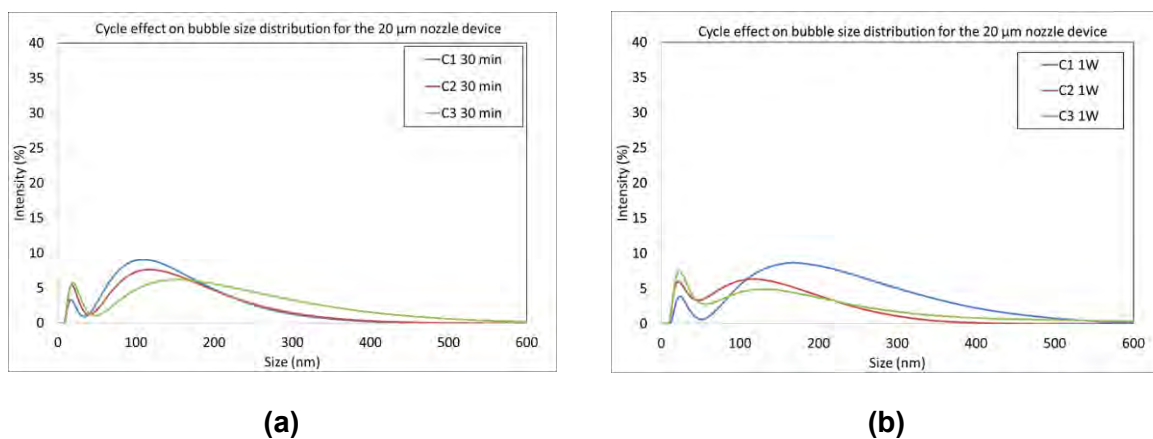


Figure 4. 8 Bulk nanobubbles size distributions by intensity 30 minutes (a) and 1 week after generation (b) via 20 μ m nozzle device from a 0.6 cmc Triton X-100 solution through 3 generation cycles (C1, blue - C2, red - C3, green). The results represent the average of three experiments.

In Figure 4. 8, the graphs (a) and (b) illustrate the cycle effect on the bubble size distribution obtained from a 0.6 cmc Triton X-100 aqueous solution injected through the 20 μ m nozzle device. The three cycles generated a bimodal distribution with a first peak below 50 nm and a second broader peak at 100-150 nm. One week after generation, the distributions showed similar trends. Interestingly, the same generation cycles had created a bimodal nanobubble distribution in pure water as reported in Figure 4. 4 with a Z-average diameter ranging from 400 to 200 nm. In Figure 4. 9, the Z-average diameter evolution for the three generation cycles, 30 minutes and 1 week after generation via the 20 μ m nozzle device is represented:

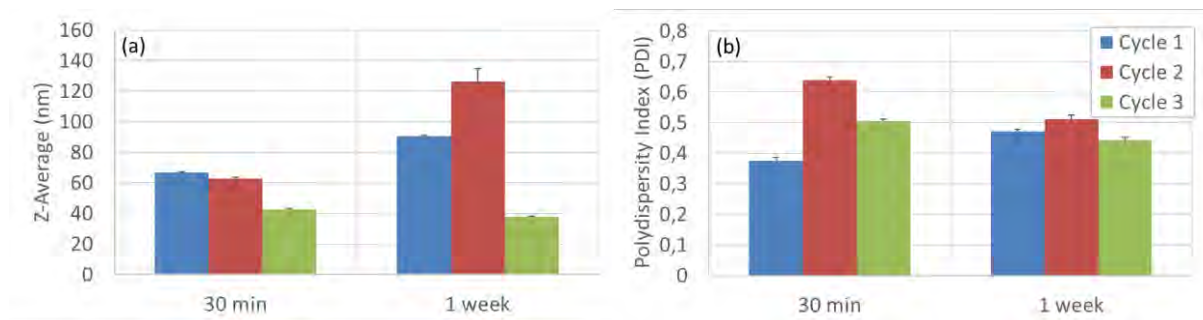


Figure 4. 9 Evolution of the Z-average diameter (a) and the Polydispersity Index (PDI, (b)) describing the bulk nanobubbles distribution in Triton X-100 solution per cycle of generation for the 20 μm nozzle. The results represent the average of three experiments.

The difference in Z-average diameter after 30 minutes between the pure water solution and the Triton X-100 solution is striking. Indeed, the Z-average diameter varied between 400 to 200 nm for pure water compared to 60 to 40 nm for Triton X-100. The cycle repeat reduced slightly the Z-average diameter.

The evolution of the PDI with the cycle repeat, thirty minutes and one week after generation demonstrates that the size difference between the two populations part of the bimodal distribution illustrated in Figure 4. 8 has increased with the cycle repeat. Firstly, the PDI range resulting from Triton X-100 is greater (from $37.0 \pm 1.0 \times 10^{-2}$ to $64.0 \pm 1.0 \times 10^{-2}$ after 30 minutes) than the one obtained with pure water (from $30.0 \pm 1.0 \times 10^{-2}$ to $35.0 \pm 2.0 \times 10^{-2}$). This result can be related to the increased in the number of smaller nanobubbles in solution for a fixed or reduced number of larger nanobubbles. Therefore, it was considered that the cycle generation and the presence of Triton X-100 enhanced the formation of smaller nanobubbles in solution. These results suggested that the presence of Triton X-100 in solution did not prevent the formation of nanobubbles in solution. On the contrary, it is believed that surfactant molecules caused the formation of smaller nanobubbles by adsorbing themselves onto the nanobubble surface and thus reducing their surface tension.

Furthermore, the nanobubbles generated were also stable up to one week at least and showed a zeta potential of approximately $- 27.7 \pm 1.2$ mV. Nevertheless, this value is lower compared to the value obtained in pure water. The surfactant adsorption on the nanobubble surface could screen partially the nanobubble surface charge, thus reducing the zeta potential.

4.2.3.2 Effect of nanoparticles on nanobubbles formation & stability

In this section, the effect of two sizes (30 and 200 nm) of hydrophilic nanoparticles at fixed concentration of 0,01% (wt.%) on the generation and stability of bulk nanobubbles in pure water and in Triton X-100 solutions was investigated.

i. Effect of 200 nm hydrophilic PS nanoparticles

In this paragraph, the effect of the addition of a fixed concentration of 200 nm hydrophilic PS nanoparticles on nanobubble size distribution generated via the 20 μ m nozzle microfluidic device was studied. The reference nanoparticle size distribution is represented in Figure 4. 10.

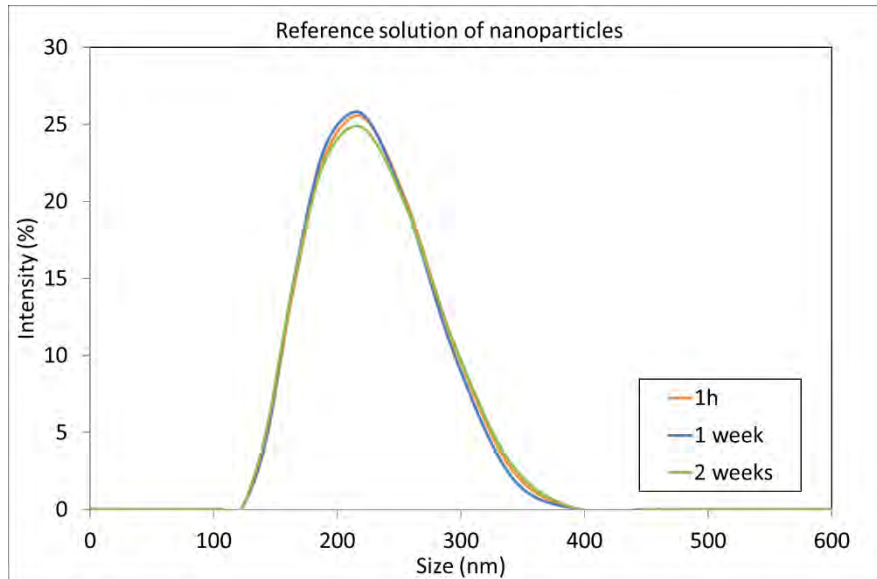


Figure 4. 10 200 nm hydrophilic polystyrene particle size distribution by intensity over time (1h, orange – 1 week, blue – 2 weeks, green lines). The results represent the average of two experiments.

The nanoparticle reference solution was submitted to three cycle of flow and recycling through the 20 μm nozzle microfluidic device. In Figure 4. 11 are presented the size distributions for three generation cycles from the initial nanoparticle size distribution illustrated in Figure 4. 10, resulting from the average of three experiments.

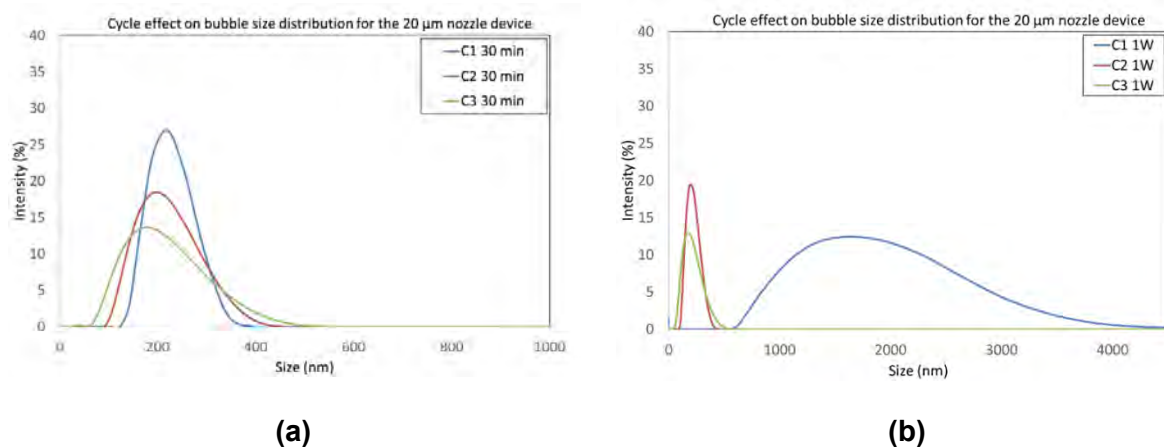


Figure 4. 11 Bulk nanobubbles-nanoparticles size distributions by intensity 30 minutes (a) and one week (b) after generation from a nanoparticle aqueous solution through 3 generation

cycles (C1, blue - C2, red - C3, green lines). The results represent the average of two experiments.

The evolution of the nanobubble-nanoparticle suspension was compared to the initial monodisperse nanoparticle distribution centred at 200 nm. From Figure 4. 11 (a), by C1, 30 minutes after generation, it was found that the nanoparticles distribution was not impacted significantly. This is because the nanobubble concentration was not high enough to be noticeable compared to the concentration of nanoparticles in solution despite being diluted. By C2 and C3, the distribution was shifted towards the smaller size nanobubbles. Indeed, at C2 and C3, the number of smaller nanobubbles increased as observed previously for the pure water case. Additionally, the initial nanoparticle peak slowly faded throughout the generation cycles. This confirmed the increase in the number of nanobubbles compared to a fixed number of particles and finally the overcome of the number of nanoparticles in solution by the third cycle. As a result, the Z-average diameter describing the nanobubble-nanoparticle dispersion decreased with the repeat of the generation cycle as illustrated in Figure 4. 12.

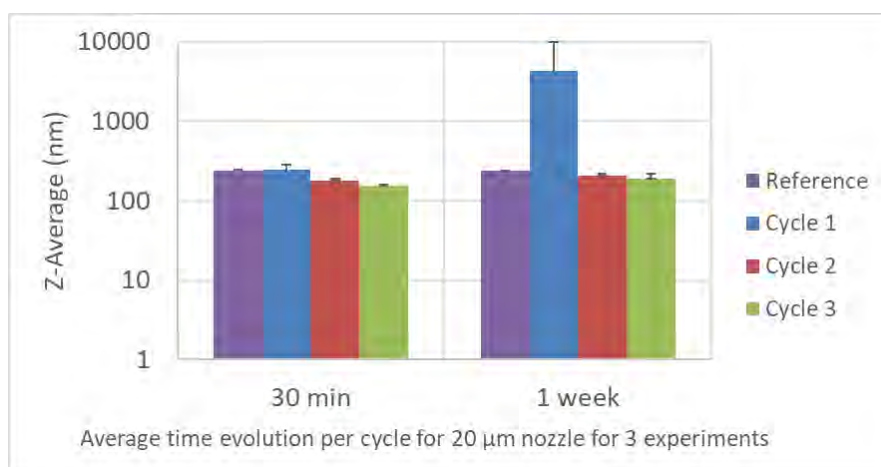


Figure 4. 12 Evolution of the Z-average diameter describing the bulk nanobubbles - nanoparticles distribution per cycle of generation for the 20 µm nozzle. The results represent the average of two to three measurements per sample (cycle or reference).

Reversely, the PDI increased with the repeat of the generation cycle because the nanobubble population became more and more important compared to the reference nanoparticle solution as represented in Figure 4. 13.

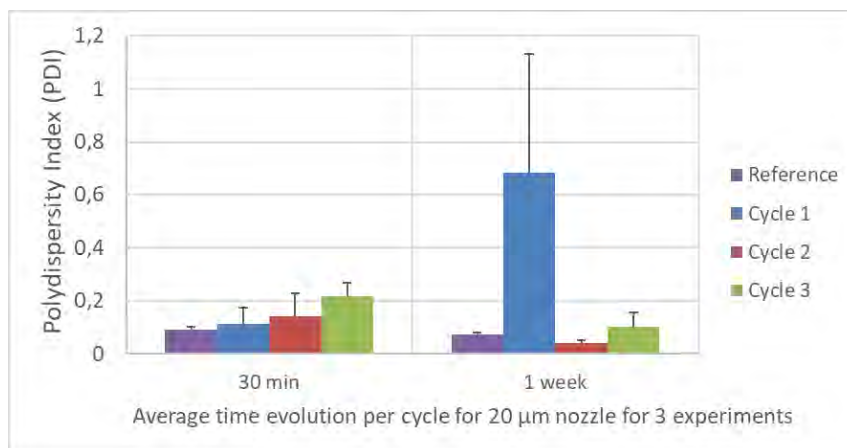


Figure 4. 13 Evolution of the Polydispersity Index (PDI) describing the bulk nanobubbles - nanoparticles distribution per cycle of generation for the 20 µm nozzle. The results represent the average of two to three measurements per sample (cycle or reference).

After one week, the C2 and C3 distributions stayed the same. However, the C1 distribution showed the formation of a broad peak centred at 1500 nm. The nanoparticle peak was no longer visible.

The experiment was repeated three times. Each time, the C1 distribution evolved after two days or one week into a broad distribution of micron-size agglomerate whereas C2 and C3 were stable up to one month. Despite the variability of the size of the aggregate obtained at C1, the Z-average diameter and PDI evolution in Figure 4. 12 and Figure 4. 13 respectively confirmed the singularity of the C1 aggregation compared to C2 and C3.

The nanobubbles generated by C1 could have triggered the aggregation of 200 nm PS nanoparticles in solution. Indeed, Knüpfer *et al.* (2017) demonstrated that bulk nanobubbles were enhancing the aggregation of hydrophobic powders compared to

hydrophilic powders dispersed in liquid. Furthermore, Zhang and Seddon (2016) found the existence of a threshold size of gold nanoparticles (60 nm) at which nanobubbles could attach themselves and form a nanobubble-nanoparticle aggregate. Thereby, there may exist a threshold size required for nanobubbles to enhance the aggregation of 200 nm nanoparticles.

From the previous experiments in pure water, it was observed that the smallest nanobubbles were more stable and their number was enhanced by the cycle repeat. The larger nanobubbles being generated at C1 may not be as stable as the C2 and C3 ones. Therefore, the C1 nanobubbles could be more likely to adsorb themselves at the nanoparticle surface and bridge two nanoparticles together, creating the beginning of an agglomerate. This could explain why the phenomenon was observed for C1 and not C2 and C3. Besides, a minimum size of nanobubble closed to the size of the particle would be required to build a bridge strong enough between the 200 nm nanoparticles.

The nanoparticle solution was whirl-mixed for 1 minute and then immediately analysed by DLS and the zeta potential was measured: the same peak observed initially was obtained.

A zeta potential of -20.7 ± 0.3 mV was measured for the reference nanoparticle solution. Indeed, the nanoparticles were slightly negatively charged due to the chemical coating present on the surface. The zeta potential was also measured after 1 generation cycle; this time, the value was equal to -40.7 ± 2.4 mV. This demonstrated the generation of nanobubbles despite the presence of nanoparticles.

To investigate further the effect of bulk nanobubbles on particle aggregation, Triton X-100 was added to the solution to limit the nanoparticle aggregation by surfactant absorption either at nanoparticles or at nanobubbles interface.

ii. Effect of Triton X-100 + PS NP's

The effect of the addition of 1.2 cmc Triton X-100 to the previous nanoparticle solution used to generate bulk nanobubbles via microfluidics on the bubble-nanoparticle size distribution is reported in Figure 4. 15. The initial concentration of surfactant was doubled due to the presence of nanoparticles in solution. The reference size distribution for the solution made of surfactant and nanoparticles is depicted in Figure 4. 14.

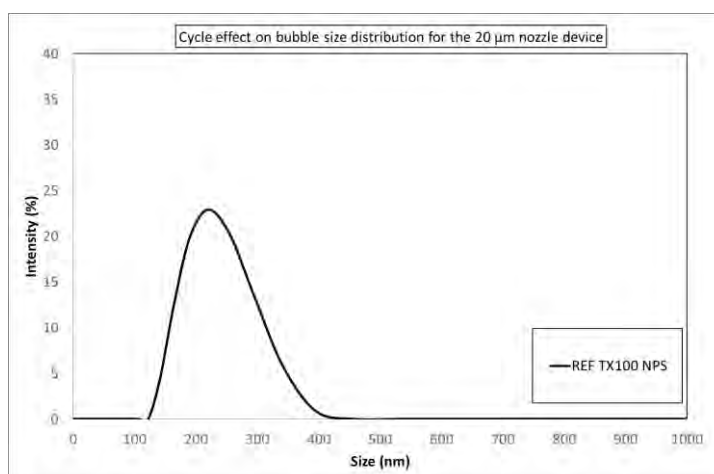


Figure 4. 14 200 nm hydrophilic polystyrene - Triton X-100 dispersion particle size distribution by intensity.

The presence of Triton X-100 in solution did not change the initial particle size distribution of nanoparticles represented in Figure 4. 10.

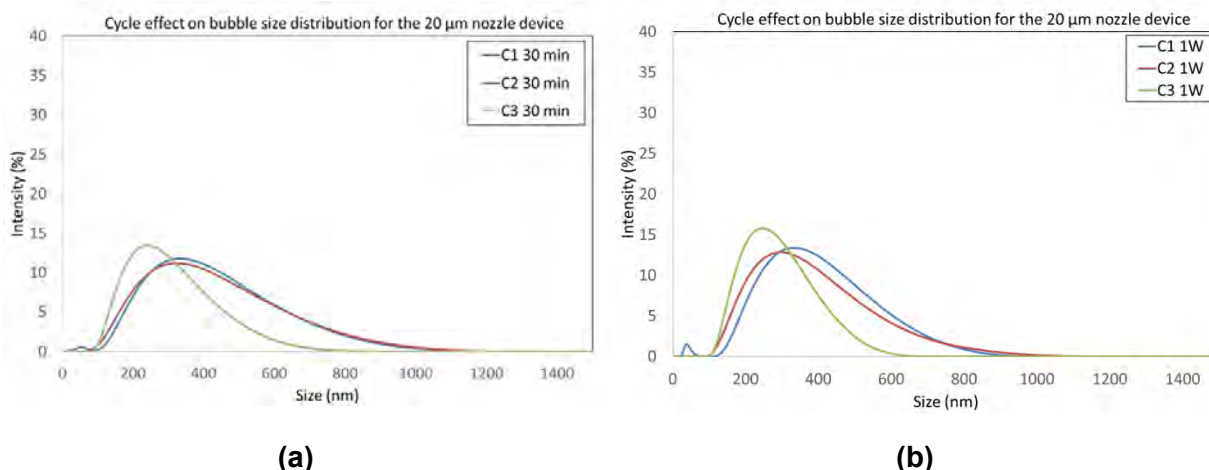


Figure 4. 15 Bulk nanobubbles-nanoparticles size distributions by intensity (a) 30 minutes and (b) one week after generation from a 1.2 cmc Triton X-100 + nanoparticle aqueous solution through 3 generation cycles (C1, blue – C2, red - C3, green lines). The results represent the average of three experiments.

Thirty minutes after generation, by C1 and C2, a broad single peak centred at 300 nm was obtained ranging from 100 to 1000 nm by intensity. Nevertheless, a small peak at C1 was visible and confirmed by the number distribution. This peak corresponded previously to nanobubbles generated in combination with Triton X-100. In the number distribution, the C1 population presented also a broad second peak centred at 200 nm ranging from 100 to 700 nm. For C2, a broad distribution centred at 100 nm varying from 50 to 700 nm. By C3, the intensity distribution was also broad and centred at 200 nm up to 600 nm.

Interestingly, the repeat of the generation cycle caused the peak originally corresponding to the nanoparticles to shift slightly towards the smallest sizes compared to the initial distribution. It was found from previous experiment that increasing the cycles was enhancing the number of smaller nanobubbles with or without Triton X-100 for a fixed number of nanoparticles in solution. This trend was confirmed by the evolution of the Z-average diameter in Figure 4. 16. As seen in the size distribution graphs, the shift towards the smallest size of nanobubbles, and the

corresponding decrease of the Z-average diameter with the cycle repeat was not as striking as the pure water case. Furthermore, the strong increase of the PDI from the reference to the cycles introduced in Figure 4. 16 (b) confirmed the generation of nanobubbles.

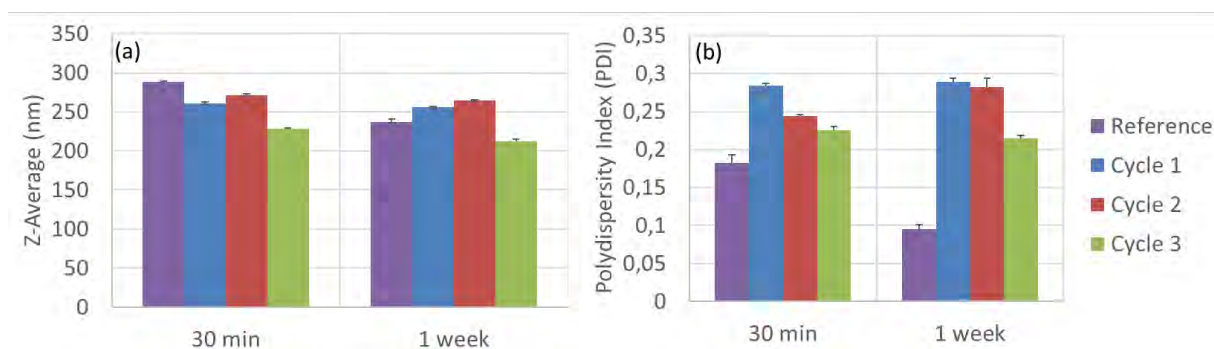


Figure 4. 16 Evolution of the Z-average diameter (a) and Polydispersity Index (PDI, (b)) describing the bulk nanobubbles - nanoparticles – Triton X-100 distribution per cycle of generation for the 20 µm nozzle. The results represent the average of two to three measurements per sample (cycle or reference).

From Figure 4. 15 (b) and Figure 4. 16, one week after generation, the distributions stayed unchanged. Furthermore, no agglomerate was observed in solution compared to the agglomerate observed at C1 for the nanobubble-nanoparticle case.

These results suggest that Triton X-100 helped preventing effectively the agglomeration of the nanoparticles due to a potential bridging via nanobubbles by adsorbing either at the nanobubble interface and/or at the nanoparticle interface.

To evaluate if the nanoparticle size is a determining factor in the formation of the agglomerate between particles, smaller hydrophilic nanoparticles were added to the solution at the same solid content in solution than the previous PS nanoparticles solution studied.

iii. Effect of 30 nm hydrophilic silica NP's

In this section, the effect of 30 nm hydrophilic silica nanoparticles on the bubble size distribution in solution was investigated. The reference size distribution corresponding to the nanoparticle solution is depicted in Figure 4. 17.

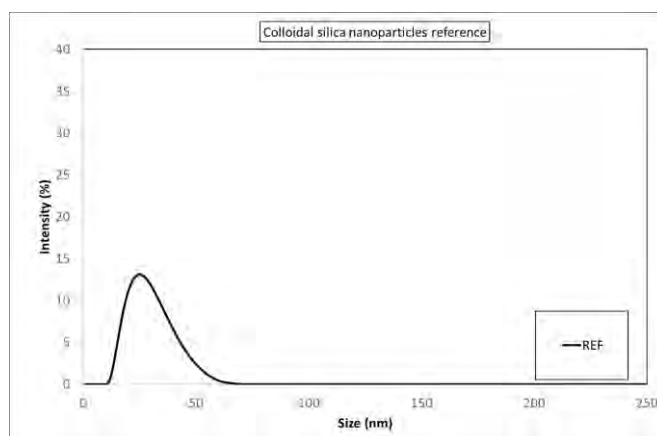


Figure 4. 17 Reference silica nanoparticle size distribution by intensity. The results represent the average of two experiments.

The nanoparticle solution was monodispersed and stable up to 1 month. The nanoparticles were hydrophilic, slightly negatively charged with measured reference zeta potential of $- 7.3 \pm 1.9$ mV. The resulting nanobubble-nanoparticle size distribution is illustrated in Figure 4. 18.

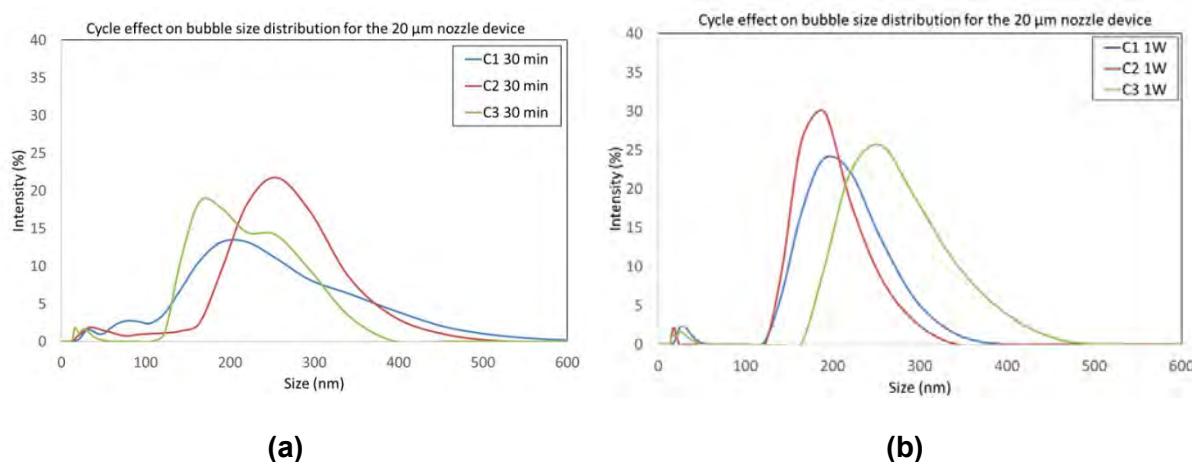


Figure 4. 18 Bulk nanobubbles-nanoparticles size distributions by intensity 30 minutes (a) and one week (b) after generation from silica nanoparticle aqueous solution through 3 generation cycles (C1, blue - C2, red - C3, green lines). The results represent the average of three experiments.

The graphs (a) and (b) in Figure 4. 18 reflect the nanobubble-nanoparticle size distribution obtained 30 minutes and 1 week after microfluidics generation from an aqueous solution containing a fixed amount of silica nanoparticles. Each cycle presented a bimodal distribution containing one peak below 50 nm and a second broader peak centred between 150 and 250 nm, corresponding respectively to the nanoparticles and the nanobubbles generated. From Figure 4. 19 representing the evolution of the Z-average diameter and PDI for the nanobubble-nanoparticle suspension throughout the various cycle of generation, it was found that the Z-average diameter of the solution increased with the cycle repeat. Interestingly, this trend is opposed to the one previously observed with the 200 nm nanoparticles. Indeed, the nanobubbles generated are larger than the nanoparticles.

Therefore, the resulting Z-average diameter after C1 is greater than the reference average diameter in solution.

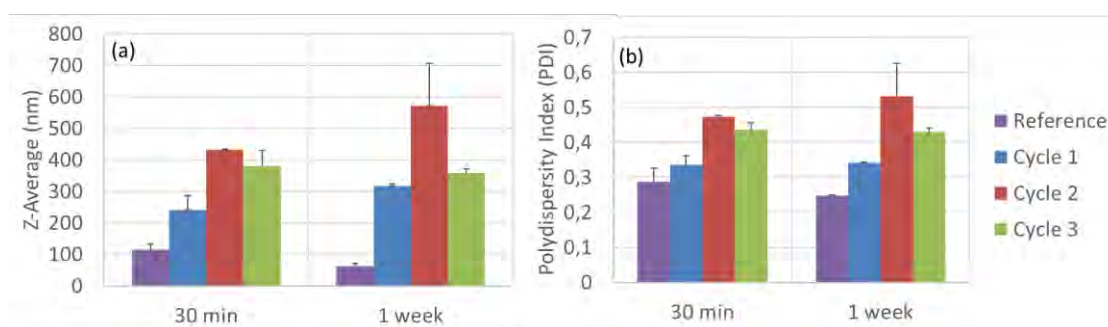


Figure 4. 19 Evolution of the Z-average diameter (a) and Polydispersity Index (PDI, (b)) describing the bulk nanobubbles - nanoparticles distribution per cycle of generation for the 20 µm nozzle. The results represent the average of two to three measurements per sample (cycle or reference).

However, it had been demonstrated in pure water that the nanobubble diameter would decrease with the cycle repeat. Thus, the Z-average diameter would be expected to decrease after C2 or C3. Nevertheless, the Z-average diameter kept increasing. Additionally, the evolution of the PDI illustrating the nanobubble-nanoparticle dispersion in Figure 4. 19 (b) supported that larger bubbles were being generated throughout the cycle for a steady size of nanoparticles in solution because the polydispersity increased from an initial monodisperse nanoparticle solution centred around 50 nm. All in all, these results showed that the hydrophilic silica nanoparticles did not prevent the generation of bulk nanobubbles via microfluidics.

Furthermore, no signs of interaction between the nanobubbles and nanoparticles leading to micron-size nanoparticle agglomeration were detected. This could be due to the existence of a nanobubble threshold size above which the bridging phenomenon could occur between hydrophilic nanoparticles. Moreover, the zeta potential of the reference nanoparticle dispersion and of nanobubble-nanoparticle dispersions were measured and reported as -7.3 ± 1.9 mV and -46.2 ± 1.3 mV respectively. The presence of nanobubbles is therefore confirmed by the strong zeta potential value.

Nonetheless, the increase in the Z-average diameter of the nanobubble-nanoparticle suspension contrarily to the decrease in the Z-average diameter with the cycle repeat previously observed for the larger size nanoparticles could indicate a phenomenon occurring between the nanobubbles and the nanoparticles that generated a larger Z-average suspension steady after one week. A possible explanation could be the adsorption of the nanoparticle onto the nanobubble surface leading to an increase in size of the nanobubble-nanoparticle structure.

To further investigate the role of nanobubbles in colloidal systems, one last system was investigated made of glycerol in water solution. Indeed, glycerol is a standard component added to formulations for instance in foams to enhance the foam stability by increasing the liquid phase viscosity. The results for this set of experiment were placed in Appendix A.4.

4.3 Conclusions

The present study was designed to determine the effect of several parameters on the bulk nanobubbles generation and properties generated via microfluidics.

This work has shown that the nozzle diameter and the cycle generation were key parameters in controlling bulk nanobubbles microfluidics generation. Two main experimental parameters impacted the nanobubble generation:

- (i) The cycle repeat increased the overall bubble concentration.
- (ii) The broader the nozzle and the greater were the average bubble diameter and the polydispersity index.

For further studies, the device itself could be optimised so that a water stream meets consecutively series of depth changes within one device and in one cycle of generation. Nevertheless, this would require adapting the device structure so that the pressure drop is kept effective throughout the device which is challenge.

The second important finding was that surfactants were influencing the bulk nanobubble properties.

The results suggested that SDS was enhancing the formation of intermediate size of bubbles by potential coalescence of smaller nanobubbles leading to an increase of

intermediate sizes despite a very high value of zeta potential. Then, it was found that Triton X-100 molecules were enhancing the formation of smaller nanobubbles by very likely adsorbing themselves at the nanobubbles surface. Thus, the nanobubble surface tension was reduced and the formation of the smallest nanobubbles exhibiting highest internal pressure was thus favoured.

Thirdly, the investigation of nanobubble-nanoparticle interactions initiated by Zhang and Seddon (2016) was pushed further in this work.

Two sizes of hydrophilic nanoparticles were studied. The investigation of the largest size of nanoparticle has shown the formation of an agglomerate over time for the first cycle of generation. This result could be explained by the existence of a threshold nanobubble size required to form a bridge between two nanoparticles and thus to form an agglomerate for a specific size of nanoparticle. The presence of Triton X-100 prevented the formation of the agglomerate due to the potential adsorption of surfactant molecules on nanobubble and/or nanoparticle surface. For the smallest size of nanoparticles, no agglomerate was observed. But the results suggested that a possible adsorption of the nanoparticles on nanobubble surface could lead to the increase in the Z-average observed experimentally.

In the next chapter, microfluidics will be employed to study the action of bulk nanobubbles at the foam gas-liquid interface for two kinds of surfactant-stabilised foams at various concentrations.

4.4 List of references

- Braibanti, M., Vigolo, D. and Piazza, R. (2008) 'Does Thermophoretic Mobility Depend on Particle Size?', *Physical Review Letters*. American Physical Society, 100(10), p. 108303. doi: 10.1103/PhysRevLett.100.108303.
- Bunkin, N. F. *et al.* (2014) 'Study of the nanobubble phase of aqueous NaCl solutions by dynamic light scattering', *Quantum electronics*. Woodbury, NY :, pp. 1022–1028. doi: 10.1070/QE2014v044n11ABEH015462.
- Etchepare, R. *et al.* (2017) 'Nanobubbles: Generation using a multiphase pump, properties and features in flotation', *Minerals Engineering*, 112, pp. 19–26. doi: <https://doi.org/10.1016/j.mineng.2017.06.020>.
- Gaillard, T. (2016) *Confined flow at high and low Reynolds : Millifluidic foaming and drainage of thin copolymer films*. Université Paris Saclay. Available at: <https://tel.archives-ouvertes.fr/tel-01402333>.
- Knüpfer, P., Ditscherlein, L. and Peuker, U. A. (2017) 'Nanobubble enhanced agglomeration of hydrophobic powders', *Colloids and Surfaces A: Physicochemical and Engineering Aspects*, 530, pp. 117–123. doi: 10.1016/j.colsurfa.2017.07.056.
- Lou, S. *et al.* (2002) 'Studies of nanobubbles produced at liquid/solid interfaces', *Materials Characterization*, 48, pp. 211–214. doi: [http://dx.doi.org/10.1016/S1044-5803\(02\)00241-3](http://dx.doi.org/10.1016/S1044-5803(02)00241-3).
- Nirmalkar, N., Pacek, A. W. and Barigou, M. (2018a) 'Interpreting the interfacial and colloidal stability of bulk nanobubbles', *Soft Matter*. The Royal Society of Chemistry, p. doi: 10.1039/C8SM01949E.
- Nirmalkar, N., Pacek, A. W. and Barigou, M. (2018b) 'On the Existence and Stability of Bulk Nanobubbles', *Langmuir*, 34, pp. 10964–10973. doi: 10.1021/acs.langmuir.8b01163.
- Oliveira, H., Azevedo, A. and Rubio, J. (2018) 'Nanobubbles generation in a high-rate hydrodynamic cavitation tube', *Minerals Engineering*, 116, pp. 32–34. doi: <https://doi.org/10.1016/j.mineng.2017.10.020>.
- Peyman, S. A. *et al.* (2012) 'Expanding 3D geometry for enhanced on-chip microbubble production and single step formation of liposome modified microbubbles', *Lab on a Chip*, 12, pp. 4544–4552. doi: 10.1039/C2LC40634A.
- Peyman, S. A. *et al.* (2016) 'On-chip preparation of nanoscale contrast agents towards high-resolution ultrasound imaging', *Lab on a Chip*, 16, pp. 679–687. doi: 10.1039/C5LC01394A.
- Seddon, J. R. T. *et al.* (2012) 'A Deliberation on Nanobubbles at Surfaces and in Bulk', *ChemPhysChem*, 13, pp. 2179–2187. doi: 10.1002/cphc.201100900.
- Tuziuti, T., Yasui, K. and Kanematsu, W. (2018) 'Influence of addition of degassed water on bulk nanobubbles', *Ultrasonics Sonochemistry*. doi:

<https://doi.org/10.1016/j.ultsonch.2018.01.015>.

Zhang, M. and Seddon, J. R. T. (2016) 'Nanobubble–Nanoparticle Interactions in Bulk Solutions', *Langmuir*, 32, pp. 11280–11286. doi: 10.1021/acs.langmuir.6b02419.

CHAPTER 5

EFFECT OF BULK NANOBUBBLES ON

SURFACTANT STABILISED FOAM

PROPERTIES

5.1. Introduction

Stability is one of the key issues in any industrial processes involving foams. Foam stability is primarily determined by three destabilising events namely, drainage, coarsening, and coalescence (Saint-Jalmes and Langevin, 2002; Saint-Jalmes, 2006). To prevent those events to occur, surfactants (Manev and Nguyen, 2005), nanoparticles (Binks and Horozov, 2005; Hunter *et al.*, 2008) or a combination of both (AlYousef *et al.*, 2018) can be employed.

Despite the development and improvement of such combination, this is not always enough to ensure foam stability depending on the application. For example, in Enhanced Oil Recovery (Nguyen *et al.*, 2014; Guo and Aryana, 2016; Yekeen *et al.*, 2018), foams are exposed to high-temperature and high-pressure conditions that make foam stability a real challenge.

Foams need to be resistant but as importantly, compatible with their surroundings. Indeed, foams are omnipresent in everyday life and constantly likely to interact with their environment from biological systems such as cells (Barbetta *et al.*, 2005; Salerno and Netti, 2014) to oceans for enhanced oil recovery (Quennouz *et al.*, 2014). This compatibilization relies on the use of more environmental-friendly stabilising agents. Thereby, one of the main goals of nowadays foam formulations is to reduce the environmental impact by reducing the quantity of surface-active agents or replacing them by biocompatible and/or biodegradable surface active-agents.

Thus, scientists have exploited bio-based and biocompatible products such as chitosan to generate and to stabilise foams (Andrieux *et al.*, 2017, 2018). Nevertheless, these products remain costly by their extraction and processing.

In the last two decades, a new kind of bubbles called nanobubbles was discovered and investigated (Seddon *et al.*, 2012; Oh and Kim, 2017). These bubbles have been introduced and employed in a wide range of applications from surface cleaning (Liu, Wu and Craig, 2008; Chen *et al.*, 2009) to froth flotation (Fan *et al.*, 2010a, 2010b) because of their extraordinary stability. This super stability is not fully understood but the main theories considered the surface tension (Hernandez *et al.*, 2018) and the bubble surface charge density (Nirmalkar *et al.*, 2018) as determining factors for their stability. Indeed, the ion-stabilisation model explains the single nanobubble stability by the existence of an electrostatic pressure that balances the high internal Laplace pressure (Weijs *et al.*, 2012). Additionally, the DLVO (Derjaguin-Landau-Verwey-Overbeek) theory describing colloidal stability, describes successfully the dependence of bulk nanobubbles stability on parameters such as pH and electrolytes in solution as well expressed by Nirmalkar *et al.* (2018).

The research about the interactions of these bubbles with their surrounding composed of nanoparticles or surfactants has recently emerged. These findings suggest that bulk nanobubbles could impact colloidal systems stabilised via surfactants and/or nanoparticles.

Karakashev and Nguyen (2009) demonstrated that the presence of dissolved gasses had a significant effect on thin liquid film rupture. Consequently, surface or bulk nanobubbles could have a strong influence on film rupture.

Ushida *et al.* (2012) showed that the presence of nanobubbles with anionic surfactants solution was enhancing the cloth cleaning efficiency (from 3 to 7% washing rate). The 80 nm diameter nanobubbles were generated via a nanobubble

generator. The nanobubble-surfactant and pure surfactant surface tensions at 17°C were measured via Du Noüy ring method. The effect of nanobubbles on three surfactants including polyoxyethylene lauryl ether (nonionic surfactant), benzalkonium chloride (cationic surfactant), and laurylbenzene sulfonic acid sodium salt (anionic surfactant) for concentrations below or equal to 2 cmc were investigated. The results showed evidence that nanobubbles were decreasing by 10% the surface tensions compared to the pure aqueous surfactant solutions only for the anionic surfactant case. However, the graphs plotting the surface tension versus the surfactant concentration did not present any error bars, and the measurements were not performed at constant temperatures with two different kinds of ring (brass and platinum). Notwithstanding these limitations, the study suggested that nanobubbles acted on the interfacial properties of the surfactant stabilised gas-liquid interface.

A theoretical study was performed by Yasui *et al.*, (2018) to evaluate the role of nanobubbles in decreasing surface tension. Based on the dynamic equilibrium model considering that bulk nanobubbles are partly covered with a hydrophobic material, it was stressed out that a liquid film could be more easily ruptured due to the presence of nanobubbles at the liquid surface, thus decreasing the value of surface tension in Du Noüy ring method.

Furthermore, nanobubbles have been combined for specific application with surfactants such as Pluronic F127 for contrast agent for diagnostic and therapeutic ultrasound (Nieves *et al.*, 2017) or Pluronic L10 in (Hernandez *et al.*, 2018).

Additionally, Zhang and Seddon (2016) highlighted a potential nucleation or attachment of nanobubbles onto negatively charged gold nanoparticles above a

threshold nanoparticle size (60 nm). Very recently, the important role of bulk nanobubbles in colloidal stability was well established by Zhang *et al.* (2019). Indeed, it was found that the ratio of nanoparticle to nanobubbles in solution could be used to tune the zeta potential of the resulting dispersion of initially positively charged Polystyrene latex nanoparticles. Thus, the decrease of the concentration of nanoparticles for a fixed nanobubbles concentration induced an episode of nanoparticle aggregation at point of zero charge followed by re-stabilisation or condensation stage.

However, thus far, no research has been undertaken to determine if these nanobubbles could affect colloidal systems such as foams. All this made us wonder how these bubbles would impact foam stability in the case of foam solely stabilised with surfactant. Therefore, this work investigated for the first time how nanobubbles generated via microfluidics in a very well-controlled and reproducible way could affect foam properties solely stabilised by surfactants (Peyman *et al.*, 2012, 2016).

Two surfactants were studied: Triton X-100, a non-ionic surfactant and Sodium Dodecyl Sulfate (SDS), an anionic surfactant. Triton X-100, a non-ionic surfactant, was chosen for this work because Triton X-100 is commonly employed to stabilise foams in combination with nanoparticles (Hunter *et al.*, 2009). Furthermore, a non-ionic surfactant should be able to reach the negatively charged nanobubble surface (-40 mV) (Cho *et al.*, 2005) without being repelled. Thus, nanobubbles could attract Triton X-100 molecules and then affect the action of triton X-100 at the foam gas-liquid interface as a potential foaming or defoaming agent.

Then, SDS was selected to study the interaction between an anionic surfactant and nanobubbles. In this case, nanobubbles and the SDS molecules would be expected to repel each other. This repulsion could affect the distribution of the surfactant at the interface and in the bulk.

The foam was generated for each formulation via a flow-focusing microfluidics device at fixed gas and liquid pressures of 1000 mbar and 1900 mbar respectively. Bulk nanobubbles were produced beforehand via one microfluidics generation cycle at 1000 mbar air pressure and $90 \mu\text{L min}^{-1}$ liquid flow rate as described in Chapter 4. In addition, it was also considered that the solution both during nanobubble generation and foam generation were saturated in air due to a continuous air injection to ensure an optimum nanobubble generation. Indeed, it has been demonstrated that the gas saturation could have a significant impact on bulk nanobubbles properties in solution (Tuziuti *et al.*, 2018).

Building upon the knowledge established in the previous chapter, it is our intention to examine the influence of bulk nanobubbles on foam solely stabilised by two kinds of surfactants, a non-ionic surfactant, Triton X-100 and its anionic counterpart, SDS for various concentrations from 0.5 to 5 times the critical micellar concentration (cmc).

5.2. Results & discussions

The results will be divided in two parts; the first one will focus on the nanobubble - Triton X-100 set of experiments and the second one will be dedicated to the nanobubble-SDS investigation.

5.2.1. Effect of bulk nanobubbles on the stability of foams solely stabilised by Triton X-100

In this sub-section, the aim was to establish the effect of bulk nanobubbles on non-ionic surfactant stabilised foams. Four surfactant concentrations were studied from 0.5, 1, 2.5 to 5 cmc. In each case, the nanobubble-surfactant foam properties were analysed and confronted to the surfactant stabilised foam properties. The solutions were analysed via tensiometry (Maximum Bubble Pressure tensiometer, described in Chapter 3) to verify if nanobubbles were impacted the surfactant stabilising action at the interface. The results are presented in Figure 5. 1.

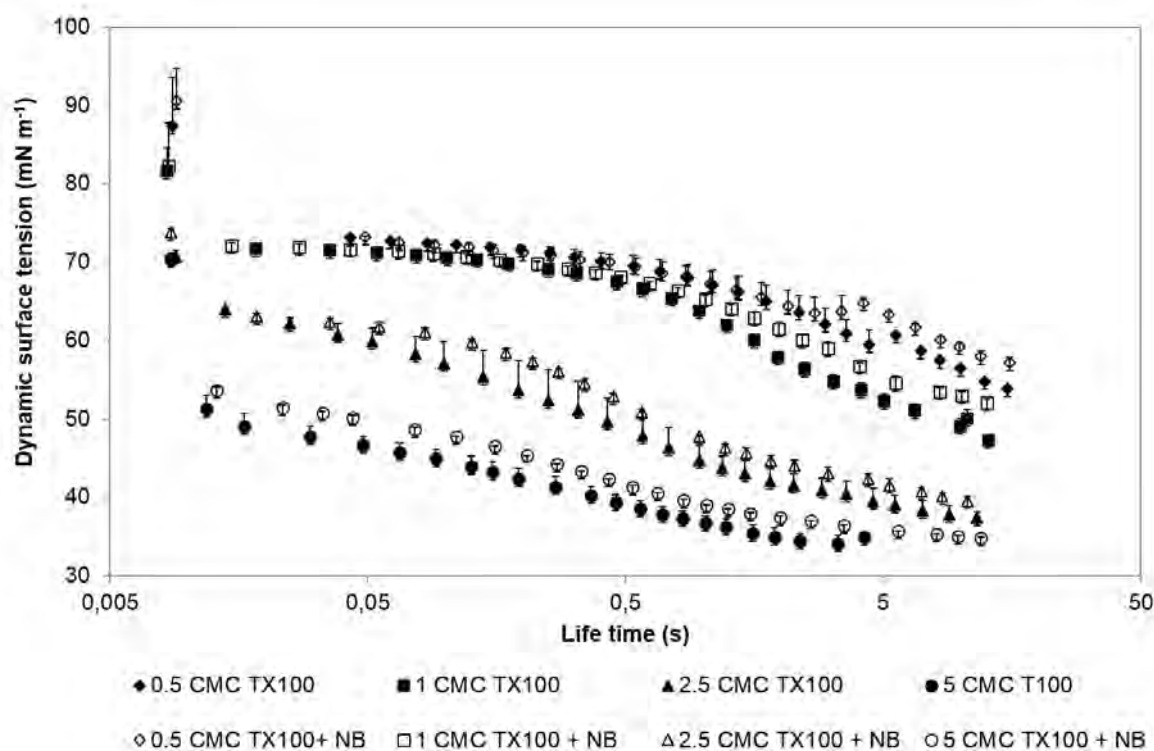


Figure 5. 1 Dynamic Surface Tension results for the set of Triton X-100 solutions from 0.5 (◆,◇), 1 (■,□), 2.5 (▲,△ and 5 cmc (●,○) described by filled symbols for reference and by unfilled symbols for nanobubble-surfactant solutions. Each curve represents the average of three experiments per formulation.

This characterisation step showed that nanobubbles could impact the surfactant action at the gas-liquid interface. This action varied with the surfactant concentration

for a fixed nanobubble concentration. The explanation behind this effect resides both in the dynamic of adsorption and desorption of the surfactant from the foam gas-liquid interface and from the nanobubble surface but also in the surfactant diffusion from the volume to the interface.

For Triton X-100, from 0.5 to 5 cmc, the nanobubble surface tension is globally greater than the reference towards the longest bubble life time (starting after 5s at 0.5 cmc until the whole bubble life time range at 5 cmc. This indicates that the nanobubbles interfere with the non-ionic surfactant adsorption towards the longest bubble life time at the lowest surfactant concentration. Thereby, nanobubbles can have a destabilising action at the foam gas-liquid interface by removing available surfactants from the solution and by inducing a lower “effective” concentration. However, this effect remains small due to the variability of the measurement. Interestingly, at low surfactant concentration, the surface tension is almost equal to the surface tension of pure water (72.8 mN m^{-1} at 20°C). Indeed, $\sigma = 70 \text{ mN m}^{-1}$ until 0.5s.

It is known that Triton X-100 is a surfactant which diffuses slowly to the interface compared to SDS due to its high molecular weight. Indeed, Weinheimer *et al.* (1981) reported that Triton X-100 presented a diffusion coefficient of $7.4 \times 10^{-7} \text{ cm}^2 \text{ s}^{-1}$ at 0.45 g L^{-1} compared to SDS with a diffusion coefficient of $1.76 \times 10^{-6} \text{ cm}^2 \text{ s}^{-1}$ at 0.01 M . This is noticeable in Figure 5. 1 because the equilibrium surface tension is reached only after a certain time, unlike SDS which gets to the interface much faster and shows a steady surface tension very quickly as illustrated in Figure 5. 8.

Furthermore, the evolution of the nanobubble-surfactant population was followed before and after foaming denotes respectively “NB” and “NB foamed” as illustrated in Figure 5. 2. It was observed that the foaming process did not affect significantly the nanobubble-surfactant distribution as the distributions were consistently the same throughout the different concentrations for the reference and foamed solutions. Secondly, a peak beyond 200 nm composing a bimodal distribution appeared and grew with the surfactant concentration. However, it was noticed that the foaming process would reduce this peak for all the cases above the cmc. It is difficult to evaluate the nature of this peak which could be due to nanobubbles, to an agglomerate of surfactants for the highest concentrations via a supramolecular structure, or to a combination of both.

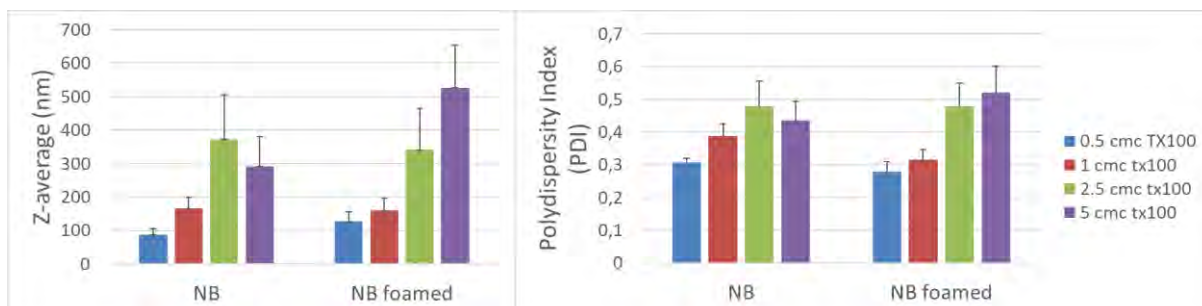


Figure 5. 2 Z-average diameter & Polydispersity evolution for the nanobubble-surfactant dispersion before and after foaming for various surfactant concentrations. Each value is obtained from an average of three experiments per sample.

The evolution of the nanobubble dispersion zeta potential was also measured before and after foaming for each solution as depicted in Figure 5. 3 .

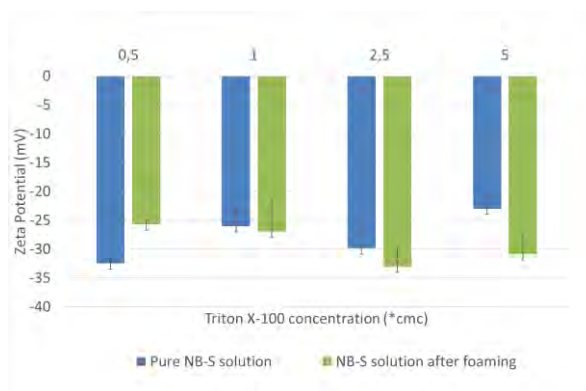


Figure 5. 3 Zeta potential evolution of the nanobubble-surfactant dispersion in water for various Triton X-100 concentrations (0.5, 1, 2.5 and 5 cmc) before (blue) and after (green) foaming. Each value is obtained from an average of three experiments per sample.

From Figure 5. 3, it was found that by increasing the surfactant concentration in solution, the zeta potential before foaming slightly decreased. This effect was observed previously for the case of thin-liquid films stabilized by non-ionic surfactants and electrophoresis experiments on air bubbles (Karraker and Radke, 2002). A « dilution » effect of the charges caused by the adsorption of the surfactant molecules at the nanobubble interface can reduce the density of charges on the nanobubble surface. Thereby, the more non-ionic surfactants added, the better the dilution of the nanobubble surface charge.

The foaming step from the lowest to the highest surfactant concentrations, at first decreased the initial zeta potential at 0.5 cmc, then increased it slightly only at 5 cmc. This could be related to the action of the surfactants on the nanobubbles depending on the concentration and if the nanobubbles adsorb at the gas-liquid interface.

During the foaming process, a new interface is formed. The change in nanobubble zeta potential could be explained by the desorption of the surfactant from the nanobubble interface to reach the newly formed foam gas-liquid interface. The foaming process generates much larger interfaces to be covered so it may be more

energetically favourable for the surfactant to stabilise the foam rather than the nanobubble.

Additionally, the foam structure evolution was tracked throughout the various formulations obtained for the same experimental conditions. The resulting structures are represented in Figure 5. 4. It was seen that by increasing the surfactant concentration in both cases, the foam was composed more and more of small bubbles. From the pictures, it seemed that the foam containing nanobubbles was able to retain more liquid in its structure than the reference as larger gas bubbles are observed for the reference solutions compared to the nanobubble cases. The pictures were taken at the early stage of the foam life. This difference was more striking at 0.5 and 1 cmc compared to 2.5 and 5 cmc which showed similar structures.

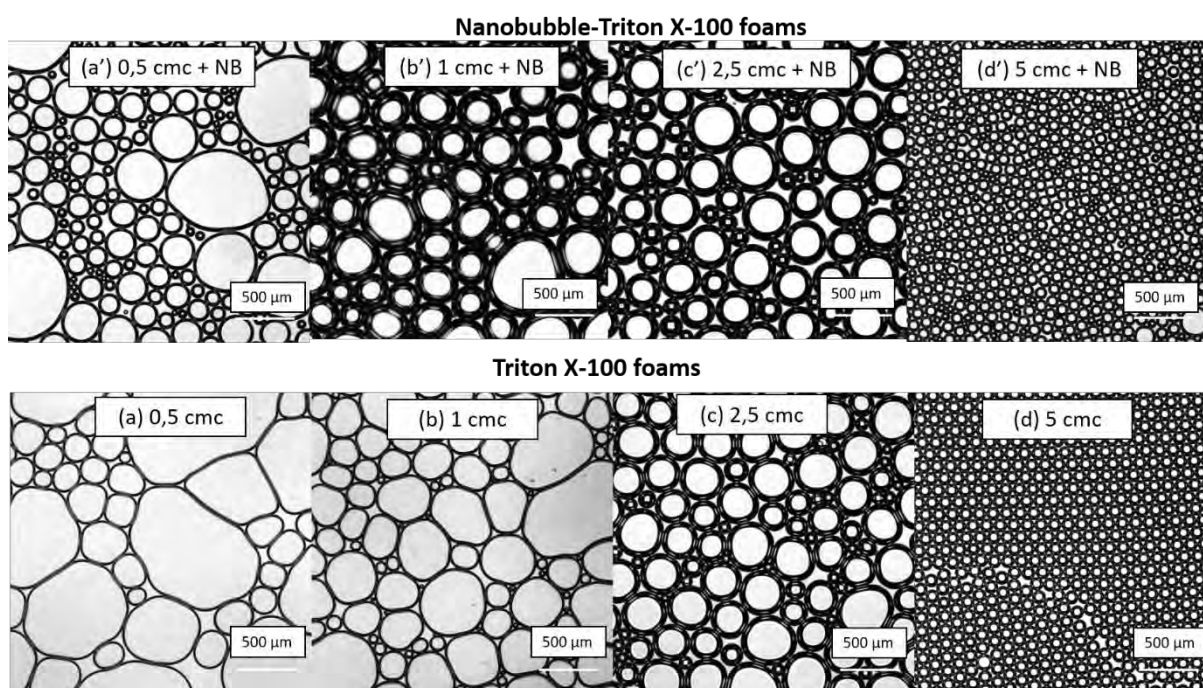
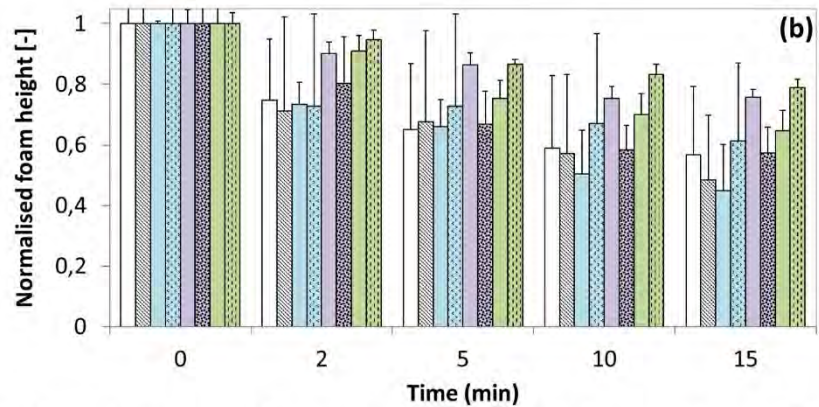
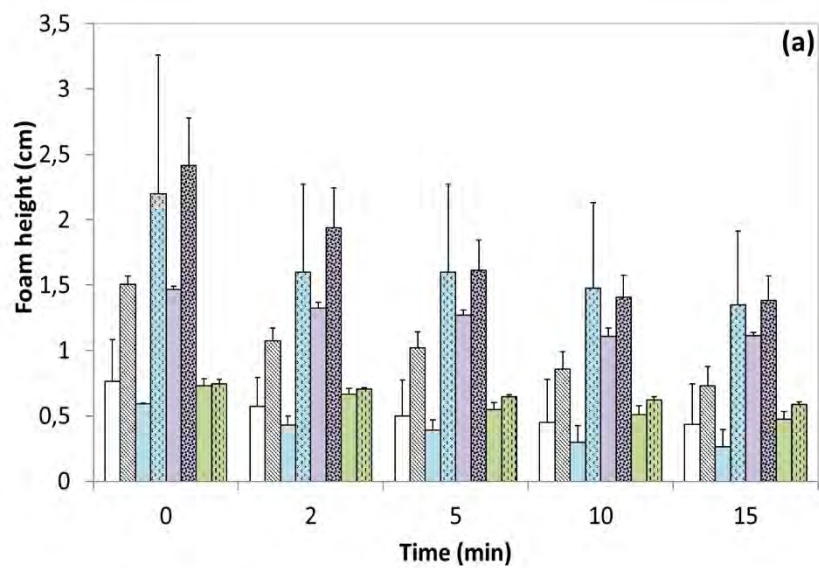


Figure 5. 4 Foam structure evolution after 5s deposition on a glass slide under a cover slip for various concentration of Triton X-100 (0.5 (a), 1 (b), 2.5 (c), 5 (d)) solutions & Triton X-100 – nanobubbles solutions at 0.5 (a'), 1 (b'), 2.5 (c') and 5 cmc (d').

In the next paragraphs, the study of the foamability and foam stability per set of formulation highlighted the influence of nanobubbles on the thin liquid film stability and resulting foam properties.

Thus, the foamability could be evaluated by analysing the evolution of the foam height in Figure 5. 5 (a) and of the foam liquid fraction in Figure 5. 6 (a). The foam stability could be quantified by comparing the normalised foam height evolution in Figure 5. 5 (b) and by assessing the evolution of the liquid fraction in Figure 5. 6.



□ 0.5 cmc tx100 ▨ 0.5 cmc tx100 + nb □ 1 cmc tx100 ▨ 1 cmc tx100 + nb
 ▨ 2.5 cmc tx100 ▨ 2.5 cmc tx100 + nb □ 5 cmc tx100 ▨ 5 cmc tx100 + nb

Figure 5. 5 Foam height (a) and normalised foam height (b) evolution after 1-minute foaming for 0.5 (white), 1 (blue), 2.5 (purple) and 5 (green) cmc Triton X-100 solution (plain colours) versus bulk nanobubbles + Triton X-100 solution for 0.5 (dotted light grey), 1 (dotted blue), 2.5 (dotted dark grey) and 5 cmc (dotted green). Each value is obtained from an average of three experiments per sample.

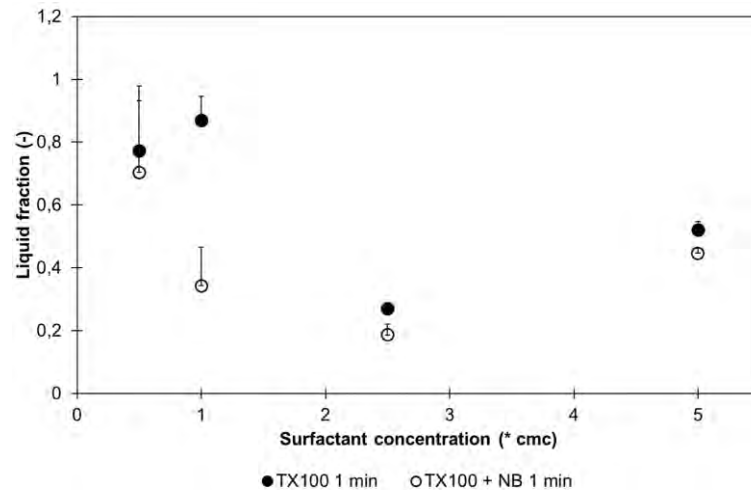


Figure 5. 6 Initial foam liquid fraction for Triton X-100 solutions (filled symbols) versus bulk nanobubbles + Triton X-100 solutions (unfilled symbols) for various surfactant concentrations. Each value is obtained from an average of three experiments per sample.

5.2.1.1 0.5 cmc Triton X100

This investigation was started by studying the effect of bulk nanobubbles on foam properties made of 0.5 cmc Triton X-100. Nanobubbles were generated beforehand via microfluidics by flowing a reference solution made of 0.5 cmc Triton X-100 through a two-depth flow-focusing microfluidic device. The resulting nanobubble-surfactant solution was employed as the foaming solution to generate foam via a second microfluidic device. The foam properties (height evolution and initial liquid fraction) were studied. The results are depicted in Figure 5. 5 and in Figure 5. 6.

The presence of nanobubbles in solution enhanced the foamability of the solution compared to the reference solution. Indeed, the foam height for the nanobubble solution was almost doubled compared to the reference. The decrease in height over time was slightly higher for the NB case (0.7 cm for the NB case compared to 0.5 cm foam height decrease for the reference). This disparity in foam rate of decay can be better assessed by comparing the normalised foam height evolution (foam height normalised by the initial foam height) in Figure 5. 5 (b). A fastest decay of the

nanobubble-surfactant solution was observed. Consequently, the nanobubble-surfactant foam appeared more slightly unstable than the reference. To complete our analysis, the initial liquid fraction evolution with the surfactant concentration is represented in Figure 5. 6. The two solutions presented almost the same liquid content ranging from 0.7 to 0.8 characteristic of a bubbly liquid. At 0.5 cmc, the nanobubble-surfactant population presented slightly lower initial liquid fraction than the reference.

It was hypothesised that nanobubbles attracted surfactants molecules at their surface and prevented them from stabilising the foam gas-liquid interface. Indeed, for non-ionic surfactant, the main force balancing the attractive Van der Waals force is steric contribution to the disjoining pressure. Thus, by removing surfactant molecules from the interface, the steric contribution and the foam stability decrease.

This hypothesis was confirmed by the evolution of the dynamic surface tension with and without nanobubbles in solution in Figure 5. 1. The sudden peak of destabilisation at 15/20 minutes could be related to the rise in surface tension for the nanobubble solution compared to the reference observed towards the longest bubble life time in Figure 5. 1.

From Figure 5. 2, the nanobubble size distribution before and after foaming showed a similar peak for each configuration. Thus, the foaming process didn't change the size distribution in solution. It is believed that at this surfactant concentration, the nanobubbles stayed in the bulk of the solution without adsorbing themselves at the foam gas-liquid interface. Their main action is then to attract surfactant at their surface. Therefore, the nanobubbles stability and distribution is not affected

significantly by the foaming process. From Figure 5. 3, the surfactant-nanobubble dispersion showed an initial zeta potential of -35 mV that changed to -25 mV after foaming. This decrease in zeta potential could be due to the non-ionic surfactant adsorption at the nanobubble interface.

Below the cmc, the foamability is mainly determined by the diffusion of the surfactant from the volume to the surface. It was hypothesized that nanobubbles were removing surfactant molecules from the foam gas-liquid interface by attracting them on their surface, leading to foam destabilisation. However, it was found that despite the slight instability created by the nanobubble presence in solution, the foamability was still higher for the nanobubble-surfactant solution compared to the reference. Therefore, the possibility that some nanobubbles could adsorb at the foam gas-liquid interface and enhance locally the thin film stability cannot be ruled out. Indeed, the adsorption of negatively charged nanobubbles at the foam gas-liquid interface could increase the electrostatic repulsion between the two interfaces and prevent them from touching and breaking as illustrated in Figure 5. 7:

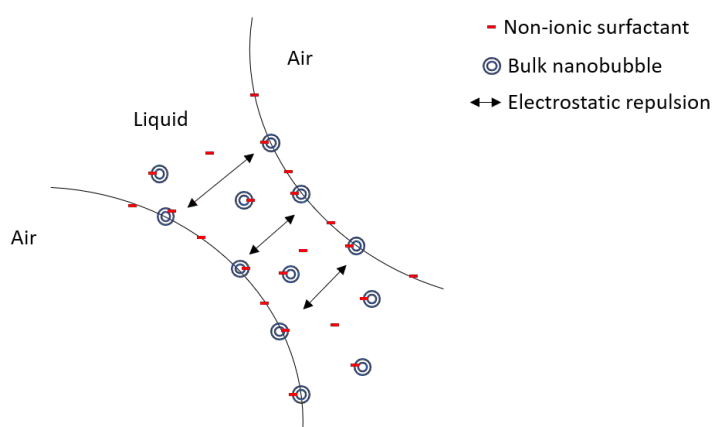


Figure 5. 7 Schematic representation of the gas-liquid interface for the nanobubble-Triton X-100 mixture. A change of trend on the nanobubble effect was observed with a threshold at 1 cmc which will be further studied in the following paragraph.

5.2.1.2 1 cmc Triton X-100

For the exact same foaming conditions, the presence of nanobubbles increased the foam height compared to our reference. Surprisingly, it was noticed that the rise in concentration increased significantly the initial foam height only in the NB case from 1.5 to 2.25 cm whereas the reference foam height went down from 0.77 to 0.59 cm. The same increase in surfactant concentration caused the decrease in foam height to be almost doubled: from a difference of 0.7 cm between the initial and final foam heights at 0.5 cmc to a difference of 1.25 cm at 1 cmc for after 15 min in the NB case due to the increase in the initial foam height. Thus, the foamability doubled for the nanobubbles case whereas it decreased slightly for the reference.

However, in terms of stability, the rate of height decay based on the normalised foam height was higher for the reference compared to the nanobubble case as observed in the evolution of the normalised foam height at 10 and 15 minutes.

Strangely, the rise in surfactant concentration caused the foam height decay rate to increase for the reference solution and to decrease for the nanobubble-surfactant solution. Thus, for this concentration, the nanobubble-surfactant foam is more stable than the foam solely stabilised by surfactant.

Considering the initial liquid fraction in Figure 5. 6, the nanobubble-surfactant presented much lower liquid fraction (0.4) than the reference (0.8). The stabilising effect of nanobubbles at 1 cmc is striking. The nanobubbles showed the smaller liquid content, and the highest stability and foamability. On the contrary, the reference solution exhibited the smallest foamability and the highest and fastest increase in liquid fraction.

At this concentration for the reference case, it was assumed that the foam gas-liquid interface is fully covered, and micelles are appearing in solution.

At the timescale of the bubble formation composing the foam (0.5 ms), the surfactant dynamic is very similar between 0.5 and 1 cmc, with and without nanobubbles. However, nanobubbles influence on the foamability and on the foam stability was greater at 1 cmc. The foamability and foam stability have been significantly enhanced by the presence of nanobubbles. Thereby, it is believed that the electrostatic repulsion between the two interfaces composing the thin liquid film was increased because more nanobubbles were adsorbed at the foam gas-liquid interface.

Nanobubbles may still affect the foam stability by influencing the dynamic of adsorption-desorption at the interface by attracting surfactant molecule to its interface. This action may enhance the number of nanobubbles adsorbed at the foam gas-liquid interface by anchoring more nanobubbles via a greater surfactant coverage of the nanobubble surface and/or a higher number of nanobubbles covered by surfactants.

At lamellae scale, these properties can be related to the effect of nanobubbles and surfactants molecules on the determining force balance between the capillary and the disjunction pressure. From Figure 5. 4, the two foams at 1 cmc were composed of relatively big bubbles compared to the one obtained at 5 cmc implying a low capillary pressure due to a low liquid pressure in the liquid film for a high gas pressure within the bubbles. In this case, the film stability is driven by the balance between the repulsive electrostatic forces, the Van der Waals and the steric forces.

For these values of surface tension, the foamability is normally low. However, the presence of nanobubbles enhanced the foamability. Assuming a fixed liquid fraction and steady film thickness, the stronger the repulsive forces and the better the foamability. Therefore, a hypothesis was formed that nanobubbles, by adsorbing at the foam gas-liquid interface enhance the electrostatic repulsion existing between the two interfaces of the thin film and thus the foam stability and the foamability.

This second set of results highlighted the strong surfactant concentration dependence of the nanobubbles effect on foam stability. It is believed that the surfactant adsorption on the nanobubble surface helped the nanobubble adsorption at the foam gas-liquid interface. The more surfactant covered the nanobubble surface and the better was the nanobubble adsorption and the more nanobubbles were adsorbed.

In addition to the electrostatic repulsive contribution, it has been demonstrated that nanobubbles can enhance the interfacial properties estimated by Langmuir-Blodgett trough. Hernandez *et al.* (2018) showed that the combination of bulk nanobubbles with a non-ionic surfactant (Pluronic F127) could decrease the equilibrium surface tension by almost 30%. Thereby, the nanobubbles adsorbed at the foam gas-liquid interface could potentially act as insoluble surfactants and enhance the interfacial viscoelastic moduli.

5.2.1.3 2.5 cmc TX100

At first, the solution containing nanobubbles presented a higher foamability than the reference solution for the exact same foaming conditions. Indeed, the foamability was again enhanced compared to 1 cmc for both solutions by evaluating the initial foam

height: from 2.2 to 2.4 cm and from 0.7 to 1.4 cm for the nanobubble-surfactant and for the reference solutions respectively. The rise in foamability was greater for the reference compared to the nanobubble case. Indeed, for the reference, more surfactants in solution enhanced the foamability by reaching the equilibrium surface tension faster as showed in Figure 5. 1.

At this surfactant concentration, the nanobubble-surfactant and the surfactant foams reached their maximum foamability. Thus, nanobubbles adsorbed at the foam gas-liquid interface and kept enhancing the repulsive electrostatic forces acting between the two interfaces forming the thin liquid film.

From Figure 5. 6, it was found that the presence of nanobubbles kept stabilising the resulting foam by reducing slightly the initial liquid content compared to the reference. This concentration presented the smallest liquid content among all the concentrations. Overall, in both cases, increasing the surfactant concentration enhanced film stability.

At 2.5 cmc, both solutions presented the same foam structure with smaller bubbles than at 1 cmc. The change in diameter from 1 to 2.5 cmc was more significant for the reference compared to the nanobubble solution. This foam structure implied a stronger capillary pressure than previously (high liquid pressure for a low gas pressure inside the bubble). To generate such stable foam, the capillary pressure needed to be balanced by disjunction pressure. Based on the previous hypothesis, it is considered that the increase of surfactant concentration enhanced the adsorption of nanobubbles at the interface, resulting in a rise in electrostatic repulsion and disjunction pressure, thus further improving foam stability and foamability.

All in all, at 2.5 cmc, both nanobubble and reference solutions demonstrated the highest foamability and foam stability. The next section is dedicated to the highest surfactant concentration (5 cmc TX100) investigated and its effect on foam properties.

5.2.1.4 5 cmc TX100

The action of bulk nanobubbles on foams solely stabilised by Triton X-100 at 5 cmc was studied in this section.

In Figure 5. 5 (a), it was analysed that the foam generated in one minute reached the same height with or without nanobubbles. Surprisingly, the foam height was much less compared to the 2.5 cmc for both solutions: 1.5 cm at 2.5 cmc versus 0.7 cm at 5 cmc for the reference and 2.5 cm at 2.5 cmc versus 0.75 cm at 5 cmc for the nanobubble solution. This time, from Figure 5. 1, the dynamic surface tensions were similar for both solutions and the equilibrium surface tensions were reached much faster compared to the 2.5 cmc cases. Consequently, the surface tension couldn't be the reason for the huge decrease in foamability for both cases.

It was also observed that both foams presented a structure made of very small bubbles as depicted in Figure 5. 4. This size of bubbles was produced due to a low gas pressure for a high liquid pressure, so for a high capillary pressure.

Nevertheless, at this concentration, the nanobubble-surfactant solution presented also its lowest foamability. It is believed that at this concentration, the nanobubbles surface coverage and the number of surfactant-coated nanobubbles anchored at the foam gas-liquid interface reached its maximum. Thereby, the repulsive forces between the two interfaces forming the gas-liquid interface were the highest. However, the huge number of nanobubbles adsorbed at the foam interface might

have led to an increase of the interfacial moduli, leading to a reduction of the foamability.

From Figure 5. 3, the zeta potential for the nanobubble-surfactant solution before foaming was the lowest among all the concentrations. Our hypothesis is that this phenomenon is related to the partial “dilution” of the nanobubble negative surface charges by the surfactant molecules in solution. This dilution can act on the nanobubble in the bulk but also on the nanobubbles adsorbed at the foam gas-liquid interface. Thus, the repulsive electrostatic forces that used to enhance the foamability were reduced. Nonetheless, it appeared that the foam made of bulk nanobubbles was more stable than the reference solution. This statement was confirmed by the initial liquid fraction for the nanobubbles-surfactant foam compared to the surfactant foam in Figure 5. 6. For the exact same foaming conditions, the resulting foam containing bulk nanobubbles showed a lower liquid content than the reference solution.

Thereby, despite a decrease in foamability, the presence of nanobubbles helped stabilising the foam via its adsorption at the interface. Despite the reduction of foamability, the nanobubbles prevented the destabilisation thanks to their adsorption.

Finally, bulk nanobubbles showed a strong impact on foam properties for the whole range of non-ionic surfactant concentrations investigated. Both foam stability and foamability were strongly affected by the presence of nanobubbles in the bulk and potentially at the foam gas-liquid interface via surfactant adsorption at the nanobubble surface.

In the next section, the effect of the interactions between an anionic surfactant (SDS) and bulk nanobubbles in solution on the foam properties for various SDS concentrations were assessed.

5.2.2. Effect of bulk nanobubbles on the stability of foams solely stabilised by SDS

Firstly, the solutions with and without nanobubbles were analysed via tensiometry. The results are summarised in Figure 5. 8.

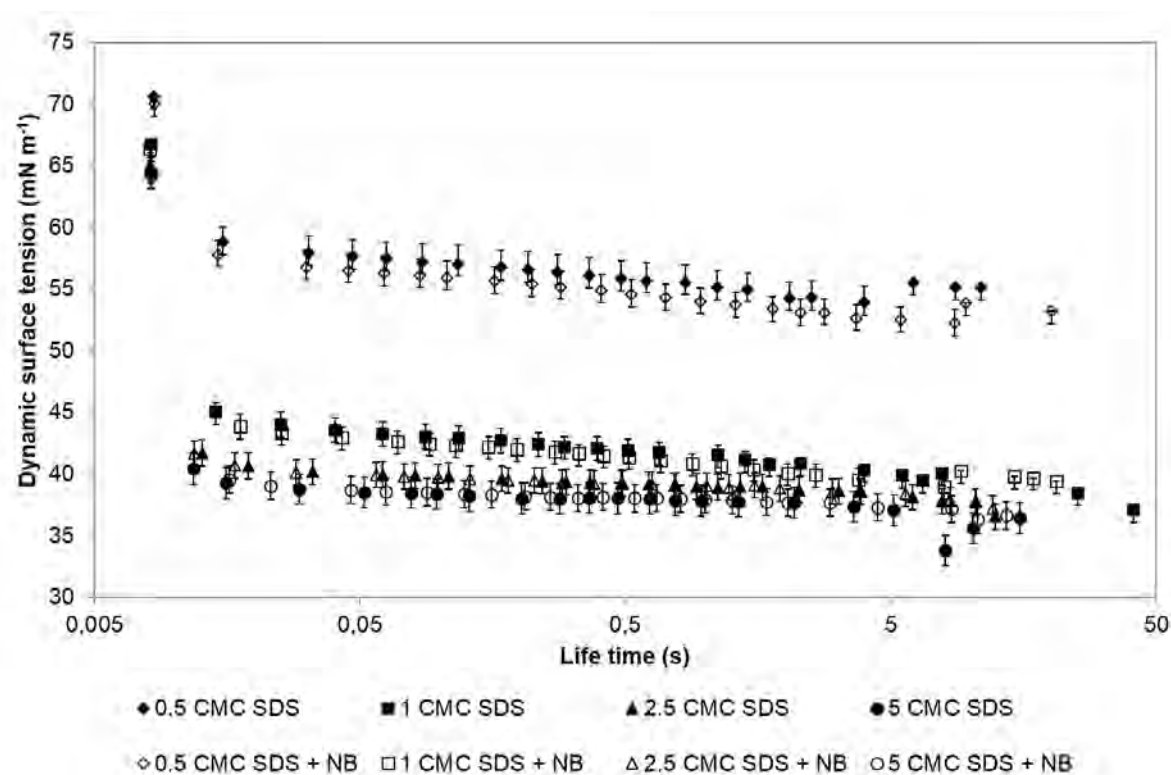


Figure 5. 8 Dynamic surface tension results for the set of SDS solutions from 0.5 (◆,◇), 1 (■,□), 2.5 (▲,△) and 5 cmc (●,○) described by filled symbols for reference and by unfilled symbols for nanobubble-surfactant solutions. Each curve represents the average of three experiments per formulation.

Unlike Triton X-100, it seemed that the presence of nanobubbles didn't impact significantly the dynamic surface tension of the solution. The more surfactant was added to the solution, the lowest was the surface tension. At 0.5 cmc SDS, the presence of nanobubbles slightly lowered the surface tension compared to the

reference. Otherwise, it was observed that the equilibrium surface tension was reached much faster for SDS than for Triton X-100. Indeed, SDS molecules show a faster diffusion rate as it has a lower molecular weight compared to Triton.

In addition, the evolution of the nanobubble-surfactant size distribution was followed before and after the foaming step as reported in Figure 5. 9 for the different surfactant concentrations investigated for a fixed nanobubble concentration in solution.

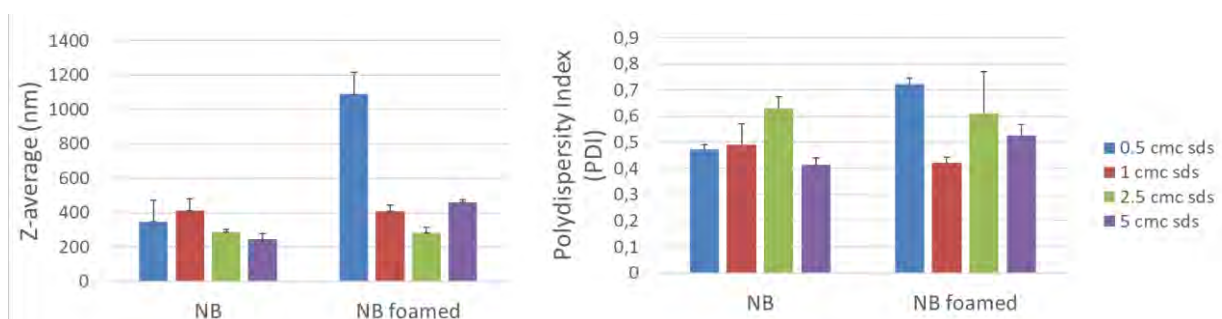


Figure 5. 9 Z-average diameter & Polydispersity (PDI) evolution for the SDS nanobubble-surfactant dispersion before and after foaming for various surfactant concentrations (0.5, 1, 2.5 and 5 cmc). Each value is obtained from an average of three experiments per sample.

Throughout the various concentrations, the size distribution remained steady for the nanobubble-surfactant solutions before foaming. However, from these results, it was observed that the foaming process had impacted the nanobubble distribution. However, it was difficult to conclude if it had generated or enhanced something from the initial nanobubble solution. To improve our understanding of the phenomena occurring during the foaming step, the zeta potential characterising the nanobubble-surfactant colloidal stability was analysed in solution.

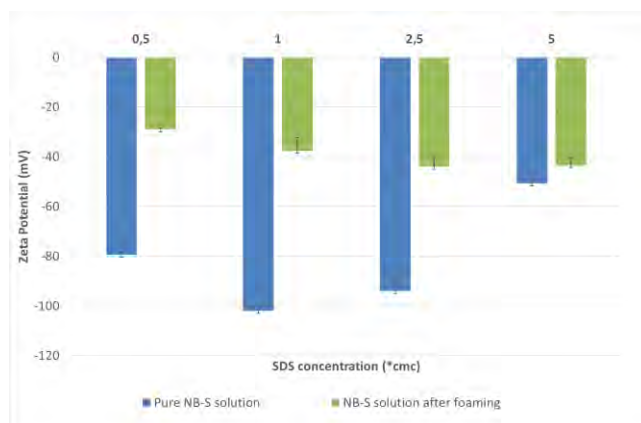


Figure 5. 10 Zeta potential evolution of the nanobubble-surfactant dispersion in water for various SDS concentrations (0.5, 1, 2.5 and 5 cmc) before (blue) and after (green) foaming. Each value is obtained from an average of three experiments per sample.

In Figure 5. 10, it was found that from 0.5 to 2.5 cmc, the initial nanobubble-surfactant dispersions exhibited a very negative zeta potential varying from -80 to -100 mV. Only the 5 cmc sample showed a zeta potential of -40 mV. Very negative values were also reported in the literature for the combination of SDS and nanobubbles generated via ultrasonic cavitation (Nirmalkar, Pacek and Barigou, 2018). SDS was said to enhance the nanobubble charge density in solution. After foaming, the zeta potential for the three lowest concentrations dropped by half, ranging from -25 to -40 mV. It seemed that foaming destabilised the nanobubbles population in solution. As observed for Triton X-100, this decrease could be linked to the adsorption of nanobubbles at the foam gas-liquid interface. Throughout the various concentrations, the foam structure evolutions with and without nanobubbles were captured and reported in Figure 5. 11. All the solutions showed foam structures made of very small spherical bubbles resulting in high capillary pressure in the thin liquid film.

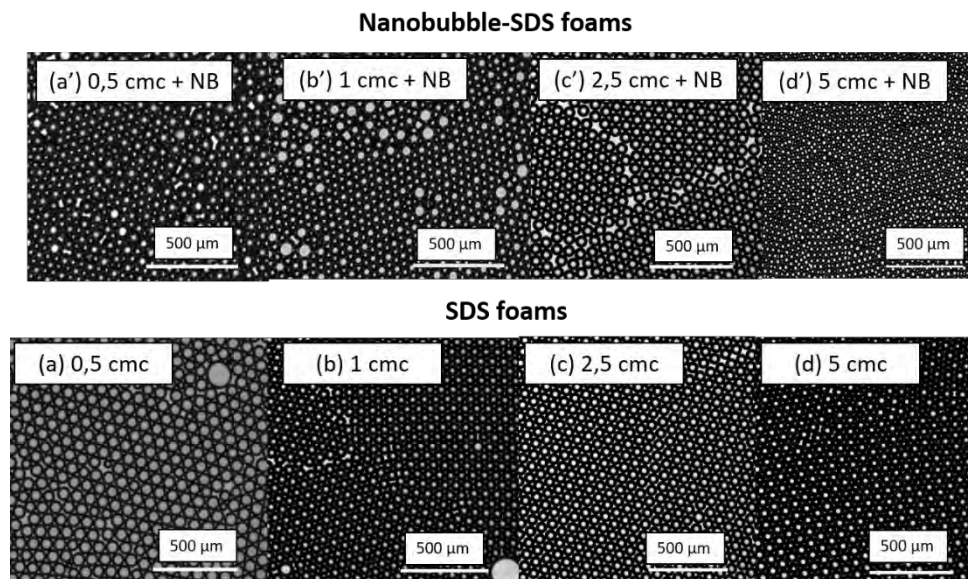


Figure 5. 11 Foam structure evolution after 5s deposition on a glass slide under a cover slip for various concentration of SDS (0.5 (a), 1 (b), 2.5 (c), 5 (d)) solutions & SDS – nanobubbles solutions at 0.5 (a'), 1 (b'), 2.5 (c') and 5 cmc (d').

These foam structures were drastically different from the one obtained for the same experimental conditions with Triton X-100. The difference between Triton X-100 and SDS foams resides in the disparities existing between the two surfactant diffusion dynamics. Indeed, by considering an experimental timescale of 5 ms, SDS adsorbing faster at the interface than Triton X-100, even at the lowest concentration, can stabilise very efficiently and rapidly the interface so that the surface tension can be reduced enough to minimise the bubble surface area. Thus, even at the lowest concentration, foams made of small bubbles were generated. These characterisations steps enabled to better define the nanobubble-surfactant interactions and their effect on the foamability and foam stability. As previously, the effect of bulk nanobubbles was firstly analysed on foam properties stabilised solely by SDS at 0.5 cmc. Thereby, the foamability could be evaluated by analysing the evolution of the foam height in Figure 5. 12 (a) and of the foam liquid fraction in Figure 5. 13 (a). The foam stability could be quantified by comparing the normalised

foam height evolution in Figure 5. 12 (b) and by assessing the evolution of the normalised liquid fraction in Figure 5. 13 (b).

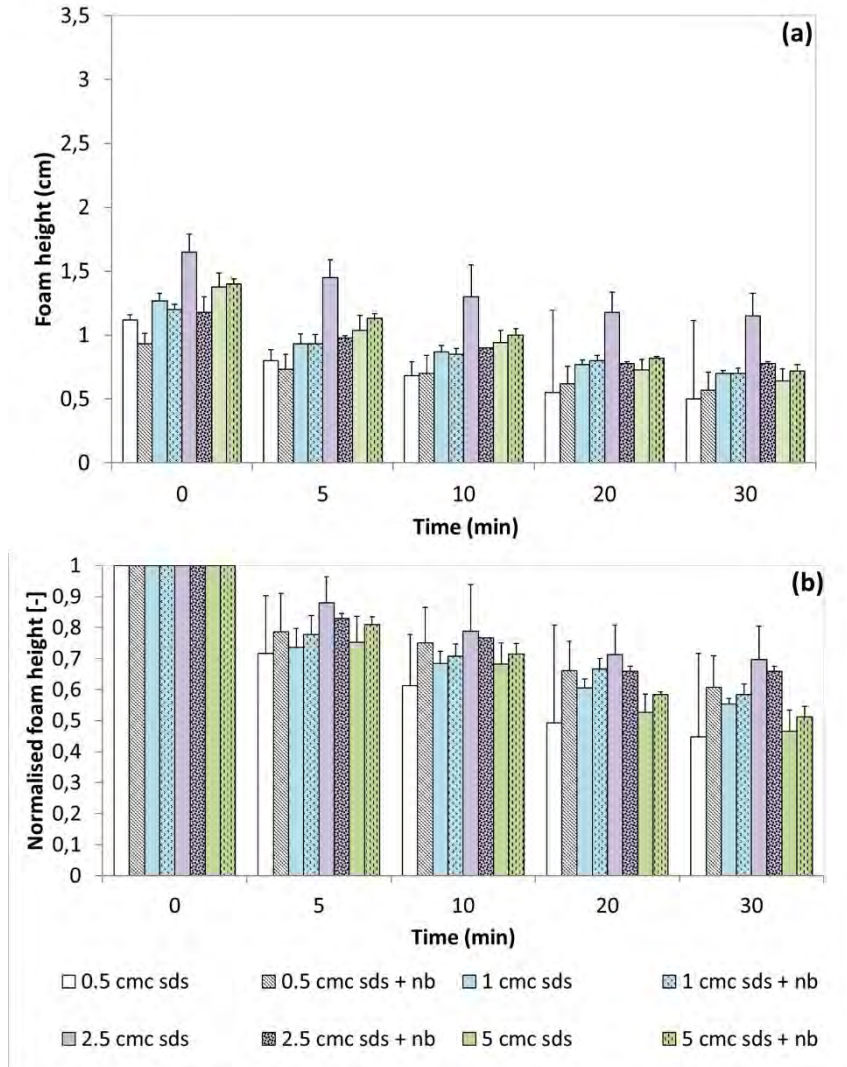


Figure 5. 12 Foam height (a) and normalised foam height (b) evolution after 1-minute foaming for 0.5 (white), 1 (blue), 2.5 (purple) and 5 (green) cmc SDS solution (blank colours) versus bulk nanobubbles + SDS solutions for 0.5 (dotted light grey), 1 (dotted blue), 2.5 (dotted dark grey) and 5 cmc (dotted green). Each value is obtained from an average of three experiments per sample.

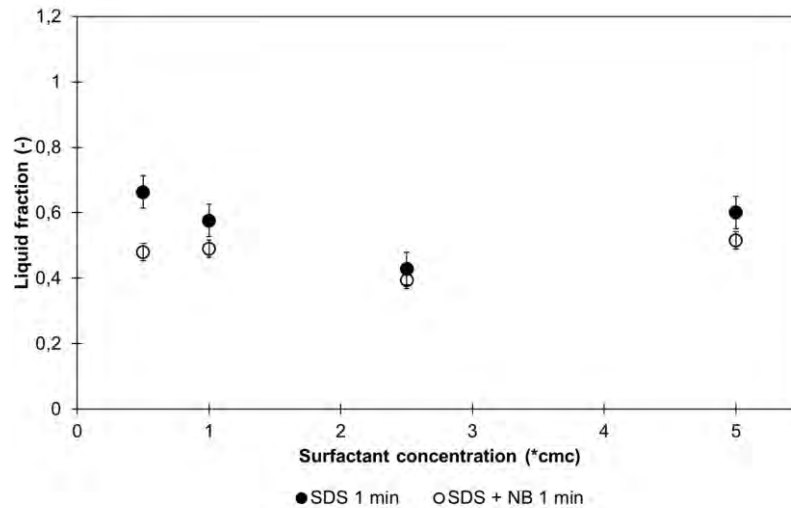


Figure 5. 13 Initial foam liquid fraction evolution for SDS solutions (filled symbols) versus bulk nanobubbles + SDS solutions (unfilled symbols) at various surfactant concentrations. Each value is obtained from an average of three experiments per sample.

5.2.2.1 0.5 cmc SDS

The results of the foam height evolution are reported in Figure 5. 12 (a). At 0.5 cmc, the presence of nanobubbles in solution decreased the foamability compared to the reference solution. Indeed, the foam reached initially 1.1 cm and ended at 0.5 cm for the reference whereas the nanobubble foaming liquid went up to 0.9 cm and down to 0.6 cm. Despite the lowest foamability, the nanobubble-surfactant foam stability was higher than the reference because the height decay was lesser (0.3 cm compared to 0.56 cm respectively) for the same experimental duration.

The foam height decay rate was estimated in Figure 5. 12 (b) by studying the evolution of the normalised foam height for the two formulations: it was observed that the nanobubble-surfactant foam was more stable than the foam solely stabilised by surfactants.

The initial liquid fraction in Figure 5. 13 further confirmed our previous observations. Indeed, the reference showed a greater initial liquid fraction of 0.66 than the nanobubble-surfactant solution (0.42). Thereby, it was found that nanobubbles enhanced foam stability at 0.5 cmc SDS but decreased by the foamability.

It was shown from the zeta potential evolution that SDS molecules adsorb at the nanobubble interface. Therefore, nanobubbles as observed for Triton X-100 removed surfactants molecules from the foam gas-liquid interface.

However, the impact of this phenomenon was balanced by the strong disjunction pressure existing between the two interfaces forming the thin liquid film separating two bubbles. Indeed, SDS being anionic, a strong repulsive contribution to the disjunction pressure arose and balanced the high capillary pressure. This repulsive contribution enhanced foam stability in the reference case.

Despite surfactant removal from the interface, the nanobubble-surfactant stabilised foam was more stable than the reference. Consequently, it was considered that nanobubbles were adsorbing at the foam gas-liquid interface, hence, reinforcing the repulsive contribution to the disjoining pressure.

Furthermore, other phenomena arising from the nanobubble presence at the interface could act to enhance foam stability by reducing the liquid drainage: the presence of nanobubble at the interface could generate a gradient of surface tension and induce a Marangoni effect. The gradient of surface tension could induce a counterflow that could balance the flow of liquid from the film to the Plateau borders due to capillary suction (Cantat *et al.*, 2013). This phenomenon may be enhanced in the following section exposing the 1 cmc SDS results.

5.2.2.2 1 cmc SDS

At 1 cmc, it is assumed that the interface is covered with SDS molecules and that micelles are forming in solution ensuring the number of surfactants at the surface while influencing the dynamic of adsorption and desorption.

In Figure 5. 12 (a), the initial foam height was slightly increased for both solutions. The foamability was enhanced by the increase in surfactant concentration for both solutions. Indeed, the initial foam height went from 0.9 cm at 0.5 cmc to 1.2 cm at 1 cmc for the nanobubble-surfactant foam and from 1.1 cm at 0.5 cmc to 1.3 cm at 1 cmc for the reference.

This small improvement could be correlated to the increase in the initial nanobubble zeta potential in Figure 5. 10 which varied from -80 up to -100 mV. By increasing the nanobubble-surfactant charge density, the repulsive electrostatic contribution to the disjoining pressure could have improved partly the foamability. However, the decrease in surface tension for both solutions could have increased similarly the foamability. Therefore, it is not possible to designate the first or the second cause to be the main driving force for this mechanism.

From Figure 5. 12, the height reduction for both solutions was almost steady compared to 0.5 cmc: for the reference, the foam height varied from 1.3 to 0.7 cm (0.6 cm difference) at 1 cmc whereas it had decreased from 1.1 down to 0.5 cm (0.6 cm difference) at 0.5 cmc. For the nanobubble solution, the foam height had gone from 1.2 down to 0.7 cm (0.5 cm difference) compared to reduction from 0.9 down to 0.6 cm (0.3 cm difference) at 0.5 cmc. These results suggested that the decrease in

surface tension due to the rise in surfactant concentration enhanced the reference foam stability whereas it decreased slightly the nanobubble-surfactant foam stability.

In Figure 5. 13, by increasing the surfactant concentration, the initial liquid content slightly decreased from 0.66 at 0.5 cmc to 0.54 at 1 cmc for the reference solution whereas the nanobubble-surfactant foam presented a steady value of initial liquid content at about 0.5 showing that the nanobubble foam even at 0.5 cmc presented a better stability than the reference at 1 cmc at the initial stage of its formation.

It is believed that even at 1 cmc, the presence of nanobubbles in the volume still affected the number of surfactants present at the foam gas-liquid interface, thus destabilising the foam. Nevertheless, the number of nanobubbles adsorbed at the foam gas-liquid interface had increased as more surfactants were covering nanobubbles, leading to a higher repulsive contribution to the disjunction pressure and a better foamability. The steady surface tension and foam structure with and without nanobubbles demonstrated that the driving forces of the nanobubble-surfactant stabilisation at the foam gas-liquid interface were the repulsive electrostatic contribution to the disjoining pressure and the adsorption of the nanobubble-surfactant at the interface which can enhance the interfacial viscoelastic moduli.

The next paragraph will introduce the action of nanobubbles on the mechanisms affecting the foam gas-liquid interface for the SDS concentration of 2.5 cmc.

5.2.2.3 2.5 cmc SDS

In this paragraph, the effect of nanobubbles on foam solely stabilised by 2.5 cmc SDS was analysed.

The increase in concentration augmented significantly the initial foam height for the reference (from 1.27 to 1.65 cm) but not for the nanobubble-surfactant solution (1.2-1.18 cm).

Thus, the foam stability and the foamability so far for the reference have increased linearly with the concentration. Oppositely, the presence of nanobubbles kept limiting the foamability but enhancing foam stability until 2.5 cmc where the nanobubble-surfactant foam liquid fraction was slightly lower than the reference as expressed by the evolution of the initial liquid fraction in Figure 5. 13.

From Figure 5. 11, the bubbles starting from 1 cmc presented the smallest size which means a high capillary pressure. Consequently, the more repulsive electrostatic contribution to the disjoining pressure to balance the strong capillary pressure, the better should have been the foam stability and foamability.

However, at 1 cmc, the foam stability was still impacted by the surfactant removal effect of nanobubbles from the foam gas-liquid interface, unlike at 2.5 cmc where enough surfactants were available to cover the nanobubbles and the foam gas-liquid interface. Therefore, from 1 cmc to 2.5 cmc, the foam stability and foamability increased. Nevertheless, the foam gas-liquid interface may have reached a peak of disjoining pressure at 2.5 cmc where nanobubbles effect on foam stability was no longer effective.

This phenomenon could explain why the foamability was not further enhanced compared to the reference solution. Indeed, at 2.5 cmc, the gas-liquid interface may have been saturated with adsorbed nanobubble-surfactant which led to a limited foamability for the system.

5.2.2.4 5 cmc SDS

Surprisingly, in Figure 5. 12, unlike previously, the presence of nanobubbles kept enhancing the foamability while decreasing the foam stability compared to the reference.

In fact, the initial reference height was lesser compared to 2.5 cmc (from 1.65 to 1.4) but the nanobubble foam height kept increasing from 1.2 to 1.4 cm. From Figure 5. 13, the initial liquid fraction was close to 0.5. All in all, at 5 cmc SDS, the presence of nanobubbles in solution kept enhancing foam stability and foamability compared to the reference.

From Figure 5. 8, the two solutions showed the same dynamic surface tension at about 37 mN m^{-1} . Interestingly, from Figure 5. 10, the zeta potential of the nanobubble-dispersion had decreased drastically compared to the other formulations.

At 5 cmc, there might have been the formation of supramolecular surfactant structure which could have altered the zeta potential of nanobubbles and the nanobubble adsorption at the foam gas-liquid interface.

Indeed, 3D surfactants structures existing at high surfactant concentrations can help to integrate insoluble components to the system: the nonpolar tail of the surfactants can act as a medium to enhance the solubility of the insoluble component.

Thus, these insoluble counterparts could insert themselves in the micelles at the interface. This action could improve the foamability and the foam stability by increasing the interfacial viscoelastic moduli. It is suspected that nanobubbles could potentially act as an insoluble entity at this concentration. Oppositely, at this

concentration, nanobubbles and these structures could also compete to adsorb themselves at the foam interface.

Beyond a certain concentration, the surfactants structures could replace some nanobubbles adsorbed reversibly at the foam interface. Doing so, the foam stability and the foamability could potentially re-increase. The presence of these supramolecular structures could act either as a screen to the nanobubbles electrostatic stabilising action and/or adsorb preferably at the foam liquid-interface as an insoluble surfactant competing with nanobubble-surfactant adsorption. In both cases, the resulting electrostatic repulsive forces would be less efficient than the previous surfactant concentrations to stabilise the foam gas-liquid interface.

5.3. Conclusion

From this work, the influence of bulk nanobubbles on foam stability was investigated for two surfactants. Two main effects dependent upon the surfactant concentration and nature were identified.

The existence of nanobubbles at a constant concentration with surfactants in solution induced an improved foamability for the non-ionic surfactant concentrations investigated up to 5 cmc and an enhanced stability for all the concentrations.

The presence of nanobubbles at a fixed concentration with anionic surfactants in solution caused an increase in foam stability for all the concentrations investigated and a decrease in foamability from 0.5 to 2.5 cmc.

For both surfactants, the enhancement of the foamability and foam stability was explained by an increase in the disjoining pressure within the thin liquid film led by

the rise in repulsive forces between the two contiguous interfaces forming the film led by the anchoring of nanobubbles at the interface. This effect is suspected to be possible by the adsorption of surfactant molecules at the nanobubbles interface. However, this action can be counteracting at the lowest surfactant concentrations because the nanobubbles, by attracting surfactant at their interface, remove surfactant molecules from the foam gas-liquid interface and reduce the foam stability. Nevertheless, this effect was negligible for anionic stabilised foams because their disjoining pressure was already balancing the destabilisation thanks to a higher repulsive contribution to the disjoining pressure compared to non-ionic surfactants.

Through this chapter, the performances of promising new kind of surface-active agent termed bulk nanobubbles were evaluated on the study of foam stability in static conditions. Alternately, foam stability can be studied in dynamic conditions. The dynamic study of foam stability consists in assessing the persistence of foam properties while the foam is being continuously deformed. This aspect of foam stability will be studied in the next chapter. A new microfluidics approach will be developed to study the property of foam recovery after a deformation.

5.4. List of references

- AlYousef, Z. A., Almobarky, M. A. and Schechter, D. S. (2018) 'The effect of nanoparticle aggregation on surfactant foam stability', *Journal of Colloid and Interface Science*, 511, pp. 365–373. doi: <https://doi.org/10.1016/j.jcis.2017.09.051>.
- Andrieux, S., Drenckhan, W. and Stubenrauch, C. (2017) 'Highly ordered biobased scaffolds: From liquid to solid foams', *Polymer*. doi: <http://doi.org/10.1016/j.polymer.2017.04.031>.
- Andrieux, S., Drenckhan, W. and Stubenrauch, C. (2018) 'Generation of Solid Foams with Controlled Polydispersity Using Microfluidics', *Langmuir*. doi: [10.1021/acs.langmuir.7b03602](https://doi.org/10.1021/acs.langmuir.7b03602).
- Barbetta, A. *et al.* (2005) 'Scaffolds Based on Biopolymeric Foams', *Advanced Functional Materials*, 15, pp. 118–124. doi: [10.1002/adfm.200400072](https://doi.org/10.1002/adfm.200400072).
- Binks, B. P. and Horozov, T. S. (2005) 'Aqueous Foams Stabilized Solely by Silica Nanoparticles', *Angewandte Chemie International Edition*. Wiley-Blackwell, 44(24), pp. 3722–3725. doi: [10.1002/anie.200462470](https://doi.org/10.1002/anie.200462470).
- Cantat, I. *et al.* (2013) *Foams: Structure and Dynamics*. OUP Oxford. Available at: <https://books.google.fr/books?id=yShoAgAAQBAJ>.
- Chen, H. *et al.* (2009) 'Defouling and cleaning using nanobubbles on stainless steel', *Biofouling*, 25, pp. 353–357. doi: [10.1080/08927010902807645](https://doi.org/10.1080/08927010902807645).
- Cho, S.-H. *et al.* (2005) 'Ultrasonic formation of nanobubbles and their zeta-potentials in aqueous electrolyte and surfactant solutions', *Colloids and Surfaces A: Physicochemical and Engineering Aspects*, 269, pp. 28–34. doi: <http://dx.doi.org/10.1016/j.colsurfa.2005.06.063>.
- Fan, M. *et al.* (2010a) 'Nanobubble generation and its application in froth flotation (part I): nanobubble generation and its effects on properties of microbubble and millimeter scale bubble solutions', *Mining Science and Technology (China)*, 20, pp. 1–19. doi: [https://doi.org/10.1016/S1674-5264\(09\)60154-X](https://doi.org/10.1016/S1674-5264(09)60154-X).
- Fan, M. *et al.* (2010b) 'Nanobubble generation and its applications in froth flotation (part II): fundamental study and theoretical analysis', *Mining Science and Technology (China)*, 20, pp. 159–177. doi: [https://doi.org/10.1016/S1674-5264\(09\)60179-4](https://doi.org/10.1016/S1674-5264(09)60179-4).
- Guo, F. and Aryana, S. (2016) 'An experimental investigation of nanoparticle-stabilized CO₂ foam used in enhanced oil recovery', *Fuel*, 186, pp. 430–442. doi: [10.1016/j.fuel.2016.08.058](https://doi.org/10.1016/j.fuel.2016.08.058).
- Hernandez, C. *et al.* (2018) 'Role of Surface Tension in Gas Nanobubble Stability under Ultrasound', *ACS Applied Materials and Interfaces*, 10, pp. 9949–9956. doi: [10.1021/acsami.7b19755](https://doi.org/10.1021/acsami.7b19755).
- Hunter, T. N. *et al.* (2008) 'The role of particles in stabilising foams and emulsions', *Advances in Colloid and Interface Science*, 137(2), pp. 57–81. doi: <https://doi.org/10.1016/j.cis.2007.07.007>.

- Hunter, T. N. *et al.* (2009) 'Non-ionic surfactant interactions with hydrophobic nanoparticles: Impact on foam stability', *Colloids and Surfaces A: Physicochemical and Engineering Aspects*, 347, pp. 81–89. doi: <https://doi.org/10.1016/j.colsurfa.2008.12.027>.
- Karakashev, S. I. and Nguyen, A. V (2009) 'Do Liquid Films Rupture due to the So-Called Hydrophobic Force or Migration of Dissolved Gases?', *Langmuir*. American Chemical Society, 25(6), pp. 3363–3368. doi: 10.1021/la8034648.
- Karraker, K. A. and Radke, C. J. (2002) 'Disjoining pressures, zeta potentials and surface tensions of aqueous non-ionic surfactant/electrolyte solutions: Theory and comparison to experiment', *Advances in Colloid and Interface Science*, 96(1–3), pp. 231–264. doi: 10.1016/S0001-8686(01)00083-5.
- Liu, G., Wu, Z. and Craig, V. S. J. (2008) 'Cleaning of protein-coated surfaces using nanobubbles: An investigation using a Quartz Crystal Microbalance', *Journal of Physical Chemistry C*, 112, pp. 16748–16753. doi: 10.1021/jp805143c.
- Manev, E. D. and Nguyen, A. V (2005) 'Effects of surfactant adsorption and surface forces on thinning and rupture of foam liquid films', *International Journal of Mineral Processing*, 77, pp. 1–45. doi: <https://doi.org/10.1016/j.minpro.2005.01.003>.
- Nguyen, P., Fadaei, H. and Sinton, D. (2014) 'Pore-Scale Assessment of Nanoparticle-Stabilized CO₂ Foam for Enhanced Oil Recovery', *Energy & Fuels*, 28, pp. 6221–6227. doi: 10.1021/ef5011995.
- Nieves, L. *et al.* (2017) 'Effect of the surfactant pluronic on the stability of lipid-stabilized perfluorocarbon nanobubbles', in *IEEE International Ultrasonics Symposium, IUS*. doi: 10.1109/ULTSYM.2017.8092148.
- Nirmalkar, N., Pacek, A. W. and Barigou, M. (2018) 'Interpreting the interfacial and colloidal stability of bulk nanobubbles', *Soft Matter*. The Royal Society of Chemistry, p. doi: 10.1039/C8SM01949E.
- Oh, S. H. and Kim, J.-M. (2017) 'Generation and Stability of Bulk Nanobubbles', *Langmuir*. doi: 10.1021/acs.langmuir.7b00510.
- Peyman, S. A. *et al.* (2012) 'Expanding 3D geometry for enhanced on-chip microbubble production and single step formation of liposome modified microbubbles', *Lab on a Chip*, 12, pp. 4544–4552. doi: 10.1039/C2LC40634A.
- Peyman, S. A. *et al.* (2016) 'On-chip preparation of nanoscale contrast agents towards high-resolution ultrasound imaging', *Lab on a Chip*, 16, pp. 679–687. doi: 10.1039/C5LC01394A.
- Quennouz, N. *et al.* (2014) 'Microfluidic study of foams flow for enhanced oil recovery (EOR)', *Oil and Gas Science and Technology*, 69, pp. 457–466. doi: 10.2516/ogst/2014017.
- Saint-Jalmes, A. (2006) 'Physical chemistry in foam drainage and coarsening', *Soft Matter*, 2, pp. 836–849. doi: 10.1039/B606780H.
- Saint-Jalmes, A. and Langevin, D. (2002) 'Time evolution of aqueous foams: drainage and coarsening', *Journal of Physics: Condensed Matter*, 14, p. 9397.

Available at: <http://stacks.iop.org/0953-8984/14/i=40/a=325>.

Salerno, A. and Netti, P. A. (2014) '1 - Introduction to biomedical foams', in *Biomedical Foams for Tissue Engineering Applications*. Woodhead Publishing, pp. 3–39. doi: <https://doi.org/10.1533/9780857097033.1.3>.

Seddon, J. R. T. *et al.* (2012) 'A Deliberation on Nanobubbles at Surfaces and in Bulk', *ChemPhysChem*, 13, pp. 2179–2187. doi: 10.1002/cphc.201100900.

Tuziuti, T., Yasui, K. and Kanematsu, W. (2018) 'Influence of addition of degassed water on bulk nanobubbles', *Ultrasonics Sonochemistry*. doi: <https://doi.org/10.1016/j.ultsonch.2018.01.015>.

Ushida, A. *et al.* (2012) 'Effect of mixed nanobubble and microbubble liquids on the washing rate of cloth in an alternating flow', *Journal of Surfactants and Detergents*, 15(6), pp. 695–702. doi: 10.1007/s11743-012-1348-x.

Weijjs, J. H., Seddon, J. R. T. and Lohse, D. (2012) 'Diffusive Shielding Stabilizes Bulk Nanobubble Clusters', *ChemPhysChem*. John Wiley & Sons, Ltd, 13(8), pp. 2197–2204. doi: 10.1002/cphc.201100807.

Weinheimer, R. M., Evans, D. F. and Cussler, E. L. (1981) 'Diffusion in surfactant solutions', *Journal of Colloid and Interface Science*, 80(2), pp. 357–368. doi: [https://doi.org/10.1016/0021-9797\(81\)90194-6](https://doi.org/10.1016/0021-9797(81)90194-6).

Yasui, K. *et al.* (2018) 'Is surface tension reduced by nanobubbles (ultrafine bubbles) generated by cavitation?', *Ultrasonics Sonochemistry*. doi: <https://doi.org/10.1016/j.ultsonch.2018.11.020>.

Yekeen, N. *et al.* (2018) 'A comprehensive review of experimental studies of nanoparticles-stabilized foam for enhanced oil recovery', *Journal of Petroleum Science and Engineering*, 164, pp. 43–74. doi: <https://doi.org/10.1016/j.petrol.2018.01.035>.

Zhang, M. and Seddon, J. R. T. (2016) 'Nanobubble–Nanoparticle Interactions in Bulk Solutions', *Langmuir*, 32, pp. 11280–11286. doi: 10.1021/acs.langmuir.6b02419.

Zhang, M., Seddon, J. R. T. and Lemay, S. G. (2019) 'Nanoparticle–nanobubble interactions: Charge inversion and re-entrant condensation of amidine latex nanoparticles driven by bulk nanobubbles', *Journal of Colloid and Interface Science*, 538, pp. 605–610. doi: 10.1016/j.jcis.2018.11.110.

CHAPTER 6

MICROFLUIDICS APPROACH TO INVESTIGATE FOAM HYSTERETIC BEHAVIOUR

6.1 Introduction

Aqueous foams can behave like a shear-thinning fluid over time after being subjected to deformation (Bekkour and Scrivener, 1998). This property, called "thixotropy", plays an important role in foam stability (Mewis, 1979; de Souza Mendes, 2009; Mewis and Wagner, 2009; Larson, 2015). Thixotropy implies the creation of a change in foam properties before and after the deformation, thus, a hysteresis.

Foam rheology and more precisely foam thixotropy or foam hysteretic behaviour is mainly studied by rheometry (Miquelim and Da Silva Lannes, 2009). The two most common tests employed to study how a fluid recovers after a deformation are the three-step test and the creep test (Mezger, 2014). The three-step test consists in three consecutive stages of rest, deformation and rest. The initial rest viscosity is taken as reference for the study of the fluid recovery after a gradual or sharp deformation. This test has been adapted to fragile products such as foams by applying a non-destructive deformation to preserve the sample (Asnacios, 1999). An example of a thixotropy study by performing an oscillatory test within the linear viscoelastic range is given by Saint-Jalmes (2009).

However, foams evolve over time due to the simultaneous destabilising events which are the key actors of its stability kinetic (e.g. drainage, coalescence and coarsening) (Saint-Jalmes *et al.*, 2004; Pitois *et al.*, 2005; Saint-Jalmes, 2006). This aging process, in addition to the quantity of product required and the cost of the equipment, demonstrate the limitations of macroscale rheometry to study foam rheology. Since a decade, a novel and innovative use of microfluidics have been developed at first to measure the viscosity of single phase fluids (Guillot *et al.*, 2006) and further to

measure the properties of viscoelastic fluids such as the relaxation times (Pipe and McKinley, 2009; Galindo-Rosales *et al.*, 2013; Koser *et al.*, 2013).

Microfluidics rheometry matches the standards of its macroscopic counterpart with the advantages of requiring much less amount of sample and lower cost. Thus, extending this use of microfluidics to two-phase fluids can bring a new perspective in studying how the shear viscosity, the surface viscosity and other properties influence their rheological behaviour. Here, a new way to study and to evaluate the parameters influencing the property of recovery of foam after a gradual deformation at the wall in a microchannel was implemented as illustrated in Figure 6. 1.

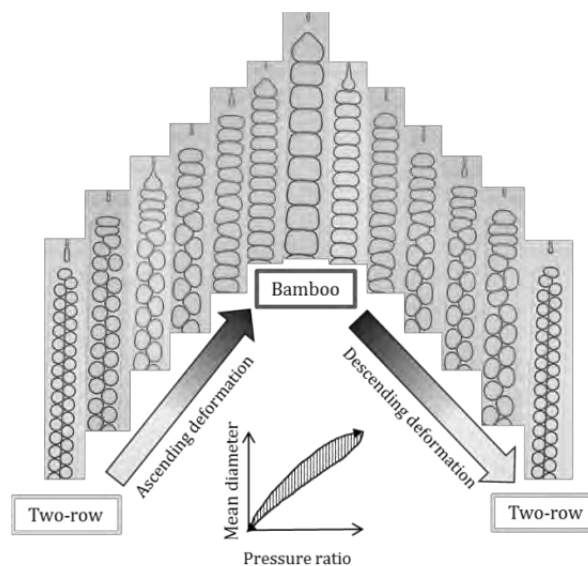


Figure 6. 1 Schematic of the three-step test consisting in an ascending and descending pressure ramp obtained by varying the gas pressure for a constant liquid pressure

Three parameters (viscosity, surface elasticity and shear-thinning property) and their effects on the property of foam recovery after a deformation induced by the change of gas pressure for a fixed liquid pressure were investigated. All the details of the method and the various solutions employed are reported in chapter 3.

6.2 Results and discussion

6.2.1 Foaming solutions properties and foam regime map

SDS is a common anionic surfactant used in a wide range of foam industrial applications (Weaire and Phelan, 1996). A concentration above cmc (critical micellar concentration) was chosen to ensure a constant concentration of surface active agent throughout the whole experiment. Glycerol (GLY, Sigma Aldrich) was used at 20 and 40% (wt.) to increase the dynamic viscosity of the reference solution. Dodecanol (DOH, Sigma Aldrich) was added to the reference solution at a concentration of 0.15 g L^{-1} to study the effect of surface elasticity on the foam hysteretic behaviour. Xantham gum (XG, Sigma Aldrich) was employed at 0.01 g L^{-1} with 5% (wt.) glycerol to facilitate the dissolution in our reference solution, to study the effect of the shear-thinning property of the continuous phase. XG is used as a thickener in industry which implies that at low deformation, it increases the solution viscosity which then decreases with an increasing deformation due to its shear-thinning characteristic. The equilibrium surface tensions at 25°C of the different solutions investigated were measured via Maximum Bubble Pressure technique (SINTERFACE, BPA-1) and summarized in Table 6. 1 below:

Table 6. 1 Summary of foaming solutions investigated: (A) 5 cmc SDS, (B) 5 cmc SDS + 20% (wt.) glycerol, (C) 5 cmc SDS + 40% (wt.) glycerol (D) 5 cmc SDS + 0.15 g L^{-1} DOH and (E) 5 cmc SDS + 0.01 g L^{-1} + 5% (wt) glycerol. An average of three measurements were performed for each formulation.

Solutions	σ , equilibrium surface tension (mN m^{-1})
A) 5 cmc SDS	36.3 ± 2.7
B) 5 cmc SDS + 20% wt GLY	37.6 ± 4.8
C) 5 cmc SDS + 40% wt GLY	45.5 ± 4.2
D) 5 cmc SDS + 0.15 g L^{-1} DOH	36.7 ± 3.6
E) 5 cmc SDS + 0.01 g L^{-1} XG + 5% wt GLY	46.3 ± 4.7

The solution viscosities were investigated via a shear rate sweep from 5 to 100 s⁻¹ via a cone-plate geometry (2-degree truncation, 60 mm diameter) on the rheometer (DHR-1, TA).

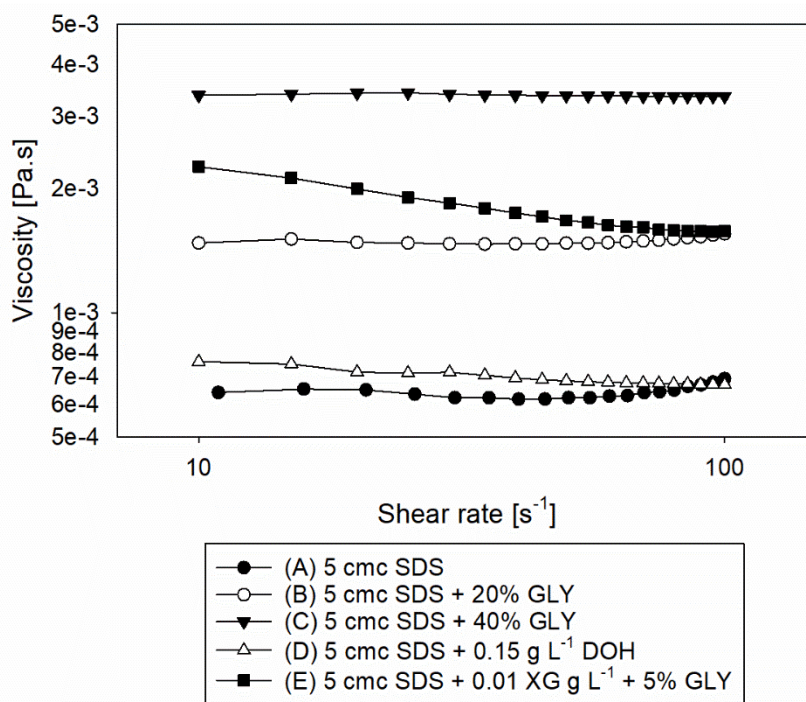


Figure 6. 2 Rheological properties of solutions investigated: (A) 5 cmc SDS, (B) 5 cmc SDS + 20% (wt.) glycerol, (C) 5 cmc SDS + 40% (wt.) glycerol, (D) 5 cmc SDS + 0.15 g L⁻¹ DOH and (D) 5 cmc SDS + 0.01 g L⁻¹ XG + 5% (wt.) glycerol.

Most of the solutions showed a Newtonian behaviour with a steady viscosity ranging from 0.6 mPa s for the reference solution (A), and reference + DOH (D), 1.5 mPa s for the reference +20% (wt.) glycerol (B) to 3.5 mPa s for the reference + 40% (wt.) glycerol (C). The solution (E) presented a non-Newtonian behaviour with a decrease of viscosity for an increasing shear rate from 2.5 down to 1.5 mPa s, characteristic of a shear-thinning fluid.

A foam regime map (FRM), which gives detailed view of all the different foam patterns available for a specific geometry, was firstly generated for each solution by changing the gas and inlet pressures between 200 and 1400 mbar. Thus, areas of

steady patterns of bamboo and two-row foam could be identified and selected for our study. The “bamboo” pattern or “hex-one” (Garstecki and Whitesides, 2006) is described as a single layer of bubbles containing only one bubble in the full width of the channel. The “two-row” pattern or “hex-two” (Garstecki and Whitesides, 2006) can be depicted as a single layer containing two rows of bubbles in the width of the channel.

The foam regime maps obtained for each foaming liquid are presented in Figure 6. 3.

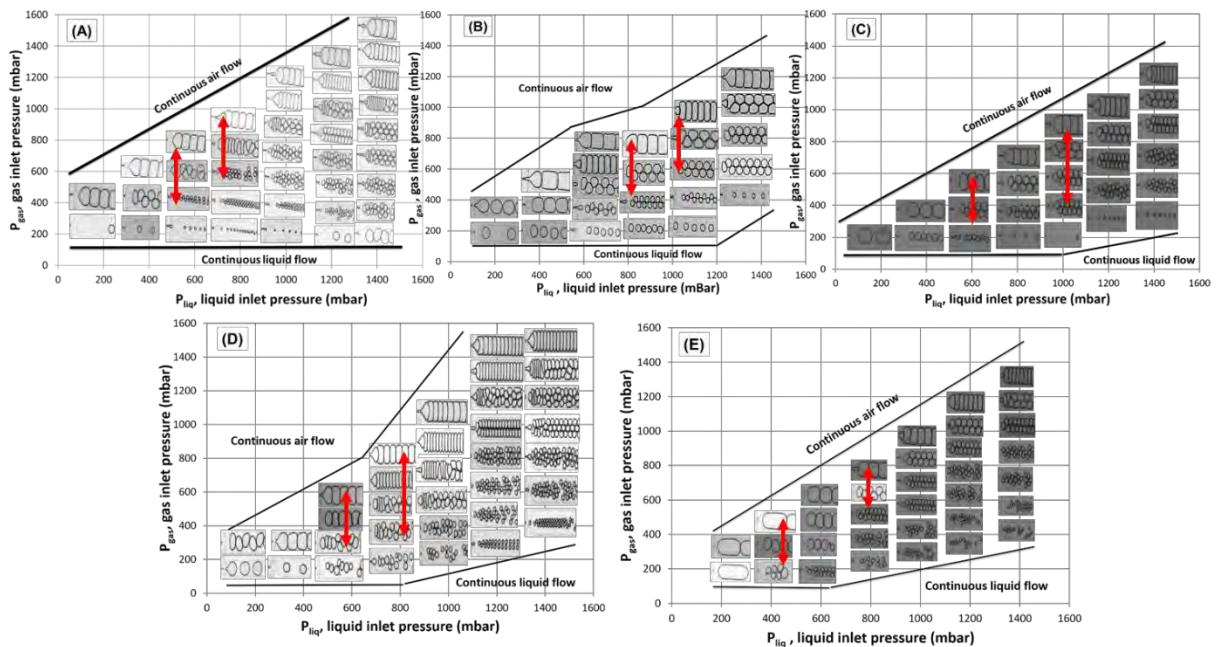


Figure 6. 3 Foam regime maps for the following solutions: (A) 5 cmc SDS, B) 5 cmc SDS + 20% (wt.) glycerol, (C) 5 cmc SDS + 40% (wt.) glycerol, (D) 5 cmc SDS + 0.15 g L⁻¹ DOH and (E) 5 cmc SDS + 0.01 g L⁻¹ XG + 5% (wt.) glycerol. The red arrows from left to right represent the low (P1) and high (P2) pressure ranges investigated for each formulation.

In Figure 6. 3, the impact of the viscosity, surface elasticity and shear-thinning property on the patterns available in the foam regime map was already noticeable. This showed that foam response to the induced deformation at the wall was directly influenced by these properties.

First, the effect of viscosity was analysed for a fixed value of the surface tension by comparing the FRM (B) versus our reference FRM (A). It was found that for a certain pressure set, the mean bubble diameter for the two-row pattern was smaller compared to the reference. Indeed, by comparing the mean bubble area evolution at 400 mbar gas pressure and 600 mbar liquid pressure, it was observed that at 20% glycerol, the area obtained had been reduced from 12891 μm^2 for 5 cmc SDS down to 5530 μm^2 for the 20% glycerol solution. Nevertheless, at 40% glycerol, a two-row pattern was generated depicting a mean bubble area of 6620 μm^2 which is still lower than the reference but slightly higher than the 20% glycerol. Despite the increase in viscosity, which tends to create smaller bubbles for a given flow rate, the solution with 40% glycerol showed also an increase in surface tension responsible for the creation of slightly larger bubbles compared to the sample containing 20% glycerol.

Indeed, by comparing our reference solution (A) to the 40% glycerol (C), the differences in viscosity and surface tension caused the range of available patterns to reduce as the surface tension had increased from 36.7 to 45.5 mN m^{-1} . From (Ruiz, Díaz-López and Aguiar, 2008), which described the evolution of the micellization of SDS with the glycerol concentration in solution, it had been demonstrated that the addition of glycerol increased the solubility of the SDS hydrophobic part. As a result, the miscibility of the hydrophilic part of the molecule decreased as the solution presented a higher affinity to the hydrophobic component. Thus, the stabilising action of SDS at the interface was limited and the surface tension increased.

Then, the addition of DOH modified the resulting FRM (D): the bamboo pattern region was extended towards the higher gas pressure thanks to the increase in

surface elasticity. The resulting interface facing the induced deformation was “stiffer” albeit having the same surface tension as the reference solution.

Karakashev and Nguyen (2007) explained that DOH molecules adsorb at the gas-liquid interface and limit the surface mobility of surfactant molecules due to their carbon backbone. DOH is not expected to affect significantly the dynamic adsorption of SDS to the interface and thus the surface tension.

Finally, the Xantham gum + SDS FRM (E) illustrated well its effect on the foam pattern: considering that the shear viscosity of the foaming liquid was greater in (E) than in (A) for a fixed deformation, the higher viscosity of the liquid phase resulted in a higher resistance of the gas phase to the liquid phase action. A bubble was formed by the pinching of the gas stream by both liquid streams at the junction. At low liquid pressure, the liquid viscosity was higher, therefore the average bubble diameter obtained for (E) was greater than the one obtained in (A) for this range of deformation.

Indeed in Figure 6. 3, the size of the bamboo pattern obtained for a gas and liquid pressure of 200 mbar was greater in the case of XG (E) than for our reference solution (A).

Yet, at higher liquid pressure, the liquid viscosity has decreased due to the shear-thinning property of XG, and the pinching was more effective. Consequently, in Figure 6. 3, the two-row pattern was observable in (E) but not in (A) or (C) for a gas pressure of 200 mbar and a liquid pressure of 600 mbar. Furthermore, the addition of XG had increased the surface tension from 36.3 to 46.3 mN m⁻¹. Nedjhioui *et al.* (2009) showed that the interactions between XG and SDS can affect the surface tension of the polymer-surfactant mixture. Above the cmc, for any concentration of

XG in the range from 0.1 to 0.5 % (wt.), the surface tension varied between 47 to 40 mN m⁻¹ (Nedjhioui *et al.*, 2009). The SDS molecules were adsorbing on the XG polymeric chains and this caused the surface tension to increase compared to the pure surfactant solution. Thus, the formation of new interface in the shape of single bubbles and their stabilisation at 200 mbar gas pressure for (E) was more difficult than for our reference solution (A) for the highest liquid pressures.

From this preliminary characterisation step, two steady foam patterns from the FRM were identified and defined as low deformation (P1, two-row) and high deformation (P2, bamboo) at the wall. The low/high deformation at the wall was defined regarding how much of the bubble surface was in contact with the wall and thus subjected to friction. Consequently, the bamboo pattern presented a larger surface in contact with the wall (30000 to 40000 μm²) than the two-row of bubbles (4000 up to 6000 μm²) per single bubble as mentioned earlier. The response of the foam to the deformation was identified via the comparison of the evolution of the apparent mean bubble diameter over time in an ascending versus a descending ramp.

6.2.2 Reference solution: 5 cmc SDS

The evolution of the hysteresis with the pressure ramps of 0.5 and 2 mbar s⁻¹ was evaluated in this section for low (P1, corresponding to 600 mbar liquid inlet pressure for a gas pressure ranging from 400 to 600 mbar) and high (P2, corresponding to 800 mbar liquid inlet pressure for a gas pressure ranging from 500 to 800 mbar) pressure sets.

Figure 6. 4 showed the evolution of the pressure ratio per pressure ramp and set. The pressure ratio is set as the ratio of the gas pressure over the liquid pressure.

Each hysteresis value was obtained from the average of two experiments with three repeats for each setting (ramp & set). From the inset, it was concluded that qualitatively, the foam formed from the 5 cmc SDS solution didn't present any hysteresis both at the low and high-pressure ramps and sets. The average of the area in between the ascending and descending curves obtained for several experiments was taken as the "noise" of the measurement which represented our zero-reference value to determine if a foam presented a hysteretic behaviour or not. Thus, the value obtained for this sample, $1.5 \pm 0.7 \times 10^{-3}$ (represented by the red continuous line in Figure 6.4, 6.11, 6.13 and 6.16) was considered as the qualitative reference number describing a negligible hysteresis.

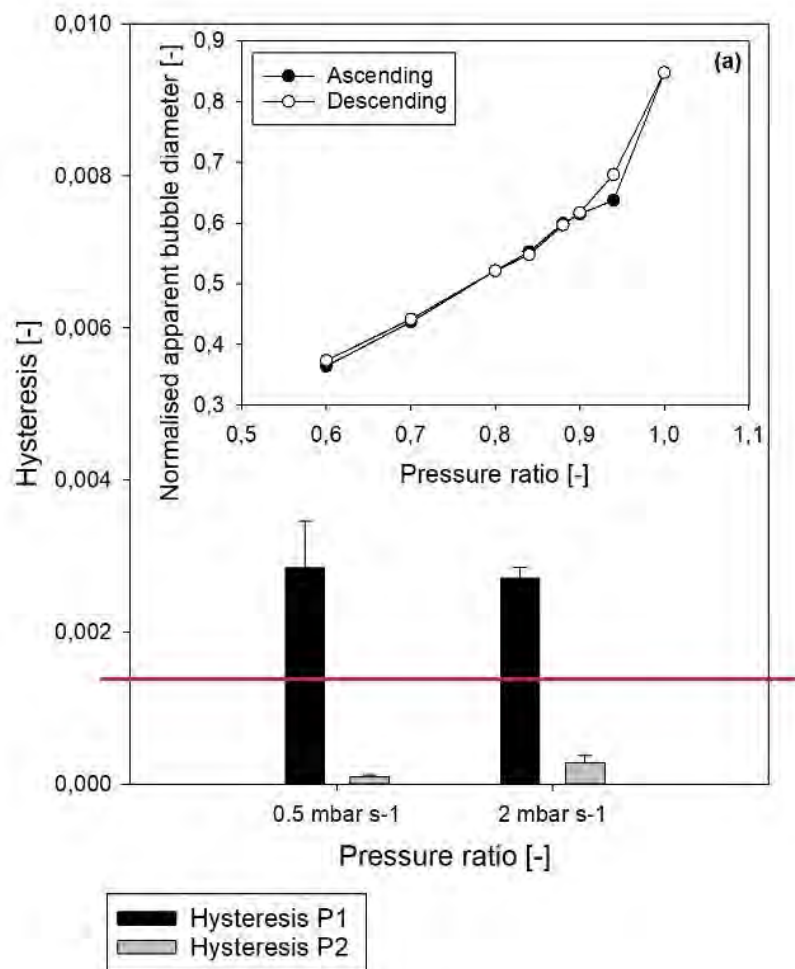


Figure 6. 4 Hysteresis evolution for 5 cmc SDS at low (P1, black) and high pressure (P2, grey) sets for both pressure ramps (0.5 & 2 mbar s⁻¹). In the inset, a typical hysteresis curve for P1 at 0.5 mbar s⁻¹.

From these results, the analogous of an experimental flow curve was obtained by plotting the shear stress at the wall due to the drag force versus the shear rate as illustrated for our reference in Figure 6. 5.



Figure 6. 5 Experimental flow curves plotting the shear stress due to the drag force versus the shear rate for 5 cmc SDS solution at P2 and 0.5 mbar s⁻¹ obtained from the ascending (blue) and descending (red) pressure ramps.

The set of equations (3-1), (3-2) and (3-3) introduced in chapter 3 were used to obtain the equivalent of a flow curve plotting the stress due to the drag force versus the apparent shear rate. Firstly, two different regions could be identified where the bamboo or the two-row pattern were dominant.

The duration of local bubble rearrangement is an important characteristic in this test because it is going to impact directly the look of these curves. It is known from literature that the duration of rearrangement is dependent upon the product of the shear rate and the ratio of the fluid viscosity upon the confinement pressure (average

contact force which pushed bubbles against each other) for coarsening wet foams (Le Merrer *et al.*, 2012; Le Merrer *et al.*, 2013). It can also be correlated to the dilatational surface viscosity over the surface tension in the case of dry foams for the low strain rate regime (Durand and Stone, 2006). Thus, from this test, the link between the recovery properties and the microstructure dynamic during the deformation can be examined. Two characteristic times were determined from the transition between two-row and bamboo patterns:

- The local rearrangement time of T1 bubble rearrangement duration described as an irreversible bubble neighbour switching event (Dennin, 2004).
- A non-dimensional time depicting the overall two-row to bamboo transition designed by the experimental conditions. It is expressed as the transition time required for complete transition from the two-row to bamboo foam structure in the channel divided by the overall experimental time of foam deformation during the ascending or descending ramp.

The local bubble rearrangement was estimated at 1.25 ms for 400 mbar gas pressure and 600 mbar liquid pressure. The time evolution is represented in Figure 6.

6.

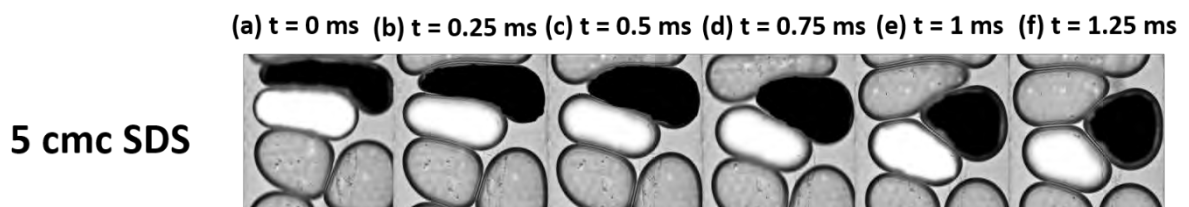


Figure 6. 6 Time lapses of the T1 bubble rearrangements for a fixed pressure set ($P_{\text{gas}} = 400$ mbar, $P_{\text{liq}} = 600$ mbar) for 5 cmc SDS from (a-f).

The non-dimensional time was approximated at $8.6 \pm 0.8 \times 10^{-2}$ for P1 and at for $17.0 \pm 6.1 \times 10^{-2}$ at P2 for both pressure ramps. No hysteresis was observed therefore, the transition time in the ascending and descending were very similar.

6.2.3 Effect of viscosity on hysteresis

Two different cases are presented here to highlight the effect of viscosity and the combined influence of viscosity and surface tension on foam hysteresis.

6.2.3.1 5 cmc SDS + 20 wt. % glycerol

The effect of the increase in pressure ramp from 0.5 to 2 mbar s^{-1} is depicted in Figure 6. 7 for low (P1, corresponding to 800 mbar liquid inlet pressure for a gas pressure ranging from 500 to 800 mbar) and for high (P2, corresponding to 1000 mbar liquid inlet pressure for a gas pressure ranging from 800 to 980 mbar) pressure sets.

From the inset in Figure 6. 7, it was found that the hysteresis was significantly emphasized by the increase in viscosity for a fixed surface tension. The hysteresis increased with both pressure sets and ramps. However, a synergetic effect was observed at P2 and 2 mbar s^{-1} . Indeed, the hysteresis increased two times with the pressure ramp at P1 and almost twenty times with the pressure set at 2 mbar s^{-1} .

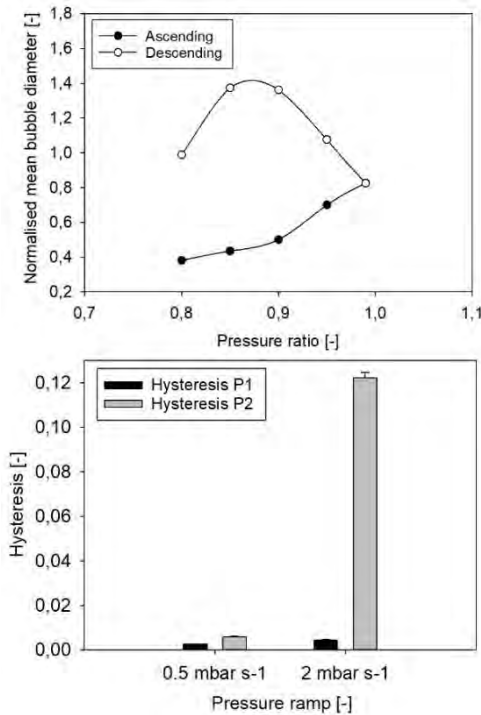


Figure 6. 7 Hysteresis evolution for 5 cmc SDS + 20% (wt.) glycerol at low (P1, black) and high (P2, grey) pressure sets for both pressure ramps (0.5 & 2 mbar s⁻¹). In the upper graph, a typical curve presenting the hysteresis versus the pressure ratio for P2 at 2 mbar s⁻¹.

The flow curves obtained for 20% glycerol were shifted towards the lowest shear stresses for the same range of shear rate because the average bubble diameter had decreased with the viscosity increase leading to less drag force at the channel wall.

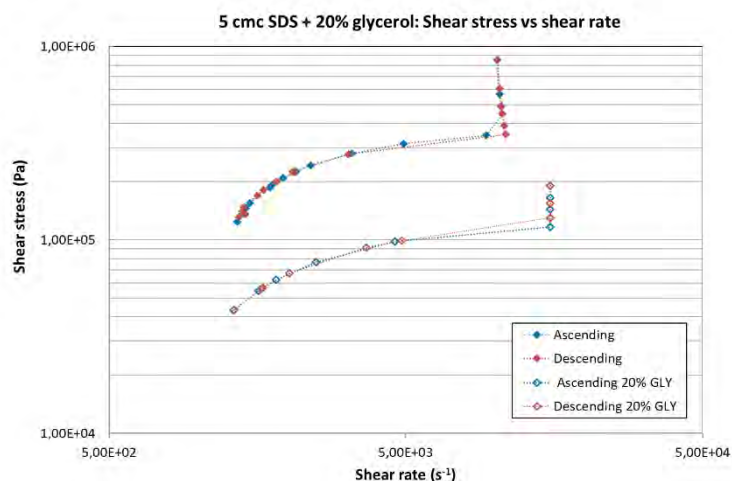


Figure 6. 8 Experimental flow curves plotting the shear stress due to the drag force versus the shear rate for 5 cmc SDS solution (filled symbols) at P2 (800 mbar liquid pressure) and 0.5 mbar s⁻¹ versus 5 cmc SDS + 20% wt. GLY (unfilled symbols) at P1 (800 mbar liquid pressure) and 0.5 mbar s⁻¹ obtained from the ascending (blue) and descending (red) pressure ramps.

The local bubble rearrangement duration was estimated at 5 ms via image analysis for 700 mbar gas pressure and 800 liquid pressure as illustrated in Figure 6. 9. A value of 3 ms was obtained for SDS for the same range of pressure set (800 mbar gas and 900 mbar liquid pressures).

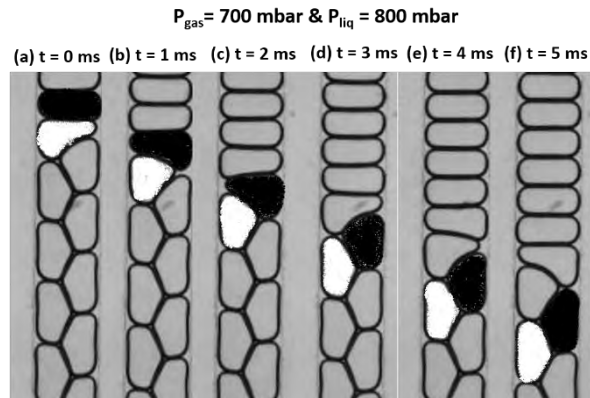


Figure 6. 9 Time lapses describing the local bubble rearrangement for 5 cmc SDS + 20% wt. glycerol for 700 mbar gas pressure and 800 mbar liquid pressure.

Therefore, the increase in viscosity enhanced the local bubble rearrangement as bubbles required more time to rearrange themselves in an ordered lattice.

In coarsening wet foams, rigid interfaces promote longer bubble rearrangement duration compared to mobile interfaces whose driving force, the osmotic pressure Π_o , pushes the bubbles against each other (capillary suction). Indeed, as a bubble travels a distance d upon rearrangement, a volume of liquid is moved through the interstices of the bubble network such as K , the network permeability that can be expressed as $K = \alpha_p R^2$ (Lorenceanu *et al.*, 2009) with α_p the permeability coefficient of the medium. This displacement, slowed down by a viscous friction acting against the capillary force defines the relaxation time such as $\tau_{T1} \approx \eta \phi_l / (\Pi_o \alpha_p)$, diverging at the jamming transition ($\Pi_o \rightarrow 0$) (Le Merrer *et al.*, 2012; Cohen-Addad *et al.*, 2013).

Furthermore, from the existing relationship described by Durand and Stone (2006) limited to the case of dry foams at low strain rate regime, the T1 bubble rearrangement relaxation time τ_{T1} was described as the product of the shear rate times the ratio of surface dilatational viscosity κ over the surface tension σ such as $\tau_{T1} \approx \frac{\kappa}{\sigma} \times \dot{\gamma}$. The change from two-row to bamboo foam pattern implies the transition from wet foam to dry foam. Therefore, the two relaxation time expressions need to be considered to study the impact of the various parameters investigated in this work.

A non-dimensional transition time of $3.8 \pm 0.3 \times 10^{-2}$ was obtained at P1 for both pressure ramps. At P2, the ascending transition time was similar than the one obtained at P1. However, the descending transition time could not be measured because the hysteresis persisted longer than the descending ramp, preventing the transition from bamboo to two-row pattern.

6.2.3.2 5 cmc SDS + 40 wt. % glycerol

The addition of glycerol to our reference solution impacted significantly the foam recovery property throughout the deformation cycle. The impact of the increase in pressure ramp from 0.5 to 2 mbar s⁻¹ was shown in Figure 6. 10 for low (P1, corresponding to 600 mbar liquid inlet pressure for a gas pressure ranging from 400 to 600 mbar) and for high (P2, corresponding to 1000 mbar liquid inlet pressure for a gas pressure ranging from 600 to 900 mbar) pressure sets.

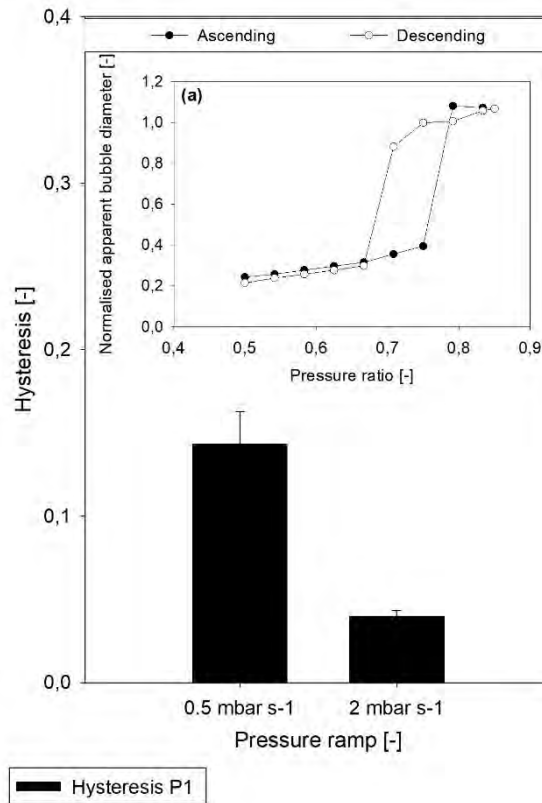


Figure 6. 10 Hysteresis evolution for 5 cmc SDS + 40% (wt.) glycerol at low pressure set (P1, black) for both pressure ramps (0.5 & 2 mbar s⁻¹). In the inset, a typical curve for P1 at 2 mbar s⁻¹.

From Figure 6. 10, for the low pressure set (P1), a large hysteresis was observed. This could be explained by the fact that at lower pressure set, the resistance to the deformation at the wall was higher due to the increase in viscosity.

Thus, once the bamboo/annular pattern had been reached, after the high deformation plateau, in the descending ramp, the foam held for longer the bamboo pattern. This was because at higher viscosity, the foam took longer time to rearrange itself. The foam response to the deformation was then slower. This caused a retardation phenomenon in the foam response to the deformation leading to an enhanced hysteretic behaviour.

However, this hysteresis was reduced with a higher-pressure ramp. Indeed, more energy per second was given to the foam to operate the change in pattern due to the increase in gas pressure. Despite the increase in viscosity which slowed down the process, the retardation was limited as more energy was given to the foam to respond to the deformation. Thus, the foam recovery after the high deformation stage was improved.

Furthermore, it was observed that coalescence (merging of two neighbour bubbles due to film thinning) occurrence was increased towards the end of the ascending ramp.

In the channel, drainage and coarsening were prevented: gravity was negligible, and the bubble distribution was monodispersed. Thus, the hysteresis observed in the channel was mainly due to the factors (surface tension, viscosity) impacting the thinning of the film between two neighbouring bubbles leading to coalescence.

In our case, the main parameter which could cause film breakage was the raise in surface tension caused by the addition of glycerol in solution. In this peculiar case, the hysteresis was primarily triggered by the change in viscosity but then enhanced by the surface tension increase.

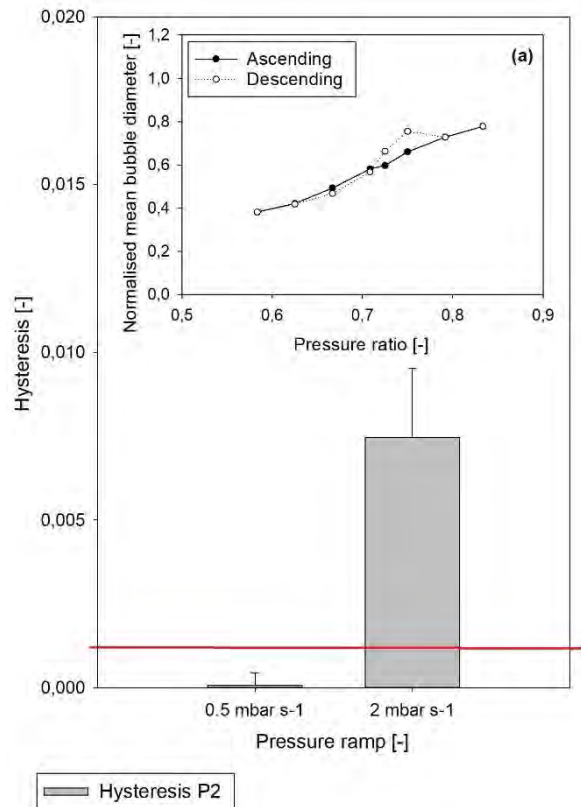


Figure 6. 11 Hysteresis evolution for 5 cmc SDS + 40% (wt.) glycerol at high pressure set (P2, grey) for both pressure ramps (0.5 & 2 mbar s⁻¹). In the inset, a typical curve for P2 at 2 mbar s⁻¹

From Figure 6. 11, at high pressure set, the foam response to the deformation was different: the hysteresis was negligible at low pressure ramp and raised up to nine times our reference value with the change in pressure ramp.

Foams by definition are yield-stress fluids (Höhler and Cohen-Addad, 2005; Cohen-Addad and Höhler, 2014). The yield stress is defined as the stress at which the foam behaviour changes from solid-like to liquid-like. Unlike the lower pressure case, here increasing the pressure ramp enhanced the hysteretic behaviour. It is believed that this difference in foam response was due to the change in pressure set. Below the yield stress, foam behaved as a solid-like (elastic) fluid and above, as a liquid-like (viscous) fluid. This change in behaviour led to different foam response to the deformation. Therefore, we considered that the foam generated presented a critical

pressure set P_c located between P_1 and P_2 at which its rheological behaviour switched from solid-like (elastic) to liquid-like (viscous). Thus, at $P_2 > P_c$, the foam was characterised by a liquid-like behaviour. Giving more energy to the system per second had a counter effect: the interface became more subjected to the deformation, and hysteresis increased with the ramp.

On the contrary, at $P_1 < P_c$, the foam behaved as a solid-like fluid. In this case, providing more energy to the system per second reduced the hysteresis by helping the system to respond faster to the deformation. Finally, the hysteretic behaviour of the foam depended also on the level of deformation applied compared to the foam apparent yield stress for the specific device employed.

This dependence was observed upon the level of deformation only in the case of the 5 cmc SDS + 40% (wt.) glycerol (C) compared to the other solutions investigated ((A), (B), (D) and (E)). This could be explained by the fact that the rise in viscosity increased the foam yield stress as more energy was required to make the foam flow at higher viscosity. Additionally, it was considered that the yield stress for the other formulations presenting lower viscosities was negligible in the range of pressure investigated.

In Figure 6. 12, a slight change of slope between our reference solution and the 40% glycerol solution was observed. The transition between the two-row and the bamboo was slightly “smoother” due to the increase in the duration of local bubble rearrangements linked to the rise in the liquid viscosity for a fixed confinement pressure. To support this explanation, the local bubble rearrangement duration was estimated via image analysis. At 40% glycerol, the transition between bamboo and two-row was estimated at 8.7 ms for 900 mbar gas pressure and 1000 mbar liquid

pressure compared to 3 ms obtained for 5 cmc SDS at 800 mbar gas pressure and 900 mbar liquid pressure. Thus, the highest the viscosity, the longest was the duration of the local bubble rearrangement.

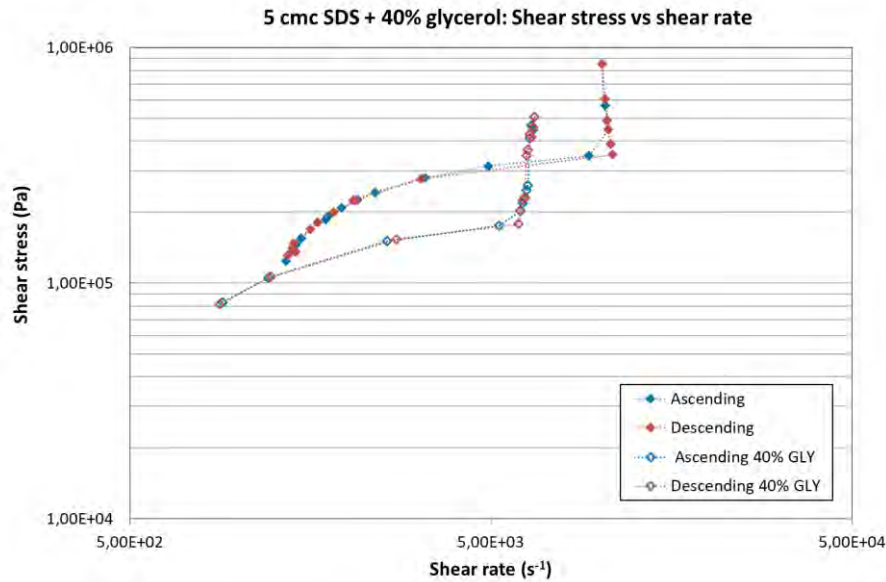


Figure 6. 12 Experimental flow curves plotting the shear stress due to the drag force versus the shear rate of the reference (filled symbols) versus the 40 % glycerol in water solution at P2 and 0.5 mbar s⁻¹ (unfilled symbols) obtained for the ascending (blue) - descending (red) pressure ramps.

However, the range of stress for a similar shear rate applied was not altered significantly. From the equation (3-2) in chapter 3 of the shear stress due to the drag force, despite the increase in viscosity, the liquid velocity decreased for the same pressure set applied which counterbalanced the effect of the viscosity.

The non-dimensional transition time of $1.9 \pm 0.4 \times 10^{-2}$ was obtained for the ascending deformation and $6.0 \pm 2.1 \times 10^{-2}$ at P1 for both pressure ramps. At P2, the ascending transition time was approximated at $4.2 \pm 1.9 \times 10^{-2}$ whereas, a descending transition time of $6.5 \pm 2.1 \times 10^{-2}$ was obtained. Consequently, at P1 and P2, the descending transition took longer than the ascending transition the retardation phenomenon leading to hysteresis.

6.2.4 Effect of surface elasticity

From past studies about foam flow in which drainage is occurring, it has been shown that the liquid velocity varies as a power law with the liquid flow rate (Pitois *et al.*, 2005; Feitosa and Durian, 2008; Stevenson and Li, 2010). The power law exponent depends upon the mobility of the surface of the bubbles. If the interface is rigid, the liquid flow between the bubbles is Poiseuille-like whereas for mobile interface the flow is plug-like. The surface mobility depends primarily on the surface-active species: surfactants such as SDS will lead to mobile surfaces whereas surfactant mixture such as SDS-DOH mixture will create rigid surfaces. In fact, DOH molecules adsorb at the gas-liquid interface reducing the surfactant mobility in the plateau borders (Karakashev and Nguyen, 2007). Indeed, when the surfaces of the plateau borders are said to be “rigid”, the molecules speed at the interface tends towards zero (Dame *et al.*, 2005). However, the surface behaviour relies also on the foaming solution viscosity and on the bubble size. Here, the continuous phase viscosity was steady throughout the whole experiment as illustrated in Figure 6. 2. A transition between the rigid and the mobile surface behaviour was noted while increasing the bulk viscosity or the bubble size (Safouane *et al.*, 2006; Gauchet *et al.*, 2015). Adding DOH to our reference solution increased the surface elasticity significantly: the results of this can be appreciated in the foam regime map where the bamboo pattern is available for a higher gas inlet pressure for fixed liquid pressure. It has been also reported by Saint-Jalmes *et al.* (2004) that for surfactant solutions above cmc the surface dilatational viscosity rose from 0.08 $\mu\text{Pa m s}$ for SDS to 1.8 $\mu\text{Pa m s}$ for SDS-DOH solutions. From Figure 6. 13, both values for the hysteresis at 0.5 and 2 mbar s^{-1}

¹ at P1 (corresponding to 600 mbar liquid inlet pressure for a gas pressure ranging from 350 to 620 mbar) can be considered negligible.

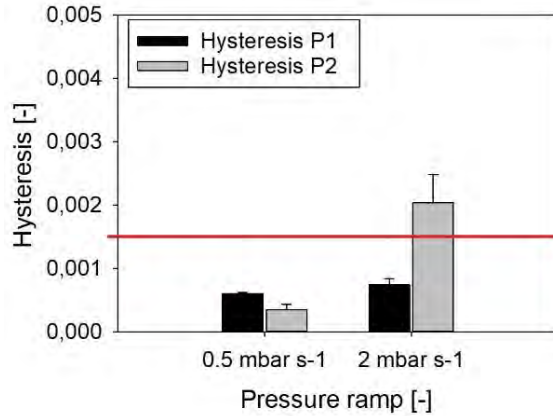


Figure 6. 13 Hysteresis evolution for 5 cmc SDS + 0.15 g L⁻¹ DOH with the pressure ramp at low (P1, black) and high (P2, grey) pressure sets.

At P2 (corresponding to 800 mbar liquid inlet pressure for a gas pressure ranging from 550 to 820 mbar), the jump in ramp caused the hysteresis to rise above the reference value although marginally. Thus, depending on the kind of deformation at the wall applied, the increase in surface elasticity could lead to a rise in hysteresis.

From the existing relationship described by Durand and Stone (2006) limited to the case of dry foams at low strain rate regime, the T1 bubble rearrangement relaxation time τ_{T1} can be expressed. The latter is described as the product of the shear rate times the ratio of surface dilatational viscosity κ over the surface tension σ such as

$$\tau_{T1} \approx \frac{\kappa}{\sigma} \times \dot{\gamma}.$$

In this specific case, for a fixed surface tension, the duration of rearrangement of the plastic events in the channel should increase due to the rise in surface elasticity. The duration of a single T1 event for a fixed pressure set (400 and 600 mbar gas and liquid pressures respectively) was estimated by image analysis. Thus, the values of 1.25 and 3.5 ms for our reference solution and for the solution containing DOH were

obtained respectively for the local bubble rearrangements as represented in Figure 6. 14.

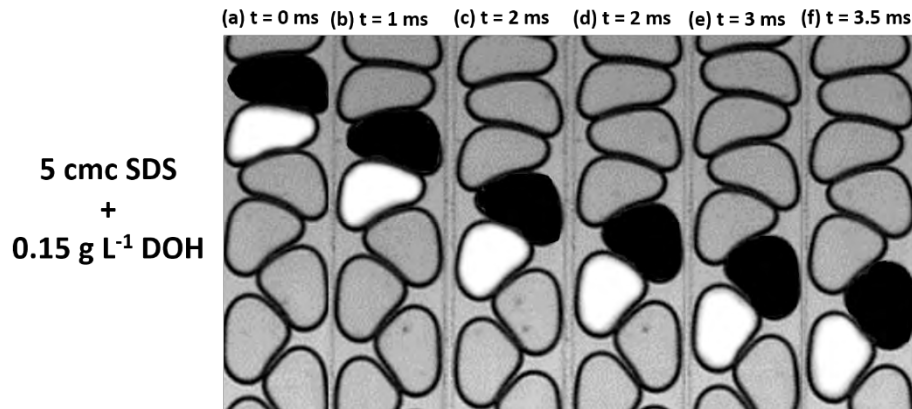


Figure 6. 14 Time lapses of the T1 bubble rearrangements for a fixed pressure set ($P_{\text{gas}} = 400$ mbar, $P_{\text{liq}} = 600$ mbar) for 5 cmc SDS + 0.15 g L^{-1} DOH from (a-f).

Above a critical level of deformation, foam undergoes a topological rearrangement between neighbouring bubbles. During this rearrangement, the foam stored elastic energy until it reached saturation. This saturation is the reason of the existence of a yield stress (Marze *et al.*, 2008). In our case, during the ascending ramp, it was considered that the elastic energy storage increased with the ascending deformation until complete transition between two-row to bamboo pattern. Then, a steady plateau of high deformation at the wall was set for 60 seconds and then the descending ramp started. It was observed experimentally that the hysteresis occurred either at the start of the high deformation plateau or following this step, at the start of the descending ramp.

It was considered that the system couldn't relax properly if it was submitted to an increasing deformation. The system was not able to relax this excess of elastic energy during the ascending ramp as the deformation increased. The excess of elastic energy caused a local strain to build up. This accumulation of local strain triggered the hysteresis and the retardation observed in the channel. By extending

the duration of the local rearrangements, the amount of total elastic energy stored was heightened and so was the hysteresis. A retardation phenomenon was occurring due to the excess of elastic energy stored. By increasing the pressure set, the deformation at the wall was augmented.

Nevertheless, the bubble rearrangement relaxation time τ_{T1} is expressed as the product of the shear rate times the ratio of surface dilatational viscosity κ over the surface tension σ . Thereby, by increasing the deformation at the wall and the shear rate applied, τ_{T1} increased linearly with the deformation. So, at higher deformation/pressure set, the amount of energy stored, and the hysteresis were enhanced. Similarly, the rise in pressure ramp (i.e., more energy per second to be stored) caused an increase of the hysteresis.

Furthermore, it was shown by Kabla and Debrégeas (2003) that at higher shear rate compared to the inverse of the T1 relaxation time, a shear-banding developed through a self-amplification process. Indeed, bubble rearrangement locally weakened the foam structure by increasing its “frozen” stress disorder which imposed an additional mechanical constraint to the foam. Thus, at high shear rates compared to the inverse of the relaxation time, a hysteretic behaviour linked to the bubble rearrangement dynamics was likely to occur.

The effect of DOH on the transition between the two-row to the bamboo was highlighted by comparing the experimental flow curves plotting the shear stress versus the shear rate in Figure 6. 15.

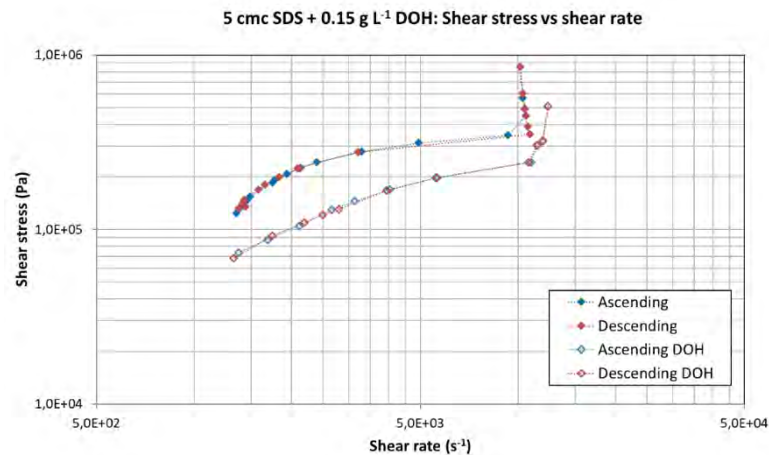


Figure 6. 15 Experimental flow curves plotting the shear stress due to the drag force versus the shear rate of the reference (filled symbols) versus the 5 cmc SDS + 0.15 g L⁻¹ DOH in water solution at P2 and 0.5 mbar s⁻¹ (unfilled symbols) obtained for the ascending and descending pressure ramps.

Indeed, by adding DOH in solution, the transition from the two-row to the bamboo became almost linear compared to the reference. The increase of the dilatational surface viscosity enhanced the duration of local rearrangements for a fixed surface tension as demonstrated in Figure 6. 14. Thus, the transition was much “smoother” compared to the initial transition for the reference. The same trend was observed for the various ramps and pressure sets applied.

At P1, non-dimensional transition time lasted $73.0 \pm 0.9 \times 10^{-2}$ for both pressure ramps. No hysteresis was occurring, therefore, the foam structure evolution between the ascending and the descending ramp was very symmetrical. At P2, the transition time was approximated at $50.0 \pm 1.5 \times 10^{-2}$ both at 0.5 and 2 mbar s⁻¹ in the ascending ramp and at $65.0 \pm 0.9 \times 10^{-2}$ in the descending ramp. This discrepancy between the ascending and descending ramp resided in the expression of the hysteretic behaviour enhanced by the surface elasticity. Indeed, the increase in surface elasticity enhanced the amount of elastic energy stored by the system. Thus,

this excess of elastic energy caused the transition time in the descending ramp to last longer than in the ascending ramp, emphasizing a hysteretic behaviour.

6.2.5 Effect of shear-thinning property

Xanthan gum (XG) is a water-soluble polysaccharide which is commonly used in the food industry as a thickener and in other fields such as EOR as an additive to enhance foam stability in porous media. Pu *et al.* (2017) depicted the effect of different polymer-surfactant mixtures on foam stability and properties. Two main stabilising effects of polymer-surfactant foam were reported: it could retard the liquid drainage of the liquid films and/or enhance the adsorption behaviour of film surface.

Indeed, the addition of XG led to an increase in viscosity (see Figure 6. 2) which then reduced the liquid drainage. In Pu *et al.* (2017) work, the continuous phase, an aqueous solution of XG and Lauramidopropyl Hydroxy SulfoBetaine (LHSB, zwitteronic surfactant), showed a shear-thinning behaviour which was expressed by a decrease in viscosity from 50 to 8 mPa s⁻¹ for a shear rate ramp from 10 to 150 s⁻¹.

Here, it was considered that the thickening effect of the polymer-surfactant mixture was limited due to the low concentration of polymer in solution (0.01% wt. compared to 0.2 % wt. in (Pu *et al.*, 2017)) which resulted in a much lower range of viscosity varying from 1.5 to 1 mPa s⁻¹ (see Figure 6. 2). Furthermore, it was rated that the polymer-surfactant synergetic effect was not effective in this case because the surface tension did not decrease (Pu *et al.*, 2017).

On the contrary, it was observed a rise in surface tension (see Table 6. 1) due to the adsorption of SDS on the polymer chain (Nedjhioui *et al.*, 2009). This increase in surface tension could lead partially to an increase in the retardation effect as seen for

the SDS – glycerol mixture. Reversely, the hysteresis was almost negligible in most cases as seen in Figure 6. 16.

At P1 (corresponding to 400 mbar liquid inlet pressure for a gas pressure ranging from 250 to 420 mbar), the hysteresis was almost negligible at 0.5 and 2 mbar s⁻¹.

At P2 (corresponding to 800 mbar liquid inlet pressure for a gas pressure ranging from 700 to 820 mbar), both pressure ramps presented a hysteresis. Because of the range of viscosity investigated, it was considered that the thickening/shear-thinning effect of XG was limited in our case. However, two different foam responses to the increase in pressure ramp could be distinguished. These two responses could be explained by the expression of the thickening/shear-thinning behaviour of the continuous phase which relied on the deformation applied at the interface.

At lower pressure set (P1), the thickener nature and the consecutive shear-thinning property of XG was effective and the continuous phase viscosity was at first enhanced in the range of deformation applied. Then, unlike the 20% wt. glycerol case, the viscosity decreased with an increasing deformation at the wall. Thereby, the resulting hysteresis became almost negligible.

On the contrary, at higher pressure set (P2), the shear-thinning property of the continuous phase, although still present, was small compared to the high deformation applied. Thus, the hysteresis at P2 was no longer negligible and decreased with the pressure ramp. At P2, the initial viscosity was lower than the initial P1 viscosity as the foam itself was shear-thinning. The continuous phase shear-thinning property acted with a similar magnitude on a lower initial viscosity. Thus, the gas-liquid interface becoming more unstable due to the rise in surface tension, faced an additional

decrease in viscosity which promoted the thin film breakage, the consecutive bubble coalescence and the resulting hysteresis.

At higher pressure ramp, the hysteresis was reduced because the foam was given more energy per second to react to the deformation. To support this hypothesis, the range of apparent shear rate applied to the bubble was estimated from the average bubble velocity, measured using the application PIVlab in Matlab (William Thielicke, 2014), divided by the film thickness estimated via image analysis.

At low pressure set (P1), the estimated shear rate was ranging from 188 to 1869 s^{-1} with a bubble velocity varying from 0.017 to 0.043 m s^{-1} and a liquid thickness from $91 \pm 19 \mu\text{m}$ to $23 \pm 3 \mu\text{m}$. At higher pressure set (P2), the apparent shear rate was ranging from 2277 to 6592 s^{-1} for a bubble velocity ranging from 0.11 to 0.13 m s^{-1} and a film liquid thickness ranging between $48 \pm 2 \mu\text{m}$ to $20 \pm 3 \mu\text{m}$. From Figure 6. 2, which represents the continuous phase viscosity evolution for a range of shear rate from 5 to 100 s^{-1} , a decrease in viscosity of about 70% was measured, caused by the increase in shear rate which then plateaued at 100 s^{-1} .

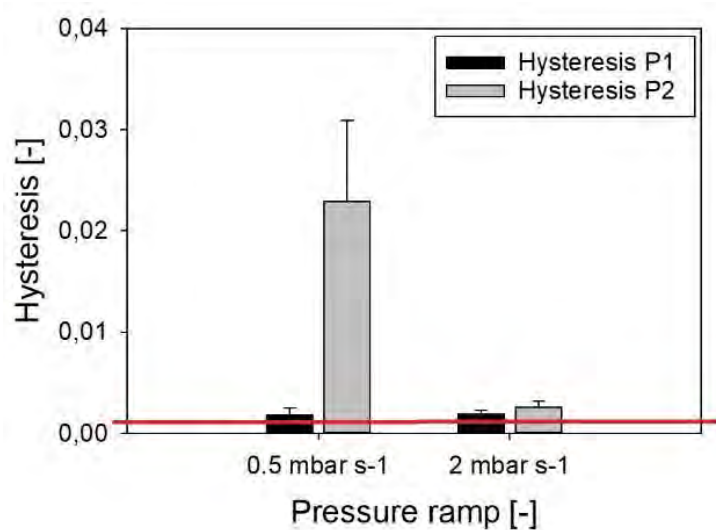


Figure 6. 16 Hysteresis evolution for 5 cmc SDS + 0.01 g L⁻¹ XG + 5 % (wt.) glycerol at low (P1, black) and high (P2, grey) pressure sets for both pressure ramps (0.5 & 2 mbar s⁻¹).

Furthermore, the effect of the polymer-surfactant interaction on the hysteresis needs also to be kept in mind. In fact, Pu *et al.* (2017) demonstrated that the combination of XG and LHSB was generating liquid film with a high interfacial viscoelastic modulus. Thus, XG molecules combined with SDS may have also increased the interfacial viscoelastic modulus. This effect could be a subsidiary cause of the reduction of hysteresis at higher deformation despite the rise in surface tension.

In Figure 6. 17, the effect of the XG on the transition observed from the two-row to the bamboo pattern is represented in the graph plotting the shear stress due to the drag force versus the apparent shear rate and compared to our reference solution for the P2 pressure set at 0.5 mbar s^{-1} pressure ramp. The slope obtained with XG was almost as linear as the DOH case. The shear-thinning property of XG permitted to generate a gradual transition from the two-row to the bamboo pattern. Indeed, in the previous case, the transition between the two-row to the bamboo was marked by an oscillating or flashing transition whereas in this case, the front was gradually advancing towards the complete bamboo transition. Due to XG, the foam viscosity decreased for an increasing shear rate, thus the bamboo pattern was submitted to higher shear rate for a similar pressure set applied because the bubble velocity had augmented. Then, the resulting stress was lesser for XG than for the reference due to less dissipation provoked by the decrease in viscosity. Finally, the increase of interfacial viscoelastic modulus could not be verified experimentally, but this fact could explain the smoothing in the transition from the two-row to the bamboo pattern despite the rise in surface tension compared to our reference.

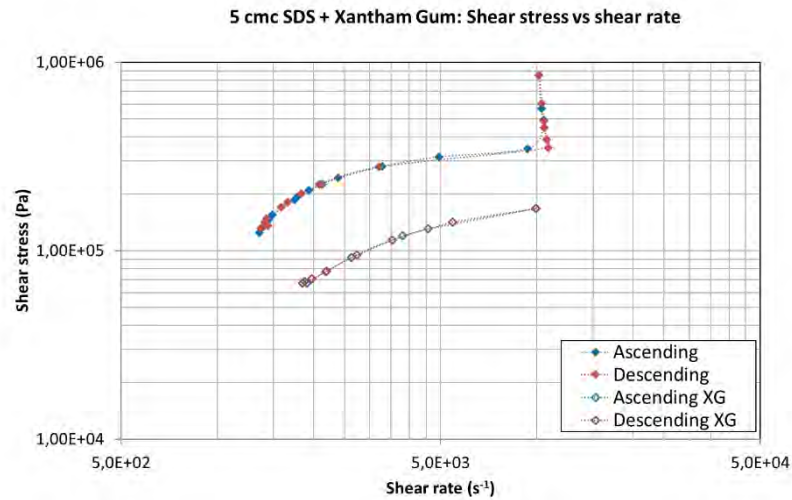


Figure 6. 17 Experimental flow curves plotting the shear stress due to the drag force versus the shear rate of the 5 cmc SDS (filled symbols) versus the 5 cmc SDS + XG solution at P2 & 0.5 mbar s⁻¹ (unfilled symbols) obtained for the ascending (blue) -descending (red) pressure ramps.

The local rearrangement duration could be estimated at 5.1 ms at 400 mbar gas pressure and 400 mbar liquid pressure. Thereby, the local transition from two-row to bamboo was slower for XG at low deformation compared to the reference or the 20% glycerol solution. These results could be explained by the rise in viscosity at low deformation due to the thickening property of XG.

Regarding the bamboo/two-row transition, the non-dimensional transition time was estimated at $56.0 \pm 2.8 \times 10^{-2}$ at P1 for both pressure ramps, and at $77.0 \pm 1.9 \times 10^{-2}$ at P2 for both pressure ramps.

6.3 Conclusions

In this work, a novel approach to evaluate foam thixotropy in a microchannel was established. The foam response to a gradual deformation at the wall based on the transition between the two-row to the bamboo pattern was studied. The impact of different parameters from the foaming liquid viscosity, surface elasticity to shear-thinning property were assessed on the foam recovery properties.

Throughout the different solutions investigated, the following observations were made:

- (i) A viscosity increase in the foaming solution for a constant surface tension led to a retardation effect causing a hysteresis both at low and high ranges of deformation.
- (ii) An increase of the foaming liquid surface tension emphasized the hysteresis and the resulting retardation effect depending on the level of deformation applied.
- (iii) A higher surface elasticity created a smaller but non-negligible hysteresis due to an excess in elastic energy caused by the increase of the duration of the bubble rearrangements. The effect was highlighted in the experimental flow curves extracted from the hysteresis graph. Indeed, the increase in the duration of rearrangements smoothen the transition between the two patterns.
- (iii) The thickening/shear-thinning behaviour of the continuous phase impacted differently the foam hysteresis depending on the level of the deformation applied. At low deformation (i.e., low pressure, P1), the thickener nature of XG at low deformation was counterbalanced by the shear-thinning effect leading to a negligible hysteresis. At high deformation (high pressure, P2), the shear-thinning effect was

small compared to the instability arising from the rise in surface tension and thus the hysteresis was no longer negligible.

The next chapter aimed to elucidate which kind of elasticity (surface or bulk) influence the most foam recovery in a microchannel. To do so, a new system was investigated by combining a new surfactant (TTAB) with dodecanol and/or PEO at various concentrations to vary the level of surface and bulk elasticity respectively.

6.4 List of references

- Asnacios, R. H. and S. C.-A. and A. (1999) 'Rheological memory effect in aqueous foam', *EPL (Europhysics Letters)*, 48(1), p. 93. Available at: <http://stacks.iop.org/0295-5075/48/i=1/a=093>.
- Bekkour, K. and Scrivener, O. (1998) 'Time-Dependent and Flow Properties of Foams', *Mechanics of Time-Dependent Materials*, 2, pp. 171–193. doi: 10.1023/a:1009841625668 LB - Bekkour1998.
- Cohen-Addad, S. and Höhler, R. (2014) 'Rheology of foams and highly concentrated emulsions', *Current Opinion in Colloid & Interface Science*, 19(6), pp. 536–548. doi: <https://doi.org/10.1016/j.cocis.2014.11.003>.
- Cohen-Addad, S., Höhler, R. and Pitois, O. (2013) 'Flow in Foams and Flowing Foams', *Annual Review of Fluid Mechanics*, 45, p. 241. Available at: <http://dx.doi.org/10.1146/annurev-fluid-011212-140634>.
- Dame, C. *et al.* (2005) 'Relations between physicochemical properties and instability of decontamination foams', *Colloids and Surfaces A: Physicochemical and Engineering Aspects*, 263, pp. 210–218. doi: <https://doi.org/10.1016/j.colsurfa.2004.12.053>.
- Dennin, M. (2004) 'Statistics of bubble rearrangements in a slowly sheared two-dimensional foam', *Phys. Rev. E. American Physical Society*, 70(4), p. 41406. doi: 10.1103/PhysRevE.70.041406.
- Durand, M. and Stone, H. A. (2006) 'Relaxation Time of the Topological T1 Process in a Two-Dimensional Foam', *Physical Review Letters*, 97, p. 226101. Available at: <https://link.aps.org/doi/10.1103/PhysRevLett.97.226101>.
- Feitosa, K. and Durian, D. J. (2008) 'Gas and liquid transport in steady-state aqueous foam', *The European Physical Journal E*, 26, pp. 309–316. doi: 10.1140/epje/i2007-10329-6 LB - Feitosa2008.
- Galindo-Rosales, F. J., Alves, M. A. and Oliveira, M. S. N. (2013) 'Microdevices for extensional rheometry of low viscosity elastic liquids: a review', *Microfluidics and Nanofluidics*, 14, pp. 1–19. doi: 10.1007/s10404-012-1028-1 LB - Galindo-Rosales2013.
- Garstecki, P. and Whitesides, G. M. (2006) 'Flowing Crystals: Nonequilibrium Structure of Foam', *Physical Review Letters*, 97, p. 24503. Available at: <https://link.aps.org/doi/10.1103/PhysRevLett.97.024503>.
- Gauchet, S., Durand, M. and Langevin, D. (2015) 'Foam drainage. Possible influence of a non-newtonian surface shear viscosity', *Journal of Colloid and Interface Science*, 449, pp. 373–376. doi: <https://doi.org/10.1016/j.jcis.2014.12.060>.
- Guillot, P. *et al.* (2006) 'Viscosimeter on a Microfluidic Chip', *Langmuir*, 22, pp. 6438–6445. doi: 10.1021/la060131z.
- Höhler, R. and Cohen-Addad, S. (2005) 'Rheology of liquid foam', *Journal of Physics: Condensed Matter*, 17, p. R1041. Available at: <http://stacks.iop.org/0953-8984/17/i=41/a=R01>.
- Kabla, A. and Debrégeas, G. (2003) 'Local stress relaxation and shear banding in a

dry foam under shear', *Physical Review Letters*, 90(25 1), pp. 2583031–2583034. Available at: <https://www.scopus.com/inward/record.uri?eid=2-s2.0-0043269803&partnerID=40&md5=48e8806b361a5f806afda87ad904d11a>.

Karakashev, S. I. and Nguyen, A. V (2007) 'Effect of sodium dodecyl sulphate and dodecanol mixtures on foam film drainage: Examining influence of surface rheology and intermolecular forces', *Colloids and Surfaces A: Physicochemical and Engineering Aspects*, 293, pp. 229–240. doi: <https://doi.org/10.1016/j.colsurfa.2006.07.047>.

Koser, A. E. *et al.* (2013) 'Measuring material relaxation and creep recovery in a microfluidic device', *Lab on a Chip*, 13, pp. 1850–1853. doi: 10.1039/c3lc41379a.

Larson, R. G. (2015) 'Constitutive equations for thixotropic fluids', *Journal of Rheology*, 59, pp. 595–611. doi: 10.1122/1.4913584.

Lorenceanu, E. *et al.* (2009) 'Permeability of aqueous foams', *The European Physical Journal E*, 28(3), pp. 293–304. doi: 10.1140/epje/i2008-10411-7.

Marze, S., Langevin, D., Saint-Jalmes, A. (2008) 'Aqueous foam slip and shear regimes determined by rheometry and multiple light scattering', *Journal of Rheology*, 52, p. 1091. Available at: <http://dx.doi.org/10.1122/1.2952510>.

Le Merrer, M., Cohen-Addad, S. and Hoehler, R. C. N.-01239411 (2013) 'Duration of bubble rearrangements in a coarsening foam probed by time-resolved diffusing-wave spectroscopy: Impact of interfacial rigidity', *Physical Review E: Statistical, Nonlinear, and Soft Matter Physics*. Institut des Nanosciences de Paris (INSP) Laboratoire de Physique des Matériaux Divisés et des Interfaces (LPMDI), 88, p. 22303. doi: 10.1103/PhysRevE.88.022303.

Le Merrer, M., Cohen-Addad, S. and Höhler, R. (2012) 'Bubble Rearrangement Duration in Foams near the Jamming Point', *Physical Review Letters*, 108. Available at: <http://dx.doi.org/10.1103/PhysRevLett.108.188301>.

Mewis, J. (1979) 'Thixotropy - a general review', *Journal of Non-Newtonian Fluid Mechanics*, 6, pp. 1–20. doi: [https://doi.org/10.1016/0377-0257\(79\)87001-9](https://doi.org/10.1016/0377-0257(79)87001-9).

Mewis, J. and Wagner, N. J. (2009) 'Thixotropy', *Advances in Colloid and Interface Science*, 147–148, pp. 214–227. doi: <https://doi.org/10.1016/j.cis.2008.09.005>.

Mezger, T. G. (2014) *The Rheology Handbook, 4th Edition For users of rotational and oscillatory rheometers*. 4th Editio. Edited by European Coating Tech Files. Hanover, Germany: Vincents Network.

Miquelim, J. N. and Da Silva Lannes, S. C. (2009) 'Egg albumin and guar gum influence on foam thixotropy', *Journal of Texture Studies*, 40, pp. 623–636. doi: 10.1111/j.1745-4603.2009.00201.x.

Nedjhioui, M. *et al.* (2009) 'Investigation of combined effects of xanthan gum, sodium dodecyl sulphate, and salt on some physicochemical properties of their mixtures using a response surface method', *Journal of Dispersion Science and Technology*, 30, pp. 1333–1341. doi: 10.1080/01932690902735538.

Pipe, C. J. and McKinley, G. H. (2009) 'Microfluidic rheometry', *Mechanics Research Communications*, 36, pp. 110–120. doi: <https://doi.org/10.1016/j.mechrescom.2008.08.009>.

Pitois, O., Fritz, C. and Vignes-Adler, M. (2005) 'Liquid drainage through aqueous

- foam: study of the flow on the bubble scale', *Journal of Colloid and Interface Science*, 282, pp. 458–465. doi: <https://doi.org/10.1016/j.jcis.2004.08.187>.
- Pu, W. F. *et al.* (2017) 'Experimental investigation of viscoelastic polymers for stabilizing foam', *Journal of Industrial and Engineering Chemistry*, 47, pp. 360–367. doi: 10.1016/j.jiec.2016.12.006.
- Ruiz, C. C., Díaz-López, L. and Aguiar, J. (2008) 'Micellization of Sodium Dodecyl Sulfate in Glycerol Aqueous Mixtures', *Journal of Dispersion Science and Technology*, 29, pp. 266–273. doi: 10.1080/01932690701707571.
- Safouane, M. *et al.* (2006) 'Viscosity effects in foam drainage: Newtonian and non-newtonian foaming fluids', *European Physical Journal E*, 19, pp. 195–202. doi: 10.1140/epje/e2006-00025-4.
- Saint-Jalmes, A. (2006) 'Physical chemistry in foam drainage and coarsening', *Soft Matter*, 2, pp. 836–849. doi: 10.1039/B606780H.
- Saint-Jalmes, A., Zhang, Y. and Langevin, D. (2004) 'Quantitative description of foam drainage: Transitions with surface mobility', *The European Physical Journal E*, 15, pp. 53–60. doi: 10.1140/epje/i2004-10036-x LB - Saint-Jalmes2004.
- Saint-Jalmes, S. M. R. M. G. A. (2009) 'Oscillatory rheology of aqueous foams: surfactant, liquid fraction, experimental protocol and aging effects', *Soft Matter*, 5, p. 1937. Available at: <http://dx.doi.org/10.1039/b817543h>.
- de Souza Mendes, P. R. (2009) 'Modeling the thixotropic behavior of structured fluids', *Journal of Non-Newtonian Fluid Mechanics*, 164, pp. 66–75. doi: <https://doi.org/10.1016/j.jnnfm.2009.08.005>.
- Stevenson, P. and Li, X. (2010) 'A viscous–inertial model of foam drainage', *Chemical Engineering Research and Design*, 88, pp. 928–935. doi: <http://doi.org/10.1016/j.cherd.2010.01.014>.
- Weaire, D. and Phelan, R. (1996) 'The physics of foam', *Journal of Physics: Condensed Matter*, 8, p. 9519. Available at: <http://stacks.iop.org/0953-8984/8/i=47/a=055>.
- William Thielicke, E. J. S. (2014) 'PIVlab – Towards User-friendly, Affordable and Accurate Digital Particle Image Velocimetry in MATLAB', *Journal of Open Research Software*, 2(1). doi: <http://doi.org/10.5334/jors.bl>.

CHAPTER 7

STUDY OF THE EFFECT OF BULK VERSUS

SURFACE ELASTICITY ON FOAM

HYSTERESIS IN A MICROCHANNEL

7.1 Introduction

One of the key parameters influencing foam stability is the foaming liquid rheological properties (Safouane *et al.*, 2001; Saint-Jalmes and Langevin, 2002; Wang *et al.*, 2016). Foam stability is intrinsically related to the thin liquid film stability (Scheid *et al.*, 2010). Therefore, several dimensions need to be considered to determine the parameters influencing foam stability. Thus, both 2D and 3D rheological foaming liquid properties need to be considered for the study of the impact of elasticity on foam recovery properties after a gradual deformation.

A small body of literature addressed the impact of bulk elasticity or the use of Boger fluids (constant viscosity elastic fluid (Boger, 1977)) as foaming liquid on the bubble generation via microfluidics (Fu *et al.*, 2011, 2012; Wang *et al.*, 2015; Kim *et al.*, 2017).

Fu *et al.* (2011) analysed the bubble formation, flow patterns and bubble break-up mechanism in Boger fluids in a microfluidic T-junction. It was found that the increase in bubble size evolved non-linearly with the gas-liquid flow rate ratio and decreased with the concentration of polymer in solution. Later, Fu *et al.* (2015) studied the bubble coalescence mechanisms in dilute polymer solutions in a microfluidic expansion device.

Bulk elasticity is related to the elastic behaviour (opposed to the viscous behaviour) which is used to describe a viscoelastic material. Therefore, bulk elasticity is linked to the property of a fluid while being deformed to store deformation energy, and to return this energy to its surrounding once the deformation has ceased (Mezger, 2014). The recovery property after deformation is linked to the proportion of

deformation energy which was stored and made available to be given back to the surrounding. Thus, bulk elasticity is expected to impact significantly foam hysteretic behaviour.

Bulk elasticity can be tuned by adding various polymers in solution such as Poly(ethylene oxide) (PEO) which will modify the solution elongational viscosity and thus the bulk elasticity. This additional resistance to normal stresses is associated to the deformation of the polymer chains by the flow and also to the level and speed of deformation (Safouane *et al.*, 2001). Interestingly, Safouane *et al.* (2001) identified two rheological behaviours depending on the PEO molecular weight (Mw) on the foam drainage dynamics :

- For low Mw, the front drainage velocity evolved similarly to the Newtonian glycerol-water mixture.
- For high Mw, the drainage velocities increased compared to the viscosity equivalent glycerol-water mixture.

Its 2D counterpart termed surface elasticity describes the interfacial viscoelasticity which represents the response of a surface to a shearing or dilatation/compression. Surface elasticity was found to play an important role in foam stability (Pitois *et al.*, 2005; Feitosa and Durian, 2008; Stevenson and Li, 2010). Indeed, the surface elasticity impacts the flow of liquid through the plateau borders and thus the nature (rigid or mobile) of the gas-liquid interface. If the interface is rigid, the liquid flow in the PB's is Poiseuille-like whereas for mobile interface the flow is plug-like. Interfacial viscoelasticity relies on the surfactant concentration and solubility, but also on the deformation timescale at which the interface is submitted to. Interfacial viscoelasticity

can be adjusted by introducing insoluble surfactants to a system such as dodecanol (DOH) (Karakashev and Nguyen, 2007). For instance, DOH molecules by adsorbing at the gas-liquid interface, can reduce the surfactant mobility in the plateau borders.

In the previous chapter, an anionic surfactant, Sodium Dodecyl Sulfate (SDS) was employed to introduce a new approach to investigate foam hysteresis in a microchannel. A preliminary study was carried out on the effect of three parameters: the viscosity, the surface elasticity and the shear-thinning property. Based on the previous work presented in Chapter 6, the previous study was expanded by determining the effect of two kinds of elasticity on the foam recovery properties evaluated by microfluidics.

Foams were generated by co-injection of air and various solutions made of 5 times the critical micellar concentration of tetradecyltrimethylammonium bromide (TTAB) through a microfluidic flow-focusing device.

TTAB is selected to investigate the effect of two kinds of elasticity (surface and bulk elasticity) on foam thixotropy based on the method introduced in chapter 6. Indeed, TTAB unlike SDS, do not form complexes with PEO. Indeed, Safouane *et al.* (2006) showed that the combination of SDS and PEO can lead to complexation which will change the properties of the resulting solution.

Firstly, the effect of surface elasticity on the foam recovery properties in the channel was identified by adding DOH to our reference solution at two different concentrations (0.05 and 0.2 g L⁻¹). Subsequently, poly(ethylene oxide) (PEO) was added to a solution based on 5 cmc TTAB + 0.05 g L⁻¹ DOH solution to increase the

bulk elasticity of the continuous phase. Thereby, the effects of PEO concentration and molecular weight (Mw) on foam hysteresis were analysed.

7.2 Results and discussions

The technique employed here was introduced in chapter 6 to study the impact of various parameters on the 2D foam properties in a flow-focusing microfluidics device. The 2D foam was generated in situ and studied in the expansion channel by controlling the gas and liquid pressures. The foam was continuously renewed, and the foam pattern was very accurately controlled. All the solutions investigated here were analysed prior to experimentation by tensiometry and rheometry. The dynamic surface tension was checked via the Bubble Pressure Analyser (BPA-1 from SINTERFACE) instrument for each solution. The results are summarised in Figure 7.

1.

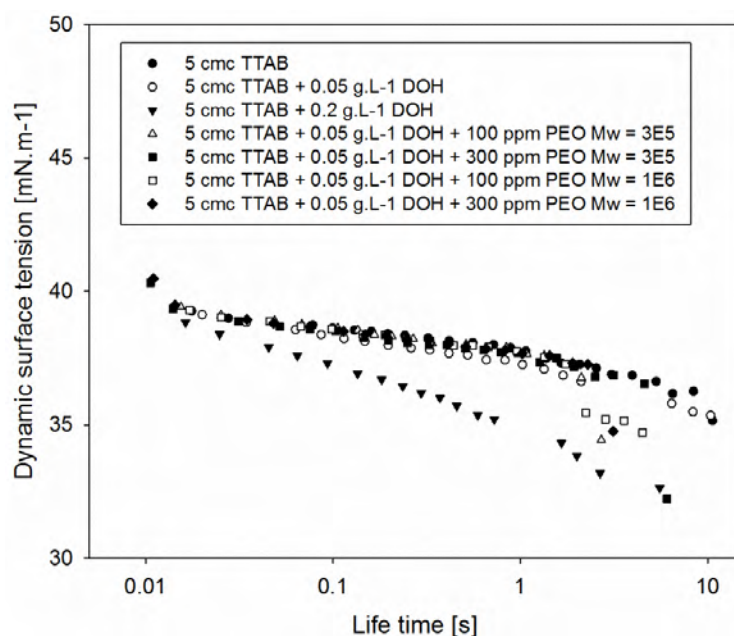


Figure 7. 1 Dynamic surface tension measurements for various solutions made of 5 cmc TTAB.

All the solutions reached their equilibrium surface tension at about 1s bubble life time except for 0.2 g L⁻¹ DOH. Most solutions surface tensions plateaued rapidly at about 37 mN m⁻¹. At the lowest DOH concentration, the surface tension remained the same. However, at 0.2 g L⁻¹ DOH, the surface tension kept decreasing until 10s without plateauing. This change in surfactant dynamic could be due to the intercalation of DOH molecules acting as insoluble surfactants and enhancing the adsorption of DOH to the gas-liquid interface. In this chapter SDS could not be employed because it could cause complexation with PEO (Cabane and Duplessix, 1982; Witte and Engberts, 1987; Brown *et al.*, 1992). Cabane and Duplessix (1982) explained that the association between a water-soluble polymer (PEO) and small surfactant molecules (SDS) in water was driven by the balance between three main forces: the attraction or repulsion forces between the macromolecule monomers when they are dissolved in water (volume of the polymer structure), the attraction force between the surfactant molecules that tend to aggregate to form micelles and the attraction force between the surfactant molecules and the monomers in solution. If water is a good solvent for the polymer and micelles are forming, an attractive and weak force between the surfactant molecules and the monomers is occurring, leading to the association/complexation of non-ionic polymers (PEO) with ionic surfactant molecules (SDS).

The solutions viscosities were measured via a DHR-1 rheometer (TA) via in a cone-plate geometry (60 mm diameter, 2° truncation angle) and reported in Figure 7. 2:

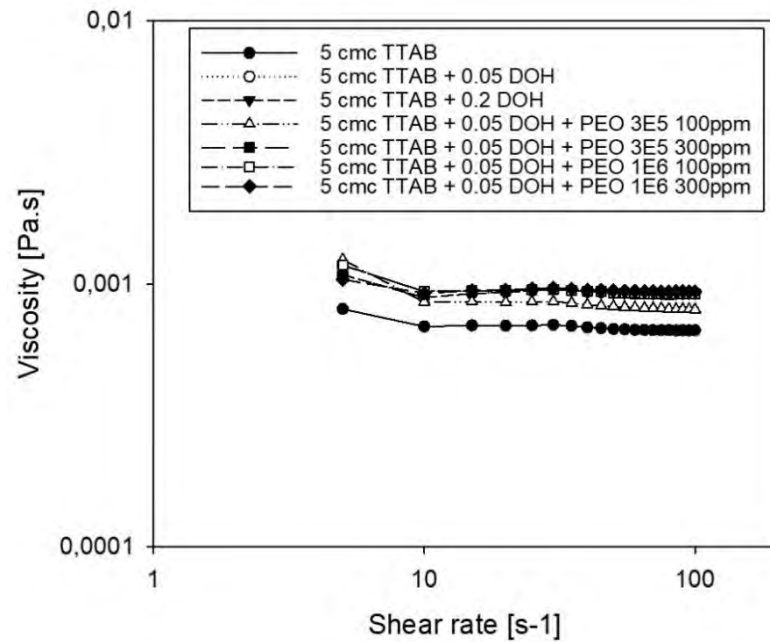


Figure 7. 2 Rheological properties of the solutions: flow curves plotting the viscosity versus the shear rate.

All the solutions presented a steady viscosity throughout the whole range of shear rate varying from 5 to 100 s^{-1} . Therefore, all the solutions presented a Newtonian behaviour with a viscosity closed to 1 mPa s at 25 °C.

The range of shear rates investigated here was not chosen to mimic the actual range of shear rate at which the foam is submitted to during the process of fabrication or generation. Indeed, the range of shear rate is expected to be much greater than these values.

From these preliminary characterisation steps, the investigation began with the building of the foam regime map for each formulation to identify the regions where the bamboo and the two-row patterns were visible. The foam recovery properties were studied via a three-step test in which an ascending and descending pressure ramps were applied. The recovery property was evaluated by comparing the foam pattern evolution over the ascending/descending deformation cycle.

Based on the previous test method, the highest deformation at the wall was obtained in the bamboo pattern whereas the low deformation stage was represented by the two-row pattern. These patterns were chosen due to their recurrence and steadiness in the foam regime map and in the various formulations investigated. The ascending/descending deformation was thus built based on the transition between the two patterns.

To analyse the effect of the various additives studied, this evaluation was based on the comparison of the results to a reference showing no sign of hysteresis throughout the deformation cycle.

7.2.1 Reference solution: 5 cmc TTAB

The solution made of five times the cmc of TTAB was employed as reference solution to study the effect of surface elasticity throughout this section. Firstly, we generated a foam regime map to identify the regions where the hysteretic behaviour of the foam could be studied as illustrated in Figure 7. 3. Two regions of low (P1) and high-pressure (P2) sets were chosen represented by two red arrows in Figure 7. 3. For each of them, two pressure ramps were studied, namely 0.5 and 2 mbar s⁻¹.

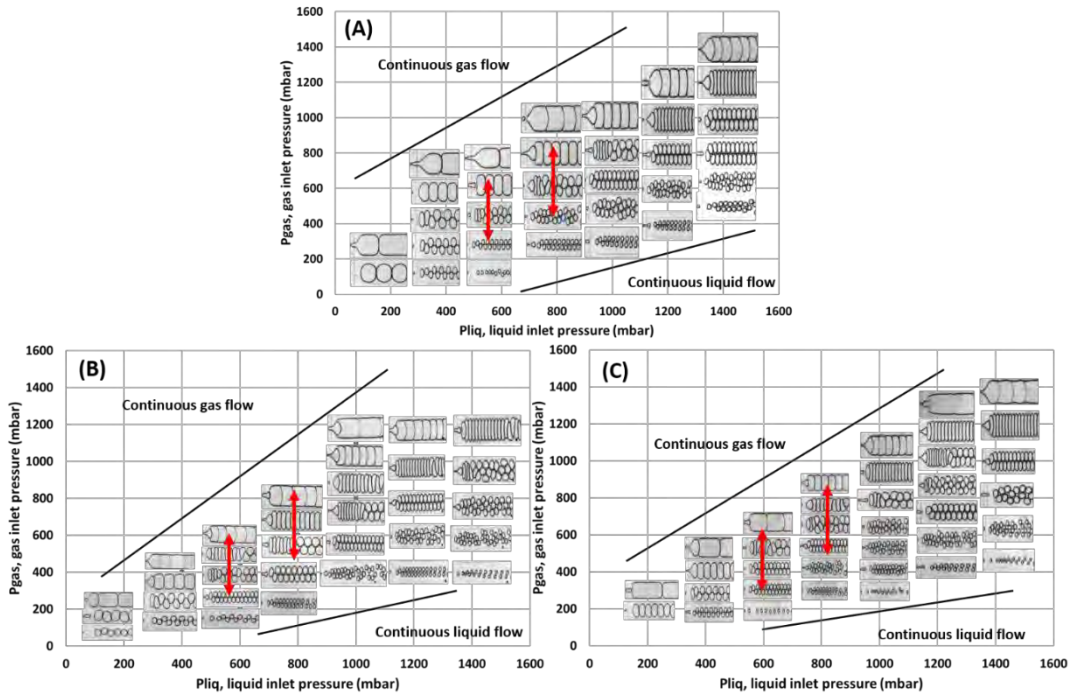


Figure 7. 3 Foam regime map plotting the gas inlet pressure (P_{gas}) versus the liquid inlet pressure (P_{liq}) for three solutions: (A) 5 cmc TTAB, (B) 5 cmc TTAB + 0.05 g L⁻¹ and (C) 5 cmc TTAB + 0.2 g L⁻¹.

From FRM (A), two regions of deformation were selected so that the first pressure set (P1) varying from 300 to 650 mbar air pressure for a fixed 600 mbar liquid pressure was defined as low deformation and the second one (P2) ranging from 450 to 850 mbar air pressure for a constant 800 mbar liquid pressure was considered as high deformation at the wall.

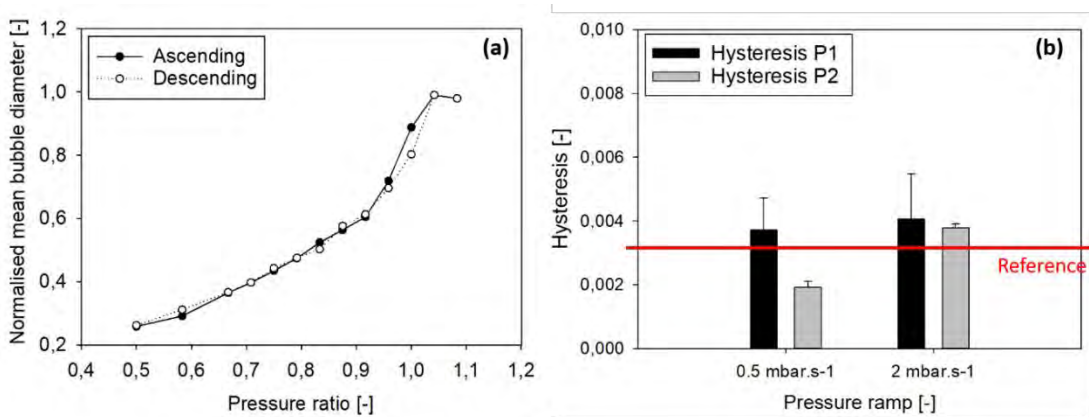


Figure 7. 4 Graph (a) introduces hysteresis evolution in an ascending (continuous black line – black dots) and descending (dotted black line – empty black dots) pressure ramps fixed at 0.5 mbar s⁻¹ for a low

pressure set (P1) from 300 to 650 mbar air pressure for a constant liquid pressure of 600 mbar. Histogram (b) summarises the hysteresis evolution for 5 cmc TTAB for two pressure sets, low pressure set (P1, black) & high pressure set (P2, grey) for two pressure ramps (0.5 and 2 mbar s⁻¹). The red line represents the average value of hysteresis to describe negligible hysteresis.

It was found that for all the different experimental set-ups (pressure set & ramp) investigated, there was no sign of hysteresis as illustrated in Figure 7. 4 (a) depicting the case of low pressure set for a pressure ramp of 0.5 mbar s⁻¹. Therefore, the reference solution made of 5 cmc TTAB presented no significant hysteresis between the ascending and the descending curves for all the various configurations. The hysteresis was quantified by measuring the area difference between the ascending and descending curves. The results are summarized in Figure 7. 4 (b).

The hysteresis values were obtained from the average of two experiments with three repeats for each setting (ramp & set). From Figure 7. 4, it was concluded that the foam formed from the 5 cmc TTAB solution didn't present any hysteresis both at the low and high-pressure ramps and sets. Consequently, the average of the area in between the ascending and descending curves obtained for these experiments was taken as the "noise" of the measurement which represented our zero-reference value to illustrate a negligible hysteresis. From all these conditions, an average value of $34.0 \pm 4.0 \times 10^{-4}$ was obtained to describe the case of negligible hysteresis. This value will be used in the following section to determine the effect of the two surface elasticities investigated on the foam hysteretic behaviour.

Furthermore, two experimental flow curves characterising the 2D foam response to the ascending (blue dots) and descending (red dots) deformation at the wall were obtained in Figure 7. 5.

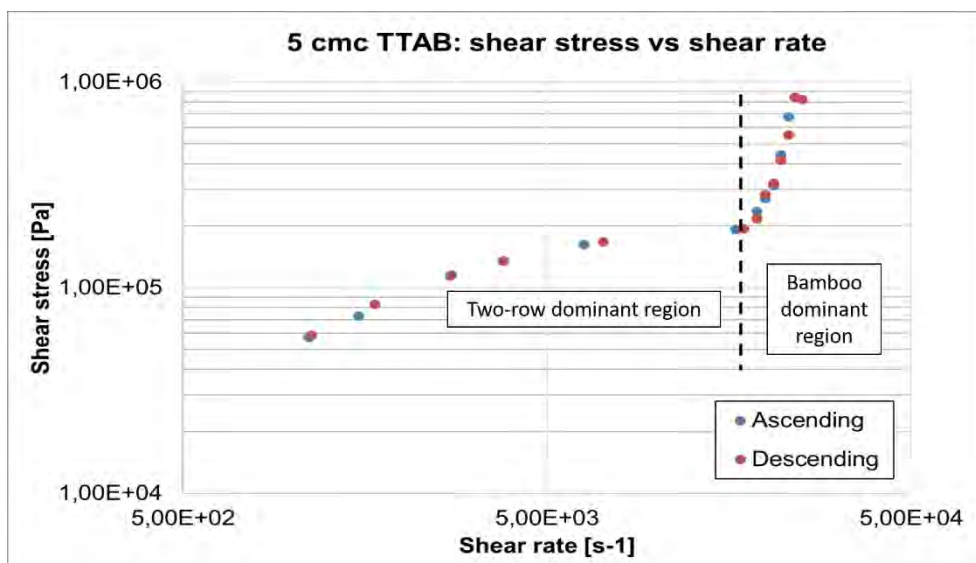


Figure 7. 5 Experimental flow curves plotting the shear stress due to the drag force versus the shear rate for 5 cmc TTAB solution at P1 and 0.5 mbar s^{-1} obtained from the ascending (blue dots) and descending (red dots) pressure ramps.

Moreover, two regions could be identified where the bamboo and the two-row patterns were dominant in the channel as represented in Figure 7. 5. Two characteristic times were employed to analyse the transition from two-row to bamboo patterns:

- The local rearrangement time of T1 bubble rearrangement duration described as an irreversible bubble neighbour switching event (Dennin, 2004).
- A second non-dimensional time defined by the overall experimental conditions and related directly to the two-row to bamboo transition. It is expressed as the transition time required for complete transition from the two-row to bamboo foam structure in the channel divided by the overall experimental time of foam deformation during the ascending or descending ramp.

The T1 rearrangement duration for 5 cmc TTAB could be estimated via image analysis at 1.5 ms and 2.25 ms at 450 and 500 mbar gas pressure respectively for

600 mbar liquid pressure as illustrated by the following time lapses represented in Figure 7. 6.

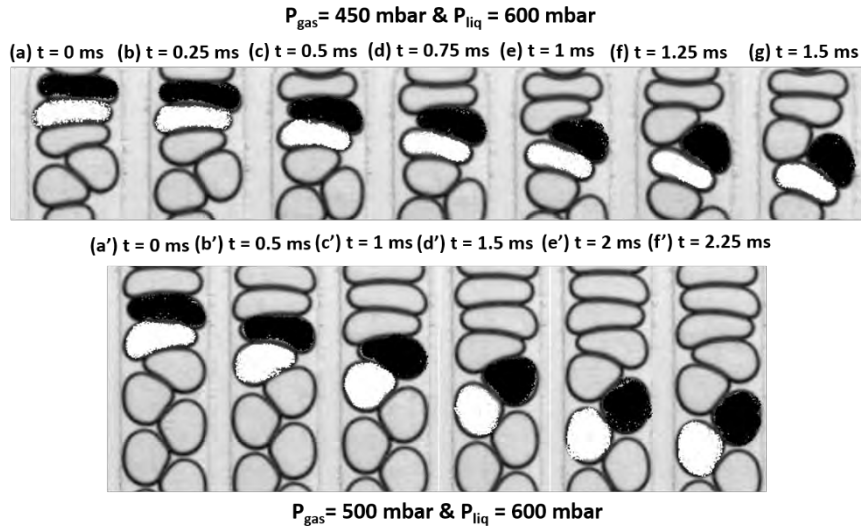


Figure 7. 6 Time lapses describing the T1 rearrangement at 450 mbar gas pressure and 600 mbar liquid pressure from (a) to (g) and at 500 mbar gas pressure and 600 mbar liquid pressure from (a') to (f') for 5 cmc TTAB.

It was found that the local rearrangement duration increased with the deformation from 1.5 to 2.25 ms for the reference solution. This evolution can be explained partially by the following relationship described by Durand and Stone (2006): the evolution of the T1 bubble rearrangement relaxation time τ_{T1} can be expressed as the product of the shear rate times the ratio of surface dilatational viscosity κ over the surface tension σ such as $\tau_{T1} \approx \frac{\kappa}{\sigma} \times \dot{\gamma}$. For a fixed surface tension, the duration of plastic events was extended by increasing the shear rate at the wall for fixed surface tension and viscosity.

At this stage, the time required for the complete transition from two-row to bamboo pattern was measured manually by identifying the initial pressure marking the start of the two-row to bamboo patterns transition in the ascending and descending transitions until complete transformation from one pattern to the other. A non-

dimensional transition time is defined as the transition time divided by the overall time of foam deformation during the ascending or descending ramp.

Thus, the transition lasted $51 \pm 0.2 \times 10^{-2}$ at P1 for both pressure ramps and $60 \pm 0.8 \times 10^{-2}$ at P2 for both pressure ramps. Furthermore, the ascending and descending transition time were similar because no hysteresis was observed. It was concluded that the pressure ramp had no significant impact on the transition time during the test whereas the increase of pressure set had increased the transition time.

In the next part, the impact of surface elasticity on foam hysteretic behaviour was analysed.

7.2.2 Effect of surface elasticity on foam hysteresis

In this section, DOH was added to the reference solution at two concentrations: 0.05 and 0.2 g L^{-1} to study the impact of low and high level of surface elasticity respectively.

7.2.2.1 5 cmc TTAB + 0.05 g L^{-1} DOH

In this section, the effect of surface elasticity on foam hysteresis in a microchannel was analysed for two pressures sets and ramps. The two sets of pressure were chosen from the foam regime map depicted in Figure 7. 3 (B) and are represented by two red arrows. The low and high-pressure sets were varying from 300 to 650 mbar air pressure for a fixed 600 mbar liquid pressure for P1 and from 500 to 850 mbar air pressure for a constant 800 mbar liquid pressure for P2, respectively. In Figure 7. 7 (a), the result of the effect of the increase of surface elasticity on the foam hysteresis at P1 and 0.5 mbar s^{-1} is illustrated.

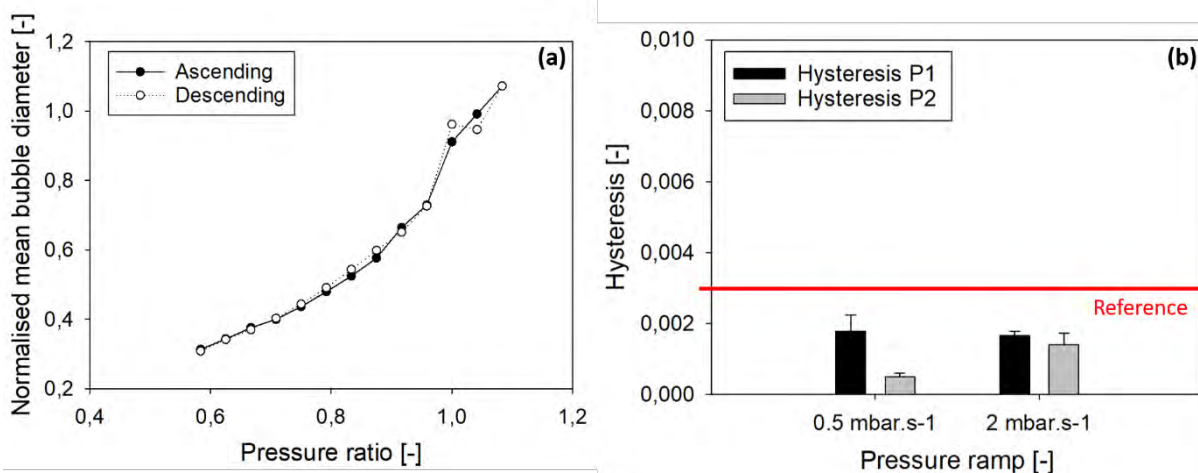


Figure 7. 7 Graph (a) presents 5 cmc TTAB + 0.05 g L⁻¹ DOH hysteresis evolution in an ascending (continuous black line – black dots) and descending (dotted black line – empty black dots) pressure ramps fixed at P1 and 0.5 mbar s⁻¹. Histogram (b) summarises the hysteresis evolution for 5 cmc TTAB + 0.05 g L⁻¹ for two pressure sets, low pressure set (P1, black) & high pressure set (P2, grey) for two pressure ramps (0.5 and 2 mbar s⁻¹).

The small differences observed between the ascending-descending were considered as negligible with regards to the hysteresis values summarised in Figure 7. 7 (b). The red line on the graph represents the reference value previously obtained to describe a negligible hysteresis. Therefore, all the configurations presented a hysteresis value lower than the reference. Thus, at this concentration, it was concluded that the presence of DOH did not enhance the foam hysteresis in the channel.

The equivalent of experimental flow curves were obtained for the ascending and descending deformations as illustrated in Figure 7. 8 at P1 and 0.5 mbar s⁻¹ and compared to the reference.

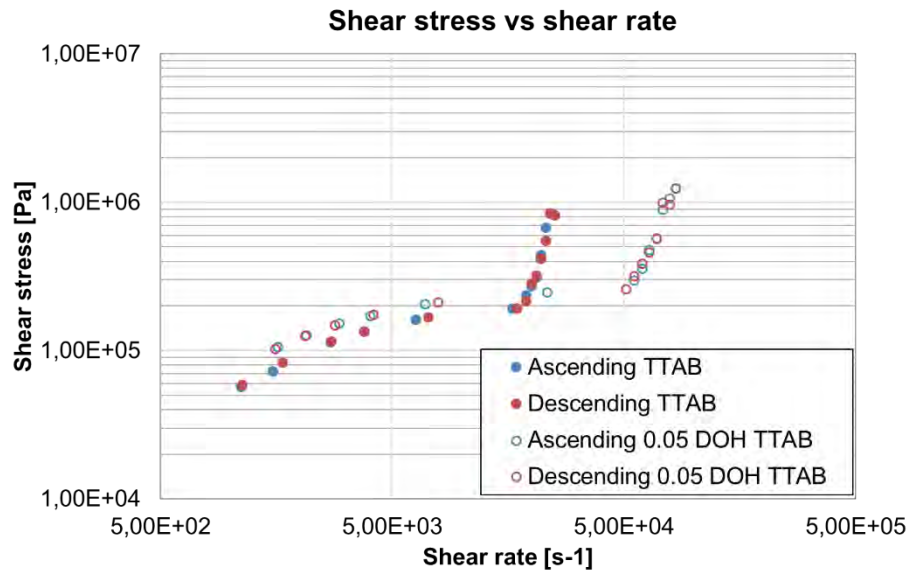


Figure 7. 8 Experimental flow curves plotting the shear stress due to the drag force versus the shear rate for 5 cmc TTAB solution (full circle) vs 5 cmc TTAB + 0.05 g L⁻¹ (empty circle) at P1 and 0.5 mbar s⁻¹ obtained from the ascending (blue) and descending (red) curves.

In this configuration, the increase in surface elasticity delayed the transition between the two-row and the bamboo patterns marked by the cross-over of two asymptotes marking the bamboo and the two-row pattern dominant areas. Indeed, the two-row dominated region was extended towards the highest shear rate at 0.05 DOH compared to the reference. At 2 mbar s⁻¹, the flow curves presented a similar trend.

The T1 rearrangement duration was estimated via image analysis for the pressure sets of 450 and 500 mbar gas pressures for 600 mbar liquid pressure. The time lapses representing the local rearrangements lasting 1.5 ms and 5 ms respectively are reported in Figure 7. 9 below:

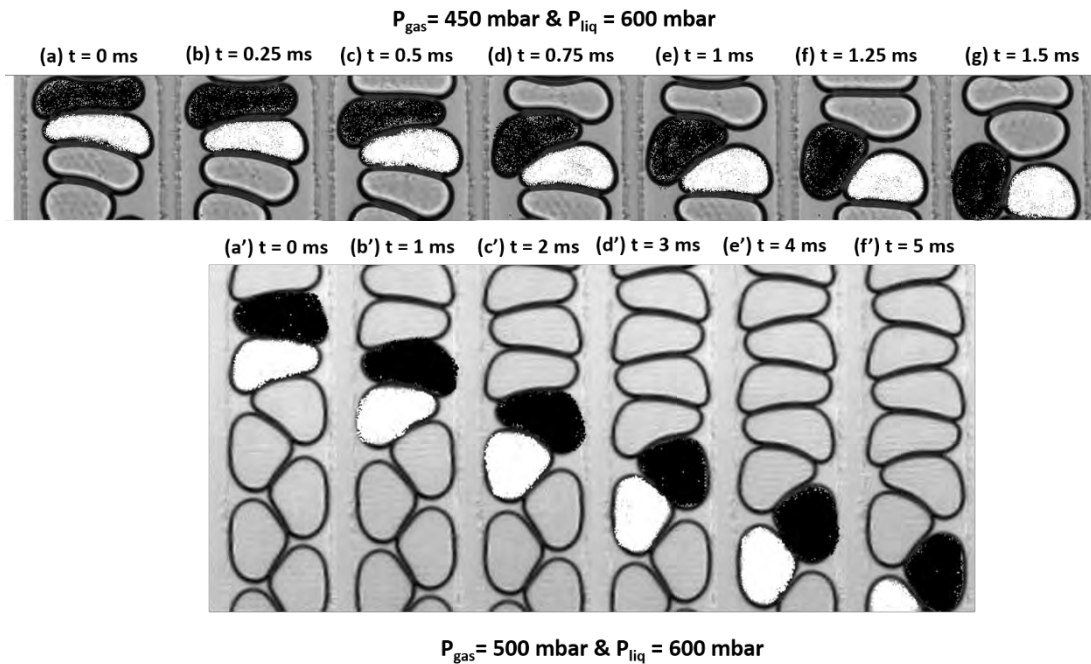


Figure 7. 9 Time lapses describing the T1 rearrangement at 450 mbar gas pressure and 600 mbar liquid from (a) to (g) and at 500 mbar gas pressure and 600 mbar liquid pressure from (a') to (f') for 5 cmc TTAB + 0.05 g L⁻¹ DOH.

Firstly, the local rearrangement duration at 450 mbar was like the one measured for the reference. However, at 500 mbar, the duration increase due to the shear rate was greater for 0.05 DOH compared to the reference. Consequently, the increase in surface elasticity enhanced the local duration of bubble rearrangement in the channel for a fixed equilibrium surface tension.

Secondly, it was found that increasing the pressure set had increased the non-dimensional transition time in the channel at P1 from $49.0 \pm 0.9 \times 10^{-2}$ at 0.5 mbar s^{-1} and $55.0 \pm 0.3 \times 10^{-2}$ at 2 mbar s^{-1} to $65.0 \pm 0.6 \times 10^{-2}$ for both pressure ramps at P2. The values obtained for transition time were closed to the one presented for the reference as no hysteresis was observed.

Therefore, here the extension of the two-row part of the curve during the ramp is due to a delayed start of the transition in the ramp compared to the reference caused by

the increase in surface elasticity that slowed down the transition by increasing the local bubble rearrangement duration. In the next section, the concentration of 0.2 g L^{-1} DOH was employed to evaluate if a higher level of surface elasticity could further enhance foam hysteresis.

7.2.2.2 5 cmc TTAB + 0.2 g L^{-1} DOH

In this paragraph, the DOH concentration was increased by four times the initial value previously investigated. The resulting FRM is illustrated in Figure 7. 3 (C).

From Figure 7. 2, the foaming liquid viscosity wasn't impacted significantly whereas the dynamic surface tension was affected as represented in Figure 7. 1. Indeed, the surface tension reached faster an equilibrium value at 0.05 than at 0.2 g L^{-1} DOH. The foam regime map introduced in Figure 7. 3 (C) is very similar to the one represented for our reference solution in Figure 7. 3 (A). Therefore, the same regions were selected to study the foam hysteretic behaviour: as low pressure set (P1), a gas inlet pressure ranging from 350 to 650 mbar for a fixed liquid pressure of 600 mbar and as a high pressure set (P2), a gas pressure varying from 450 to 850 mbar air pressure for a constant liquid pressure of 800 mbar.

At this concentration, hysteresis was observed for each experimental condition. We chose to illustrate this phenomenon with the case of P1 at 2 mbar s^{-1} in Figure 7. 10 (a).

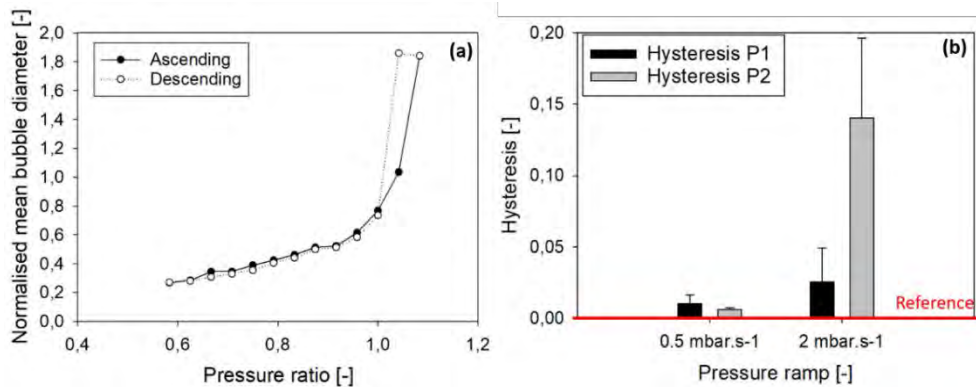


Figure 7. 10 Graph (a) describes 5 cmc TTAB + 0.2 g L⁻¹ hysteresis evolution in an ascending (continuous black line – black dots) and descending (dotted black line – empty black dots) pressure ramp fixed at 2 mbar s⁻¹ at P1. Histogram (b) summarises the hysteresis evolution for 5 cmc TTAB + 0.2 g L⁻¹ DOH for two pressure sets, low pressure set (P1, black) & high pressure set (P2, grey) for two pressure ramps (0.5 and 2 mbar s⁻¹).

A striking difference between the ascending and descending curve was observed Figure 7. 10 (a). The evolution of the hysteresis per pressure set and ramp is represented in Figure 7. 10 (b).

At 0.5 mbar s⁻¹, the hysteresis was enhanced compared to the reference (3.3×10^{-3}) with a hysteresis value of 0.01 for P1 and 6.1×10^{-3} for P2. At 2 mbar s⁻¹, the hysteretic behaviour was increased significantly with values reaching 0.025 and 0.14 for P1 and P2 respectively. Thus, from these values, at higher surface elasticity, the ramp had a stronger impact on the hysteresis than the pressure set. The rise in ramp multiplied from 2.5 to about 20 times the initial value of hysteresis whereas the increase in pressure set at best, enhanced the hysteresis by five times its initial value.

Regarding the transition between the two-row and the bamboo patterns, the experimental flow curves obtained for P1 at 2 mbar s⁻¹ are represented in Figure 7. 11.

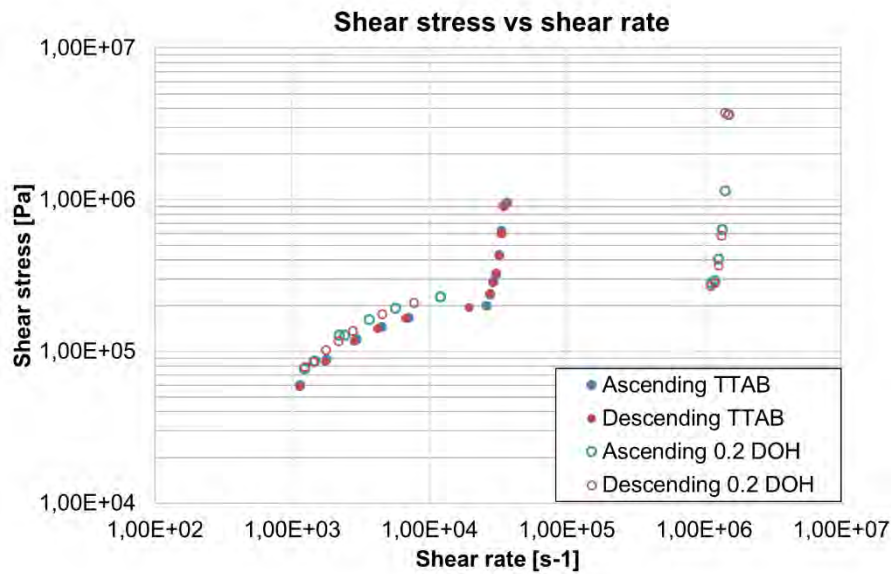


Figure 7. 11 Experimental flow curves plotting the shear stress due to the drag force versus the shear rate for 5 cmc TTAB solution (full circle) vs 5 cmc TTAB + 0.2 g L⁻¹ (empty circle) at P1 and 2 mbar s⁻¹ obtained from the ascending (blue) and descending (red) curves.

At P1 and 2 mbar s⁻¹, both two-row dominant zones presented a similar trend whereas the reference showed a shortest region towards the bamboo/annular flow region due to its negligible hysteresis. The difference in shear rate ranges observed between 0.2 DOH and the reference is due to a smaller film thickness estimated via image analysis in the case of DOH for similar velocities.

The T1 rearrangement duration was evaluated manually via image analysis and estimated at 1.5 ms and 3 ms for 450 and 500 mbar gas pressures for 600 mbar liquid pressure. The corresponding time lapses are presented in Figure 7. 12.

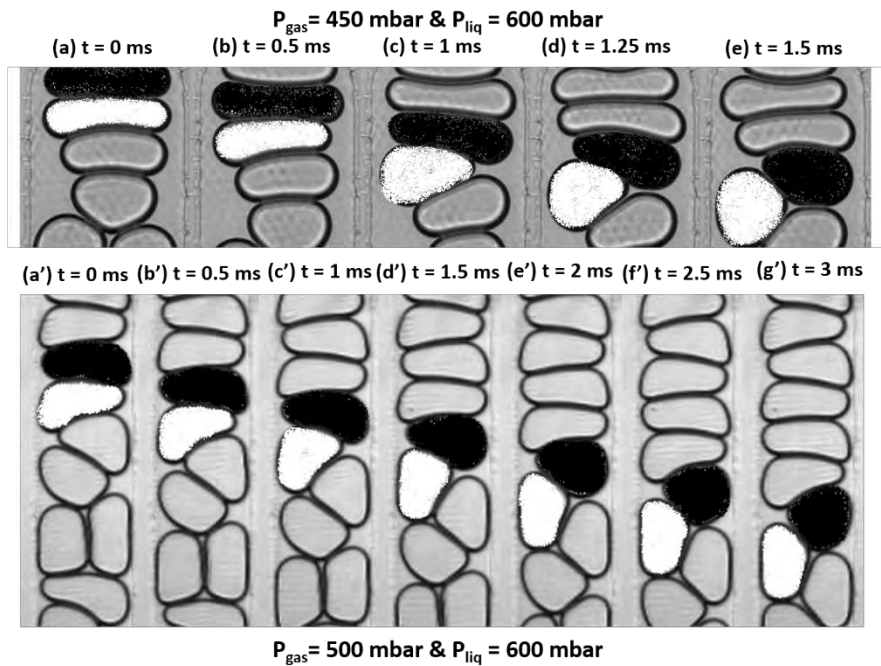


Figure 7. 12 Time lapses describing the T1 rearrangement at 450 from (a) to (e) and 500 mbar from (a') to (g') gas pressures for 600 mbar liquid pressure for 5 cmc TTAB + 0.2 g L⁻¹ DOH.

At 450 mbar gas pressure, at low and high surface elasticity, a similar rearrangement duration was obtained. Surprisingly, by increasing the amount of DOH in solution at 500 mbar gas pressure, the local rearrangement duration was reduced from 5 to 3 ms. The main measurable difference observed so far between the two DOH formulations resided in the dynamic surface tension evolution. However, the rearrangement time scale is much shorter compared to the range of bubble life time investigated from the dynamic surface tension measurement (from 5 ms to 10s). Therefore, it is difficult to conclude on the effect of DOH on the surface tension and on the resulting local rearrangement dynamic.

The non-dimensional transition time lasted in average throughout the experiments from $570.0 \pm 0.9 \times 10^{-3}$ at P1 at 0.5 mbar s⁻¹ to $54.0 \pm 0.4 \times 10^{-2}$ at 2 mbar s⁻¹. These were slightly higher than the one obtained for the reference at P1. This could be related to the increase in surface elasticity. As previously, the local rearrangement

time increased slightly compared to the reference (3 ms compared to 2.25 ms) leading to a slowing down of the transition from the two-row to the bamboo pattern. At P2, the duration increased slightly to $590.0 \pm 0.7 \times 10^{-3}$ at 0.5 mbar s^{-1} which was in the line with the reference values but decreased to $47.0 \pm 0.2 \times 10^{-2}$ at 2 mbar s^{-1} .

At high surface elasticity, the ramp had a significant impact on the non-dimensional transition time during the test than the pressure set. Indeed, an important decrease in transition time occurred at P2 by increasing the pressure ramp. At P2 and 2 mbar s^{-1} , the transition time varied between the ascending (0.55) and descending (0.39) ramp due to the enhanced hysteretic behaviour. This retardation was caused by the hysteresis. This phenomenon wasn't visible at 0.05 DOH. Indeed, at this concentration, the dynamic surface tension hadn't been impacted whereas at 0.2 DOH, more time was required to reach an equilibrium surface tension. Thus, the surface elasticity impacted the foam hysteretic behaviour by modifying the surfactant dynamic at the interface above a certain DOH concentration. In the next section, the effect of bulk elasticity on foam hysteretic behaviour in the microchannel was investigated for two kinds of PEO molecular weight and concentration.

7.2.3 Effect of bulk elasticity on foam hysteresis

Poly(ethylene oxide) is a high molecular weight water-soluble polymer that has many uses in various industrial applications. In this study, PEO with different molecular weights ranging from 3×10^5 to 1×10^6 were used at two concentrations: 100 and 300 ppm. The choice was made to add to all solutions 0.05 g L^{-1} DOH to obtain a high surface shear viscosity and a well-controlled and constant low interfacial mobility as previously employed by Safouane *et al.* (2006). This concentration showed no

impact on foam hysteretic behaviour as demonstrated in the previous section. These solutions represented model solutions having some additional elastic properties and high elongational viscosities.

The dynamic surface tensions were also evaluated to check for eventual modifications of interfacial properties. Indeed, surfactant-polymer complexation is possible at interfaces and this phenomenon influences strongly the surface tension (Witte and Engberts, 1987). The dynamic surface tension measurements were performed via a maximum bubble pressure tensiometer (Sinterface, BPA-1) and the results were reported in Figure 7. 1. For all solutions, no significant variations were observed: the measured surface tension was steady and close to 37 mN m^{-1} . These measurements confirmed that there was no surface complexation in our solutions and no modification of the surface properties. Consequently, it was considered that all the changes observed here were only due to modification in bulk solutions, the interface being always in the low surfactant mobility limit (rigid interface). The foam regime maps for the four systems investigated are summarised in Figure 7. 13.

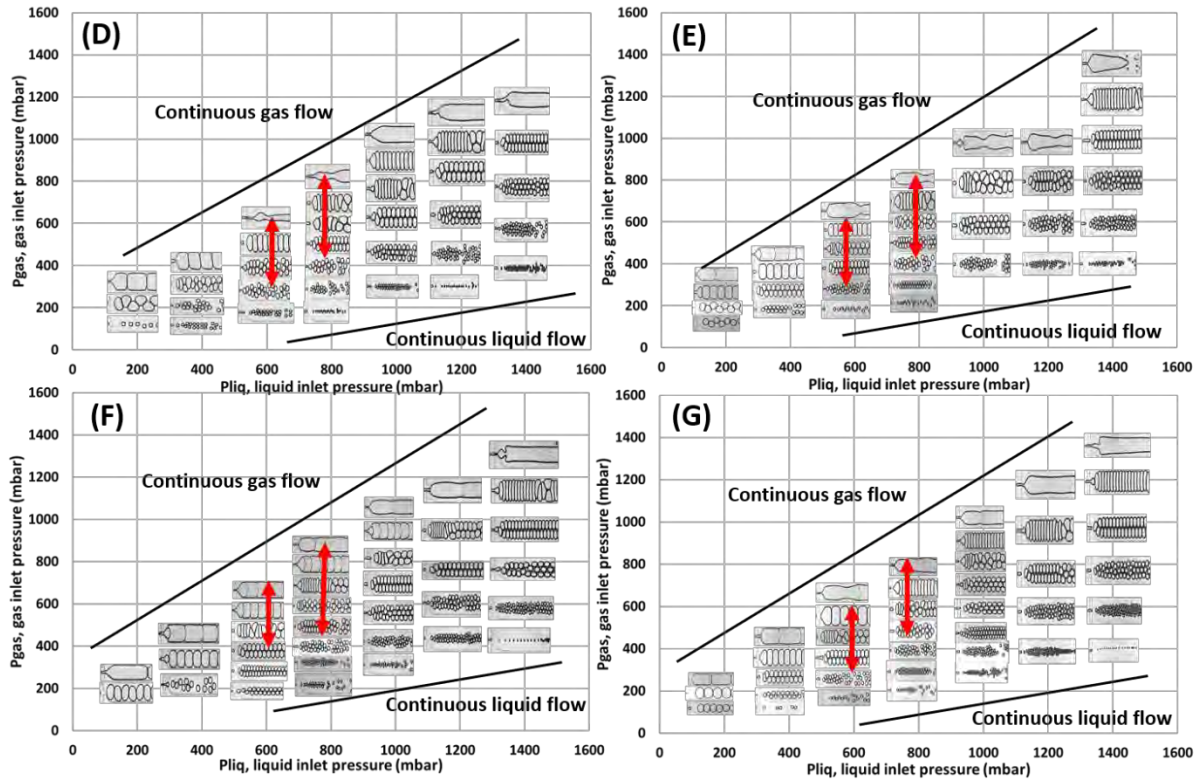


Figure 7. 13 Foam regime maps plotting the gas inlet pressure (P_{gas}) versus the liquid inlet pressure (P_{liq}) for the four solutions investigated: (D) 5 cmc TTAB solution + 0.05 g L⁻¹ DOH + 100 ppm Mw = 3×10^5 g mol⁻¹ PEO, (E) 5 cmc TTAB solution + 0.05 g L⁻¹ DOH + 300 ppm Mw = 3×10^5 g mol⁻¹ PEO, (F) 5 cmc TTAB solution + 0.05 g L⁻¹ DOH + 100 ppm Mw = 1×10^6 g mol⁻¹ PEO and (G) 5 cmc TTAB solution + 0.05 g L⁻¹ DOH + 300 ppm Mw = 1×10^6 g mol⁻¹ PEO.

The red arrows represent for each case the lowest (P_1) and the highest (P_2) pressure sets investigated. In this section, the TTAB + 0.05 DOH was taken as a reference for negligible hysteresis. The new reference value describing a negligible hysteresis is equal to $1.3 \pm 0.3 \times 10^{-3}$ and is represented by a red line in the histogram summarising the hysteresis evolution with the experimental conditions.

In the study of the effect of bulk elasticity, the impact of the lowest concentration for the lowest molecular weight was firstly investigated.

7.2.3.1 TTAB + 0.05 g L⁻¹ DOH + PEO Mw = 3×10^5 g mol⁻¹ at 100 ppm

The resulting FRM obtained for a solution made of 100 ppm PEO 3×10^5 g mol⁻¹ is reported in Figure 7. 13 (D).

As a first observation, it was noted that the foam patterns obtained were showing some differences compared to our reference solution (5 cmc TTAB + 0.05 g L⁻¹ DOH) whose FRM is represented in Figure 7. 3 (B). Indeed, the foam showed an annular flow pattern instead of a bamboo pattern forming at pressure ratio close to 1, so when the gas pressure reached the liquid pressure. This demonstrates that the bulk elasticity was impacted already the foam behaviour in the channel despite a steady surface tension and viscosity. From FRM (D), two regions represented by two red arrows in Figure 7. 13 were selected to evaluate the foam recovery property after a gradual deformation. The lowest level of deformation (P1) was studied from 350 to 650 mbar air pressure for a constant 600 mbar liquid pressure. Oppositely, the highest level (P2) was chosen from 450 to 800 mbar for a fixed 800 mbar liquid pressure. The foam hysteresis was evaluated between the ascending and the descending ramp of deformation for the different cases investigated. The highest hysteresis was observed for the highest pressure set and ramp as illustrated in Figure 7. 14 (a).

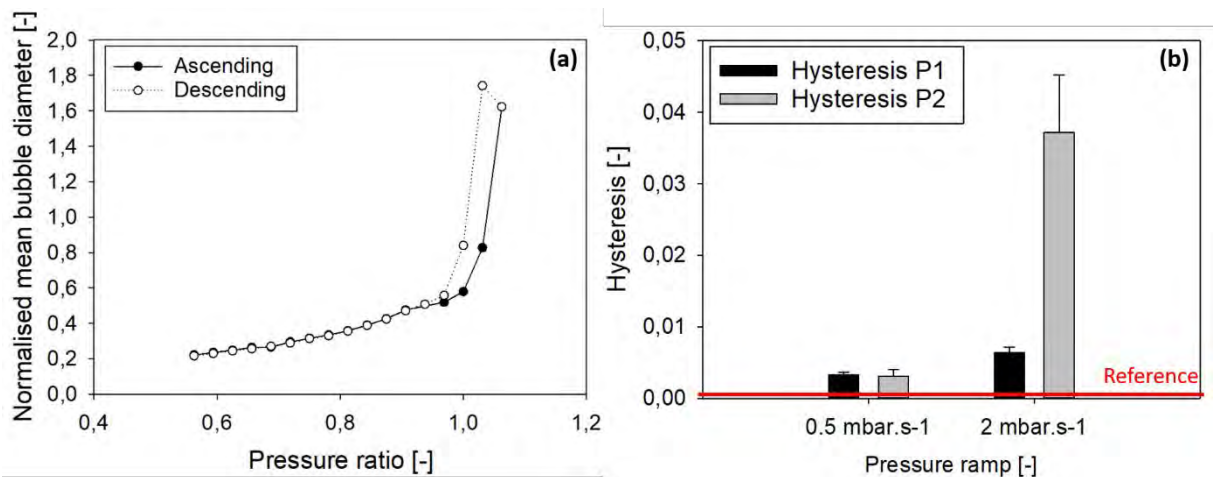


Figure 7. 14 Graph (a) presents the 5 cmc TTAB + 0.05 g L⁻¹ + 100 ppm Mw = 3 x 10⁵ g mol⁻¹ PEO hysteresis evolution in an ascending (continuous black line – black dots) and descending (dotted black line – empty black dots) pressure ramps fixed at 2 mbar s⁻¹ and P2. Histogram (b) summarises of the hysteresis evolution for 5 cmc TTAB + 0.05 g L⁻¹ DOH + 100 ppm Mw = 3 x 10⁵ g mol⁻¹ PEO for two

pressure sets, low pressure set (P1, black) & high pressure set (P2, grey) for two pressure ramps (0.5 and 2 mbar s⁻¹).

All the results are summarised in Figure 7. 14 (b). It was found that the foam hysteretic behaviour was enhanced by the presence of PEO in solution. At P1 and at P2, the hysteresis increases with the pressure ramp. Surprisingly, at 0.5 mbar s⁻¹, the hysteresis wasn't impacted by the increase in pressure set. At P2, the hysteresis was about 12 times higher at 2 mbar s⁻¹ compared to 0.5 mbar s⁻¹. Similarly, the increase in pressure set caused the hysteresis to be multiplied by 5 at 2 mbar s⁻¹. All things considered, there was a stronger effect of the pressure ramp on the foam hysteresis, but a synergetic effect of the pressure set and ramp was also observed for the highest deformation case. The impact of the increase of bulk elasticity was analysed on the experimental flow curves at P2 and 2 mbar s⁻¹ in Figure 7. 15.

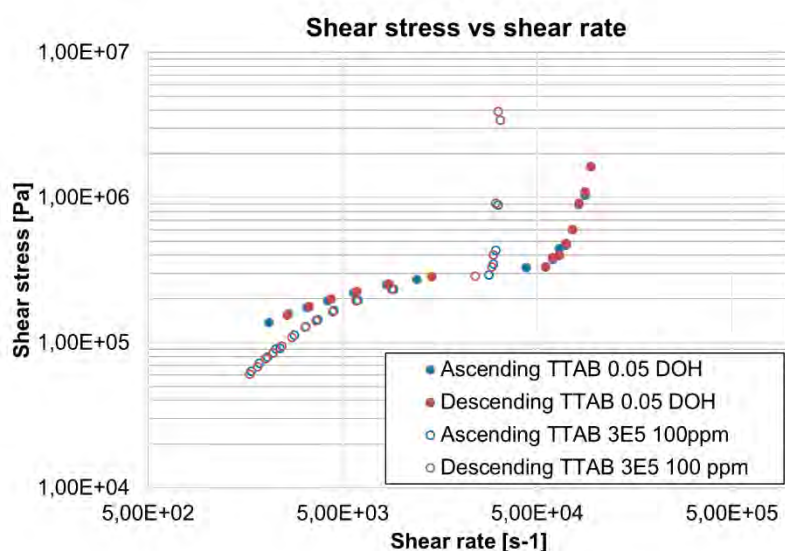


Figure 7. 15 Experimental flow curves plotting the shear stress due to the drag force versus the shear rate for 5 cmc TTAB + 0.05 g L⁻¹ solution (empty circle) vs 5 cmc TTAB + 0.05 g L⁻¹ + 100 ppm Mw = 3 x 10⁵ PEO (full circle) at P2 and 2 mbar s⁻¹ obtained from the ascending (blue dots) and descending (red dots) curves.

In Figure 7. 15, a discrepancy was found between the two formulations towards the lowest shear rates. Indeed, the addition of PEO caused the initial evolution of the

two-row pattern to be pushed towards the lowest shear stresses for the same range of shear rates. Indeed, on the FRM in Figure 7. 3 (B) and in Figure 7. 13 (C), in the 400 to 800 mbar gas pressure for a fixed 800 mbar liquid pressure region, we can see that the apparent mean bubble diameter is greater in the 0.05 DOH case compared to the 0.05 DOH + 100 ppm 3×10^5 PEO. Thus, a smaller bubble diameter led to lower drag at the wall and smaller shear stresses due to the drag force for a fixed shear rate for the PEO solution. Additionally, the transition between the two-row and the bamboo regions occurred at lower shear rates for the PEO solution compared to the reference.

Local rearrangement durations of 1.5 ms and 5.5 ms were obtained for 450 and 500 mbar gas pressures respectively for 600 mbar liquid pressure. The time lapses of the rearrangements are presented in Figure 7. 16.

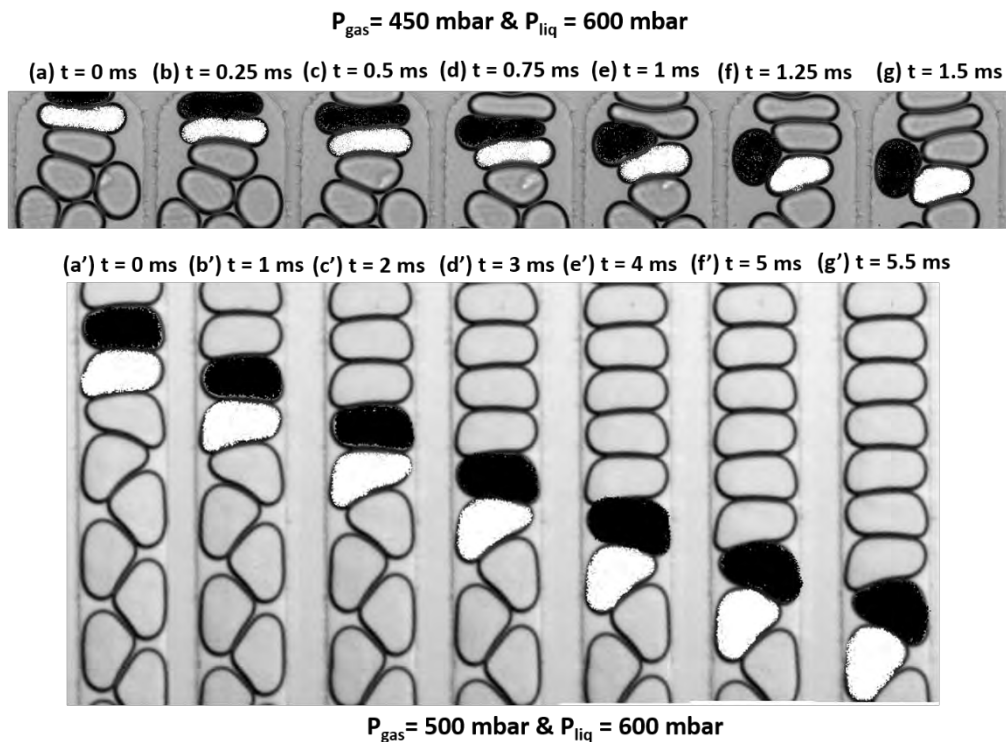


Figure 7. 16 Time lapses describing the T1 rearrangement at 450 from (a) to (g) and 500 mbar from (a') to (g') gas pressure and 600 mbar liquid pressure for 5 cmc TTAB + 0.05 g L⁻¹ DOH + 3 x 10⁵ g mol⁻¹ PEO.

These values were in the line with the results obtained for 5 cmc TTAB + 0.05 g L⁻¹ DOH. Therefore, the local bubble rearrangement compared to the reference (5 cmc TTAB + 0.05 g L⁻¹ DOH) in Figure 7. 16 wasn't impacted significantly by the presence of PEO in solution. On the non-dimensional transition time, the average duration during the deformation was steady throughout the various pressure sets and ramps at about 0.54 – 0.55. Consequently, in this case, a hysteresis was visible, but it did not impact the overall transition time because the hysteresis did not last long enough to interfere with the transition time. Indeed, the ascending-descending dynamics were very symmetrical. In the following section, a higher concentration of PEO was added in solution to verify if the concentration rise could enhance the hysteresis.

7.2.3.2 TTAB + 0.05 g L⁻¹ DOH + PEO Mw = 3 x 10⁵ g mol⁻¹ at 300 ppm

In this paragraph, the initial PEO concentration was tripled for the same molecular weight. The FRM (E) was realised and represented in Figure 7. 13. The FRM presented an annular flow pattern for the highest gas pressure for a fixed liquid pressure as previously observed at 100 ppm PEO in Figure 7. 13 (D) for a constant surface tension and viscosity compared to our reference. By comparing Figure 7. 14 (b) and Figure 7. 17 (b), it is found that the hysteresis was significantly increased with the concentration of PEO in solution for the same set of pressure and ramp.

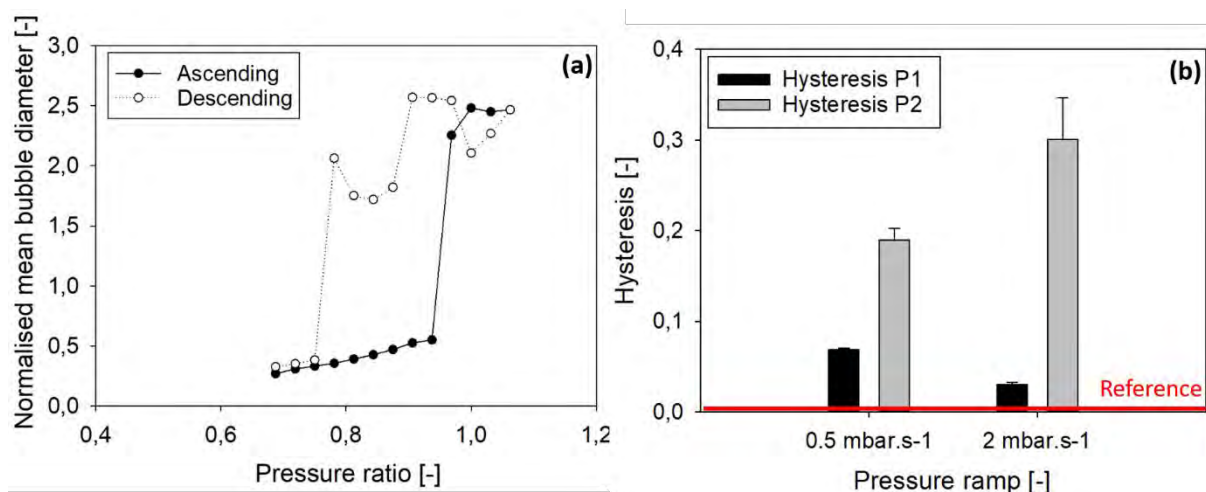


Figure 7. 17 Graph (a) introduces 5 cmc TTAB + 0.05 g L⁻¹ + 300 ppm Mw = 3 x 10⁵ g mol⁻¹ PEO hysteresis evolution in an ascending (continuous black line – black dots) and descending (dotted black line – empty black dots) pressure ramps fixed at 2 mbar s⁻¹ for the highest pressure set (P2). Histogram (b) summarises of the hysteresis evolution for 5 cmc TTAB + 0.05 g L⁻¹ DOH + 300 ppm Mw = 3 x 10⁵ g mol⁻¹ PEO for two pressure sets, low pressure set (P1, black) & high pressure set (P2, grey) for two pressure ramps (0.5 and 2 mbar s⁻¹).

Firstly, from 100 to 300 ppm, the hysteresis caused by the presence of PEO in solution was strongly heightened for a constant surface tension and viscosity. From Figure 7. 17, it was found that the increase in pressure set enhanced the hysteresis and multiplied it by 2.5 at 0.5 mbar s⁻¹ and 15 at 2 mbar s⁻¹ the initial hysteresis values. The ramp increased the hysteresis at P2 but decreased it slightly at P1. Therefore, it was considered that the pressure set had a bigger impact on the foam

hysteretic behaviour in the channel. It was also concluded the PEO concentration emphasized the pressure set impact on the foam hysteresis.

The next step in this work is to determine if the increase of the PEO concentration influenced the transition between the bamboo and the two-row pattern by comparing the experimental flow curves obtained at 100 ppm versus 300 ppm for the highest set of pressure (P2) and pressure ramp (2 mbar s⁻¹) in the graph depicted in Figure 7.

18.

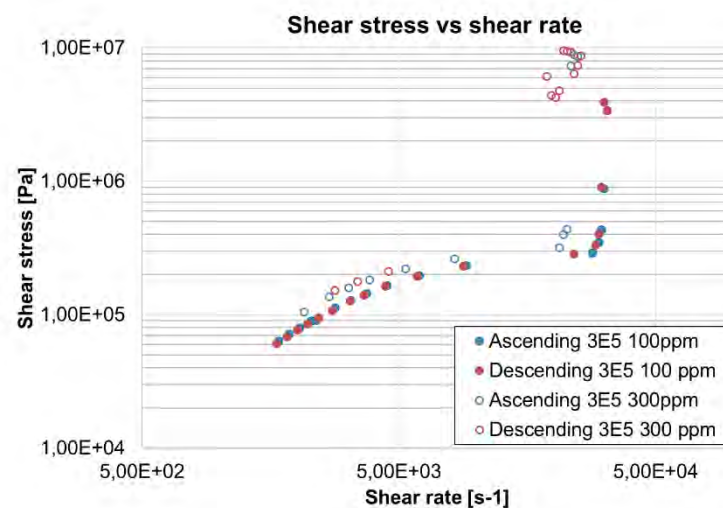


Figure 7. 18 Experimental flow curves plotting the shear stress due to the drag force versus the shear rate for 5 cmc TTAB + 0.05 g L⁻¹ 100 ppm Mw = 3 x 10⁵ g mol⁻¹ PEO solution (full circle) vs 5 cmc TTAB + 0.05 g L⁻¹ + 300 ppm Mw = 3 x 10⁵ PEO g mol⁻¹ (empty circle) at P2 and 2 mbar s⁻¹ obtained from the ascending (blue) and descending (red) curves.

In Figure 7. 18, the hysteresis broadened the bamboo dominant region towards the highest stresses and shear rates. Indeed, in the estimation of the shear rate at the wall as explained in Chapter 6, the liquid thickness reached a minimum for the bamboo or slug pattern. At 100 ppm, the bamboo dominant region in the descending curve was shorter towards the highest shear stresses and shear rates whereas at 300 ppm most of the descending curve was present towards the highest shear stresses and shear rates. This prove that for the highest deformation, the highest

concentration showed evidence of a much higher hysteretic behaviour than the lowest concentration. At 300 ppm, the curves shifted slightly towards the higher shear stresses. This could be related to the rise in elongational viscosity due to the rise in polymer concentration in solution. The local rearrangement duration was not influenced by the increase in polymer concentration.

Then, the effect on the non-dimensional transition time was evaluated in the channel. The transition time was ranging between 57.0 to $55.0 \pm 0.7 \times 10^{-2}$ at P1 for both pressure ramps. At P2, in the ascending ramp, the transition time was estimated at about $60.0 \pm 0.3 \times 10^{-2}$ and $450.0 \pm 0.9 \times 10^{-3}$ at 0.5 and 2 mbar s⁻¹ respectively.

These values are in the line with the one obtained for the 0.05 DOH solution. But, the 2 mbar s⁻¹ case showed a lower value because of the hysteresis persistence in the descending ramp. Indeed, in the descending ramp, the rearrangement was no longer visible and replaced by an abrupt change from annular flow to two-row at a specific and reproducible gas pressure for a fixed liquid pressure. Therefore, the hysteresis in this case almost inhibited the transition from bamboo to two-row pattern in the descending ramp.

Interestingly, it was explained previously by Safouane *et al.*, (2006) that PEO Mw influenced the drainage velocity measured in the plateau borders. Indeed, for a 3×10^5 PEO solution, the drainage velocity was like the one obtained for Newtonian solution made of glycerol and water mixtures whereas for highest Mw, the drainage velocity was faster compared to solutions having the same bulk viscosities. It was showed that the presence of high Mw PEO in the liquid affected the plateau border permeability, thus fastening the liquid drainage throughout the film. The presence of

high Mw PEO in solution rendered the liquid thin films more unstable. Thereby, this phenomenon could trigger the hysteresis by favouring the swapping from the bamboo to the annular flow pattern. Nevertheless, for this Mw, the drainage velocity in the PBs should not be increased and remain Newtonian.

Furthermore, it was observed that at 100 ppm, the hysteresis did not persist enough to affect the transition time whereas at 300 ppm, the hysteresis was emphasized and impacted significantly the transition time by delaying the change from bamboo/annular flow to two-row in the descending ramp. This effect can be called “retardation”. Therefore, the hysteresis observed was mainly due to the increase in bulk elasticity that created a retardation effect which kept the pattern resulting from the highest deformation for longer than expected. This phenomenon related to bulk elasticity can be termed “tension thickening” (Barnes *et al.*, 1989; Baig and Mavrantzas, 2010).

Tension-thickening can be considered as the equivalent of shear-thickening property but for extensional flow: Barnes *et al.*, (1989) described it as the property of a fluid for which the extensional viscosity increases with an increasing extensional deformation. This effect was highlighted by Saint-Jalmes (2006) and further explained by Safouane *et al.* (2006). Researchers defined the origin of this property in the increase of the elongational viscosity with the elongational strain rates.

Safouane *et al.* (2006) showed that this property could enhance the stability of liquid filaments against abrupt changes in diameter. Such diameter changes imply locally a maximum of elongational rate, and thus local higher stresses due to the tension thickening effect: the flow then react by smoothing out the section change to reduce

the stresses. Thereby, such thickening can occur while the foam pattern is changing from two-row to bamboo causing the retardation effect observed in the change from bamboo to two-row in the descending ramp.

Furthermore, the hysteresis was expressed differently depending on the polymer concentration due to the evolution of the elastic property over the viscous one. At low polymer concentration, the viscous part is dominant over the elastic one. Thus, for a fixed deformation energy, more viscous dissipation will be obtained. However, the concentration is not higher enough to enhance significantly the elastic counterpart compared to the viscous part. Therefore, at low polymer concentration, the hysteresis was triggered but did not persist for long because the tension thickening was limited. Then, at higher polymer concentration, the elastic property became greater than before and the tension-thickening was more effective.

At low polymer concentration, the viscous contribution was dominant compared to the elastic one. Thus, the increase in energy given per second was “wasted” or lost to the surrounding by viscous dissipation. Thereby, the hysteresis increased with the pressure ramp, but the hysteresis did not persist enough because the tension thickening effect was limited due to the lack of elastic contribution.

At high polymer concentration, the elastic contribution increased. At low deformation (P1), the pressure ramp decreased the hysteresis because the polymer chains acted against the deformation and enhanced the foam recovery process. In addition, the ramp increase gave more elastic energy to be stored by the foam structure and to resist to the deformation and restore the structure after deformation. At high deformation, the previous effect was overcome by the deformation and the tension

thickening effect took place. Therefore, the hysteresis increased with the pressure ramp. All in all, it was considered that the increase in polymer concentration enhanced the tension thickening which led to strengthening of the hysteresis compared to 100 ppm. The next paragraph aimed to investigate if a larger PEO molecular weight could enhance the tension-thickening effect.

7.2.3.3 TTAB + 0.05 g L⁻¹ DOH + PEO Mw = 1x10⁶ g mol⁻¹ at 100 ppm

This study on foam hysteresis was carried on with the impact of 100 ppm of Mw = 1 x 10⁶ g mol⁻¹ PEO in 5 cmc TTAB solution. From this solution, FRM (F) was realised and described in Figure 7. 13. Firstly, FRM (F) was like the one obtained previously with a lower PEO molecular weight. For the same map regions, similar foam patterns were recognized. Two of them were selected to study the low (P1) and high deformation (P2) cases at the wall corresponding to the combination of 600 mbar liquid and from 450 to 650 mbar air pressures for P1 and of 800 mbar liquid and from 550 to 820 mbar air pressures for P2. The hysteresis curves for the case of the highest pressure set and ramp (P2) are showed in Figure 7. 19 (a). This set of results presented a significant difference with the results introduced for the same polymer concentration but at a lower molecular weight in Figure 7. 14 (a). Indeed, the ascending-descending curves presented much less hysteresis than previously.

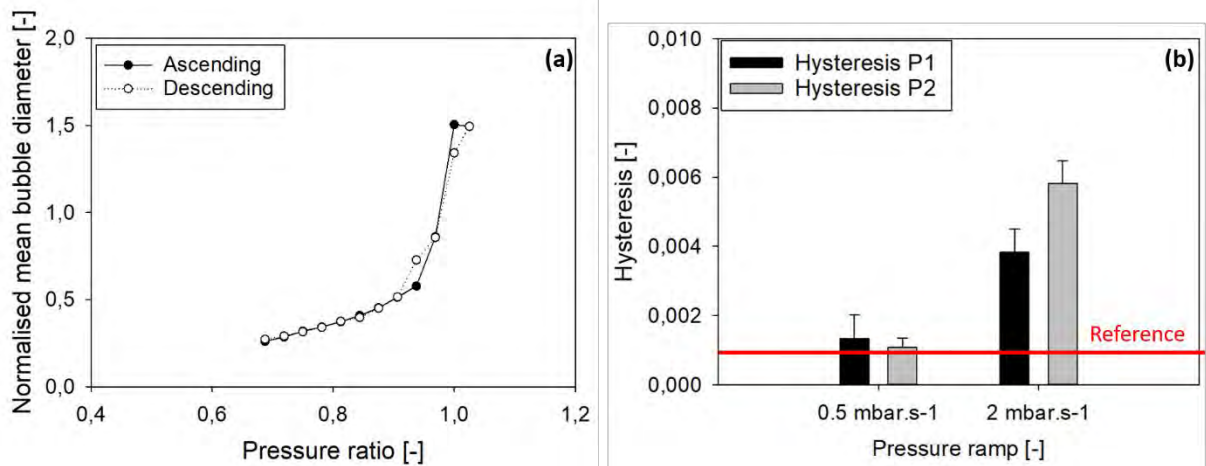


Figure 7. 19 Graph (a) illustrates 5 cmc TTAB + 0.05 g L⁻¹ + 100 ppm Mw = 1 x 10⁶ g mol⁻¹ PEO hysteresis evolution in an ascending (continuous black line – black dots) and descending (dotted black line – empty black dots) pressure ramps fixed at 2 mbar s⁻¹ for the highest pressure set (P2). Histogram (b) summarises the hysteresis evolution for 5 cmc TTAB + 0.05 g L⁻¹ DOH + 100 ppm Mw = 1 x 10⁶ g mol⁻¹ PEO for two pressure sets, low pressure set (P1, black) & high pressure set (P2, grey) for two pressure ramps (0.5 and 2 mbar s⁻¹).

Surprisingly, the range of hysteresis values reported in Figure 7. 19 was much smaller compared to the one evaluated in Figure 7. 14. At 0.5 mbar s⁻¹, a negligible hysteresis was denoted for both pressure sets. However, the pressure ramp increased the hysteresis for both pressure sets. Oppositely, the pressure set increase kept emphasizing the hysteresis only at 2 mbar s⁻¹. It was also showed by Safouane *et al.* (2006) that high PEO molecular weight could cause the drainage velocity in the PBs to increase due to PB's permeability amplification. So, the rise in permeability and in liquid flow within the plateau borders could be partially at the origin of the overall hysteresis reduction observed. At higher molecular weight, longer polymer chains cause more friction leading to more viscous dissipation. Additionally, longer chains require more deformation energy to be moved due to a higher elongational viscosity. At low polymer concentration and at 0.5 mbar s⁻¹, the viscous dissipation was dominant with regards to its elastic counterpart. Thus, the increase in pressure ramp and set increased the hysteresis. Nevertheless, at 2 mbar s⁻¹, more

deformation energy was given to the system to put in motion and stretch/direct the polymer chains in the flow direction. The resulting elasticity rose and limited the viscous dissipation. Therefore, at 2 mbar s^{-1} , some hysteresis was observed. As shown previously, the tension-thickening effect was linked to the increase of elongational viscosity via the elongational shear rate. A higher molecular weight should thus enhance the elongational viscosity. However, longer polymer chains require more energy to be moved in the flow direction despite a steady foaming liquid viscosity. Thus, for the same pressure set, the higher molecular weight caused the hysteretic behaviour and the shear thickening effect to be reduced compared to the lower molecular weight simply because the polymer network was more resistant to the deformation at the highest molecular weight. From Figure 7. 20 representing two experimental flow curves at P2 and 2 mbar s^{-1} , at a fixed PEO concentration (100 ppm) for two different molecular weights, it was found that the two curves were very alike despite the slightly upper shear stress for a fixed shear rate obtained for the high molecular weight curves.

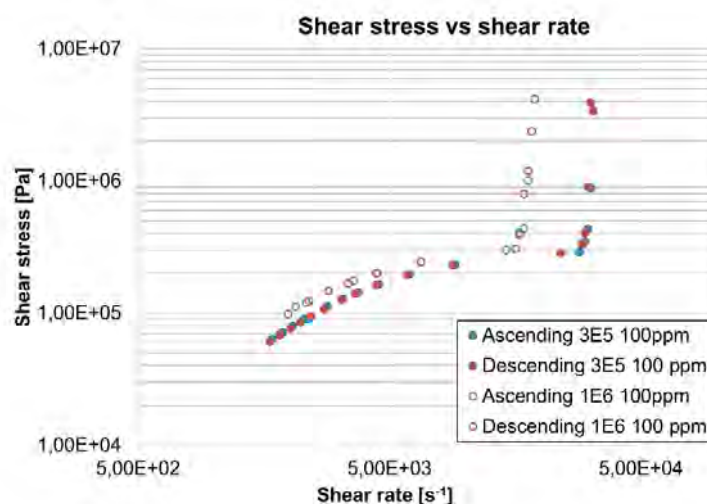


Figure 7. 20 Experimental flow curves plotting the shear stress due to the drag force versus the shear rate for 5 cmc TTAB + 0.05 g L^{-1} 100 ppm $M_w = 3 \times 10^5$ PEO solution (empty circle) vs 5 cmc TTAB + 0.05 g L^{-1} + 100 ppm $M_w = 1 \times 10^6$ PEO (full circle) at P2 and 2 mbar s^{-1} .

The local rearrangement duration was not affected by the presence of high Mw polymer chains in solution. Additionally, no change was observed with the pressure ramp for P1 with a transition time ranging from $62.0 \pm 0.3 \times 10^{-2}$. At P2, the transition time was varying from $62.0 \pm 1.0 \times 10^{-2}$ to $66.0 \pm 0.9 \times 10^{-2}$ for 0.5 and 2 mbar s⁻¹ respectively. There was no significant increase therefore, it was considered that the ramp and the pressure set did not impact significantly the average transition time. However, a difference at P2 was observed in the critical pressure at which the complete transition from the two-row to the bamboo pattern occurred. The change took place later in the descending ramp ($P_{\text{gas}} = 740$ mbar) compared to the ascending ramp ($P_{\text{gas}} = 760$ mbar). This 20-mbar difference occurred only at P2 whereas at P1 the foam pattern deformation was very reproducible between the ascending and descending ramp. The retardation linked to the hysteresis observed at P2 can be linked to the tension-thickening property evoked earlier. For the last study case, the amount of PEO in solution was increased and its impact was evaluated on the foam hysteretic behaviour.

7.2.3.4 TTAB + 0.05 DOH + PEO Mw = 1×10^6 g mol⁻¹ at 300 ppm

In this final section, the amount of polymer dissolved in solution and the bulk elasticity were enhanced. From the FRM (G) illustrated in Figure 7. 13, two sets of pressure were selected: for the low deformation range (P1), the liquid pressure was set at 600 mbar for a gas pressure varying from 350 to 650 mbar. For the high deformation domain (P2), the liquid pressure was fixed at 800 mbar for a gas pressure ranging from 500 to 800 mbar. The foam regime map presented similar features than the one depicted at 100 ppm or at a lower molecular weight. In the two regions identified by red arrows in Figure 7. 13 (G), the foam recovery property was

estimated for two different pressure ramps at 0.5 and 2 mbar s⁻¹. All the pressure sets and ramps showed significant hysteresis as summarised in Figure 7. 21 (b).

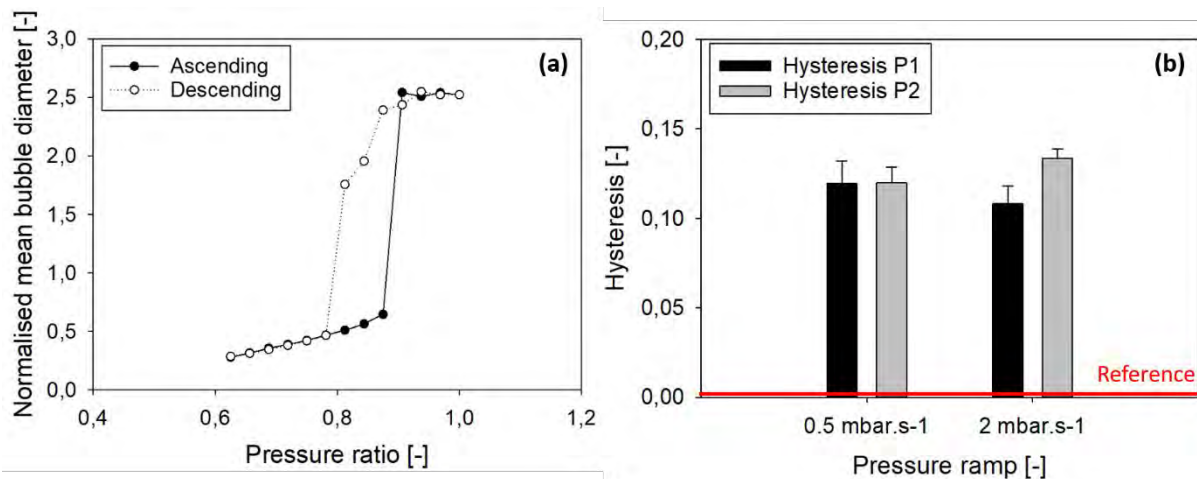


Figure 7. 21 Graph (a) depicts 5 cmc TTAB + 0.05 g L⁻¹ + 300 ppm Mw = 1 x 10⁶ g mol⁻¹ PEO hysteresis evolution in an ascending (continuous black line – black dots) and descending (dotted black line – empty black dots) pressure ramps fixed at 2 mbar s⁻¹ for the highest pressure set (P2). Histogram (b) summarises of the hysteresis evolution for 5 cmc TTAB + 0.05 g L⁻¹ DOH + 300 ppm Mw = 1 x 10⁶ g mol⁻¹ PEO for two pressure sets, low pressure set (P1, black) & high pressure set (P2, grey) for two pressure ramps (0.5 and 2 mbar s⁻¹).

Firstly, a strong difference was observed compared to the 100 ppm case illustrated in Figure 7. 19 due to the rise in polymer concentration. Unlike previously, the hysteresis was almost constant throughout the various experimental conditions investigated. From these results, it was found that hysteresis resulting from the tension-thickening phenomenon was reinforced with the polymer concentration and the molecular weight. To better identify the effect of the molecular weight at high polymer concentration on the transition from the two-row to the bamboo pattern, the experimental flow curves for the case of the highest hysteresis observed at P2 and 2 mbar s⁻¹ was studied.

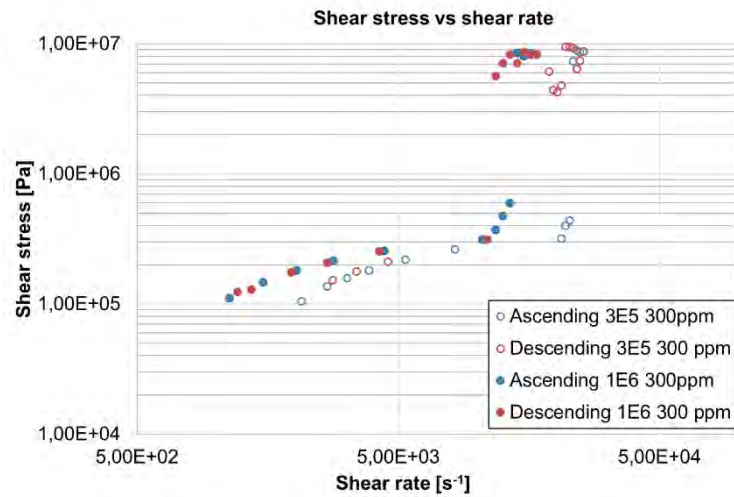


Figure 7. 22 Experimental flow curves plotting the shear stress due to the drag force versus the shear rate for 5 cmc TTAB + 0.05 g L⁻¹ 300 ppm Mw = 3 x 10⁵ g mol⁻¹ PEO solution (empty circle) vs 5 cmc TTAB + 0.05 g L⁻¹ + 300 ppm Mw = 1 x 10⁶ g mol⁻¹ PEO (full circle) at P2 and 2 mbar s⁻¹.

From Figure 7. 22, two things could be identified: firstly, the 1 x 10⁶ set of curves showed higher shear stress for a fixed shear rate compared to the 3 x 10⁵ case. Indeed, a higher molecular weight enhances the elongational viscosity and the drag force at the wall. Secondly, in the descending curve (red), it was remarked that the 3 x 10⁵ formulation showed a higher discrepancy between the two-row and the bamboo regions compared to the 1 x 10⁶ sample for the same concentration and experimental conditions. Indeed, the smallest Mw presented a higher hysteresis than the Higher Mw.

The T1 local rearrangement duration was estimated at 2 ms and 4.8 ms for 450 and 500 mbar gas pressure for 600 mbar liquid pressure respectively. Therefore, even at the highest concentration and Mw, the bulk elasticity did not impact the local rearrangement duration.

Regarding the non-dimensional transition time, at P1 it ranged from $39.0 \pm 2.7 \times 10^{-2}$ at 0.5 mbar s^{-1} to $42.0 \pm 2.3 \times 10^{-2}$ at 2 mbar s^{-1} whereas at P2, it increased slightly and varied from $52.0 \pm 3.6 \times 10^{-2}$ at 0.5 mbar s^{-1} to $49.0 \pm 4.5 \times 10^{-2}$ at 2 mbar s^{-1} .

From these values, it was noted that transition time increased with the pressure set but not with the pressure ramp. However, a closer look to the variation of the transition time with the ascending-descending ramp was necessary. Indeed, two important differences were observed between the ascending and descending ramps that resulted from the hysteresis.

The first difference resided in the gas pressure at which the bamboo pattern was fully completed in the ascending ramp and symmetrically the gas pressure at which the first two-row pattern was found in the descending ramp. This variation was observed for each pressure/ramp configurations. Indeed, in each case, a retardation was observed leading to a late swap from the bamboo to the two-row pattern in the descending ramp compared to the ascending ramp. For instance, at P1 and 0.5 mbar s^{-1} , the initial swapping was completed at 572 mbar in the ascending ramp whereas the reverse transition was completed only at 542 mbar in the descending ramp. If the foam was recovering properly after deformation, and that no hysteresis was observed, the swapping should be performed almost at the same pressure.

However, an average difference was measured at P1 reaching $26.0 \pm 1.3 \text{ mbar}$ for 0.5 mbar s^{-1} and $37.0 \pm 2.2 \text{ mbar}$ at 2 mbar s^{-1} .

At P2, the variation was estimated at $56.3 \pm 1.9 \text{ mbar}$ for 0.5 mbar s^{-1} and at 61.5 ± 1.7 for 2 mbar s^{-1} . It was found that the difference was increasing with the pressure

set and ramp. Thus, the retardation was augmenting with the pressure sets and ramps.

Despite an almost constant hysteresis value for the various experimental conditions, it was demonstrated that the retardation linked to the shear-thickening effect was enhanced with the pressure ramp and set. The second difference was due to the hysteresis leading to a retardation in the descending ramp. The retardation caused also the non-dimensional transition time to shorten in the descending ramp compared to the ascending ramp for all the cases: from 0.44 down to 0.34 for P1 at 0.5 mbar s^{-1} .

7.3 Conclusions

Throughout this chapter, the goal was to evaluate qualitatively which kind of elasticity would influence the most the foam recovery after a gradual deformation for various levels of shearing at the channel wall.

The first finding was that at high DOH concentration, the foam hysteresis was enhanced whereas at low DOH concentration, it showed a negligible hysteresis. This phenomenon was linked to the surfactant dynamics impacted by the presence of DOH in solution which caused the dynamic surface tension to change with the increase in DOH concentration. It was observed also that the ramp had a much greater impact on the foam hysteresis compared to the pressure set. By giving more deformation energy per second, more hysteresis was formed for a much greater amount of insoluble surfactant at or near the interface that could cause not only more surface elasticity but also emphasize viscous dissipation. The impact of surface

elasticity on the gas-liquid interface was confirmed by the increase in the local rearrangement duration observed for the 5 cmc TTAB + 0.05 g L⁻¹ DOH.

Secondly, it was showed that bulk elasticity could enhance even more the hysteresis by introducing a tension-thickening effect. This effect impacted both the existence of hysteresis and its persistence in the cycle of deformation. It was pointed out that the hysteresis was triggered by the presence of polymer in solution for two possible reasons depending on the Mw. For low Mw, the existence of polymer chains in solution implied an emphasis of the viscous friction in the viscoelastic liquid and an increase of the hysteresis. For high Mw, the polymer in the plateau borders rendered the liquid film unstable by enhancing the plateau border permeability and decreased the hysteresis.

Then, the pressure ramp effect on the hysteresis was concentration dependent. At low polymer concentration, the viscous dissipation dominated and the higher the ramp, the more hysteresis was gained. At high polymer concentration, the elastic counterpart became greater compared to the viscous dissipation action and limited the hysteresis by resisting the deformation.

Globally, the impact of the pressure set and the pressure ramp acted differently on the foam hysteresis. Indeed, the pressure set controlled not only the foam pattern but also the action of the liquid flow playing on the polymer chain stretching in the flow direction and thus on the tension thickening effect causing the hysteresis.

Additionally, the hysteresis was found to be reduced by the increase in the polymer molecular weight. Indeed, longer polymer chains enhanced the elongational viscosity and created more viscous dissipation. Furthermore, longer polymer chains in solution

required more energy to be unfolded, moved, stretched in the flow direction. Nevertheless, High Mw polymer enhanced the occurrence and the persistence of the hysteresis. Thus, the action of pressure set and ramp was reduced and the hysteresis was more limited than at lower molecular weight. However, the increase in polymer concentration was still increasing the tension thickening effect and reinforcing the foam hysteretic behaviour.

7.4 List of references

- Baig, C. and Mavrantzas, V. G. (2010) 'Tension thickening, molecular shape, and flow birefringence of an H-shaped polymer melt in steady shear and planar extension', *The Journal of Chemical Physics*. American Institute of Physics, 132(1), p. 14904. doi: 10.1063/1.3271831.
- Barnes, H. A. *et al.* (1989) *An Introduction to Rheology*. Elsevier Science (Rheology Series). Available at: <https://books.google.co.uk/books?id=B1e0uxFg4oYC>.
- Bekiranov, S., Bruinsma, R. and Pincus, P. (1997) 'Solution behavior of polyethylene oxide in water as a function of temperature and pressure', *Phys. Rev. E*. American Physical Society, 55(1), pp. 577–585. doi: 10.1103/PhysRevE.55.577.
- Boger, D. V (1977) 'A highly elastic constant-viscosity fluid', *Journal of Non-Newtonian Fluid Mechanics*, 3, pp. 87–91. doi: 10.1016/0377-0257(77)80014-1.
- Brown, W., Fundin, J. and Miguel, M. da G. (1992) 'Poly(ethylene oxide)-sodium dodecyl sulfate interactions studied using static and dynamic light scattering', *Macromolecules*. American Chemical Society, 25(26), pp. 7192–7198. doi: 10.1021/ma00052a019.
- Cabane, B. and Duplessix, R. (1982) 'Organization of surfactant micelles adsorbed on a polymer molecule in water: a neutron scattering study', *J. Phys. France*, 43(10), pp. 1529–1542. Available at: <https://doi.org/10.1051/jphys:0198200430100152900>.
- Dennin, M. (2004) 'Statistics of bubble rearrangements in a slowly sheared two-dimensional foam', *Phys. Rev. E*. American Physical Society, 70(4), p. 41406. doi: 10.1103/PhysRevE.70.041406.
- Durand, M. and Stone, H. A. (2006) 'Relaxation Time of the Topological T1 Process in a Two-Dimensional Foam', *Physical Review Letters*, 97, p. 226101. Available at: <https://link.aps.org/doi/10.1103/PhysRevLett.97.226101>.
- Feitosa, K. and Durian, D. J. (2008) 'Gas and liquid transport in steady-state aqueous foam', *The European Physical Journal E*, 26, pp. 309–316. doi: 10.1140/epje/i2007-10329-6 LB - Feitosa2008.
- Fu, T. *et al.* (2011) 'Bubble formation in non-Newtonian fluids in a microfluidic T-junction', *Chemical Engineering and Processing: Process Intensification*, 50(4), pp. 438–442. doi: <https://doi.org/10.1016/j.cep.2011.03.002>.
- Fu, T. *et al.* (2012) 'Breakup dynamics of slender bubbles in non-newtonian fluids in microfluidic flow-focusing devices', *AIChE Journal*. John Wiley & Sons, Ltd, 58(11), pp. 3560–3567. doi: 10.1002/aic.13723.
- Fu, T., Ma, Y. and Li, H. Z. (2015) 'Bubble coalescence in non-Newtonian fluids in a microfluidic expansion device', *Chemical Engineering and Processing: Process Intensification*, 97, pp. 38–44. doi: <https://doi.org/10.1016/j.cep.2015.08.008>.
- Karakashev, S. I. and Nguyen, A. V (2007) 'Effect of sodium dodecyl sulphate and

dodecanol mixtures on foam film drainage: Examining influence of surface rheology and intermolecular forces', *Colloids and Surfaces A: Physicochemical and Engineering Aspects*, 293, pp. 229–240. doi: <https://doi.org/10.1016/j.colsurfa.2006.07.047>.

Kim, D. Y., Shim, T. S. and Kim, J. M. (2017) 'Elastic effects of dilute polymer solution on bubble generation in a microfluidic flow-focusing channel', *Korea-Australia Rheology Journal*, 29, pp. 147–153. doi: 10.1007/s13367-017-0016-0 LB - Kim2017.

Mezger, T. G. (2014) *The Rheology Handbook, 4th Edition For users of rotational and oscillatory rheometers*. 4th Editio. Edited by European Coating Tech Files. Hanover, Germany: Vincents Network.

Pitois, O., Fritz, C. and Vignes-Adler, M. (2005) 'Liquid drainage through aqueous foam: study of the flow on the bubble scale', *Journal of Colloid and Interface Science*, 282, pp. 458–465. doi: <https://doi.org/10.1016/j.jcis.2004.08.187>.

Safouane, M. *et al.* (2001) 'Aqueous foam drainage. Role of the rheology of the foaming fluid', in *Journal De Physique. IV: JP*, pp. Pr6275-Pr6280. Available at: <https://www.scopus.com/inward/record.uri?eid=2-s2.0-0035482768&partnerID=40&md5=165856589332dd0611dccbf17a67fab3>.

Safouane, M. *et al.* (2006) 'Viscosity effects in foam drainage: Newtonian and non-newtonian foaming fluids', *European Physical Journal E*, 19, pp. 195–202. doi: 10.1140/epje/e2006-00025-4.

Saint-Jalmes, A. (2006) 'Physical chemistry in foam drainage and coarsening', *Soft Matter*, 2, pp. 836–849. doi: 10.1039/B606780H.

Saint-Jalmes, A. and Langevin, D. (2002) 'Time evolution of aqueous foams: drainage and coarsening', *Journal of Physics: Condensed Matter*, 14, p. 9397. Available at: <http://stacks.iop.org/0953-8984/14/i=40/a=325>.

Scheid, B. *et al.* (2010) 'The role of surface rheology in liquid film formation', *EPL (Europhysics Letters)*, 90, p. 24002. Available at: <http://stacks.iop.org/0295-5075/90/i=2/a=24002>.

Stevenson, P. and Li, X. (2010) 'A viscous–inertial model of foam drainage', *Chemical Engineering Research and Design*, 88, pp. 928–935. doi: <http://doi.org/10.1016/j.cherd.2010.01.014>.

Wang, J., Nguyen, A. V and Farrokhpay, S. (2016) 'Effects of surface rheology and surface potential on foam stability', *Colloids and Surfaces A: Physicochemical and Engineering Aspects*, 488, pp. 70–81. doi: <https://doi.org/10.1016/j.colsurfa.2015.10.016>.

Wang, Y.-L., White, A. R. and Ward, T. (2015) 'Pressure-driven microfluidic flow-focusing of air through a surfactant-doped dilute polymer liquid', *Microfluidics and Nanofluidics*, 18, pp. 343–356. doi: 10.1007/s10404-014-1438-3 LB - Wang2015.

Witte, F. M. and Engberts, J. B. F. N. (1987) 'Perturbation of SDS and CTAB micelles by complexation with poly(ethylene oxide) and poly(propylene oxide)', *The Journal of Organic Chemistry*. American Chemical Society, 52(21), pp. 4767–4772. doi: 10.1021/jo00230a021.

CHAPTER 8

CONCLUSION AND FUTURE WORK

8.1 Conclusions

The aim of the present research was to examine two aspects of foam stability at microscale. Microfluidics was employed to study foam stability in static and in dynamic conditions.

In static conditions, a complete microfluidic study of the impact of a new kind of surface-active agent termed bulk nanobubbles on foam stability was performed. Microfluidics was used as a mean to generate both the surface-active agent and the foam in very well-controlled and environmental-friendly way. The stability study was performed outside the microfluidics channel by studying the evolution of the foam properties over time after microfluidics generation. Bulk nanobubbles generation via microfluidics was optimised with various additives (e.g., surfactants and nanoparticles). The presence of anionic and non-ionic surfactants did not prevent the generation of bulk nanobubble via microfluidics. The properties (foamability and stability) of nanobubble-surfactant stabilised foams were assessed and compared to surfactant stabilised foams for various surfactant concentrations from 0.5, 1, 2.5 and 5 times the cmc of the two surfactants studied.

- (i) *Bulk nanobubbles impacted significantly the foamability and the foam stability for both kind of surfactants.*

This study has identified two mode of actions of nanobubbles at the foam gas-liquid interface: at low surfactant concentration, nanobubbles removed surfactants molecules from the foam gas-liquid interface. Additionally, bulk nanobubbles emphasized foam stability and foamability by enhancing the disjoining pressure in the thin liquid films by increasing the electrostatic repulsion. At low surfactant

concentration, these effects caused an increase destabilisation of non-ionic surfactant foam whereas for anionic surfactant foams, the presence of nanobubbles enhanced foam stability.

This project is the first comprehensive assessment of the effect of bulk nanobubbles on surfactant stabilised foams. These results haven't been reported thus far in the literature. Besides, a publication reporting these results is under preparation. Therefore, the present study lays the groundwork for future research into the use of bulk nanobubbles as surface-active agent for colloidal systems. Overall, this work strengthens the idea that bulk nanobubbles present a very promising and environmental-friendly alternative to reduce the amount of surfactant or nanoparticles employed in formulations for various industrial applications such as for food dairy products (ice cream) or washing liquids (shampoos, detergent). Although this study focused on foams, the findings may well have a bearing on other colloidal systems such as emulsions. Despite this very promising first results, the impact of nanobubbles concentration in the process of stabilisation or destabilisation remained unclear. Furthermore, there was a lack of understanding of the impact of bulk nanobubbles adsorption on the gas-liquid interfacial rheological properties.

The dynamic foam stability investigation was realised by generating the foam in-situ and studying its properties in the microfluidics expansion channel via optical microscopy. A feature of foam stability is represented by the foam ability to resist to the deformation and to recover its initial properties after deformation.

- (ii) *A microfluidic approach was developed to evaluate the foam recovery properties after a deformation.*

Thereby, the influence of the rheological properties of the foaming liquid on the foam hysteretic behaviour was investigated.

This is the first study of substantial duration which examines the parameters influencing foam hysteretic behaviour via microfluidics. This work generated an article published in *Microfluidics and Nanofluidics Journal*. The present study has gone some way towards enhancing our understanding of the mechanisms triggering or enhancing foam hysteresis in a microchannel. The approach introduced here has potential applications in a wide range of industrial processes where foams are generated and submitted to a series of deformation steps along the process line from food industrial applications to biological systems. This method could lead to the development of an accessible quality control tool to study the parameters (surfactant nature and properties, viscosity, viscoelasticity of the continuous phase, etc.) impacting significantly the foam recovery properties at the lamellae scale. Additionally, the insights gained from this study may be of assistance to study foam time-dependency at micron-scale, an important property when microfluidics is used to generate or to study foams for industrial purposes from the generation of solid foams (Andrieux *et al.*, 2017, 2018) to the study of foam flow through porous materials such as in the Enhanced Oil Recovery (EOR) application (Nguyen *et al.*, 2014; Quennouz *et al.*, 2014).

(iii) *The study of the effect of the surface elasticity on foam hysteresis confirmed the influence of the surface elasticity on the local bubble rearrangement duration as reported in the literature.*

The hysteresis was enhanced in the case of the highest DOH concentration assumed as highest elasticity. However, this result can only be partially related to the surface elasticity because the dynamic surface tension was also impacted by the concentration of DOH in solution.

(iv) The impact of bulk elasticity on foam hysteresis and its dependence on the polymer concentration and molecular weight (Mw) were clearly identified.

The highest hysteresis was observed for the highest concentration and the lowest Mw. Interestingly, the highest Mw decreased the hysteresis at low polymer concentration whereas it reinforced and made the hysteresis more persistent at high polymer concentration.

Two mechanisms enhancing the foam hysteretic behaviour were determined: the viscous dissipation linked to the increase in viscosity emphasized the hysteretic behaviour in the channel. Secondly, the tension-thickening phenomenon affected significantly the hysteresis and its effect depended on the polymer concentration and molecular weight.

8.2 Future work

The first part of this project was undertaken to optimise the generation of bulk nanobubbles and to evaluate their effect on surfactant-stabilised foams via microfluidics.

(i) Determination of bulk nanobubbles concentration

In Chapter 4, the effect of several parameters on the bulk nanobubbles size distribution and zeta potential was investigated. All the promising results reviewed so

far, however, suffer from the fact that there was no quantification of the concentration of nanobubbles in solution. Therefore, the study should be repeated using for instance Nanoparticle Tracking Analysis (Nanosight, NTA) which would be of great interest to evaluate the nanobubble concentration in solution as employed by Nirmalkar *et al.*, (2018). More broadly, research is also needed to determine the effect of bulk nanobubble concentration for a fixed concentration of surfactant.

(ii) *Determination of bulk nanobubbles interactions with various surfactants*

I suggest that before the nanobubble concentration contribution is introduced, a study like this one should be carried out on the effect of bulk nanobubbles on foams stabilised by cationic surfactants. More information on the electrostatic interactions would help to establish more accuracy on the matter of the mechanisms at stake in nanobubble-surfactant interactions. Additionally, further experiments, using a broader range of surfactants (molecular weight, HLB) could shed more light on the interactions between the nanobubbles and the surfactants and their impact on the surfactant adsorption at the foam interface.

(iii) *Study of bulk nanobubbles interactions with partially hydrophobized nanoparticles*

A natural progression of this work is to analyse the effect of nanobubbles on partially hydrophobized nanoparticles dispersions. Indeed, it has been demonstrated that nanobubbles are capable of attaching or nucleating on Gold nanoparticle above a critical nanoparticle diameter (Zhang and Seddon, 2016). Furthermore, bulk nanobubbles were found to enhance the aggregation of hydrophobic nanoparticles dispersions in a stirred vessel (Knüpfer *et al.*, 2017). These two papers prove that

nanobubbles can impact significantly colloidal systems where nanoparticles play a significant role, such as Pickering foams or emulsions. Therefore, a full study on the impact of bulk nanobubbles on nanoparticle stabilised systems is necessary.

(iv) Study of bulk nanobubbles impact on interfacial properties

Further research needs to examine more closely the links between the interfacial properties and the adsorption of bulk nanobubble at the gas-liquid interface. Indeed, the adsorption of nanobubbles at the gas-liquid interface need to be investigated because this parameter plays an important role in foam stability. Further work should be undertaken to explore how bulk nanobubble could compete with insoluble surfactant at the gas-liquid interface such as dodecanol. Further investigation and experimentation into the study of nanobubbles adsorption at the gas-liquid interface via Langmuir Blodgett trough is strongly recommended.

The second aim of this study was to assess the parameters influencing foam hysteretic behaviour via microfluidics.

Despite the environmental-friendly and interesting approach that offered this work, this method of analysis had a few limitations. First, this method does involve potential measurement errors due to the estimation of the film thickness at the wall via image analysis and the evaluation of the bubble velocity via PIVlab software (William Thielicke, 2014). In spite of its limitations, the study certainly adds to our understanding of the foam hysteretic behaviour that had been previously observed in microchannels. Secondly, approaches of this kind carry with them various well-known limitations among which the nature of samples that can be investigated. Indeed, the use of micron-sized channels to generate foam narrowed down the range of

viscosities that could be employed. Thirdly, the method is based on the transition between two foam structures, namely, the two-row and the bamboo patterns. Nevertheless, as observed in the various foam regime maps investigated, these two patterns were not available for all the domains of deformation. For instance, the investigation of the shear-thinning property was limited because of the Xanthan Gum effect on the foaming ability in the microchannel. Indeed, only one shear-thinning solution was studied. Nonetheless, from our preliminary results, it is believed that the shear thinning behaviour impacted significantly foam hysteresis. Further studies need to be carried out in order to validate the shear-thinning effect on foam hysteresis.

The bulk elasticity showed to impact significantly the foam hysteresis. However, the precise mechanism of how the polymer chains act when the gas-liquid interface is being deformed remains to be elucidated.

(v) *Impact of bulk elasticity on the flow of a single bubble in a microchannel*

Further research could usefully explore how the impact of bulk elasticity on the flow of a single bubble through an expansion channel with or without deformation via birefringence analysis. As an example, the elastic properties of worm-like micelles solutions were investigated via a cross-slot microfluidics device by combining PIV and birefringence analysis of the flow through a constriction as described by Dubash et al., (2012). Thus, the bulk elasticity could be tuned easily by varying the polymer concentration and molecular weight. Its effect on the bubble flow and deformation could be evaluated for various range of deformation controlled by the fluid velocity around the bubble or by the presence of obstacles on the bubble trajectory in the channel.

Further research in this field would be of great help in determining the parameters influencing the property of recovery of specific industrial products from food foams (Lazidis *et al.*, 2016) to foams employed for varicose veins treatment (Carugo *et al.*, 2015).

(vi) *Study of thin liquid film hysteretic behaviour*

To complement our microfluidics approach to evaluate foam hysteresis, an additional approach would be to study the thin film hysteretic behaviour. Indeed, Seiwert *et al.*, (2017) developed a method to reproduce at the local scale the deformations occurring in films in a 3D sample (compression, dilatation and shear) via an optical technique based on the use of fluorescent surfactant. Thus, the study of the flow evolution within a single thin liquid film submitted to various deformation can be performed. Thus, the impact of the parameters studied in this work on the single thin liquid film hysteretic behaviour could be further investigated by consecutively deforming a single film via dilatation/compression or shearing.

A greater focus on the evolution of the liquid flow within a single film submitted to consecutive stage of deformation could produce interesting findings accounting more for the actual film properties (thickness, elasticity) than our methods. Thereby, this would be a fruitful area for further work on the hysteretic behaviour at the scale of a single thin liquid film.

8.3 Reference

Andrieux, S., Drenckhan, W. and Stubenrauch, C. (2017) 'Highly ordered biobased scaffolds: From liquid to solid foams', *Polymer*. doi: <http://doi.org/10.1016/j.polymer.2017.04.031>.

Andrieux, S., Drenckhan, W. and Stubenrauch, C. (2018) 'Generation of Solid Foams with Controlled Polydispersity Using Microfluidics', *Langmuir*. doi: [10.1021/acs.langmuir.7b03602](https://doi.org/10.1021/acs.langmuir.7b03602).

Carugo, D. *et al.* (2015) 'The role of clinically-relevant parameters on the cohesiveness of sclerosing foams in a biomimetic vein model', *Journal of materials science. Materials in medicine*. 2015/10/08. Springer US, 26(11), p. 258. doi: [10.1007/s10856-015-5587-z](https://doi.org/10.1007/s10856-015-5587-z).

Dubash, N., Cheung, P. and Shen, A. Q. (2012) 'Elastic instabilities in a microfluidic cross-slot flow of wormlike micellar solutions', *Soft Matter*. The Royal Society of Chemistry, 8(21), pp. 5847–5856. doi: [10.1039/C2SM25215E](https://doi.org/10.1039/C2SM25215E).

Knüpfer, P., Ditscherlein, L. and Peuker, U. A. (2017) 'Nanobubble enhanced agglomeration of hydrophobic powders', *Colloids and Surfaces A: Physicochemical and Engineering Aspects*, 530, pp. 117–123. doi: <https://doi.org/10.1016/j.colsurfa.2017.07.056>.

Lazidis, A. *et al.* (2016) 'Whey protein fluid gels for the stabilisation of foams', *Food Hydrocolloids*, 53, pp. 209–217. doi: <https://doi.org/10.1016/j.foodhyd.2015.02.022>.

Nguyen, P., Fadaei, H. and Sinton, D. (2014) 'Pore-Scale Assessment of Nanoparticle-Stabilized CO₂ Foam for Enhanced Oil Recovery', *Energy & Fuels*, 28,

pp. 6221–6227. doi: 10.1021/ef5011995.

Nirmalkar, N., Pacek, A. W. and Barigou, M. (2018) 'Interpreting the interfacial and colloidal stability of bulk nanobubbles', *Soft Matter*. The Royal Society of Chemistry, p. doi: 10.1039/C8SM01949E.

Quennouz, N. *et al.* (2014) 'Microfluidic study of foams flow for enhanced oil recovery (EOR)', *Oil and Gas Science and Technology*, 69, pp. 457–466. doi: 10.2516/ogst/2014017.

Seiwert, J. *et al.* (2017) 'Velocity Field in a Vertical Foam Film', *Phys. Rev. Lett.* American Physical Society, 118(4), p. 48001. doi: 10.1103/PhysRevLett.118.048001.

William Thielicke, E. J. S. (2014) 'PIVlab – Towards User-friendly, Affordable and Accurate Digital Particle Image Velocimetry in MATLAB', *Journal of Open Research Software*, 2(1). doi: <http://doi.org/10.5334/jors.bl>.

Zhang, M. and Seddon, J. R. T. (2016) 'Nanobubble–Nanoparticle Interactions in Bulk Solutions', *Langmuir*, 32, pp. 11280–11286. doi: 10.1021/acs.langmuir.6b02419.

APPENDICES

A.1 Surface characterisation of nanobubbles via Atomic Force Microscopy

Atomic Force Microscope (AFM) have arisen from a well-known class of microscopy called scanning probe microscopy (SPM) (McConney, Singamaneni and Tsukruk, 2010).

AFM working principle is based on the probe-sample interactions while the probe is scanning the sample. The probe refers to the cantilever/tip assembly. During a scan, the vertical and horizontal motions of the tip are monitored via the laser beam reflected off the cantilever and tracked by a position sensitive photo-detector (PSPD) as illustrated in Figure A- 1.

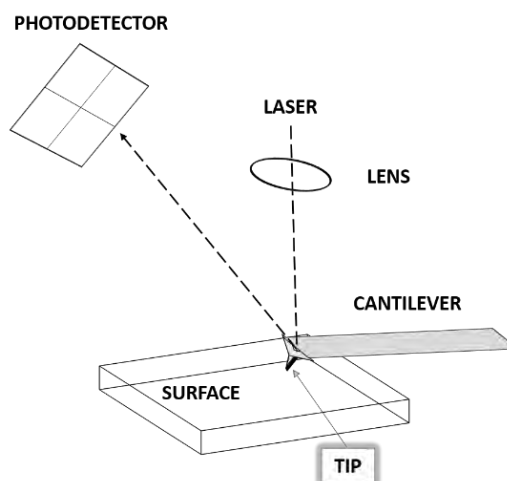


Figure A- 1 Schematic representation of AFM working principle

Thanks to its nanometre resolution, AFM enables to visualise and to probe structures down to molecular scale. Thereby, AFM was the first technique employed to study

nanoscale bubbles seating on a hydrophobic surface (Highly Orientated Pyrolytic Graphite, HOPG) (Lou *et al.*, 2000). This paper was the starting point of full body of literature dealing with the characterisation of surface nanobubbles on various surfaces and in various conditions.

The literature reporting the characterisation of bulk nanobubbles on a surface using AFM is almost inexistent. Indeed, the few papers that are likely to present those results mainly imply surface nanobubbles: from the generation techniques used in these studies, both bulk and surface nanobubbles can be produced.

Furthermore, there is a relatively small body of literature that is concerned with the link between surface nanobubbles and bulk nanobubbles. Thus far, no research group claimed that the attraction of bulk nanobubbles on a surface was possible. Therefore, it is assumed that these groups managed to image bulk nanobubbles on the surface, but it is also very likely that these bubbles were only surface nanobubbles.

The first aim of this characterisation work is to prove that the entities present on a hydrophobic surface covered with pure water or with bulk nanobubble solution generated from pure water via microfluidics are nothing but bubbles and certainly not nanoparticles. The second objective is to observe if the presence of bulk nanobubbles in solution generated via microfluidics could enhance the number of bubbles observed on a hydrophobic surface.

Principle

An AFM is used to scan a surface with a tip mounted on a cantilever to obtain the surface topography. The deflection of the cantilever is recorded during the scan

which is related to the interaction between the tip and the surface (Butt, Cappella and Kappl, 2005).

Three imaging modes are available; namely, the contact and the tapping and the non-contact modes as illustrated in Figure A- 2.

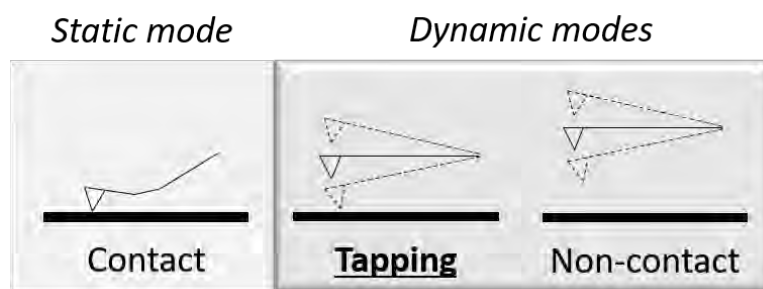


Figure A- 2 Schematic representation of AFM static (contact mode) versus dynamic modes (tapping & non-contact).

In contact mode AFM (static), the tip is permanently in contact while scanning the surface and the deflection of the cantilever is kept constant. It is therefore easier to damage the substrate while scanning as more friction forces are occurring. Only topography image is obtained. It is possible to use contact mode AFM to image nanobubbles (Holmberg *et al.*, 2003) but the experimental conditions have to be very well controlled to prevent from moving the bubble upon contact

In dynamic modes such as tapping mode AFM, the cantilever is oscillated at its resonance frequency via a piezoelectric driver. The oscillating tip at its resonance frequency and at certain amplitude is intermittently contacting the surface. Upon contact, the resonant frequency, the amplitude and the phase of oscillation are influenced due to the tip-sample interactions (McConney, Singamaneni and Tsukruk, 2010). From the evolution of the amplitude and the phase, two kinds of image can be obtained:

- The height image related to the surface topography of the substrate.
- The phase image linked to the surface properties of the substrate.

Thus far, tapping mode AFM have been widely used to characterise surface nanobubbles. The phase image gives a first idea of the physical properties of an entity on a surface but it will not enable to differentiate between a nanodroplet and a nanobubble (Berkelaar *et al.*, 2014).

In (Ishida *et al.*, 2000; Lou *et al.*, 2000), researchers reported for the two first times the imaging of surface nanobubbles using tapping mode AFM on HOPG surface. Later, in (Bharat, Yuliang and Abdelhamid, 2008), surface nanobubbles were imaged on a polystyrene surface via tapping mode AFM.

Protocol

AFM was performed with a JPK Nanowizard instrument. A “V”-shaped soft contact silicon nitride (Si_3N_4) cantilever was purchased from Budget Sensors (UK) with a 15 nm tip radius, a nominal spring constant (k_c) of 0.27 N m^{-1} and a resonance frequency of 30 kHz in air. This cantilever is suitable for both tapping mode imaging and force spectroscopy in contact mode measurement in liquid. In the literature, cantilever spring constants employed to characterise nanobubbles were reported and varied from 0.06 to 0.58 N m^{-1} (Zhang *et al.*, 2005; Zhang and Ducker, 2007).

To remove any organic contaminants, the cantilever was left prior to experiment for 25 min on a clean glass slide under UV light. Each cantilever was used maximum three times to preserve the quality of the measurement. All AFM experiments were performed at ambient temperature. Depending on the scan resolution (512 by 512 or

1024 by 1024) and the scan speed, it took between 10 to 40 minutes to obtain an image.

Surface nanobubbles were generated by direct deposition of a droplet of aqueous solution on HOPG using a 10 -100 μL automatic pipette. The atomically flat HOPG surface was freshly cleaved before each experiment by peeling off the outermost layers with glossy tape. A typical tapping-mode AFM image in air of HOPG after cleavage is shown in Figure A- 4 .

Bulk nanobubbles were freshly generated beforehand via microfluidics. The bulk nanobubbles water was left to settle for 30 minutes on the surface before scanning. In this work, the interface between HOPG (ZYB grade, 22 by 22 mm from Bruker Ltd) and various aqueous solutions is investigated by AFM. All the solutions in this section were prepared using Millipore distilled water (18.2 mS cm^{-1}).

As a control method to generate and to characterise surface nanobubbles on a surface, an electrochemical generation method was employed. Indeed, in (Zhang *et al.*, 2006; Yang *et al.*, 2009), surface nanobubbles were generated on HOPG surface via electrolysis of various aqueous solution. More precisely, in (Zhang *et al.*, 2006), hydrogen nanobubbles were generated by applying sufficient negative voltage to the a diluted solution of sulfuric acid (0.01M). The electrochemical generation of nanobubbles consists in applying a voltage (positive or negative) on a conductive surface (HOPG) placed in an electrolyte solution. The conductive surface acts either as the cathode (negative electrode) or as the anode (positive electrode). When a negative voltage is applied, hydrogen nanobubbles are formed on the conductive surface such as $2 \text{ H}^+ + 2\text{e}^- \rightarrow \text{H}_2$, whereas when a positive voltage is applied, the

following reaction takes place, $\text{H}_2\text{O} \rightarrow 2\text{H}^+ + 2\text{e}^- + 0.5 \text{O}_2$ and oxygen nanobubbles are generated.

The JPK Electrochemical cell (EC cell) was operated to generate hydrogen surface nanobubbles on a HOPG surface attached to a copper substrate via a two-part conductive adhesive. A Platinum wire dipped in the diluted acidic solution was used as a counter electrode. The Ag/AgCl electrode was employed both as reference electrodes. The diluted sulfuric acid solution was prepared one day prior to experimentation by dissolving sulfuric acid powder in distilled water. A pH of 2.6 was measured at 20°C. The electrodes were connected to a potentiostat-galvanostat (Autolab Pgstat 101 from Metrohm). A voltametric cycle with ramp of voltage from -0.5 to -1.5 V was applied. Tapping mode AFM was then used to image the surface and force spectroscopy in contact mode was employed to measure the physical properties of the nanobubbles on the surface by applying a load of 500 pN.

A.1.1 Direct force measurement: Atomic Force Microscopy (AFM)

Once showing the existence of nanoscale entities on the hydrophobic surface, it was necessary to evaluate their physical properties by probing their surface with a very small force (500 pN) to prove that these entities were indeed softer compared to the surface.

Principle

AFM resolution makes it a powerful tool to probe the forces at stake in colloidal systems. Indeed, interactions forces such as Van der Waals attractive forces and repulsive electrostatic forces between the tip and sample can be evaluated by AFM force spectroscopy.

In this mode, a chip onto which a cantilever is attached, is moved up or down by applying a voltage to the piezoelectric translator while measuring the cantilever deflection (Butt, Cappella and Kappl, 2005). While the chip is being moved, the cantilever reacts to its surrounding and deflects due to the interactions existing between the cantilever and its environment (sample, surface). Thus, when the cantilever is approached or withdrawn to/from a surface or sample, the cantilever deflection relates to the forces the cantilever is submitted to for a specific load applied and distance.

Force spectroscopy measurement provides a force versus tip-sample separation distance curve both in approach (red) and in retraction (blue). As described in (Butt, Cappella and Kappl, 2005), this curve is obtained from the measure of the cantilever deflection (Z_c) versus the position of the piezoelectric translator normal to the surface (Z_p) which corresponds to the force F versus the d , the tip-sample separation distance such as $F = Z_c k_c$ with k_c the cantilever spring constant and $d = Z_c + Z_p$ respectively. The schematic of the measuring steps during a single force measurement is given in Figure A- 3.

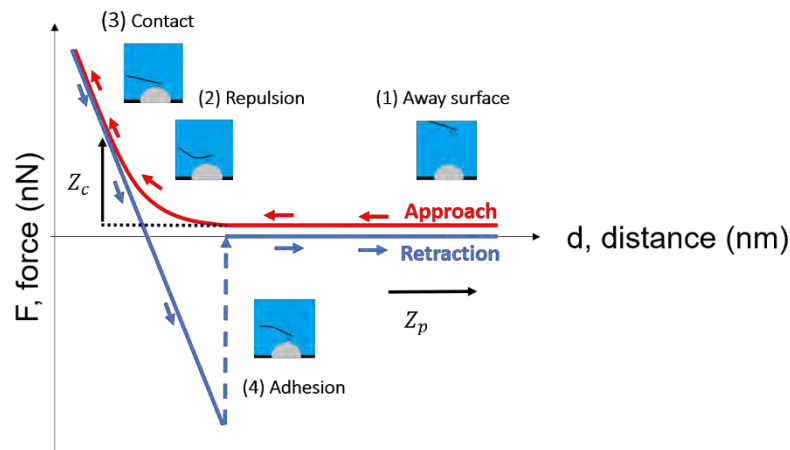


Figure A- 3 Schematic representation of a typical cantilever deflection vs piezo height (Z_c vs Z_p) which can be simplified as a force versus distance curve throughout the different steps composing the cycle of approach (red) and retraction (blue).

The deflection is obtained by the optical lever technique: a beam from a laser diode is focused onto the end of the cantilever and the position of the reflected beam is recorded by a position sensitive photo-detector (PSPD) (Butt, Cappella and Kappl, 2005). Consequently, when a force is applied, the cantilever bends and the reflected beam moves through an angle equal to twice the change of the cantilever endslope (dZ_c/dx) (Butt, Cappella and Kappl, 2005).

In the literature, three main AFM force spectroscopy techniques were used to study surface nanobubbles: direct force spectroscopy in contact mode, Peak-Force Quantitative Nanomechanics (PF-QNM), and the colloidal probe technique.

Here, force measurement in contact mode was employed. In this method, the tip approaches the surface at a constant speed and with a constant load. The tip is considered as being in contact with the surface when the resultant of the force applied balances the initial load applied. After contacting the surface, the tip retracts from the surface and goes back to its original z-position. The term “force mapping” describes a function of force spectroscopy mode creating a 2D map at the same z position ($1 \mu\text{m}$) from an area/image.

Derived from the tapping mode force spectroscopy, the mode called PF-QNM consists in measuring the same force than contact mode but repeated at each tapping on the surface at high frequency and at low amplitude for bubbles. In (Zhao *et al.*, 2013), PF-QNM was used to measure the stiffness of surface nanobubbles in various conditions. In (Song *et al.*, 2014), force-distance curves were obtained for nanobubble generated by ethanol-water exchange. In (An, Tan and Ohl, 2016), PDMS nanodroplets and hydrogen nanobubbles were compared and characterised by PF-QNM.

Finally, the colloidal probe technique consists in employing a micron-sized sphere with a well-defined radius glued onto the end of a tipless cantilever. The sphere radius can vary from 1 to 50 μm and can be made of different materials (Silica (Ducker, Xu and Israelachvili, 1994), glass (Butt, 1991)..). With the colloidal probe technique, forces can be analysed more quantitatively because the surface area in contact with the sample is larger and of known geometry. Therefore, the total interaction force is higher and thus the measurement more sensitive.

In the past 20 years, experiments were made to measure forces between gas bubbles and hydrophobic or hydrophilic particles in liquid media such as glass sphere in water in (Butt, 1991). In the field of surface nanobubbles, the colloidal probe technique was used in (Hampton, Donose and Nguyen, 2008) to study the effect of different solvent-water exchanges on the number and size of nanobubbles on the surface using a silica sphere attached to a cantilever in water. In (Zhang, Kumar and Scales, 2011), the interactions between a carbon sphere and nanobubbles in ethanol-water solutions on Highly Orientated Pyrolytic Graphite (HOPG) were examined.

In this work, force spectroscopy in contact mode was preferred to determine the physical properties of surface nanobubbles and of bulk nanobubbles attracted to a surface. This technique is efficient and straightforward. Indeed, the force measurement can be done directly after the imaging with the same tip after calibration on the surface in the medium.

Force spectroscopy data analysis

The analysis of the force curve enables to determine the forces acting between the tip and the sample. Several phenomena can be encountered: from the repulsive electrostatic forces occurring at very small distances to the Van der Waals attractive forces due to overlapping of electron orbitals between tip and sample atoms, to the hydrophobic-hydrophobic or hydrophobic-hydrophilic interactions. Nanobubbles present a negative surface charge due to their negative zeta potential (Cho *et al.*, 2005). Therefore, a repulsive electrostatic interaction could be observed because in (Butt, 1991), it was showed that the silicon nitride tip is hydrophilic and slightly negatively charged due to hydroxyl groups on its surface.

From a force versus distance curve, the interactions between the tip and the sample can be studied and the physical properties of a sample can be evaluated. Indeed, the stiffness of the material being probed can be obtained from the slope in the contact region of the force versus distance curve previously represented in Figure A- 8.

As stated in (Butt, Cappella and Kappl, 2005), if we consider the tip-sample separation distance d such as $d = Z_p + Z_c + \delta$ with δ the tip indentation. In contact, d is equal to 0 and with k_s the sample stiffness, then if the system is in equilibrium $k_s \delta = k_c Z_c$.

By substituting, the following relationship is obtained:

$$k_c Z_c = - \frac{k_c k_s}{k_c + k_s} = k_{eff} Z_p \quad (3-1)$$

If the sample is much stiffer than the cantilever ($k_s \gg k_c$), then $k_{eff} \approx k_c$; if the sample is softer than the cantilever ($k_c \gg k_s$), then $k_{eff} \approx k_s$ (Butt, Cappella and Kappl, 2005).

In (Attard and Miklavcic, 2001), it was showed that microbubble behave like Hookean springs. Thus, equation (3-5) was used to determine the bubble stiffness k_b from the slope measured in the contact line, k_{eff} :

$$\frac{1}{k_{eff}} = \frac{1}{k_c} + \frac{1}{k_b} \quad (3-2)$$

The stiffness measured in (Zhang, Maeda and Craig, 2006) prove that the bubble was softer than the HOPG surface. In (Zhao *et al.*, 2013), it was reported that the stiffness of surface nanobubbles generated by ethanol-water exchange on HOPG measured by PF-QNM was in the range of 0.06 to 0.12 N m⁻¹ compared to the stiffness of HOPG estimated at 0.6 to 0.8 N m⁻¹ in distilled water. In (Ducker, Xu and Israelachvili, 1994), a silica nanoparticle attached to cantilever was employed to measure the stiffness of an air microbubble in water. The bubble stiffness reported was 0.065 N m⁻¹. The values reported in the literature will be used as benchmark values for this work. Thus, force spectroscopy in contact was chosen to evaluate the properties of nanoscale entities observed on an atomically flat hydrophobic surface within a liquid droplet and to compare these physical properties to the surface properties in water.

Protocol

After confirming the presence of nanobubbles on the surface using tapping mode imaging, the tip calibration was performed in liquid on HOPG using force spectroscopy mode for a force or set-point of 500 pN. To locate the tip on the nanobubble during force spectroscopy measurement, force mapping function was used to determine the tip-surface interaction via a force versus distance curve obtained for each pixel composing the map. Therefore, 32 by 32 or 16 by 16 pixels force map was realised on a well-defined area which was imaged previously in intermittent contact mode: the set-point was fixed at 500 pN, the z-length at 1 μm , and the scan rate 2 $\mu\text{m s}^{-1}$. The 500 pN set-point was carefully selected considering the deformable and fragile nature of nanobubbles (Zhao *et al.*, 2013).

Each force curve corresponding to a dedicated pixel on the map was analysed. The JPK data processing software was employed for AFM image and force distance curve processing. The stiffness was extracted from the measurement of the slope in the contact region of the force versus distance curve and further computed via equation (3-5) The results obtained for each force versus distance curve are presented in histogram representing the stiffness distribution throughout the map.

A.1.2 Results and discussion

A.1.2.1 Pure water versus bulk nanobubbles water generated via microfluidics

As described previously, Atomic Force Microscopy (AFM) was employed to probe the physical properties of nanobubbles on a surface. Two kinds of solutions were analysed on HOPG: pure water and bulk nanobubbles water generated via microfluidics. The reference surface, HOPG, was firstly imaged in air via tapping-mode AFM. Thus, the root-mean-square (RMS) surface roughness and the peak-to-

valley roughness were approximated to 261 pm and 1.2 nm respectively. This showed that HOPG was atomically flat. The height and phase images of HOPG in air are represented in Figure A- 4:

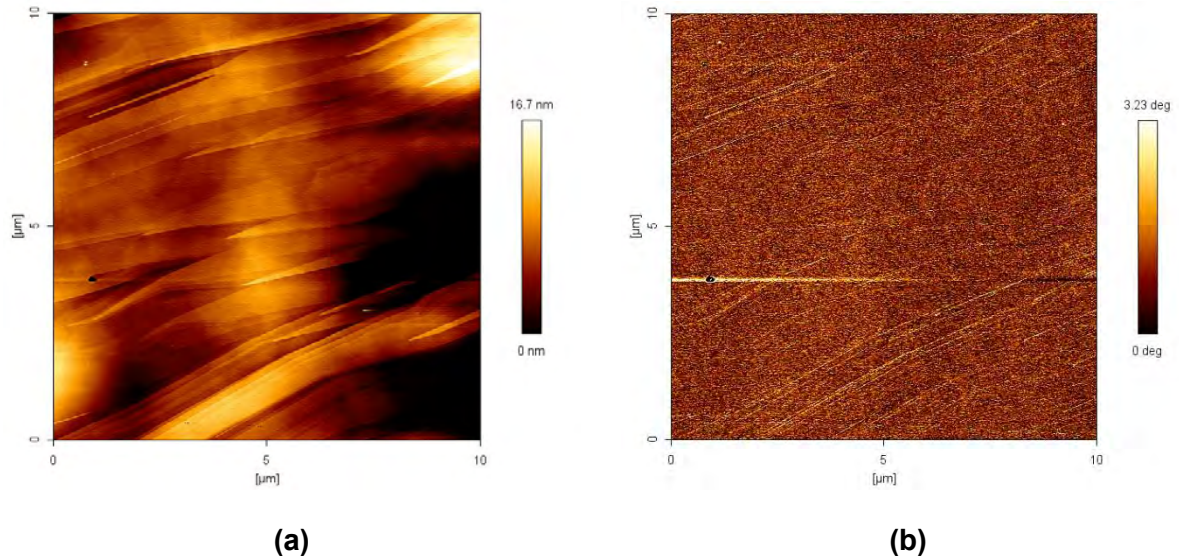


Figure A- 4 10 by 10 um height (a) and phase (b) images of HOPG in air imaged by tapping mode AFM.

Then, a droplet of pure water was deposited on the surface. An area of 2.5 by 2.5 μm was imaged by tapping-mode AFM. The resulting height and phase images are showed in Figure A- 5.

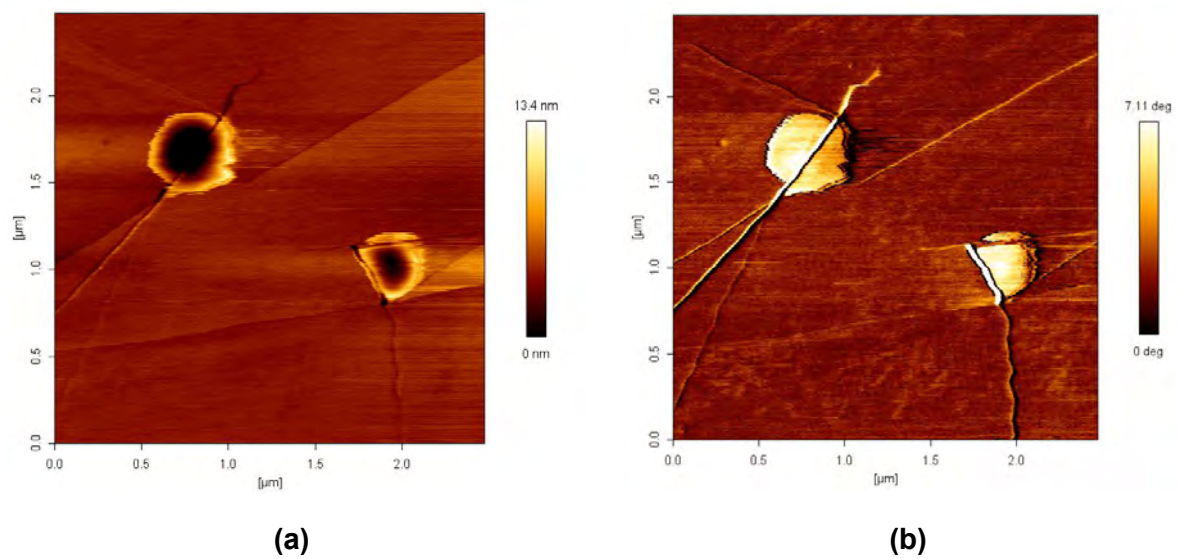
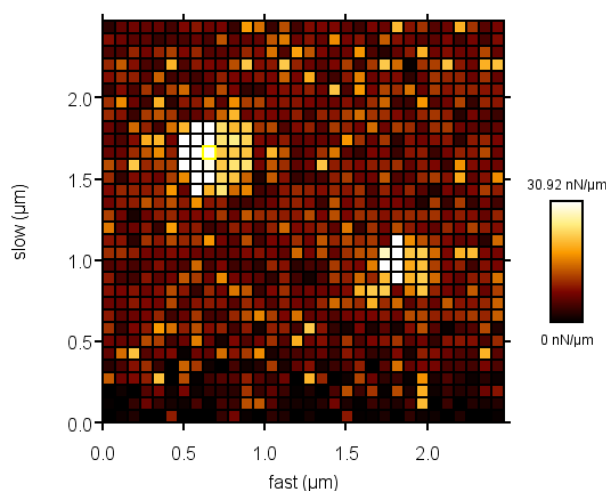


Figure A- 5 2.5 by 2.5 μm height (a) and phase (b) images obtained by tapping-mode AFM in a droplet of pure water deposited on HOPG.

From the phase image which describes the surface properties, it was possible to see that the two entities presented on the surface present a different physical nature than the hard HOPG surface. With the use of the cross-section tool on the JPK Nanowizard software, it was found that the diameters and heights of these entities were respectively ranging from 300 to 500 nm and from 9 to 14 nm. They were randomly distributed on the surface and their number could vary between the experiments. The features were like spherical-like caps.

To confirm this observation, direct force measurement was used to characterise the bubbles by applying a force of 500 pN on the surface and on the bubble and by measuring the resulting mechanical motion of the cantilever. Force mapping mode was employed to cover methodically as many measurement points as possible on the image obtained by tapping mode. The force map obtained is depicted in Figure A- 6.



Slope [N/m] map in retraction

Figure A- 6 32 by 32 pixels relative stiffness map realised from the slope of the retraction curve obtained for each pixels of the map from the previous 2.5 by 2.5 μm area.

A significant contrast could be observed between the bubbles and the surface. Thus, we demonstrated that the entities presented different physical properties from the surface. A closer look to a typical force versus distance curves for the HOPG surface in water and for the bubble on HOPG in water was required to understand the surface forces at stake in the different situations encountered during this experiment.

In Figure A- 7 is represented a typical force versus distance curve obtained for the HOPG surface in distilled water for this experiment. The red and blue curves correspond to the approach and retraction curves respectively. The different phenomena occurring between the tip and the surface in water during the approach and retraction are represented by the different drawings numbered from 1 to 4.

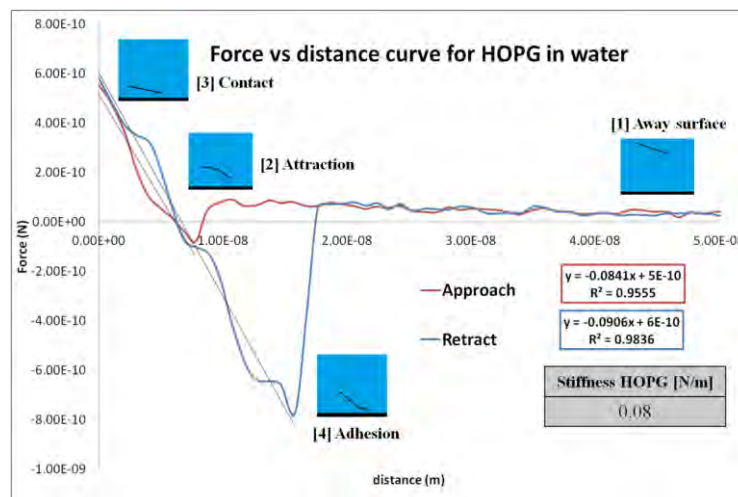


Figure A- 7 Force versus distance curves for the cycle of approach (red) and retraction (blue) of the cantilever dipped in pure distilled water contacting the HOPG surface.

Then, in Figure A- 8, for the same load applied, the force versus distance curve illustrating the tip-bubble interactions is provided. The different phenomena occurring between the tip and the bubble on the surface in water during the cycle of approach and retraction are represented by the different drawings numbered from 1 to 5.

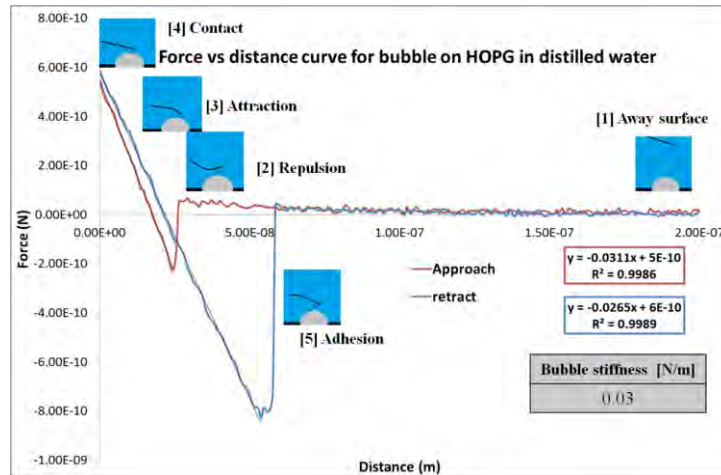


Figure A- 8 Force versus distance curves for the cycle of approach (red) and retraction (blue) of the cantilever dipped in pure distilled water contacting the bubble surface seating on the HOPG surface.

While approaching in the first position, the tip reacted firstly the electrical double layer and the Van der Waals forces acting between the tip and the sample. Therefore, in second position, a very small repulsion was expected between the tip and bubble during the approach. Upon contacting the surface, the hydrophobic-hydrophilic attraction took place between the tip and the bubble causing the jump-to-contact of the tip onto the surface in third position and the adhesion in approach to occur between the fourth and fifth stages.

The indentation can be measured from the force versus distance curve. The tip penetrated 20 nm down the entity whereas the entity height measured by the cross-section was 12 nm. Therefore, it can be considered that the tip was very likely touching the solid surface at the end of the contact zone. It is assumed that the tip while penetrating the bubble surface was not piercing the bubble. Otherwise, the bubble would simply burst and disappear.

Considering the tip was covered by a thin film of water while penetrating and reaching the solid surface, upon retraction, the tip tried to pull off the surface but bent due to the adhesion force.

As exposed previously, the slope in the contact region can be averaged as the stiffness of the substrate as a first approximation. Considering the full map realised previously, each pixel of the map representing a force versus distance curve was analysed to generate the two distributions illustrated in Figure A- 9 extracted from the map corresponding to the bubble (blue) versus the surface (red) relative stiffness (slope) distributions.

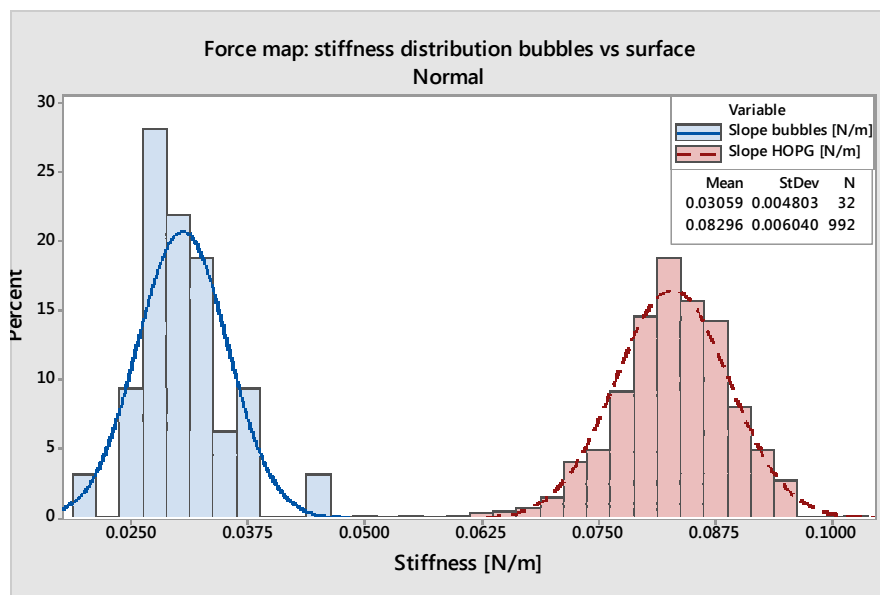


Figure A- 9 Relative stiffness distribution obtained from the force map representing the stiffness measured from surface pixels in red versus the bubble pixels in blue.

This histogram emphasizes well the contrast observed previously. If the slope in the contact region was considered directly as the stiffness, then the HOPG surface stiffness, $0.08 \pm 0.0002 \text{ N m}^{-1}$ was greater than the bubble stiffness, $0.03 \pm 0.0007 \text{ N m}^{-1}$. Using the Hooke's law approximation, the effective stiffness was calculated. The surface stiffness, 0.2 N m^{-1} appeared much greater than the bubble stiffness

approximated at 0.03 N m^{-1} . This difference was highlighted in Figure A- 10 presenting the graph plotting the effective stiffness versus the lateral dimension along the bubble cross-section for 500 pN load applied.

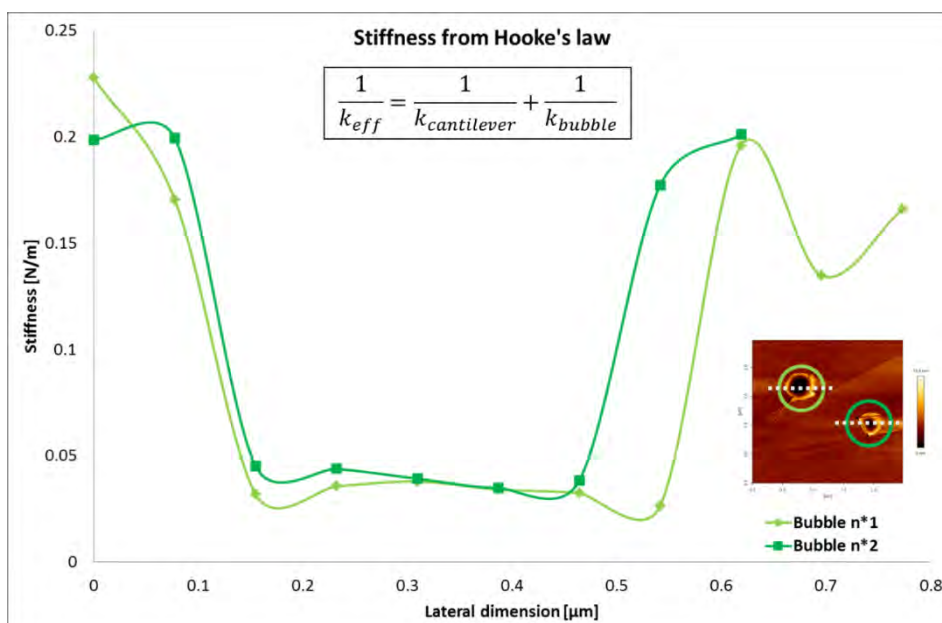


Figure A- 10 Graph plotting the relative stiffness computed via the Hooke's law versus the lateral dimension along the bubbles (light and dark green) cross-sections represented by a dotted white line on the height image.

These results were in line with the values reported in the literature obtained via PF-QNM and colloidal probe technique. This set of results showed that the entity present on a hydrophobic surface was indeed a bubble and not a nanoparticle.

The same experiment was repeated with a solution containing bulk nanobubbles freshly generated via microfluidics. The solution was left to settle for 30 minutes on the surface before imaging.

This step aimed to determine the presence of contaminants or residues on the surface which could have been induced during bulk nanobubbles generation via microfluidics. Firstly, several 10 by 10 μm areas of the surface were imaged to identify any bubbles or contaminants. Only bubbles randomly distributed were

observed on the surface. The 1.2 by 1.2 μm height and phase images presented in Figure A- 11 were obtained for the bulk nanobubbles solution deposited on HOPG surface. The number of nanobubbles on the surface was not enhanced by the presence of bulk nanobubbles in solutions compared to pure water deposited on HOPG.

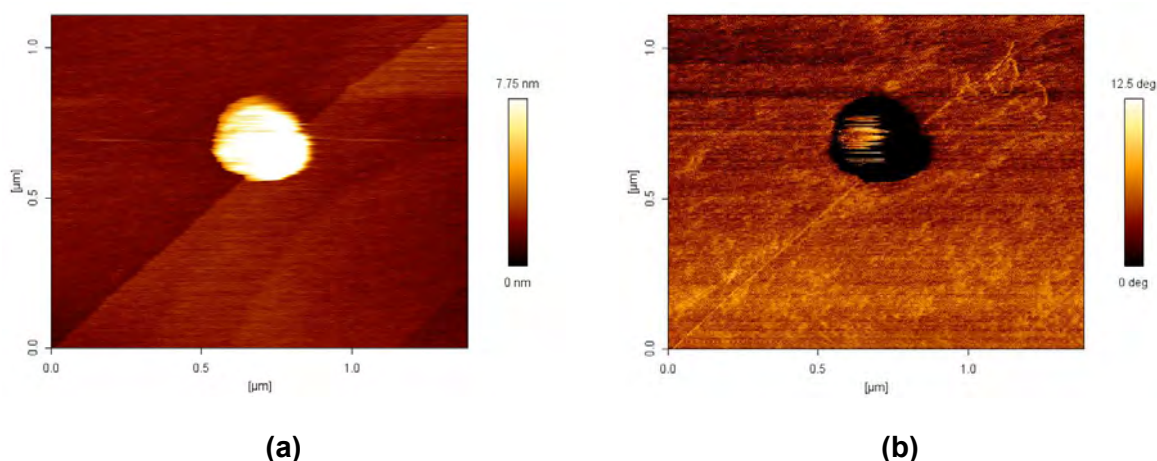
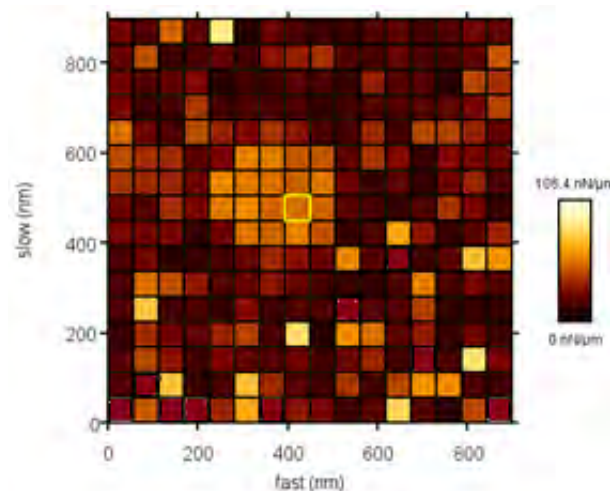


Figure A- 11 1.2 by 1.2 μm height (a) and phase (b) images obtained by tapping-mode AFM in a droplet of bulk nanobubbles water deposited on HOPG.

From Figure A- 11, the mean diameter and the height of the bubble were determined via the cross-section tool on the JPK Nanowizard software and estimated at 300 and 16 nm. The bubble appearance varied compared to previously because the image quality and properties depend on the imaging conditions (force, cantilever properties).

As previously for pure water, force spectroscopy measurement in contact mode was performed to determine the physical properties of these entities. A 16 by 16 pixels force map was realised from the image previously shown and the map distribution of the slope in the contact region of the force versus distance curve for each pixel composing the map was realised in Figure A- 11.



Relative slope map in retraction

Figure A- 12 16 by 16 pixels relative stiffness map realised from the slope of the retraction curve obtained for each pixels of the map from the previous 1.2 by 1.2 μm area.

From Figure A- 12, a difference could be observed between bubble and surface. This difference was quantified in Figure A- 13 presenting the histogram translating the two relative stiffness distributions corresponding to the bubble in bulk nanobubble water on HOPG surface and the surface itself in solution.

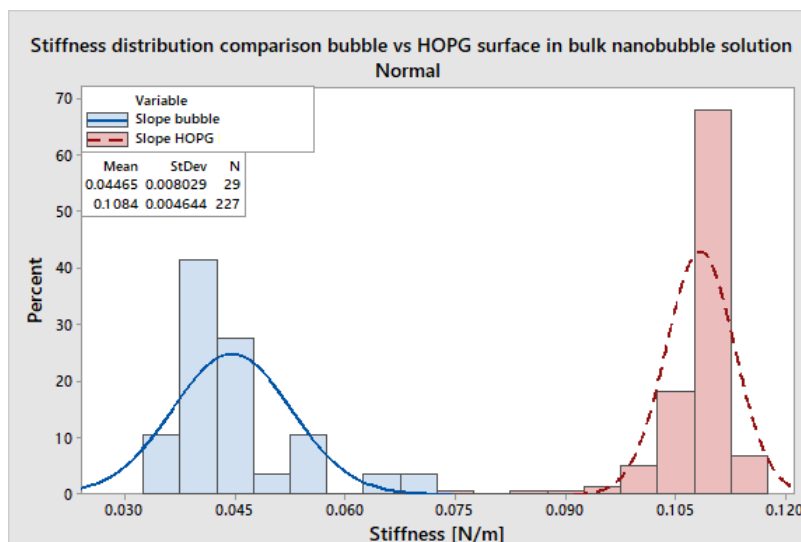


Figure A- 13 Relative stiffness distribution obtained from the force map representing the stiffness measured from surface pixels in red versus the bubble pixels in blue, in bulk nanobubbles solution.

As expressed previously, by computing the slope in the contact region both in approach and retraction, it was found that the bubble appeared softer than the surface: $0.045 \pm 0.002 \text{ N m}^{-1}$ for the bubble compared to $0.11 \pm 0.0003 \text{ N m}^{-1}$ for the HOPG surface in terms of relative stiffness. By applying the Hooke's law approximation, the bubble and surface stiffness become 0.06 and 0.19 N m^{-1} respectively. Thus, HOPG was stiffer than the bubble on HOPG in bulk nanobubble solution and in pure water. In addition, the nanobubbles probed in water and in bulk nanobubbles solution presented the same physical properties.

One could argue however that the gaseous nature of the entity hasn't been proven yet. Indeed, it was showed only that the nanoentities visible on the surface were softer than the surface. Consequently, a third set of experiment was performed where the properties observed for nanobubbles generated via electrochemical generation were compared to the one measured in acidic solution before applying any voltage.

A.1.2.2 Bubbles in acidic solution versus bubbles generated via electrochemical reaction

The aim of this part was to employ a technique called electrochemical generation which is based on the electrolysis of an acidic solution to generate either hydrogen or oxygen nanobubbles depending on the polarity applied to the electrodes as described in (Takenouchi, 2010). By applying a voltage to a conductive surface/electrolyte/electrode dipped in solution, only bubbles can be generated. Thus, by employing this technique that can only generate bubbles in acidic solution, the properties of bubble in acidic solution before and after electrochemical generation could be probed and compared.

Here are compiled the results obtained for bubbles nucleated on a HOPG surface in an acidic solution. An area of 1.5 by 1.5 μm was imaged by TM-AFM and the resulting height and phase images are showed in Figure A- 14.

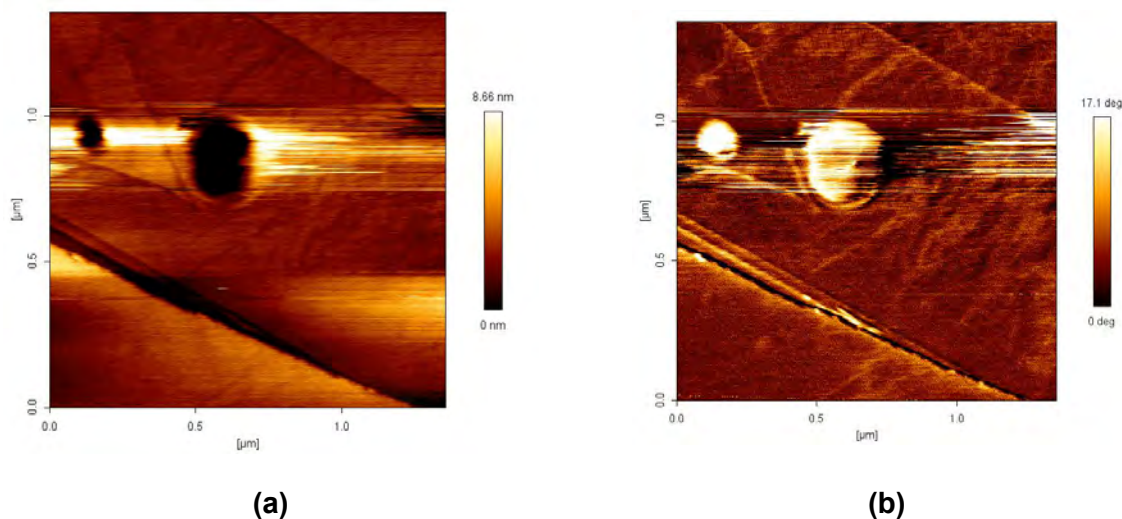
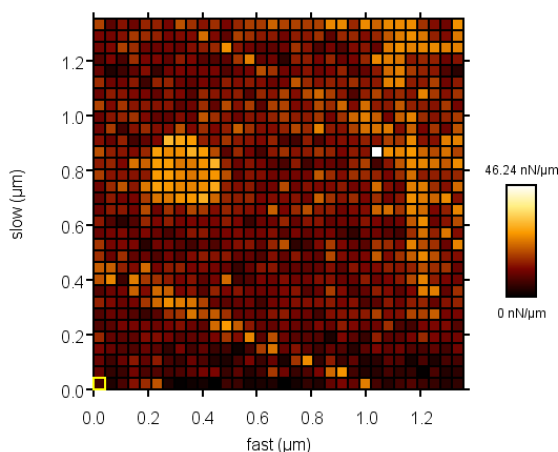


Figure A- 14 1.5 by 1.5 μm height (a) and phase (b) images obtained by tapping-mode AFM in a droplet of acidic solution deposited on HOPG.

Then, force spectroscopy measurement in contact mode was performed to determine the physical properties of this entity. A 32 by 32 pixels force map was generated from the 1.5 by 1.5 μm image and presented in Figure A- 15.



Relative slope map in retraction

Figure A- 15 32 by 32 pixels relative stiffness map obtained from the slope of the retraction curve obtained for each pixels of the map from the previous 1.5 by 1.5 μm area.

As previously realised, the force map can be translated into a histogram in Figure A-16 presenting two distinct distributions: the blue distribution representing the bubble showed a lower value of average slope around $0.03 \pm 0.0007 \text{ N m}^{-1}$ than the red distribution corresponding to the HOPG surface of about $0.09 \pm 0.0002 \text{ N m}^{-1}$.

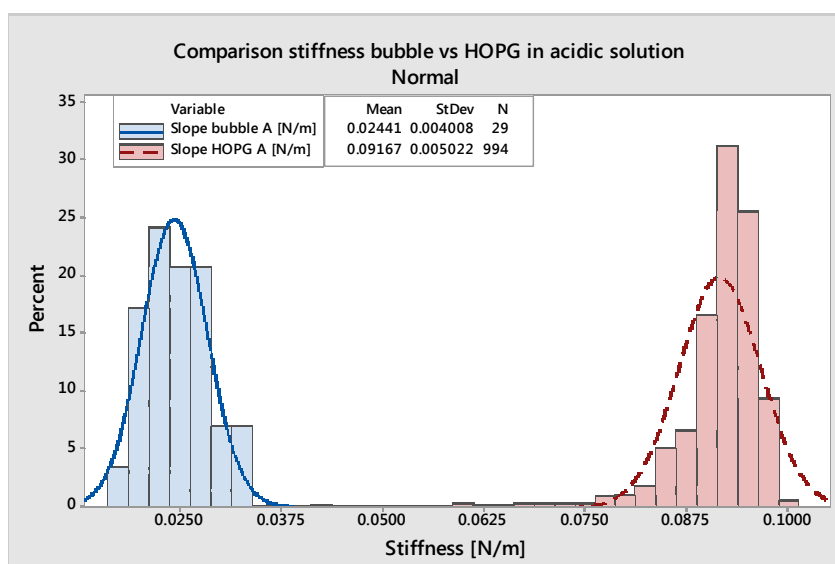


Figure A- 16 Relative stiffness distribution obtained from the force map representing the stiffness measured from surface pixels in red versus the bubble pixels in blue, in acidic solution.

These values become 0.06 and 0.23 N m^{-1} via the Hookean approximation. Thus, the surface appeared stiffer than the bubble. The same experiment was conducted with bulk nanobubbles generated via electrochemical generation from the same acidic solution to verify if bulk nanobubbles could influence in any way the surface nanobubbles formed on the surface and to prove the gaseous nature of the entities previously observed in acidic and in pure water solutions. The height (a) and phase (b) images of an entity present on HOPG surface and generated by electrochemical reaction are shown in Figure A- 17.

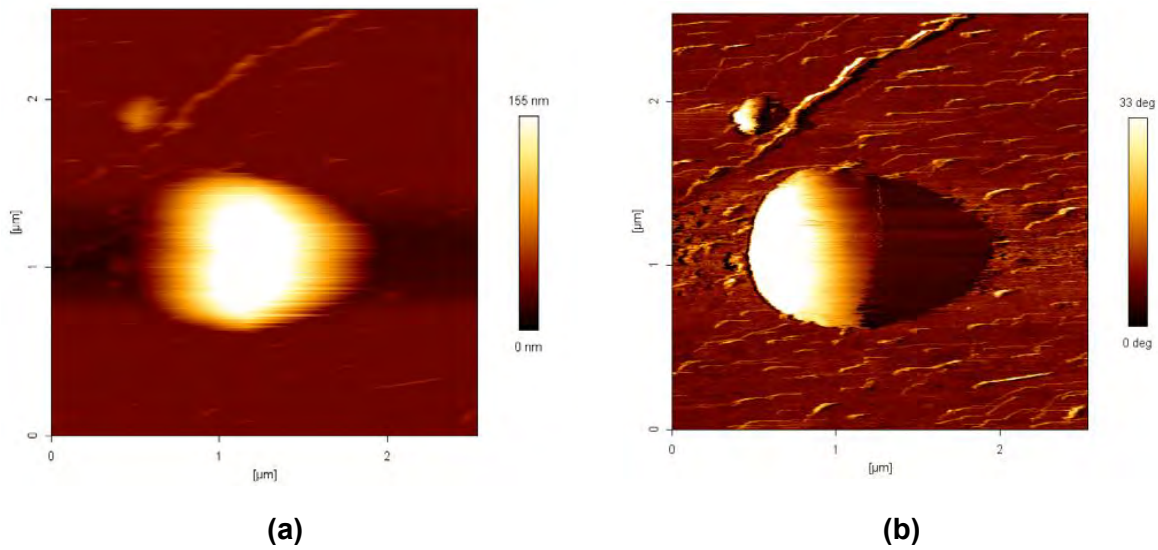
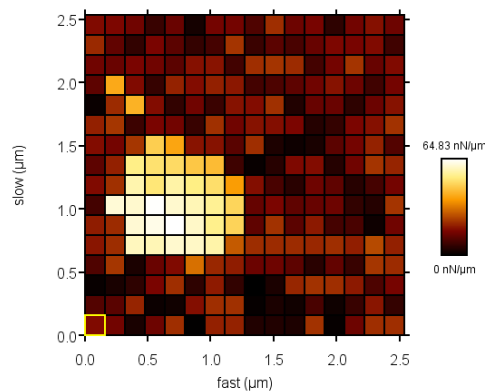


Figure A- 17 2.5 by 2.5 μm height (a) and phase (b) images obtained by tapping-mode AFM in a droplet of acidic solution deposited on HOPG and after electrochemical generation.

From these images, force spectroscopy measurement in contact mode was realised within a 16 by 16 pixels force map. This mode of generation created much more bubbles on the surface and in a faster way. The resulting map of relative stiffness is presented in Figure A- 18:



Relative slope/stiffness map in retraction

Figure A- 18 16 by 16 pixels relative stiffness map realised from the slope of the retraction curve obtained for each pixels of the map from the previous 2.5 by 2.5 μm area.

Similarly, the histogram in Figure A- 19 presents two different distributions: the HOPG distribution after electrochemical reaction (red) and the bubble distribution on HOPG after electrochemical reaction towards the lowest values of stiffness.

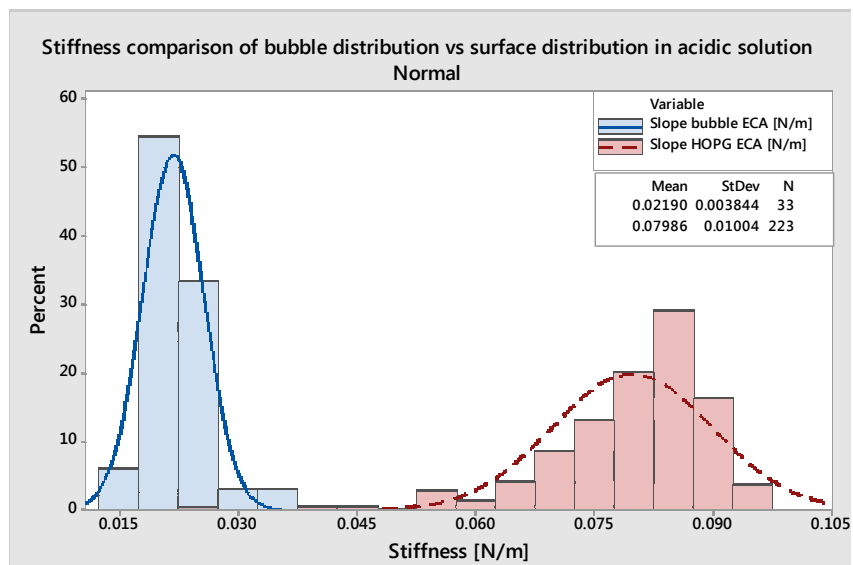


Figure A- 19 Relative stiffness distribution obtained from the force map representing the stiffness measured from surface pixels in red versus the bubble pixels in blue, in acidic solution after electrochemical generation.

The bubble distribution is centred at around $0.02 \pm 0.0007 \text{ N m}^{-1}$ whereas the HOPG surface distribution at about $0.08 \pm 0.0007 \text{ N m}^{-1}$. This is equivalent via the Hookean approximation to 0.06 and 0.23 N m^{-1} respectively.

A.2 Effect of gas inlet pressure for a fixed liquid flow rate and nozzle diameter

The results of the size distribution by intensity are illustrated in Figure A- 20.

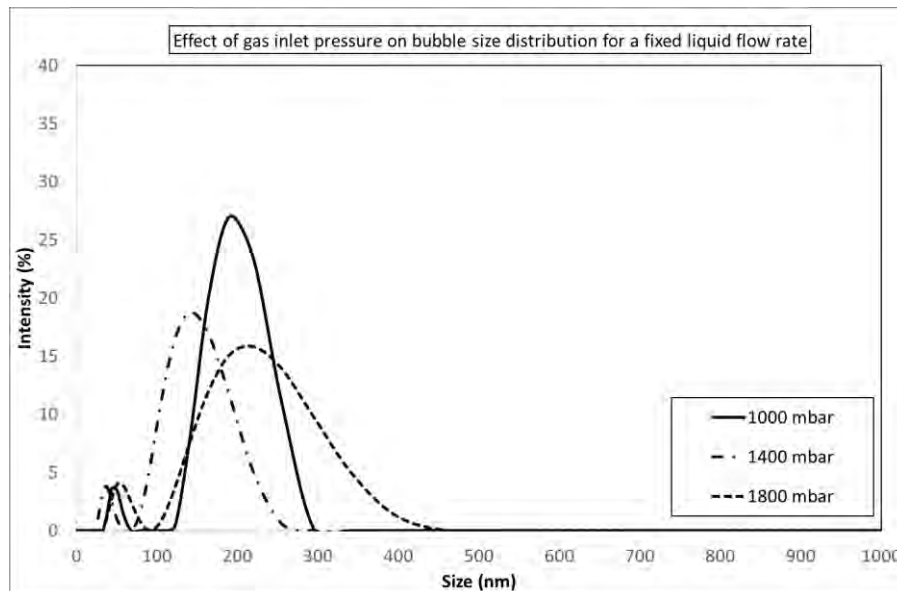


Figure A- 20 Effect of gas inlet pressures from 1000 (continuous line), 1400 (dotted – point line) to 1800 (smallest dotted line) mbar on bubble size distribution by intensity for a fixed liquid flow rate.

From 1000 to 1800 mbar, a similar range of nanobubble size was obtained from 50 to 450 nm. All the pressures presented a bimodal distribution (1000, 1200, 1400, 1600 and 1800 mbars) composed of a small peak below 100 nm and a larger peak centred between 150 to 300 nm. The results by number are represented in Figure A- 21.

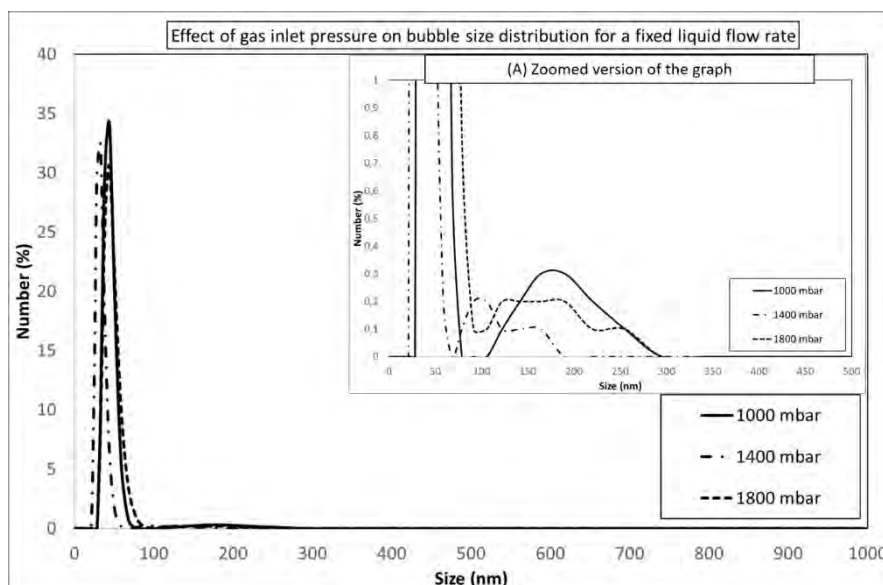


Figure A- 21 Effect of gas inlet pressure ranging from 1000 (continuous line), 1400 (dotted – point line) to 1800 (smallest dotted line) mbar on bubble size distribution by number for a fixed liquid flow rate. An inset in (A) describes the zoomed view of the regions towards the smallest number percentages and sizes.

Bimodal distributions were also observed by number. Indeed, contrary to the intensity distribution, the peak below 100 nm was much greater compared to the smaller peak centred at 150-200 nm. These results suggest that the number of nanobubbles in solution below 100 nm was greater than the number of 200 nm diameter nanobubbles for these cases and that the number of 200 nm decreased with the increase in gas pressure. This observation was further confirmed by the Z-average and PDI evolution in Figure A- 22.

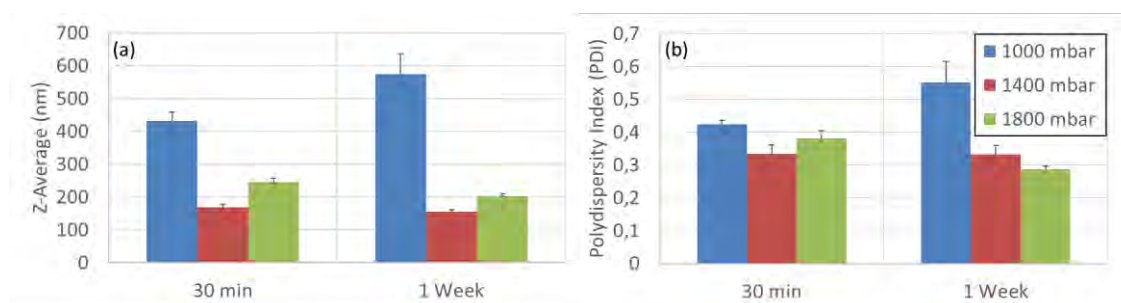


Figure A- 22 Effect of the gas inlet pressure on the evolution of the Z-average diameter (a) and Polydispersity Index (PDI, (b)) describing a bulk nanobubble distribution generated via the 20 µm nozzle.

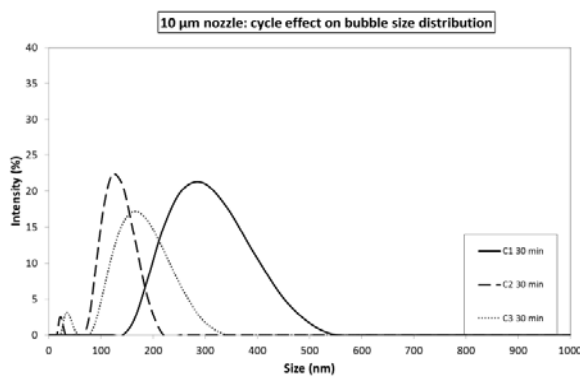
Indeed, the Z-average diameter decreased with an increasing gas inlet pressure due to a higher number of smaller bubbles in solution. The rise in gas inlet pressure and consequently gas flow rate, led to higher gas spraying generating smaller bubbles in solution. Thereby, the Z-average diameter decreased, and the bubble distribution narrowed down slightly due to the reduction in the number of bigger bubbles compared to the number of smaller bubbles in solution as illustrated in Figure A- 22 (b).

It was found that the gas inlet pressure impacted the bubble size distribution by enhancing the spraying phenomenon and by increasing the number of smaller nanobubbles. The zeta potential of all the distributions was varying between - 40 to - 50 mV. A negative zeta potential was reported previously by (Cho *et al.*, 2005) in various solutions.

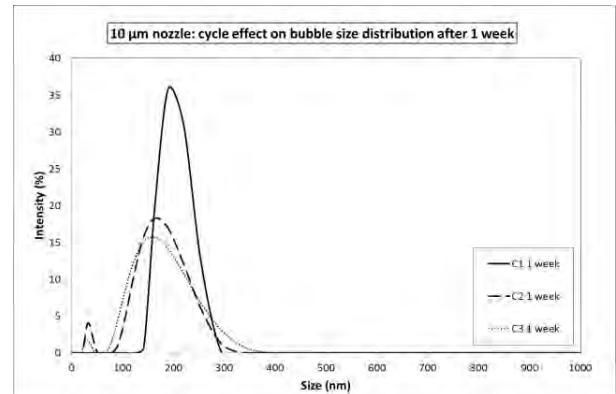
A.3 Effect of generation cycle on the nanobubble size distribution per nozzle

i. 10 μm nozzle

In Figure A- 23 are reported the average size distribution evolution by intensity of two experiments for the 10 μm nozzle for three generation cycles realised at 1000 mbar gas pressure and 90 $\mu\text{L min}^{-1}$ liquid flow rate.



(a)



(b)

Figure A- 23 Bulk nanobubbles intensity size distributions in pure water 30 min (a) and 1 week after generation (b) over time and through three generation cycles (C1, plain black - C2, dotted black line - C3, smallest dotted black line) via the 10 μm nozzle microfluidic device.

This first set of results shows that repeating the cycle of generation is impacting the bubble size distribution. For the 10 μm nozzle, the size distribution was shifted towards the smaller size of bubbles as illustrated by the evolution of the Z-average diameter per cycle of generation in Figure A- 24.

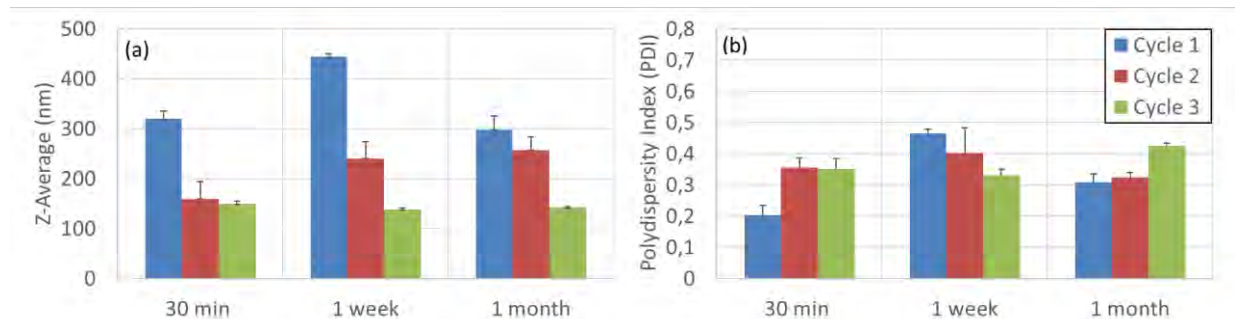


Figure A- 24 Evolution of the Z-average diameter (a) and Polydispersity Index (PDI, (b)) describing the bulk nanobubbles distribution in solution per cycle of generation for the 10 μm nozzle.

It was observed that the concentration of smaller bubbles increased with the cycle. The Z-average diameter evolution for two experiments confirmed that the cycle repeat for 10 μm nozzle enhanced the generation of smaller nanobubbles so that polydispersity index almost doubled between cycle 1 and cycle 2 & 3, 30 minutes after generation as represented in Figure A- 24 (b). Each distribution from C1 to C3

was stable up to 1 month. Interestingly, the C3 presented the most stable z-average diameter and PDI.

ii. 15 μm nozzle

In Figure A- 25 are presented the results of the effect of the generation cycle on the bubble size distribution for the 15 μm nozzle:

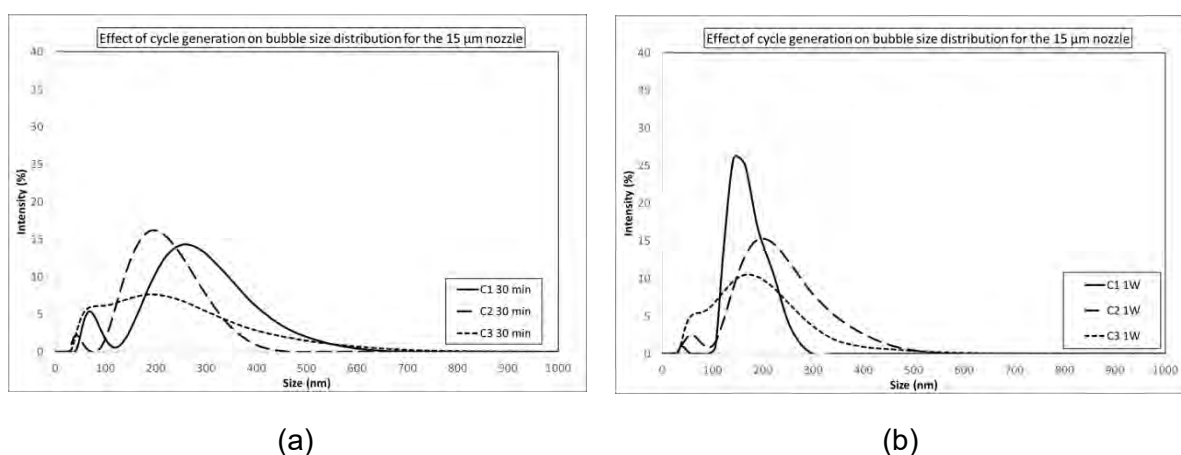


Figure A- 25 Bulk nanobubbles size distributions by intensity in pure water through three generation cycles (C1, plain black - C2, dotted black line - C3, smallest dotted black line) via the 15 μm nozzle microfluidics device 30 minutes (a) and 1 week after generation (b).

30 minutes after generation via the 15 μm nozzle device, a bimodal distribution was obtained. This distribution persisted throughout the generation cycles and similarly up to 1 week after generation as represented in Figure A- 25(b). However, the distribution described in the graphs (a) and (b) in Figure A- 25 demonstrated that the bubble distribution was impacted by the generation cycle. At C3, the peak of the biggest bubbles (150-200 nm) was reduced compared to the peak below 100 nm. This was due to a higher number of small bubbles in solution compared to the largest ones. This change could be due to the number increase of the small bubbles to the detriment of the bigger bubbles which were transformed/split into smaller bubbles by the repeat of the generation cycle. This hypothesis was supported by the evolution of the z-average that went from 260 nm at C1 down to 140 nm at C3. From Figure A-

25(b), one week after generation, the intensity distribution was still bimodal, however, the peaks became thinner compared to the 30 minutes distribution. The disappearance of the largest nanobubbles with time could be the reason for this result. From Figure A- 26, one week and one month after generation, the same cycle effect on the bubble distribution was observed: the more cycle, the bigger number of smaller nanobubbles were present in solutions.

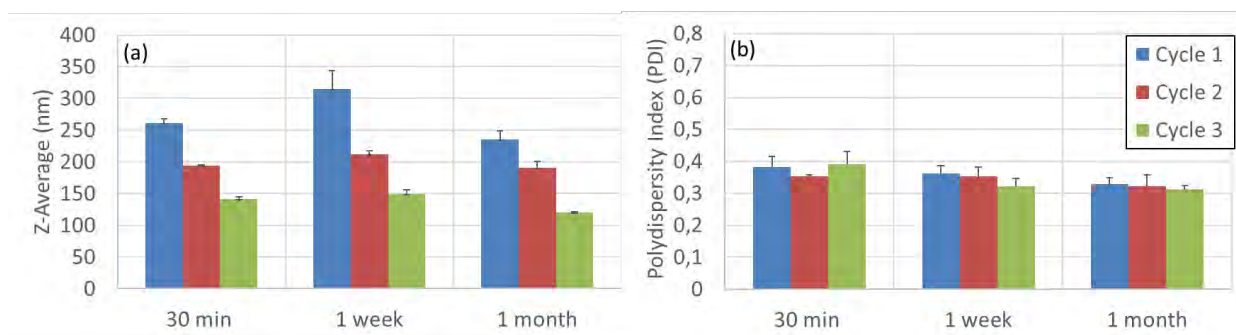


Figure A- 26 Evolution of the Z-average diameter describing the bulk nanobubbles distribution in solution per cycle of generation for the 15 μ m nozzle.

From Figure A- 26 (b), thirty minutes after generation, the PDI evolution was not significantly impacted by the cycle effect. Nevertheless, the cycle repeat affected similarly the PDI evolution: the more cycles, the narrower the bubble distribution became due to an increase in the number of small nanobubbles in solution for a limited or decreasing number of larger nanobubbles in solution. In addition, all the bubbles generated via the various cycles persisted similarly up to one month.

A.4 Effect of viscosity on nanobubbles formation & stability

i. Effect of adding 10% wt. glycerol in solution

Lastly, there is a real need to understand if the increase in viscosity due to the addition of glycerol in solution can prevent the formation of nanobubbles.

Consequently, the effect of the increase in viscosity on the bubble size distribution obtained via microfluidics is illustrated in Figure A- 27.

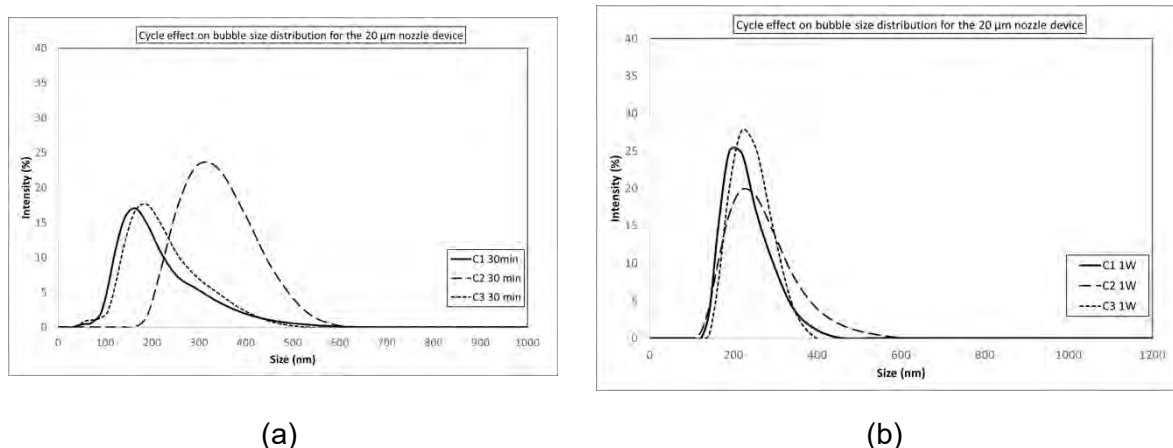


Figure A- 27 Bulk nanobubbles-nanoparticles size distributions by intensity (a) 30 minutes and (b) one week after generation from 10% wt. glycerol aqueous solution through 3 generation cycles (C1, plain black - C2, dotted black line - C3, smallest dotted black line)

In Figure A- 27 (a), 30 minutes after generation, a monodisperse peak was observed centred between 200 to 300 nm for each cycle.

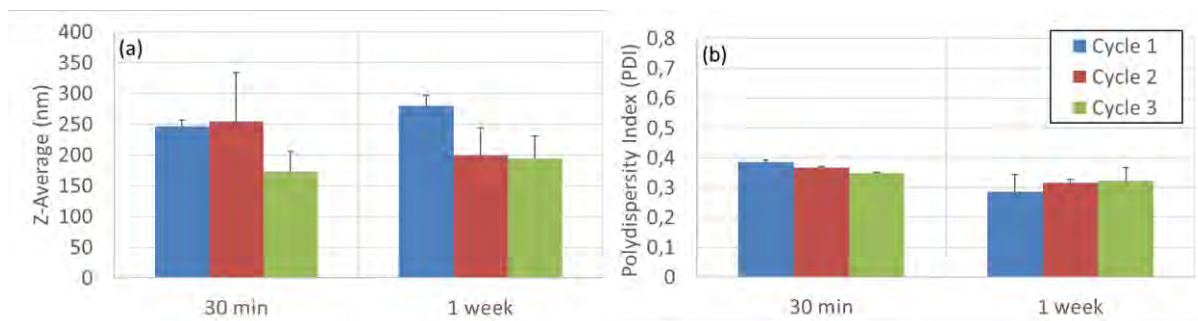


Figure A- 28 Evolution of the Z-average diameter (a) and the Polydispersity Index (PDI, (b)) describing the bulk nanobubbles distribution per cycle of generation for the 20 μm nozzle.

From Figure A- 28 (a) depicting the Z-average diameter evolution, it is found that the cycle effect is limited at higher viscosity. Indeed, the differences between the three cycles are minimised due to the variability of the measurement. From the PDI evolution described in Figure A- 28 (b), the same observation can be made, the three cycles present a similar bubble distribution. From Figure A- 27 (b) after one week,

similar monodispersed distributions centred at 200 nm were found for all cycles. Besides, the average zeta potential throughout the cycles and the repeats was approximated to -28.8 ± 1.42 mV. Therefore, the nanobubbles generation in solution despite the increase in viscosity was confirmed and the nanobubbles formed were as stable as previously.

Furthermore, the increase in viscosity caused an increase in the mean bubble diameter with the cycle effect as summarised in Figure A- 28. Indeed, with pure water by C3, the bubble size tended to be shifted towards the smallest size whereas in this case, it persisted at around 200 nm.

The viscosity increase could have acted at two levels: at the nanobubble stability level by opposing the expansion of the bubble, but also during the bubble formation by spraying.

It is well-known that the spraying process in a Rayleigh-Taylor instability is enhanced by an increase in viscosity because it heightened the viscous effect and the time required for the instability to propagate (Gaillard, 2016). Thus, the jet has more time to thin before being split, forming smaller bubbles. Nevertheless, the increase in viscosity caused the liquid action on the gas for the same flow rate to be less effective. Therefore, the atomisation like-spray required more energy to be realised, causing a lesser level of bubble splitting and the formation of larger nanobubbles in solution.

A.5 List of references

- An, H., Tan, B. H. and Ohl, C. D. (2016) 'Distinguishing Nanobubbles from Nanodroplets with AFM: The Influence of Vertical and Lateral Imaging Forces', *Langmuir*, 32, pp. 12710–12715. doi: 10.1021/acs.langmuir.6b02519.
- Attard, P. and Miklavcic, S. J. (2001) 'Effective Spring Constant of Bubbles and Droplets', *Langmuir*, 17, pp. 8217–8223. doi: 10.1021/la010969g.
- Berkelaar, R. P. *et al.* (2014) 'Exposing nanobubble-like objects to a degassed environment', *Soft Matter*, 10, pp. 4947–4955. doi: 10.1039/C4SM00316K.
- Bharat, B., Yuliang, W. and Abdelhamid, M. (2008) 'Coalescence and movement of nanobubbles studied with tapping mode AFM and tip–bubble interaction analysis', *Journal of Physics: Condensed Matter*, 20, p. 485004. Available at: <http://stacks.iop.org/0953-8984/20/i=48/a=485004>.
- Butt, H.-J. (1991) 'Measuring electrostatic, van der Waals, and hydration forces in electrolyte solutions with an atomic force microscope', *Biophysical Journal*, 60, pp. 1438–1444. doi: [http://dx.doi.org/10.1016/S0006-3495\(91\)82180-4](http://dx.doi.org/10.1016/S0006-3495(91)82180-4).
- Butt, H.-J., Cappella, B. and Kappl, M. (2005) 'Force measurements with the atomic force microscope: Technique, interpretation and applications', *Surface Science Reports*, 59, pp. 1–152. doi: <http://dx.doi.org/10.1016/j.surfrep.2005.08.003>.
- Cho, S.-H. *et al.* (2005) 'Ultrasonic formation of nanobubbles and their zeta-potentials in aqueous electrolyte and surfactant solutions', *Colloids and Surfaces A: Physicochemical and Engineering Aspects*, 269, pp. 28–34. doi: <http://dx.doi.org/10.1016/j.colsurfa.2005.06.063>.
- Ducker, W. A., Xu, Z. and Israelachvili, J. N. (1994) 'Measurements of Hydrophobic and DLVO Forces in Bubble-Surface Interactions in Aqueous Solutions', *Langmuir*, 10, pp. 3279–3289. doi: 10.1021/la00021a061.
- Gaillard, T. (2016) *Confined flow at high and low Reynolds : Millifluidic foaming and drainage of thin copolymer films*. Université Paris Saclay. Available at: <https://tel.archives-ouvertes.fr/tel-01402333>.
- Hampton, M. A., Donose, B. C. and Nguyen, A. V (2008) 'Effect of alcohol–water exchange and surface scanning on nanobubbles and the attraction between hydrophobic surfaces', *Journal of Colloid and Interface Science*, 325, pp. 267–274. doi: <http://dx.doi.org/10.1016/j.jcis.2008.05.044>.
- Holmberg, M. *et al.* (2003) 'Nanobubble Trouble on Gold Surfaces', *Langmuir*, 19, pp. 10510–10513. doi: 10.1021/la0352669.
- Ishida, N. *et al.* (2000) 'Nano Bubbles on a Hydrophobic Surface in Water Observed by Tapping-Mode Atomic Force Microscopy', *Langmuir*, 16, pp. 6377–6380. doi: 10.1021/la000219r.
- Lou, S.-T. *et al.* (2000) 'Nanobubbles on solid surface imaged by atomic force microscopy', *Journal of Vacuum Science & Technology B*, 18, pp. 2573–2575. doi: <http://dx.doi.org/10.1116/1.1289925>.

McConney, M. E., Singamaneni, S. and Tsukruk, V. V (2010) 'Probing Soft Matter with the Atomic Force Microscopies: Imaging and Force Spectroscopy', *Polymer Reviews*. Taylor & Francis, 50(3), pp. 235–286. doi: 10.1080/15583724.2010.493255.

Song, Y. *et al.* (2014) 'The Origin of the "Snap-In" in the Force Curve between AFM Probe and the Water/Gas Interface of Nanobubbles', *ChemPhysChem*, 15, pp. 492–499. doi: 10.1002/cphc.201301081.

Takenouchi, T. (2010) 'Behavior of hydrogen nanobubbles in alkaline electrolyzed water and its rinse effect for sulfate ion remained on nickel-plated surface', *Journal of Applied Electrochemistry*, 40, pp. 849–854. doi: 10.1007/s10800-009-0068-z LB - Takenouchi2010.

Yang, S. *et al.* (2009) 'Electrolytically Generated Nanobubbles on Highly Orientated Pyrolytic Graphite Surfaces', *Langmuir*, 25, pp. 1466–1474. doi: 10.1021/la8027513.

Zhang, L. *et al.* (2006) 'Electrochemically Controlled Formation and Growth of Hydrogen Nanobubbles', *Langmuir*, 22, pp. 8109–8113. doi: 10.1021/la060859f.

Zhang, X. H. *et al.* (2005) 'Nanobubbles at the interface of hopg and ethanol solution', *International Journal of Nanoscience*, 04, pp. 399–407. doi: 10.1142/s0219581x05003152.

Zhang, X. H. and Ducker, W. (2007) 'Formation of Interfacial Nanodroplets through Changes in Solvent Quality', *Langmuir*, 23, pp. 12478–12480. doi: 10.1021/la702453g.

Zhang, X. H., Maeda, N. and Craig, V. S. J. (2006) 'Physical Properties of Nanobubbles on Hydrophobic Surfaces in Water and Aqueous Solutions', *Langmuir*, 22, pp. 5025–5035. doi: 10.1021/la0601814.

Zhang, X., Kumar, A. and Scales, P. J. (2011) 'Effects of Solvency and Interfacial Nanobubbles on Surface Forces and Bubble Attachment at Solid Surfaces', *Langmuir*, 27, pp. 2484–2491. doi: 10.1021/la1042074.

Zhao, B. *et al.* (2013) 'Mechanical mapping of nanobubbles by PeakForce atomic force microscopy', *Soft Matter*, 9, pp. 8837–8843. doi: 10.1039/C3SM50942G.